

Final Report

AWARD NUMBER:
DE-FG07-07ID14768

AWARDEE NAME:
University of Illinois, Urbana-Champaign

Lattice Boltzmann Methods to Address Fundamental Boiling and Two-Phase Problems

Rizwan Uddin
Department of Nuclear, Plasma and Radiological Engineering
University of Illinois at Urbana-Champaign
104 S. Wright St., Urbana, IL 61801
rizwan@illinois.edu

Lattice Boltzmann Methods to Address Fundamental Boiling and Two-Phase Problems

Rizwan-uddin

Department of Nuclear, Plasma and Radiological Engineering
University of Illinois at Urbana-Champaign
104 S. Wright St., Urbana, IL 61801

The project titled above has been completed as proposed. In fact, as is not uncommon in research, additional issues that were not proposed in the original proposal also were addressed. This report is based on a PhD dissertation that resulted from this work. Research carried out under this grant has been recognized nationally. Student supported by this grant completed his PhD, and is now employed at ORNL. His research on LBM was recognized by the American Nuclear Society by the Mark Mills Award (best research work by a graduate student) for the year 2010.

Abstract

In this research, a new lattice Boltzmann model, called the artificial interface lattice Boltzmann model (AILB model), is proposed for the simulation of two-phase dynamics. The model is based on the principle of free energy minimization and invokes the Gibbs-Duhem equation in the formulation of non-ideal forcing function. Bulk regions of the two phases are governed by a non-ideal equation of state (for example, the van der Waals equation of state), whereas an artificial near-critical equation of state is applied in the interfacial region. The interfacial equation of state is described by a double well density dependence of the free energy. The continuity of chemical potential is enforced at the interface boundaries. Using the AILB model, large density and viscosity ratios of the two phases can be simulated. The model is able to quantitatively capture the coexistence curve for the van der Waals equation of state for different temperatures. Moreover, spatially varying viscosities can be simulated by choosing the relaxation time as a function of local density.

Suitable velocity and density (pressure) boundary conditions are also developed for the particle distribution functions in the framework of the proposed model. Boundary conditions for both the 2D as well as 3D domains are developed and relationships to evaluate unknown distribution functions are explicitly provided. Based on the Cahn's wetting theory, physics governing the wall-fluid interactions is also developed in the framework of the AILB model. Using it, any specified contact angle (ranging from 0° to 180°) can be simulated at the walls of

the domain. The proposed AILB model and the Lee-Fischer LB model are evaluated on several simple problems which involve interactions between two phases of a fluid and, between two phases and solid walls. Some of these problems in the order of increasing complexity are: the simulation of multi-fluid Poiseuille-Couette flow, specifying static bubbles/droplets in a periodic domain, two-bubble or two-drop coalescence, single rising bubble, break-up of a drop/bubble due to shearing walls, specifying different equilibrium contact angles on the surfaces, dynamics of drop/bubble in contact with a surface, etc.

In addition, a simulation methodology based on the Peng-Robinson (P-R) equation of state has been devised in the LB framework. The developed P-R model can accurately predict phase-coexistence curve for water and steam at different system temperatures and allows simulation of phases with varying density/viscosity ratios.

Thermal effects in the AILB model are simulated by employing a separate distribution function responsible for tracking the temperature dynamics. A phenomenological model to simulate evaporation and condensation is also developed in the framework of the proposed model. The thermal model is able to qualitatively capture the bubble growth and shrinking dynamics due to the variations in surrounding bulk temperatures.

For the numerical analyses using the LBM, a computer code is developed to solve problems in both 2D and 3D. The code can run on a single processor PC as well as on a parallel cluster. The code has been written in FORTRAN90 language and incorporates MPI paradigm for parallelization.

Following publications have resulted from this research (thus far).

- Prashant K. Jain, Adrian Tentner, Rizwan-uddin, “A Lattice Boltzmann Framework to Simulate Boiling Water Reactor Core Hydrodynamics”, Computers and Mathematics with Applications, 58, 975-986 (2009).
- Prashant K. Jain, Adrian Tentner, Rizwan-uddin, “Lattice Boltzmann Simulation of Liquid Drop Coalescence driven by Surface Tension”, Transactions of ANS Winter Meeting, Nov 15-19, 2009, Washington DC, USA (2009).
- Prashant K. Jain, Adrian Tentner, Rizwan-uddin, “A Lattice Boltzmann Framework for the Simulation of Boiling Hydrodynamics in BWRs”, Transactions of ANS Annual Meeting, June 8-12, 2008, Anaheim CA, USA (2008).
- Prashant K. Jain, Rizwan-uddin, “A 3D, Parallel LBM to Simulate Gravity Driven Bubbly and Slug Flows”, Transactions of ANS/ENS Winter Meeting, Washington DC, USA, November 11-15 (2007).
- Prashant K. Jain, Rizwan-uddin, “Lattice Boltzmann Method for Nuclear Engineers”, International Conference of Mescoscopic Methods in Engineering and Science (ICMMES), Munich, Germany, July 16-20 (2007).
- Prashant K. Jain, Suneet Singh, Yizhou Yan, Rizwan-uddin, “Advanced Computing to Bridge Micro and Macro: LBM, Advanced CFD and Coupled CFD-System Codes”, Computational Engineering and Science Conference (CESC-2007), Washington DC, USA, April 10-12 (2007).

Table of contents

Chapter 1	1
Introduction.....	1
1.1 Motivation.....	2
1.2 Several computational approaches.....	4
1.3 An overview of lattice Boltzmann method (LBM).....	7
1.4 Objectives	8
1.5 Outline.....	9
1.6 References.....	10
Chapter 2	13
Theoretical framework.....	13
2.1 Continuous Boltzmann transport equation (CBE)	14
2.2 Simplification of Boltzmann collision integral Ω_{Boltz}	14
2.3 Explicit determination of the forcing term $\mathbf{F} \cdot \nabla_{\mathbf{v}} f$	15
2.4 Series expansion of equilibrium distribution function f^{eq}	16
2.5 Links to hydrodynamics.....	16
2.6 Discretization in velocity space	17
2.7 Discrete equilibrium distribution function: f_a^{eq}	18
2.8 Determining f_a^{eq} for a D ₂ Q ₉ lattice	20
2.9 Recovery of the LBE from the discrete Boltzmann equation (DBE)	21
2.10 Apriori derivation of the LBE from the CBE	23
2.11 Summary	24
2.12 References.....	25
Chapter 3	28
Lattice Boltzmann equation for non-ideal fluids	28
3.1 Modified Boltzmann equation: Enskog equation	30
3.1.1 Approximation of Enskog collision operator Ω_{Enskog}	31
3.1.2 Evaluation of $\Omega_{Enskog}^{(0)}$	32
3.1.3 Evaluation of $\Omega_{Enskog}^{(1)}$	32
3.1.4 Evaluation of $\Omega_{Enskog}^{(2)}$	33

3.1.5	Evaluation of Ω_{Enskog}	34
3.1.6	Lattice velocity moments of J_a	34
3.2	Enskog equation based lattice Boltzmann equation.....	35
3.3	A survey of two-phase models in the LB framework.....	37
3.3.1	Shan-Chen (S-C) model	37
3.3.2	He-Shan-Doolen (HSD) model.....	39
3.3.3	Free energy based model	40
3.3.4	Pressure evolution model	41
3.4	Summary	41
3.5	References.....	42
Chapter 4	46
Artificial interface lattice Boltzmann (AILB) model.....		46
4.1	Discrete Boltzmann (DB) equation.....	47
4.2	Lattice Boltzmann (LB) equation	49
4.3	Modified distribution function $g_a(\mathbf{r}, t)$	50
4.4	Forcing terms to simulate phase segregation	51
4.4.1	Long range attractive force \mathbf{F}_{attr}	51
4.4.2	Short range repulsive force \mathbf{F}_{rep}	52
4.4.3	Net force \mathbf{F}	52
4.4.4	Gibbs-Duhem (G-D) equation	52
4.5	Chemical potential μ_0 in the Lee-Fischer LB model	53
4.6	Chemical potential μ_0 in the AILB model.....	56
4.6.1	Bulk equation of state	56
4.6.2	Interfacial equation of state.....	57
4.6.3	Proposed scaling for the van der Waals EOS in the AILB model	58
4.7	Numerical discretization schemes.....	60
4.8	Numerical implementation.....	62
4.8.1	Initialization (at time $t = 0$)	62
4.8.2	Time marching	65
4.8.3	Calculation of macroscopic properties.....	69
4.9	Simulation of equilibrium contact angles	69
4.9.1	Wettability and the contact angle θ_w	69

4.9.2	Several approaches to simulate θ_w in LBM	71
4.9.3	Cahn's theory of wetting dynamics	71
4.9.4	Implementation of Cahn's theory in the AILB model	75
4.9.5	Simulation of θ_w in the AILB model.....	77
4.10	Simulation of spatially-varying viscosities.....	79
4.11	Simulation of buoyancy effects in the LB model	80
4.12	Similarities with the phase-field modelling technique.....	81
4.13	References.....	81
Chapter 5	86
Boundary conditions for the AILB model	86
5.1	Velocity boundary conditions in 2D	88
5.1.1	South boundary	89
5.1.2	South-West (SW) corner.....	92
5.2	Density boundary conditions in 2D	94
5.2.1	South boundary	94
5.2.2	South-West (SW) corner.....	95
5.3	Velocity boundary conditions in 3D	97
5.3.1	Bottom boundary	99
5.4	Future directions of research.....	101
5.5	References.....	102
Chapter 6	104
Results and discussions	104
6.1	Multi-fluid Poiseuille-Couette flow in a 2D channel.....	104
6.1.1	Analytical solution.....	104
6.1.2	LBM simulations	107
6.1.3	Results obtained using the Lee-Fischer LB model	107
6.2	Simulation of the van der Waals coexistence curve	111
6.2.1	Saturated liquid and vapour densities from Maxwell construction ..	115
6.2.2	Spinodal decomposition.....	116
6.2.3	Comparison of LBM simulations with densities obtained via Maxwell construction for the vdW EOS	121
6.3	Simulation of a vapor bubble coexisting with liquid.....	121
6.4	Simulation of coalescence of two bubbles/droplets.....	129

6.4.1	Experimental observations and results.....	129
6.4.2	LBM simulations	133
6.5	Simulation of the Rayleigh-Taylor instability	138
6.6	Deformation and break-up of a bubble by shear forces	139
6.7	Simulation of wall contact angle(s)	142
6.8	Bubble detachment from a wall surface.....	147
6.9	Single rising bubble in a quiescent liquid.....	149
6.9.1	Experimental observations and results.....	150
6.9.2	Results obtained using the Lee-Fischer LB model	153
6.9.3	Results obtained using the AILB model	159
6.10	Some guidelines to avoid shrinkage of the dispersed phase	161
6.11	References.....	162
Chapter 7	166
Peng-Robinson Equation of State (P-R EOS) based two-phase model	166
7.1	D ₂ Q ₉ scheme with LBGK approximation.....	166
7.2	Particle interaction potential and force	167
7.3	Numerical implementation on a D ₂ Q ₉ lattice.....	168
7.4	Simulation of the body forces	169
7.5	Peng-Robinson (P-R) equation of state.....	170
7.6	Kinematic viscosities of liquid and vapor phases	173
7.7	Results and discussions.....	174
7.8	Conclusions.....	182
7.9	References.....	183
Chapter 8	184
Simulation of thermal effects	184
8.1	Thermal energy distribution LB model.....	186
8.2	Density dependent thermal diffusivities: $\alpha_T(\rho)$	187
8.3	Wall Temperature BCs (Dirichlet type).....	188
8.4	Wall Heat Flux BCs (Neumann type).....	190
8.5	Simulation of evaporation and condensation.....	190
8.6	Results and discussions.....	192
8.7	References.....	197
Chapter 9	200

Summary and Conclusions	200
Appendix A	204
Lattice Boltzmann equation to Navier-Stokes (N-S) equations.....	204
A.1 Multi-scale expansion	204
A.2 Forcing term in the LB equation.....	206
A.3 Order separation of LBE.....	206
A.4 First order macrodynamics: $E_a^{(1)}$	208
A.4.1 Mass conservation: $\sum_a E_a^{(1)} = 0$	208
A.4.2 Momentum conservation: $\sum_a v_{a\alpha} E_a^{(1)} = 0$	208
A.4.3 Evaluation of $\Pi_{\alpha\beta}^{(0)}$	209
A.5 Second order macrodynamics: $E_a^{(2)}$	210
A.5.1 Mass conservation: $\sum_a E_a^{(2)} = 0$	210
A.5.2 Momentum conservation: $\sum_a v_{a\alpha} E_a^{(2)} = 0$	211
A.6 Order-combined macro-dynamics: $\varepsilon E_a^{(1)} + \varepsilon^2 E_a^{(2)}$	212
A.6.1 Mass conservation: $\sum_a (\varepsilon E_a^{(1)} + \varepsilon^2 E_a^{(2)}) = 0$	212
A.6.2 Momentum conservation: $\sum_a v_{a\alpha} (\varepsilon E_a^{(1)} + \varepsilon^2 E_a^{(2)}) = 0$	213
A.6.3 Incompressible limit: $\rho = \text{constant}$	213
A.7 Remarks on fluid viscosity in the LB equation.....	213
Appendix B	215
Code, Parallelization and Performance	215
B.1 Domain decomposition	215
B.2 Data partition and performance	216
B.3 Efficiency with fixed problem size per processor.....	216
Appendix C	219
Velocity boundary conditions in 2D	219
C.1 North boundary	219
C.2 West boundary	220
C.3 East boundary	221

C.4	South East (SE) corner.....	222
C.5	North East (NE) corner	223
C.6	North West (NW) corner	225
Appendix D		227
Density boundary conditions in 2D		227
D.1	North, West and East boundaries.....	227
D.2	South East (SE), North East (NE) and North West (NW) corners	228
Appendix E		231
Velocity boundary conditions in 3D		231
E.1	Top boundary	231
E.2	South boundary	232
E.3	North boundary	234
E.4	West boundary	236
E.5	East boundary.....	237
Appendix F.....		240
Mathematica routine for Maxwell construction.....		240
Appendix G		242
Conversion between physical and lattice units		242
G.1	Direct conversion	242
G.1.1	Acoustics based conversion	243
G.1.2	Gravity based conversion.....	244
G.1.3	How many “physical molecules” does a “LB particle” represent?....	245
G.2	Dimensionless formulation	245
G.2.1	Governing equations in physical units.....	246
G.2.2	From physical (P) to non-dimensional (ND) system	246
G.2.3	From non-dimensional (ND) to lattice Boltzmann (LB) system	247
G.2.4	Illustrative example.....	248
G.2.5	How to appropriately pick Δt ?.....	249
G.3	References.....	250

Chapter 1

Introduction

Dynamics of two-phase flows plays an important role in many fields of applied science and engineering, including oil-water flow in porous media, boiling fluids, liquid metal melting and solidification, and many more. Typically two-phase flows manifest a wide variety of geometrical patterns (or flow regimes) of associated phases depending on the system conditions. These patterns include, but are not limited to, bubbly, slug, churn and annular flows. Most common two-phase patterns observed in a vertical tube flow-boiling experiment are shown in Fig. 1.1. These multiple flow patterns significantly affect the overall system hydrodynamics by varying the heat transfer and pressure drop characteristic of a given flow.

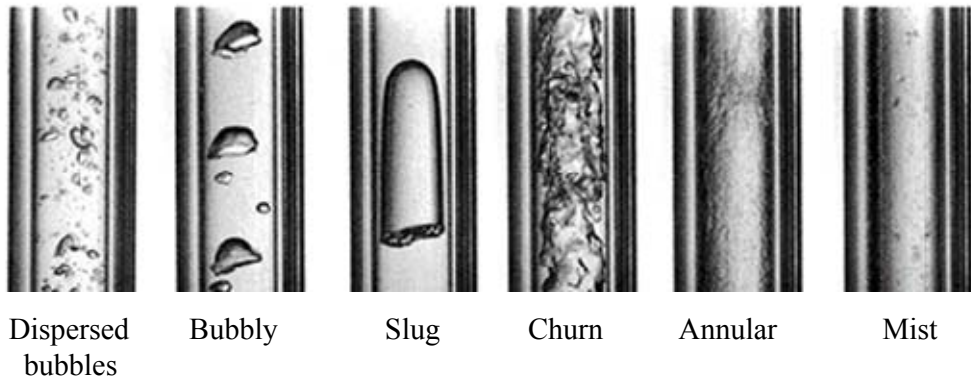


Fig. 1.1: Typical two-phase flow patterns observed in a vertical tube flow-boiling experiment (fluid: R134a, tube internal diameter: 4.34 mm, pressure: 10 bar) (Hua et al., 2004).

Due to the existence of different flow regimes and their temporal and spatial local transitions (depending upon the local system conditions), predictive modeling becomes difficult and a challenging task. Simulation and identification of these flow regimes by resolving interfaces via traditional Navier-Stokes (N-S) based simulators are computationally complex, extremely time consuming and often very inefficient partly due to the need for extensive interface tracking. Moreover, since interfaces between the two-phases of a fluid are results of unique thermodynamic effects, one also needs to know the governing equation of state to incorporate a consistent thermodynamics that is usually unknown in the interfacial

regions. Consequently, analyses of two-phase flow are still largely based on the empirical correlations developed for different flow regimes.

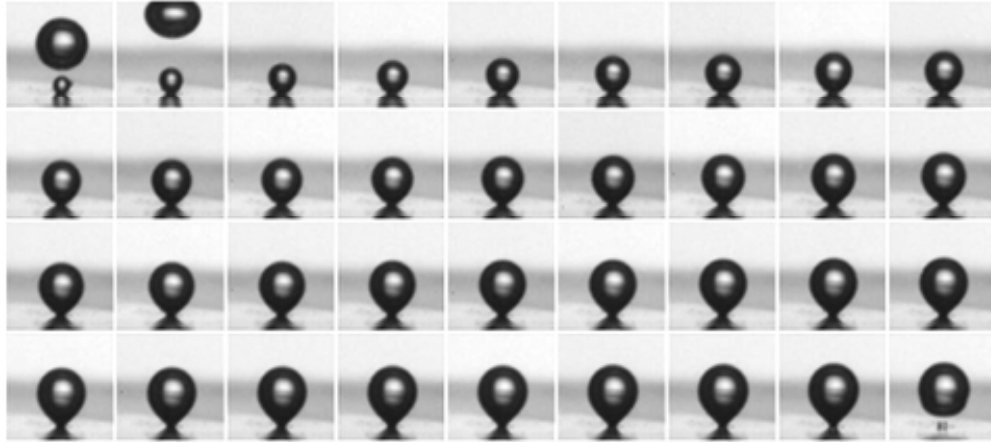
In the following sections, motivation for studying the two-phase dynamics using a lattice Boltzmann model (LBM) based approach is given. Some salient features of the LB method are outlined and its benefits over the prevalent computational fluid dynamics (CFD) approaches are highlighted.

1.1 Motivation

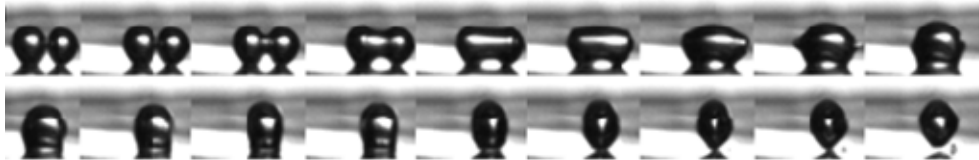
Advances in computational fluid dynamics over the last two decades or so have been very impressive. Several fields of engineering—including aeronautical, automotive, mechanical, chemical, etc.—have benefited from this progress. However, fruits of this development have been more limited for applications that involve boiling and two-phase flows, such as those in nuclear and some other branches of engineering. The reason may be the slow progress in CFD to accurately model challenging problems of interest such as those that involve boiling or multi-phase flows.

One specific example is a boiling water reactor (BWR) core, in which the coolant enters the core as liquid, undergoes a phase change as it traverses the core and exits as a high-quality two-phase mixture. Two-phase flows in BWRs typically manifest a wide variety of geometrical patterns of the co-existing phases depending on the local thermodynamic conditions (Tong & Tang, 1997).

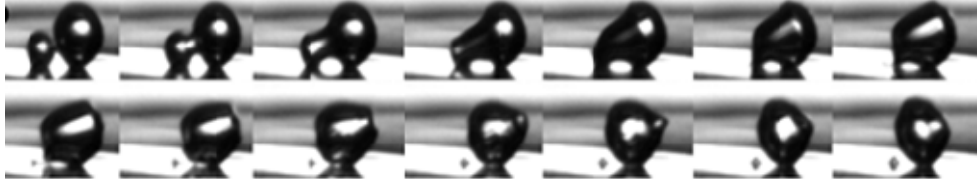
The accuracy in modeling is vital for the safety and economy of a nuclear power plant. However, modeling such flows — which involve bubble nucleation, bubble growth and coalescence, and inter-phase surface topology transitions — using CFD type approaches currently relies on empirical correlations and therefore, hinder the physics-based insightful predictions. For example, several best estimate codes in nuclear industry, such as RETINA, CATHRE still rely on the extrapolated results from some simple laboratory experiments. The empiricism in the closure relations is a major source of error in them.



(a) Single bubble growth



(b) Lateral bubble coalescence of two equal sized bubbles



(c) Lateral bubble coalescence of two unequal sized bubbles

Fig. 1.2: Experimental observations to investigate two-phase dynamics for some simple scenarios (figure adopted from Siedel et al., 2008).

To improve the accuracy, we must resolve the complexity of two-phase flow structures either by gathering information from the physical experiments (at similar system conditions) and/or from numerical/analytical methods. We should note that even now, the physics of very simple two-phase scenarios (for example, the growth of a single bubble on a heated surface and the coalescence of two bubbles) has not been fully understood. In an attempt to grasp the physics using state-of-the-art technologies, several experimental studies are currently being performed. In Fig. 1.2, photographic observations from one of such experiments by Siedel et al. (2008) are shown.

Of course, one can not directly extrapolate results from the simple laboratory experiments to the scale of a nuclear power plant, and full scale experiments may be needed to verify and benchmark the predictions. However, conducting full scale experiments on a nuclear reactor scale (such as, transients, loss of coolant or flow accident (LOCA/LOFA) etc.) are sometimes not possible (due to safety concerns) and may not even be economically feasible. Therefore, we should turn to numerical experiments in order to improve the accuracy of closure relations. Considering the limitations (cost, parameter range, safety etc.) of the physical experiments, numerical experimentation seems more promising (Hazi et al., 2002).

1.2 Several computational approaches

There are several computational methodologies we can use to model two-phase dynamics. Most conventional and popular approach is to use macroscopic Navier-Stokes (N-S) equation (supplemented with the energy equation) and include surface tension, interfaces, condensation / evaporation etc. effects by means of separate models. An excellent review of early Navier-Stokes based two-phase approaches can be found in Stewart and Wendroff (1984).

Usually in conventional best-estimate two-phase flow codes, two or more sets of partial differential equations (PDEs) along with the closure relations are numerically solved. Two phases are assumed to be distributed homogeneously throughout the system. The phase homogenization brings in a very crude approximation and is a large source of error. To relax this assumption, closure relations need to be tuned to the specific flow regime (annular, bubbly, slug etc.) under specific system conditions. However, it is difficult to find well established and constitutive relations between the system's thermodynamic conditions and the observed flow regimes (Hazi et al., 2002). Therefore, only a few available correlations, whose validity may still be in question, are commonly incorporated in the computer codes.

While some schemes, such as the level-set method and the volume-of-fluid (VOF) method, have successfully been applied to model certain two-phase systems (Krishna & Van Baten, 1999; Scardovelli & Zaleski, 1999; Esmaeeli & Tryggvason, 1998; Juric & Tryggvason, 1998), there is still a need for alternative approaches to understand the

connection between the two-phase macroscopic phenomena and their underlying micro-dynamics at a much more fundamental level. Ideally, molecular dynamics (MD) simulations can be the ‘key’ to predict these phenomena by setting up a model which describes the microscopic interactions as accurate as possible. However, MD is not yet ready to be exploited for large scale applications due to extremely high computational cost associated with such *close-to-reality* simulations (Ceperley, 1999). Consequently, a methodology which can bridge the gap between MD and CFD (sometimes referred to as the meso-scale approach) may be more suitable for the present state of computational power (Yadigaroglu, 2005). The Lattice Boltzmann Method (LBM) is a good candidate because of its coarse-grained approach to simulate fluid flows. In LBM, the dynamics is evolved by movements of fictive clusters of particles on a fixed lattice which do not follow Newtonian dynamics as in MD and thus are computationally more affordable. Moreover, use of LBM may prove highly advantageous in comparison to the continuum approaches because of its inherent ability to incorporate particle interactions to yield phase segregation.

An overview of microscopic simulations in physics and the need for multi-scale methods to interconnect phenomena occurring at different length and time scales are given in Ceperley (1999). Microscopic approaches which can be applicable in simulating nuclear reactor thermal-hydraulics are reviewed in Ninokata (1999). In Fig. 1.3, several computational approaches for fluid simulations are compared on the scale of system size, Knudsen number, computational efficiency and system complexity per unit volume. Molecular dynamics (MD) approaches are the simplest representation of fluid flow in which the Newtonian motion of all the particles composing the system are tracked in time. Interactions among the particles are implemented via prescribing the inter-particle force potential functions. Using MD-type approaches, very detailed information about the state of a system can be obtained. Due to existence of large number of particles in any real system, MD- approaches are extremely computer and time intensive even for the problems with very small length and time scales. In order to simulate fluid flow on higher scales, one has to coarsen over the real particles. In such a modeling scheme, pseudo-particles (a collection of real particles) are considered which evolve either on a fixed lattice or off-lattice. Dissipative particle dynamics and Direct Simulation Monte Carlo (DSMC) are off-lattice pseudo-particle methods in which pseudo-particles move continuously in space. LBM approach is one of the on-lattice pseudo-particle approach in which coarse-grained fictive particles travel on a fixed

lattice and interact with other such particles. In Navier-Stokes (N-S) based approaches, continuum-based partial differential equations are numerically solved for the macroscopic observables (Rabbe, 2004).

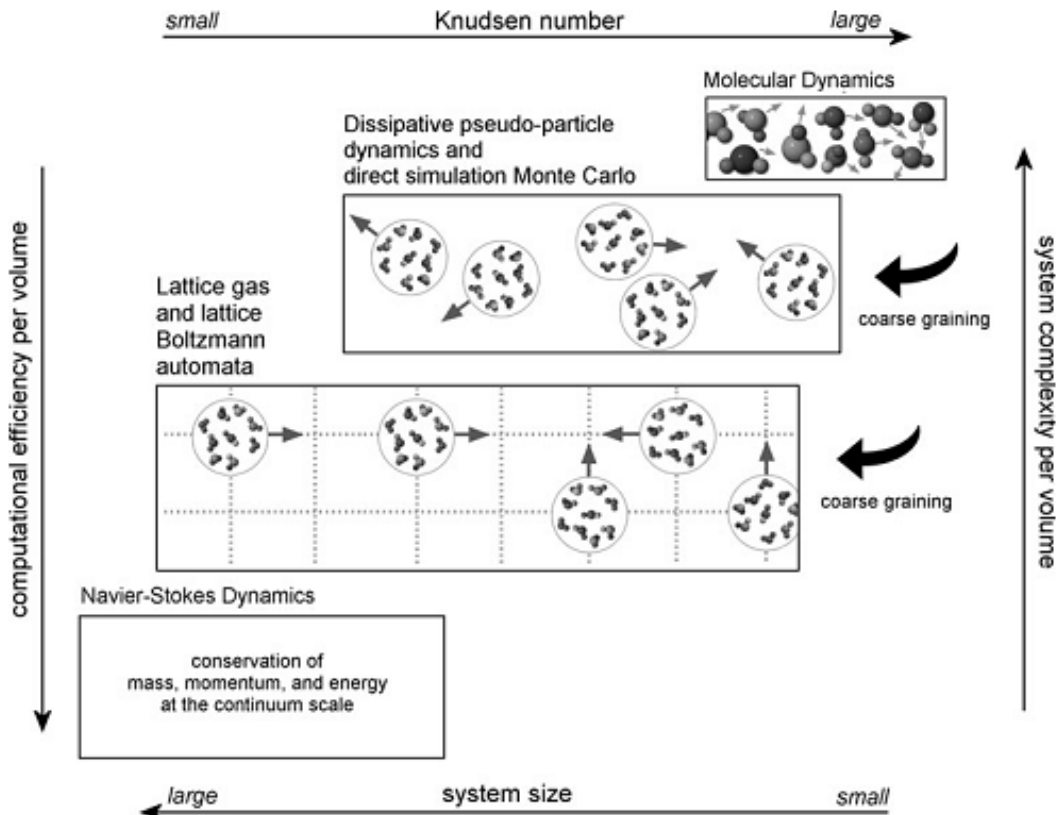


Fig. 1.3: Various approaches to simulate fluid flows at different scales. Applicability of a certain method depends upon the system size and the Knudsen number. (Figure adopted from Rabbe, 2004)

Navier-Stokes fluid dynamics is applicable at small Knudsen numbers and can be regarded as a *top-down* approach to fluid simulation, whereas pseudo-particle based methods and lattice Boltzmann models are a *bottom-up* strategy of fluid simulation which are applicable at higher Knudsen numbers. In the Navier-Stokes world, one directly deals with the variations in fluid observables i.e. density, velocity, pressure etc. and predicts the state of the fluid in terms of these observables. In contrast to above, macroscopic observables in the

pseudo-particle based approaches are computed by local averaging of number densities and momentum of the coarse-grained particles.

Several computational approaches discussed above are best suited at different time/space scales for fluid simulations. Cross-scale interactions (back-and-forth feeding of scale-specific solutions) are required at each level of scale hierarchy in order to gain better predictive modeling. This multi-scale strategy (merging results at the micro-, meso- and macro-scales) to simulate fluid flow may be able to better address the physics of complex fluids. However, advances should be first made in developing the scale-specific approach and strategies are required to merge the solutions at different scales in order to obtain reliable results (Yadigaroglu, 2005). Because of its mesoscopic nature, lattice Boltzmann (LB) methodologies are a good fit in the realm of multi-scale simulations and can address problems that involve multiple levels of physical and mathematical descriptions (Succi et al., 2001; Lantermann & Hanel, 2007).

1.3 An overview of lattice Boltzmann method (LBM)

Unlike conventional numerical schemes based on the discretizations of macroscopic continuum equations, the LBM is a particle-based approach, in which collective behavior of particles is represented by a *single-particle probability distribution function*. Roots of LBM lie in the earlier lattice gas cellular automata (LGCA) models, in which, evolution of particles on a fixed lattice simulate the overall macroscopic behavior. The uniqueness of LBM stems from the fact that the macroscopic dynamics emerges from the simulation of very simple kinetic models that incorporate the essential physics of the microscopic (or mesoscopic) processes in the system. There underlies an *artificial micro-world* of particles ‘living’, ‘propagating’ and ‘colliding’ on a fixed lattice while conserving mass and momentum (Chen, 1993, Chen et al., 1994).

For hydrodynamic simulations, LBM models are much simpler and efficient to solve on a computer compared to solving its macro-counterpart partial differential equations (PDEs). Though LBM and its variations were proposed several decades ago, it is only with the recent advances in computing power that their applications to realistic problems are becoming a reality. This approach appears to be one of the most promising approaches due to

its scalability with computing power and short as well as long term promises. Computing power will no doubt continue to increase; and hence the LBM is likely to be applicable to ever larger problems (Chen & Doolen, 1998).

1.4 Objectives

While the overall and long term goal of an LBM based simulation capability (of two and even multi- phase flows) in nuclear engineering would be to accurately predict critical heat flux (CHF) and flow regimes maps, it is recognized that this is a rather challenging goal. Work reported here consists of several steps towards that goal. Challenges include the development of capabilities in a LB model to address the following:

- Simulation of two coexisting phases in equilibrium
 - Open (such as, planar) interfaces
 - Closed (such as, circular or spherical) interfaces
- Tracking the temporal and spatial dynamics of interfacial evolution
- Modeling of surface-tension effects
- Modeling of walls in the computational domain
- Modeling of wall-fluid interaction to yield a prescribed contact angle in equilibrium
- Modeling of flow boundary conditions to be able to specify desired fluid velocities or densities at the boundaries
- Modeling of all of the above physical effects in the presence of body forces, such as gravity
- Modeling of all of the above with heat-transfer considerations

In addition, stable and efficient (parallel) numerical schemes must also be developed. Only after adequately addressing these steps, one can expect to tackle the challenging problem of predicting CHF and flow regime maps.

This report addresses the issues of development and testing of LB models for some of the individual effects—namely high density ratios of the liquid and vapor phases; wall and surface tension effects; and two phases with phase change.

1.5 Outline

This report has been divided into nine chapters. An outline of which is presented below:

In Chapter 2, theoretical aspects of lattice Boltzmann models are discussed. A consistent way to recover the lattice Boltzmann equation (LBE) from the continuous Boltzmann transport equation (CBE) is presented.

In Chapter 3, the formulation of a non-ideal Enskog equation based LBE is presented. Several existing techniques in the lattice Boltzmann framework to simulate two-phase flows are scrutinized.

In Chapter 4, an artificial interface lattice Boltzmann model (AILB) is developed to simulate two-phase dynamics. The model employs two equations of state, one for the bulk region and another for the interfacial region. Based on the Cahn's wetting theory, a model is developed for simulating different wall contact angles.

In Chapter 5, velocity and density boundary conditions are developed for the Gibbs-Duhem LB model. The formulation is presented for D_2Q_9 (in two-dimensions) and D_3Q_{19} (in three-dimensions) lattice-types.

In Chapter 6, results for several two-phase simulations are presented and compared with existing theoretical and experimental results.

In Chapter 7, a Peng-Robinson (P-R) equation of state based LB model is proposed. Model based on P-R EOS is able to quantitatively reproduce the water-steam coexistence curve in the LB simulations.

In Chapter 8, a thermal model is presented for the proposed AILB model. A phenomenological model is developed for simulating qualitative effects of evaporation and condensation.

In Chapter 9, a summary of the report is given.

In Appendix A, a derivation of incompressible Navier-Stokes (N-S) equation from the LB equation is presented.

Parallelization techniques and the efficiency and scalability of LB algorithm are discussed in Appendix B.

Details on the boundary conditions are presented in the Appendices C, D and E.

Appendix F discusses the Mathematica routine for the Maxwell construction procedure in the context of a van der Waals equation of state.

In Appendix G, relations between lattice and physical units are discussed. Some examples are given for illustrative purposes.

1.6 References

Stewart, H.B., Wendroff, B., 1984. Two-phase flow: Models and methods. Review article in J. Comp. Phys. 56, 363-409.

Ceperley, D.M., 1999. Microscopic simulations in physics. Reviews of modern physics 71(2), S438-S443.

Chen, H., 1993. Discrete Boltzmann systems and fluid flows. Computers in Physics 7(6), 632-637.

Chen, S., Doolen, G.D., Eggert, K.G., 1994. Lattice-Boltzmann fluid dynamics. Los Alamos Science, 100-111.

Chen, S., Doolen, G.D., 1998. Lattice Boltzmann method for fluid flows. Annu. Rev. Fluid Mech. 30, 329-364.

Esmaeeli, A., Tryggvason, G., 1998. Direct numerical simulations of bubbly flows. Part I. Low Reynolds number arrays. *J. Fluid Mech.* 377, 313-345.

Hazi, G., Imre, A.R., Mayer, G., Farkas, I., 2002. Lattice Boltzmann methods for two-phase flow modeling. *Annals of Nuclear Energy* 29, 1421-1453.

Huo, X., Chen, L., Tian, Y.S., Karayiannis, T.G., 2004. Flow boiling and flow regimes in small diameter tubes. *Applied thermal engineering* 24, 1225-1239.

Juric, D., Tryggvason, G., 1998. Computations of boiling flows. *Int. J. Multiphase Flow* 24(3), 387-410.

Krishna, R., Van Baten, J.M., 1999. Simulating the motion of gas bubbles in a liquid. *Nature* 398, doi:10.1038/18353.

Lantermann, U., Hanel, D., 2007. Particle Monte Carlo and lattice-Boltzmann methods for simulations of gas-particle flows. *Computers & Fluids* 36, 407-422.

Ninokata, H., 1999. Microscopic approaches in nuclear reactor thermal hydraulics computations. Ninth International Topical Meeting on Nuclear Reactor Thermal Hydraulics (NURETH-9), San Francisco, CA, October 3-8, 1999.

Rabbe, D., 2004. Overview of the lattice Boltzmann method for nano- and microscale fluid dynamics in materials science and engineering. *Topical review in Modeling Simul. Mater. Sci. Eng.* 12, R13-R46.

Scardovelli, R., Zaleski, S., 1999. Direct numerical simulation of free-surface and interfacial flow. *Annu. Rev. Fluid Mech.* 31, 567-603.

Siedel, S., Cioulachtjian, S., Bonjour, J., 2008. Experimental analysis of bubble growth departure and interactions during pool boiling on artificial nucleation sites. *Experimental Thermal and Fluid Sciences* 32, 1504-1511.

Succi, S., Filippova, O., Smith, G., Kaxiras, E., 2001. Applying the lattice Boltzmann equation to multiscale fluid problems. *Computing in Science and Engineering*, 26-37.

Tong, L.S., Tang, Y.S., 1997. Boiling heat transfer and two-phase flow. Second edition, Taylor & Francis.

Yadigaroglu, G., 2005. Computational Fluid Dynamics for nuclear applications: from CFD to multi-scale CMFD. *Nuclear Engineering and Design* 235, 153-164.

Chapter 2

Theoretical framework

Historically, the classical lattice Boltzmann equation (LBE) originated *empirically* from its Boolean counterpart, the lattice-gas cellular automata (LGCA). In LGCA, the physical space is divided into a regular lattice with each lattice point populated by discrete particles. Particles ‘hop’ from one lattice point to another with discrete particle velocities and ‘collide’ when they meet others. Boolean collision rules are explicitly defined at each lattice point. Though LGCA contributed significantly in LBE’s evolution, models based on LGCA contained several *defects* (Wolf-Gladrow D.A., 2000; Rothman & Zaleski, 1997; Rivet & Boon, 2001; Frish et al., 1986; Chopard & Droz, 1998) such as:

- Large noise due to Boolean variables
- Violation of the Galilean invariance due to Fermi-Dirac distribution
- Presence of spurious invariants due to regular lattices
- Inflexibility to adjust the viscosity, and
- An unphysical equation of state which has an explicit dependence of pressure on velocity.

The lattice Boltzmann models (LBM) evolved from the LGCA models in order to overcome the shortcomings discussed above. In LBM, sets of particle velocity distribution functions are used instead of single pseudo-particles of LGCA. Furthermore, the streaming and collision dynamics is applied over the velocity distribution functions in order to simulate the fluid flow.

In order to develop the LBM for solving two-phase flow problems, it is first necessary to understand the connection between the LBE and the continuous Boltzmann transport equation (CBE) to identify the simplifying approximations and their impact on the simulated flow physics. In the following sections, a detailed derivation of the LBE from the CBE is presented.

2.1 Continuous Boltzmann transport equation (CBE)

Lattice Boltzmann equation (LBE) is a specially discretized form of the Boltzmann transport equation which is derived from the kinetic theory of gases. Primary variable of interest in the Boltzmann transport equation is a single-particle probability distribution function $f(\mathbf{r}, \mathbf{v}, t)$ defined such that $f(\mathbf{r}, \mathbf{v}, t)d\mathbf{r}d\mathbf{v}$ is the number of particles in a phase-space control element ($d\mathbf{r}d\mathbf{v}$) about \mathbf{r} and \mathbf{v} . Here, \mathbf{r} represents a location in physical space and \mathbf{v} is microscopic velocity. Moreover, particles are assumed to be in a dilute state to have large inter particle separations and therefore, all the interactions involving more than two-particles may be neglected. With all these approximations in mind, the Boltzmann transport equation (Cercignani, 1969; Harris, 1971) can be written as:

$$\left(\frac{\partial}{\partial t} + \mathbf{v} \cdot \nabla_{\mathbf{r}} + \mathbf{F} \cdot \nabla_{\mathbf{v}} \right) f(\mathbf{r}, \mathbf{v}, t) = \Omega_{Boltz} \quad (2.1)$$

Here, \mathbf{F} is the acceleration experienced by a particle in the presence of an external force field and the collision term Ω_{Boltz} accounts for the rate of gain $\Gamma^{(+)}$ and loss $\Gamma^{(-)}$ of particles from the control element ($d\mathbf{r}d\mathbf{v}$) due to the collisions, and is equal to:

$$\Omega_{Boltz} = \Gamma^{(+)} - \Gamma^{(-)} = \int d\mathbf{p}_1 [f(\mathbf{r}, \mathbf{v}', t)f(\mathbf{r}, \mathbf{v}'_1, t) - f(\mathbf{r}, \mathbf{v}, t)f(\mathbf{r}, \mathbf{v}_1, t)] \quad (2.2)$$

where \mathbf{v}' and \mathbf{v}'_1 are after-collision velocities of the two colliding particles moving with the velocities \mathbf{v} and \mathbf{v}_1 , respectively, before collision. Also, $d\mathbf{p}_1$ is given by:

$$d\mathbf{p}_1 = d\mathbf{v}_1 |\mathbf{v}_1 - \mathbf{v}| \left(\frac{d\sigma}{d\omega} \right) d\omega \quad (2.3)$$

where $\left(\frac{d\sigma}{d\omega} \right)$ is the differential cross-section of a particle and ω is the solid angle (Chapman & Cowling, 1970; Huang, 1963; Koga, 1970; Liboff, 1969).

2.2 Simplification of Boltzmann collision integral Ω_{Boltz}

Details of the two-body interactions in the collision integral Ω_{Boltz} do not significantly influence the values of macroscopic hydrodynamic observables. Therefore, Ω_{Boltz} can be simplified by assuming that, at any given time t , particles are in a state close to thermal equilibrium and they relax to their local thermal equilibrium on a single time scale τ . This

approximation of single-time relaxation for the collision integral Ω_{Boltz} was first proposed by Bhatnagar, Gross and Krook in 1954. Using it, Ω_{Boltz} can be expressed in a form known as the BGK collision term Ω_{BGK} (Bhatnagar et al., 1954):

$$\Omega_{Boltz} = \Omega_{BGK} = -\frac{f(\mathbf{r}, \mathbf{v}, t) - f^{eq}(\mathbf{r}, \mathbf{v}, t)}{\tau} \quad (2.4)$$

where τ is the single relaxation time, and $f^{eq}(\mathbf{r}, \mathbf{v}, t)$ is an equilibrium distribution function given by the Maxwellian:

$$f^{eq}(\mathbf{r}, \mathbf{v}, t) = f^{eq} \{ \mathbf{v}, \rho(\mathbf{r}, t), \mathbf{u}(\mathbf{r}, t) \} = \frac{\rho}{(2\pi RT)^{d/2}} \exp\left(-\frac{(\mathbf{v}-\mathbf{u}) \cdot (\mathbf{v}-\mathbf{u})}{2RT}\right) \quad (2.5)$$

where d , R , T , ρ and \mathbf{u} have the units of space, gas constant, temperature, macroscopic density and macroscopic velocity, respectively. [Note that the Gas constant R has units of (Joules/kg-K) and RT has units of (m²/sec²).]

We can now write the *simplified* Boltzmann transport equation with the BGK collision approximation as:

$$\frac{\partial f}{\partial t} + \mathbf{v} \cdot \nabla_{\mathbf{r}} f + \mathbf{F} \cdot \nabla_{\mathbf{v}} f = -\frac{f - f^{eq}}{\tau} \quad (2.6)$$

2.3 Explicit determination of the forcing term $\mathbf{F} \cdot \nabla_{\mathbf{v}} f$

In order to explicitly determine the forcing term $\mathbf{F} \cdot \nabla_{\mathbf{v}} f$, we can introduce an approximation (He et al., 1998):

$$\nabla_{\mathbf{v}} f \approx \nabla_{\mathbf{v}} f^{eq} = -\frac{(\mathbf{v}-\mathbf{u})}{RT} f^{eq} \quad (2.7)$$

Above approximation is valid since f is close to the equilibrium and therefore, f^{eq} can be regarded as the leading part of f . Applying the above approximation, our *simplified* Boltzmann transport equation becomes:

$$\frac{\partial f}{\partial t} + \mathbf{v} \cdot \nabla_{\mathbf{r}} f = -\frac{f - f^{eq}}{\tau} + \frac{\mathbf{F} \cdot (\mathbf{v}-\mathbf{u})}{RT} f^{eq} \quad (2.8)$$

2.4 Series expansion of equilibrium distribution function f^{eq}

Equilibrium distribution function f^{eq} can be expanded in a series form, in the limit of constant temperature T and small velocity \mathbf{u} , up to terms of order $O(u^2)$ and gives:

$$f^{eq} = w_B(v) \left[1 + \frac{\mathbf{v} \cdot \mathbf{u}}{RT} + \frac{1}{2} \left(\frac{\mathbf{v} \cdot \mathbf{u}}{RT} \right)^2 - \frac{u^2}{2RT} \right] \quad (2.9)$$

where

$$w_B(v) = \frac{\rho}{(2\pi RT)^{d/2}} \exp\left(-\frac{v^2}{2RT}\right) \quad (2.10)$$

and $w_B(v)$ is called the Maxwell equilibrium distribution function for ‘fluid at rest’ i.e. fluid with $\mathbf{u} = 0$.

2.5 Links to hydrodynamics

The collision integral Ω_{Boltz} in the Boltzmann transport equation possesses the following properties:

$$\int \Omega_{Boltz} d\mathbf{v} = 0 \quad (2.11)$$

and

$$\int \Omega_{Boltz} \mathbf{v} d\mathbf{v} = 0 \quad (2.12)$$

i.e. conservation of collision invariants (1, \mathbf{v} and v^2) at any \mathbf{r}, t .

Similar to Ω_{Boltz} , the BGK collision term Ω_{BGK} must also satisfy the conservation of collision invariants at any \mathbf{r}, t :

$$\int \Omega_{BGK} d\mathbf{v} = \int [f(\mathbf{r}, \mathbf{v}, t) - f^{eq}(\mathbf{r}, \mathbf{v}, t)] d\mathbf{v} = 0 \quad (2.13)$$

$$\int \Omega_{BGK} \mathbf{v} d\mathbf{v} = \int [f(\mathbf{r}, \mathbf{v}, t) - f^{eq}(\mathbf{r}, \mathbf{v}, t)] \mathbf{v} d\mathbf{v} = 0 \quad (2.14)$$

A link to hydrodynamics can be accomplished through the above equations. Macroscopic density $\rho(\mathbf{r}, t)$ and velocity $\mathbf{u}(\mathbf{r}, t)$ are thus evaluated as:

$$\rho(\mathbf{r}, t) = \int f(\mathbf{r}, \mathbf{v}, t) d\mathbf{v} = \int f^{eq}(\mathbf{r}, \mathbf{v}, t) d\mathbf{v} \quad (2.15)$$

$$\mathbf{u}(\mathbf{r}, t) = \frac{1}{\rho(\mathbf{r}, t)} \int f(\mathbf{r}, \mathbf{v}, t) \mathbf{v} d\mathbf{v} = \frac{1}{\rho(\mathbf{r}, t)} \int f^{eq}(\mathbf{r}, \mathbf{v}, t) \mathbf{v} d\mathbf{v} \quad (2.16)$$

2.6 Discretization in velocity space

In the *simplified* Boltzmann transport equation, the distribution function f depends on space, velocity and time i.e. $f(\mathbf{r}, \mathbf{v}, t)$. Discrete Boltzmann equation (DBE) is obtained by discretization in the velocity space after introducing a finite set of velocities, \mathbf{v}_a and associated distribution functions, $f_a(\mathbf{r}, t)$. The DBE can be written as:

$$\frac{\partial f_a}{\partial t} + \mathbf{v}_a \cdot \nabla_r f_a = -\frac{f_a - f_a^{eq}}{\tau} + \frac{\mathbf{F} \cdot (\mathbf{v}_a - \mathbf{u})}{RT} f_a^{eq} \quad (2.17)$$

where, the discrete BGK collision term $\Omega_{a,BGK}$ is:

$$\Omega_{a,BGK} = -\frac{f_a - f_a^{eq}}{\tau} \quad (2.18)$$

$\Omega_{a,BGK}$ must satisfy the conservation of collision invariants at any \mathbf{r}, t i.e.

$$\sum_a f_a(\mathbf{r}, t) = \underbrace{\sum_a f_a^{eq}(\mathbf{r}, t)}_{=\rho} \quad (2.19)$$

$$\sum_a \mathbf{v}_a f_a(\mathbf{r}, t) = \underbrace{\sum_a \mathbf{v}_a f_a^{eq}(\mathbf{r}, t)}_{=\rho \mathbf{u}} \quad (2.20)$$

A link to hydrodynamics is established through the above equations. Macroscopic density $\rho(\mathbf{r}, t)$ and velocity $\mathbf{u}(\mathbf{r}, t)$ are thus evaluated as:

$$\rho(\mathbf{r}, t) = \sum_a f_a(\mathbf{r}, t) = \sum_a f_a^{eq}(\mathbf{r}, t) \quad (2.21)$$

$$\mathbf{u}(\mathbf{r}, t) = \frac{1}{\rho(\mathbf{r}, t)} \sum_a \mathbf{v}_a f_a(\mathbf{r}, t) = \frac{1}{\rho(\mathbf{r}, t)} \sum_a \mathbf{v}_a f_a^{eq}(\mathbf{r}, t) \quad (2.22)$$

Here we should note that, in the multi-scale Chapman-Enskog expansion procedure (see Appendix A for more details), certain fourth-order tensors made of lattice directions must be isotropic in order to recover the rotational invariance of the momentum flux tensor at the macroscopic level. The isotropy requirement limits the possible lattice structures that can be used. This is the reason, for example, in two-dimensions (2D), a choice of rectangular

spatial lattice requires nine velocities at each lattice point instead of a five-velocity lattice. Out of these nine velocity directions, four are principal axes directions, four are diagonal directions and one is rest state of zero velocity (see Fig. 2.1). It is called D_2Q_9 , or more generally D_dQ_b lattice structure with d and b representing number of spatial dimensions and discrete velocities at each lattice point, respectively (Qian et al., 1992; Qian & Orszag, 1993). [It should be noted that, in two-dimensions, a hexagonal lattice only requires seven velocities and is isotropic. However, a hexagonal lattice is more difficult to work with than a regular square lattice which is naturally implemented as an array of data on a computer.] In LB simulations, physical symmetry (symmetry attached to the velocity space and the equilibrium distribution for velocities) is necessary to obtain the correct macroscopic dynamics (Cao et al., 1997). Derivation of the incompressible Navier-Stokes equation from the standard lattice Boltzmann equation is given in Appendix A.

2.7 Discrete equilibrium distribution function: f_a^{eq}

Discrete equilibrium distribution function f_a^{eq} can be written as:

$$f_a^{eq} = w_a \left[1 + \frac{\mathbf{v}_a \cdot \mathbf{u}}{RT} + \frac{1}{2} \left(\frac{\mathbf{v}_a \cdot \mathbf{u}}{RT} \right)^2 - \frac{u^2}{2RT} \right] \quad (2.23)$$

where w_a are lattice constants which depend upon the chosen lattice structure (i.e. 2D or 3D, rectangular or hexagonal lattice) and the number of finite velocities at any lattice point. w_a are evaluated such that the lattice-velocity moments (up to fourth order) over w_a are identical to the respective velocity moments over the Maxwell distribution $w_B(v)$ and given by the following equations (Abe, 1997; Wolf-Gladrow D.A., 2000):

$$\sum_a w_a = \int_{-\infty}^{\infty} w_B(v) d\mathbf{v} = \rho \quad (2.24)$$

$$\sum_a v_{a\alpha} w_a = \int_{-\infty}^{\infty} v_{\alpha} w_B(v) d\mathbf{v} = 0 \quad (2.25)$$

$$\sum_a v_{a\alpha} v_{a\beta} w_a = \int_{-\infty}^{\infty} v_{\alpha} v_{\beta} w_B(v) d\mathbf{v} = \rho RT \delta_{\alpha\beta} \quad (2.26)$$

$$\sum_a v_{a\alpha} v_{a\beta} v_{a\gamma} w_a = \int_{-\infty}^{\infty} v_{\alpha} v_{\beta} v_{\gamma} w_B(v) d\mathbf{v} = 0 \quad (2.27)$$

$$\sum_a v_{a\alpha} v_{a\beta} v_{a\gamma} v_{a\xi} w_a = \int_{-\infty}^{\infty} v_{\alpha} v_{\beta} v_{\gamma} v_{\xi} w_B(v) d\mathbf{v} = \rho (RT)^2 (\delta_{\alpha\beta} \delta_{\gamma\xi} + \delta_{\alpha\gamma} \delta_{\beta\xi} + \delta_{\alpha\xi} \delta_{\beta\gamma}) \quad (2.28)$$

Note that the odd velocity moments vanish. In the above equations, δ_{ij} is a Kronecker-delta function given by:

$$\delta_{ij} = \begin{cases} 1 & \text{if } i = j \\ 0 & \text{if } i \neq j \end{cases} \quad (2.29)$$

and v_{ai} denotes the i^{th} -component (component in the i^{th} spatial dimension) of \mathbf{v}_a .

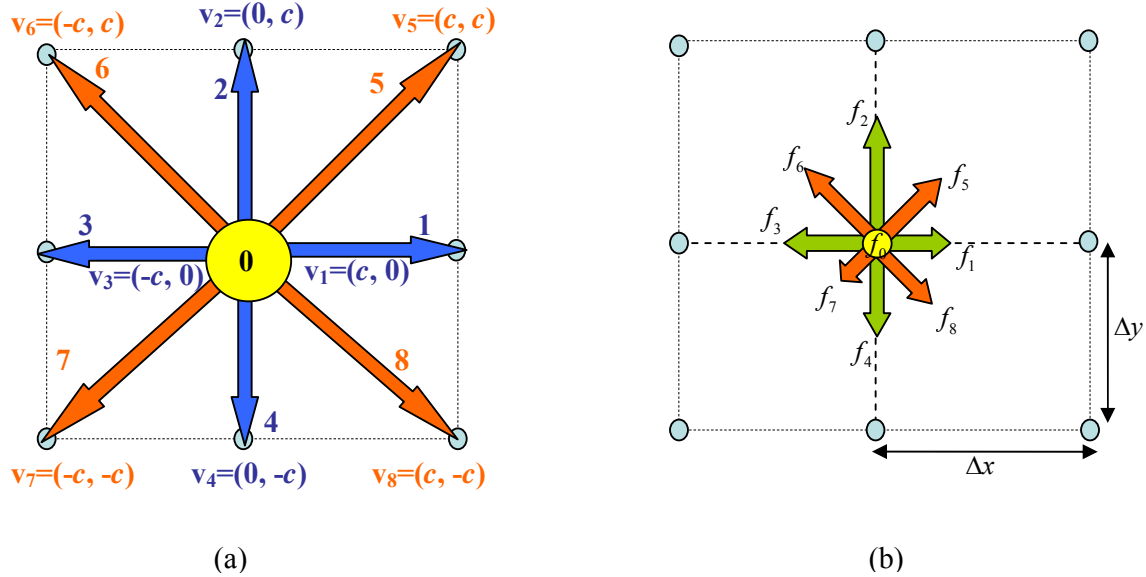


Fig. 2.1: The D₂Q₉ lattice. (a) Nine discrete velocities for the central lattice point are shown. Principal direction of travel is numbered from 1 to 4, diagonal direction from 5 to 8 and the rest state by 0. Also, velocities with the same magnitude are displayed by the same colored arrows in the figure. The lattice employs three different speeds (0, c and $\sqrt{2}c$) corresponding to the rest, principal and diagonal directions of travel and therefore, has three different weighting functions, w_{rest} , w_{prin} and w_{diag} for the discrete equilibrium distribution function.

Here, a square lattice structure is assumed to give $c = \Delta x / \Delta t = \Delta y / \Delta t$. (b) Discrete distribution functions in the nine directions of travel are shown and labeled accordingly from f_0 to f_8 . Their magnitudes are usually different in different directions and therefore, are shown with different lengths of arrows in the figure.

2.8 Determining f_a^{eq} for a D_2Q_9 lattice

The D_2Q_9 lattice, as shown in Fig. 2.1(a), includes three different microscopic speeds which are shown in the figure by different colored arrows. At any spatial point, discrete velocities in nine directions of the two-dimensional square lattice are given by:

$$\begin{aligned}
 \mathbf{v}_0 &= (v_{0x}, v_{0y}) = (0, 0) \\
 \mathbf{v}_1 &= (v_{1x}, v_{1y}) = (c, 0) & \mathbf{v}_5 &= (v_{5x}, v_{5y}) = (c, c) \\
 \mathbf{v}_2 &= (v_{2x}, v_{2y}) = (0, c) & \mathbf{v}_6 &= (v_{6x}, v_{6y}) = (-c, c) \\
 \mathbf{v}_3 &= (v_{3x}, v_{3y}) = (-c, 0) & \mathbf{v}_7 &= (v_{7x}, v_{7y}) = (-c, -c) \\
 \mathbf{v}_4 &= (v_{4x}, v_{4y}) = (0, -c) & \mathbf{v}_8 &= (v_{8x}, v_{8y}) = (c, -c)
 \end{aligned}$$

where $c = \Delta x / \Delta t = \Delta y / \Delta t$. Here, we have assumed a square lattice i.e. $\Delta x = \Delta y$.

D_2Q_9 lattice involves three different speeds: 0, c and $\sqrt{2}c$. For reason of symmetry, we can further assume that w_a for directions with identical speeds are equal. Now, we can calculate three different w_a , called w_{rest} , w_{prin} and w_{diag} , corresponding to the rest (direction 0), the principal (directions 1, 2, 3 and 4) and the diagonal (directions 5, 6, 7 and 8) velocity directions, respectively.

From equations (2.24) to (2.28), we obtain the following relations for a D_2Q_9 square lattice:

$$\sum_a w_a = w_{rest} + 4w_{prin} + 4w_{diag} = \rho \quad (2.30)$$

$$\sum_a v_{ax}^2 w_a = \sum_a v_{ay}^2 w_a = 2c^2 w_{prin} + 4c^2 w_{diag} = \rho RT \quad (2.31)$$

$$\sum_a v_{ax}^4 w_a = \sum_a v_{ay}^4 w_a = 2c^4 w_{prin} + 4c^4 w_{diag} = 3\rho (RT)^2 \quad (2.32)$$

$$\sum_a v_{ax}^2 v_{ay}^2 w_a = 4c^4 w_{diag} = \rho (RT)^2 \quad (2.33)$$

Solving above set of equations for the four unknowns, w_{rest} , w_{prin} , w_{diag} and RT , we get:

$$w_{rest} = \frac{4}{9} \rho \quad (2.34)$$

$$w_{prin} = \frac{1}{9} \rho \quad (2.35)$$

$$w_{diag} = \frac{1}{36} \rho \quad (2.36)$$

$$RT = \frac{c^2}{3} \quad (2.37)$$

Similar to the procedure above, the equilibrium distribution function may be determined for lattices in three-dimensions, i.e. of type D_3Q_{15} or D_3Q_{19} (Wolf-Gladrow, 2000).

2.9 Recovery of the LBE from the discrete Boltzmann equation (DBE)

The discrete Boltzmann equation (DBE) can be written in $\mathbf{r} \equiv (x, y, z)$ space as follows:

$$\begin{aligned} & \frac{\partial f_a}{\partial t} + v_{ax} \frac{\partial f_a}{\partial x} + v_{ay} \frac{\partial f_a}{\partial y} + v_{az} \frac{\partial f_a}{\partial z} \\ &= -\frac{f_a - f_a^{eq}}{\tau} + \left[F_x (v_{ax} - u_x) + F_y (v_{ay} - u_y) + F_z (v_{az} - u_z) \right] \frac{f_a^{eq}}{RT} \end{aligned} \quad (2.38)$$

Left hand side of the above equation is composed of the *Eulerian time derivative* ($\partial/\partial t$) and the *advective space derivatives* ($v_{ax} \partial/\partial x + v_{ay} \partial/\partial y + v_{az} \partial/\partial z$). Together they comprise the *Lagrangian derivative*, which gives the rate of change of the a -directional distribution function $f_a(x, y, z, t)$ (index a can be between 0 and $(b-1)$ depending upon the chosen lattice structure D_aQ_b) in a frame of reference which moves with the particle's velocity $\mathbf{v}_a \equiv (v_{ax}, v_{ay}, v_{az})$. Thus, by marching each of the b -directional populations in time along the characteristics $(\Delta x, \Delta y, \Delta z) = (v_{ax}, v_{ay}, v_{az}) \Delta t$, the above equation yields the standard lattice Boltzmann equation (LBE) (Chen & Doolen, 1998; He & Luo, 1997b,c):

$$\begin{aligned}
f_a(x + v_{ax}\Delta t, y + v_{ay}\Delta t, z + v_{az}\Delta t, t + \Delta t) = & f_a(x, y, z, t) - \frac{\Delta t}{\tau} \left[f_a(x, y, z, t) - f_a^{eq}(x, y, z, t) \right] \\
& + \Delta t \left[F_x(v_{ax} - u_x) + F_y(v_{ay} - u_y) + F_z(v_{az} - u_z) \right] \frac{f_a^{eq}(x, y, z, t)}{RT}
\end{aligned} \tag{2.39}$$

Here, we have used an explicit forward-difference scheme in time.

Note that, we can write the above LBE as a set of two equations:

- Collision

$$\begin{aligned}
f_a^*(x, y, z, t) = & f_a(x, y, z, t) - \frac{\Delta t}{\tau} \left[f_a(x, y, z, t) - f_a^{eq}(x, y, z, t) \right] \\
& + \Delta t \left[F_x(v_{ax} - u_x) + F_y(v_{ay} - u_y) + F_z(v_{az} - u_z) \right] \frac{f_a^{eq}(x, y, z, t)}{RT}
\end{aligned} \tag{2.40}$$

- Streaming

$$f_a(x + v_{ax}\Delta t, y + v_{ay}\Delta t, z + v_{az}\Delta t, t + \Delta t) = f_a^*(x, y, z, t) \tag{2.41}$$

Above splitting of the LBE into two equations clearly brings out the simple physical interpretation of particles colliding and streaming, which results from the fully Lagrangian character of the equation, for which the spacing between the two neighboring lattice points is the distance traveled by the particles during the time step. In the collision step, the distribution function is updated at regularly spaced lattice points. In the streaming step, the *updated* distribution function is streamed in the direction of corresponding discrete velocities, towards the neighboring lattice point. The simplicity of algorithm greatly facilitates numerical evaluations; however, it couples space-time discretization and leaves no flexibility in choosing the space-time grid-steps independently.

In a compact form, LBE can be written as:

$$f_a(\mathbf{r} + \mathbf{v}_a \Delta t, t + \Delta t) = f_a(\mathbf{r}, t) - \frac{\Delta t}{\tau} \left[f_a(\mathbf{r}, t) - f_a^{eq}(\mathbf{r}, t) \right] + B_a \Delta t \tag{2.42}$$

where B_a is the body force term given by:

$$B_a = \frac{\mathbf{F}(\mathbf{v}_a - \mathbf{u})}{RT} f_a^{eq} \tag{2.43}$$

The kinetic nature of the lattice Boltzmann equation (LBE) offers the following advantages:

- The convection operator (streaming step) in the LBE is linear, in contrast to the nonlinear convection terms in the corresponding macroscopic PDEs. Combining the simple convection with the collision operator allows the recovery of nonlinear macroscopic advection through multi-scale expansions.
- Taking the nearly incompressible limit of the LBE yields the incompressible Navier-Stokes (N-S) equations (see Appendix A). The pressure at any lattice point in this approach is calculated using an equation of state, in contrast to iteratively solving the pressure Poisson equation.
- Retaining only a minimal set of velocities and a few movement directions in the phase space extensively simplifies the transformation between the microscopic distribution function and macroscopic quantities.

2.10 Apriori derivation of the LBE from the CBE

In the absence of external forces, the continuous Boltzmann equation (CBE) can be written as:

$$\frac{\partial f}{\partial t} + \mathbf{v} \cdot \nabla_{\mathbf{r}} f = -\frac{f - f^{eq}}{\tau} \quad (2.44)$$

which essentially is:

$$\frac{Df}{Dt} + \frac{f}{\tau} = -\frac{f^{eq}}{\tau} \quad (2.45)$$

where $\frac{D}{Dt} \equiv \frac{\partial}{\partial t} + \mathbf{v} \cdot \nabla_{\mathbf{r}}$ is the Lagrangian derivative along direction of microscopic velocity \mathbf{v} .

Multiplying both sides of the above equation with integrating factor $e^{t/\tau}$, we can write:

$$\frac{D}{Dt} [f e^{t/\tau}] = -\frac{1}{\tau} e^{t/\tau} f^{eq} \quad (2.46)$$

Now, integrating the above equation along the characteristic from time t to $t + \Delta t$,

$$\int_t^{t+\Delta t} D[f e^{t/\tau}] = -\frac{1}{\tau} \int_t^{t+\Delta t} e^{t/\tau} f^{eq} Dt \quad (2.47)$$

we get:

$$f(\mathbf{r} + \mathbf{v}\Delta t, \mathbf{v}, t + \Delta t) e^{(t+\Delta t)/\tau} - f(\mathbf{r}, \mathbf{v}, t) e^{t/\tau} = -\frac{1}{\tau} \int_t^{t+\Delta t} e^{t/\tau} f^{eq} Dt \quad (2.48)$$

Assuming that Δt is very small and during a time-step (t to $t + \Delta t$), f^{eq} does not vary significantly and thus, can be treated as a constant which is evaluated at time t i.e. $f^{eq}(\mathbf{r}, \mathbf{v}, t)$, we can write:

$$f(\mathbf{r} + \mathbf{v}\Delta t, \mathbf{v}, t + \Delta t) e^{(t+\Delta t)/\tau} - f(\mathbf{r}, \mathbf{v}, t) e^{t/\tau} = -\frac{1}{\tau} f^{eq}(\mathbf{r}, \mathbf{v}, t) \int_t^{t+\Delta t} e^{t/\tau} Dt \quad (2.49)$$

which essentially is:

$$f(\mathbf{r} + \mathbf{v}\Delta t, \mathbf{v}, t + \Delta t) e^{(t+\Delta t)/\tau} - f(\mathbf{r}, \mathbf{v}, t) e^{t/\tau} = -f^{eq}(\mathbf{r}, \mathbf{v}, t) \left[e^{(t+\Delta t)/\tau} - e^{t/\tau} \right] \quad (2.50)$$

Dividing the above equation with $e^{(t+\Delta t)/\tau}$ and expanding $e^{-\Delta t/\tau}$ in a Taylor series up to term of order $O(\Delta t)$, we get:

$$f(\mathbf{r} + \mathbf{v}\Delta t, \mathbf{v}, t + \Delta t) - f(\mathbf{r}, \mathbf{v}, t) \left[1 - \frac{\Delta t}{\tau} + \dots \right] = -f^{eq}(\mathbf{r}, \mathbf{v}, t) \left[1 - \frac{\Delta t}{\tau} + \dots - 1 \right] \quad (2.51)$$

which can be written as:

$$f(\mathbf{r} + \mathbf{v}\Delta t, \mathbf{v}, t + \Delta t) - f(\mathbf{r}, \mathbf{v}, t) = -\frac{\Delta t}{\tau} \left[f(\mathbf{r}, \mathbf{v}, t) - f^{eq}(\mathbf{r}, \mathbf{v}, t) \right] \quad (2.52)$$

or,

$$f(\mathbf{r} + \mathbf{v}\Delta t, \mathbf{v}, t + \Delta t) = f(\mathbf{r}, \mathbf{v}, t) - \frac{\Delta t}{\tau} \left[f(\mathbf{r}, \mathbf{v}, t) - f^{eq}(\mathbf{r}, \mathbf{v}, t) \right] \quad (2.53)$$

which is the lattice Boltzmann equation (LBE) (He and Luo, 1997a; Luo, 1998; Lallemand and Luo, 2000).

2.11 Summary

In this chapter, a formal description of the lattice Boltzmann models (LBM) is provided. It is noted that the LB models are based on a rigorous theoretical foundation of Boltzmann's transport theory. Several approximations are made in order to simplify the mathematical and computational complexity of the Boltzmann equation in the process of retrieving the LB models. Since one of the significant assumptions of the Boltzmann theory is to account for the rarefied (dilute) gases, the standard LB equation possesses an inherent ideal

gas equation of state (which is evident after a Chapman-Enskog expansion on the LBE in certain limits and shown in Appendix A). Due to the ideal gas nature of the standard LB equation, it may not be directly applied to simulate complex fluid phenomena such as two-phase flows. Therefore, certain modifications in the LB equation are necessary to model and capture the necessary physics. In the next chapter, details are presented for an Enskog equation — a modified Boltzmann equation which accounts for finite particle sizes — based LB model in order to develop suitable models applicable for two-phase dynamics. Several other prevalent two-phase flow models in the LB framework are also discussed.

2.12 References

Abe, T., 1997. Derivation of the lattice Boltzmann method by means of the discrete ordinate method for the Boltzmann equation. *J. Comp. Phys.* 131, 241-246.

Bhatnagar, P.L., Gross, E.P., Krook, M., 1954. Model for collision processes in gases. *Phys. Rev.* 94, 511.

Cao, N., Chen, S., Jin, S., Martinez, D., 1997. Physical symmetry and lattice symmetry in the lattice Boltzmann method. *Phys. Rev. E* 55, R21-R24.

Cercignani, C., 1969. *Mathematical Methods in Kinetic Theory*. Plenum Press, New York.

Chapman, S., Cowling, T.G., 1970. *The Mathematical Theory of Non-Uniform Gases*. Cambridge University Press.

Chen, S., Doolen, G.D., 1998. Lattice Boltzmann Method for Fluid Flows. *Annu. Rev. Fluid Mech.* 30, 329–364.

Chopard, B., Droz, M., 1998. *Cellular Automata Modeling of Physical Systems*. Cambridge University Press.

Frisch, U., Hasslacher, B., Pomeau, Y., 1986. Lattice gas cellular automata for the Navier – Stokes equations. *Phys. Rev. Lett.* 56, 1505.

Harris, S., 1971. An Introduction to the Theory of the Boltzmann Equation. Holt, Rinehart and Winston, New York.

He, X., Chen, S., Doolen, G., 1998. A novel thermal model for the lattice Boltzmann method in incompressible limit. *J. Comput. Phys.* 146, 282–300.

He, X., Luo, L.-S., 1997a. Lattice Boltzmann model for the incompressible Navier–Stokes equation. *J. Stat. Phys.* 88, 927–944.

He, X., Luo, L.-S., 1997b. A priori derivation of the lattice Boltzmann equation. *Phys. Rev. E* 55, 6811–6817.

He, X., Luo, L.-S., 1997c. Theory of the lattice Boltzmann: from the Boltzmann equation to the lattice Boltzmann equation. *Phys. Rev. E* 56, 6811–6817.

Huang, K., 1963. Statistical Mechanics. John Wiley & Sons, Inc.

Koga, T., 1970. Introduction to Kinetic Theory Stochastic Processes in Gaseous Systems. Pergamon Press.

Lallemand, P., Luo, L.-S., 2000. Theory of the lattice Boltzmann method: dispersion, dissipation, isotropy, Galilean invariance, and stability. *Phys. Rev. E* 61, 6546–6562.

Liboff, R.L., 1969. Introduction to the Theory of Kinetic Equations. John Wiley & Sons, Inc.

Luo, L.-S., 1998. Unified theory of lattice Boltzmann models for nonideal gases. *Phys. Rev. Lett.* 81, 1618–1621.

Qian, Y.H., D Humieers, D., Lallemand, P., 1992. Lattice BGK models for Navier–Stokes equation. *Europhys. Lett.* 17, 479–484.

Qian, Y.H., Orszag, S.A., 1993. Lattice BGK models for the Navier–Stokes equation: nonlinear deviation in compressible regimes. *Europhys. Lett.* 21, 255–259.

Rivet, J.P., Boon, J.P., 2001. *Lattice Gas Hydrodynamics*. Cambridge University Press.

Rothman, D.H., Zaleski, S., 1997. *Lattice-Gas Cellular Automata: Simple models of complex hydrodynamics*. Cambridge University Press.

Succi, S., 2001. *The Lattice Boltzmann Equation—for Fluid Dynamics and Beyond*. Oxford Science Publications, UK.

Wolf-Gladrow D.A., 2000. *Lattice-Gas Cellular Automata and Lattice Boltzmann Models. Lecture Notes in Mathematics*. Springer.

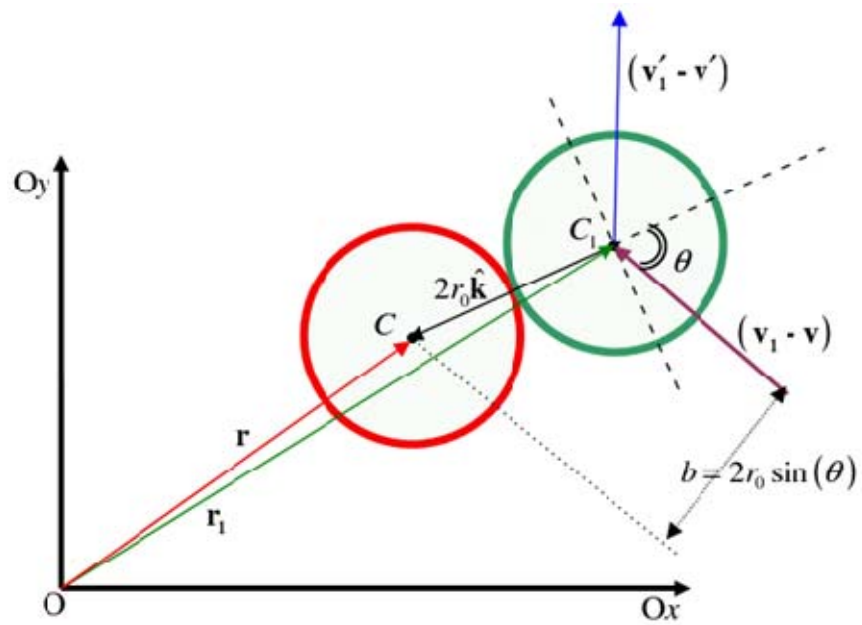
Chapter 3

Lattice Boltzmann equation for non-ideal fluids

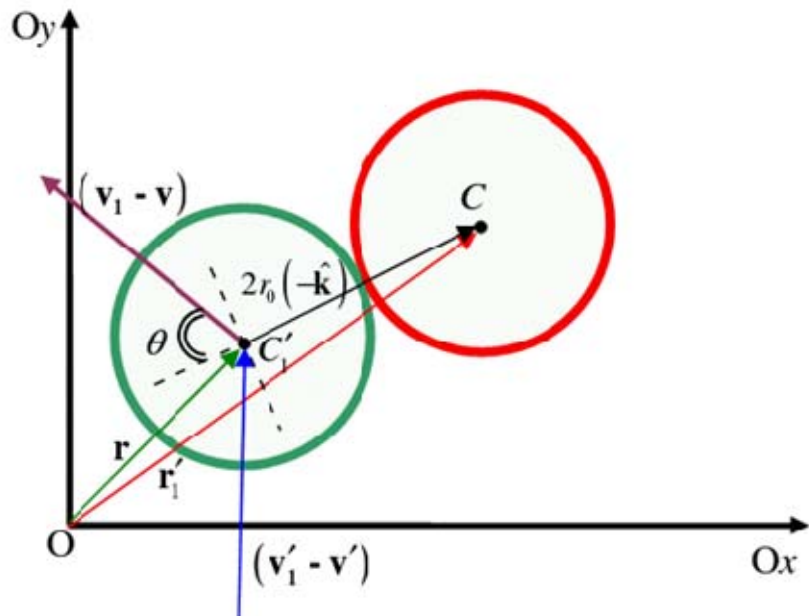
The *standard* lattice Boltzmann equation (LBE) possesses an inherent *ideal* gas equation of state and is not suitable for simulation of most of the real fluids which are denser than the ideal gases. Inapplicability of LBE for non-ideal fluids results from the fact that the LBE is based on the Boltzmann transport equation, which only describes dilute gases and is not suitable to model dense fluids. In the Boltzmann transport equation, the size of a particle is assumed to be very small compared to the average distance between particles, which is a valid assumption only for a dilute gas. Also, only binary collisions are considered and other higher order collisions are ignored.

In contrast to dilute gases, particles are closer in space in a dense fluid and their mean free path is comparable to the molecular dimensions. Therefore, particles of finite size must be taken into account. Because of the finite sizes, centers of colliding particles are not at the same point as typically assumed in a dilute gas. At the instant of collision, if the center of particle A is located at \mathbf{r} in a frame of reference fixed to particle A (i.e. moving with the same velocity as of particle A), then the center of the approaching particle, B , will be at $(\mathbf{r} - 2r_0 \hat{\mathbf{k}})$ where r_0 is the radius of the particle (here, all the particles are assumed to be of the same size) and $\hat{\mathbf{k}}$ is a unit vector in the direction from the center of approaching particle (B) to particle A (see Fig. 3.1(a)). Furthermore, we can assume that there exists an associated inverse collision corresponding to each direct collision and from Fig. 3.1 (b), the centre of the inverse collided particle will be at $(\mathbf{r} - 2r_0(-\hat{\mathbf{k}}))$.

In addition, since each particle occupies a finite volume equals to $(4/3)\pi r_0^3$, net volume available for particles to move around is reduced and therefore, frequency of collisions is increased by a factor $g(\mathbf{r})$, called the *radial distribution function*. The function $g(\mathbf{r})$ is evaluated at the point of contact of the two colliding particles just before and after the collision i.e. at $(\mathbf{r} - r_0 \hat{\mathbf{k}})$ and $(\mathbf{r} - r_0(-\hat{\mathbf{k}}))$, respectively.



(a)



(b)

Fig. 3.1: Binary collision of two hard-sphere particles of equal size (radius r_0): (a) Direct collision, and (b) Inverse collision. Red colored particle is particle A which is stationary, with a position vector \mathbf{r} in the reference frame fixed to A and is approached by the particle B shown in green color.

3.1 Modified Boltzmann equation: Enskog equation

By explicitly considering the volume exclusion effect of particles, Enskog proposed a modified Boltzmann equation (also called the *Enskog equation*) for dense gases as follows (Luo, 1998; Chapman & Cowling, 1970):

$$\left(\frac{\partial}{\partial t} + \mathbf{v} \cdot \nabla_{\mathbf{r}} + \mathbf{F} \cdot \nabla_{\mathbf{v}} \right) f(\mathbf{r}, \mathbf{v}, t) = \Omega_{\text{Enskog}} \quad (3.1)$$

Notice that the left hand side of equation (3.1) is the same as in the Boltzmann transport equation.

In Enskog equation, collision operator Ω_{Enskog} is modified to include the effects of the finite size of particles as:

$$\Omega_{\text{Enskog}} = \int d\mathbf{p}_1 \left[\begin{aligned} & g(\mathbf{r} + r_0 \hat{\mathbf{k}}) f(\mathbf{r}, \mathbf{v}', t) f(\mathbf{r} + 2r_0 \hat{\mathbf{k}}, \mathbf{v}'_1, t) \\ & - g(\mathbf{r} - r_0 \hat{\mathbf{k}}) f(\mathbf{r}, \mathbf{v}, t) f(\mathbf{r} - 2r_0 \hat{\mathbf{k}}, \mathbf{v}_1, t) \end{aligned} \right] \quad (3.2)$$

where

$$d\mathbf{p}_1 = d\mathbf{v}_1 |\mathbf{v}_1 - \mathbf{v}| b db d\phi \quad (3.3)$$

Note that, even in the Enskog equation, only two-particle collisions are considered and all the higher order collisions involving more than two particles are ignored.

For binary collision of hard spheres of radius r_0 , the impact parameter b of scattering is (see Fig. 3.2):

$$b = 2r_0 \sin(\theta) \quad (3.4)$$

where θ is the azimuthal angle ($0 \leq \theta \leq \pi/2$) between the relative velocity vector $(\mathbf{v}_1 - \mathbf{v})$ and unit vector $\hat{\mathbf{k}}$, and ϕ is the polar angle ($0 \leq \phi \leq 2\pi$) on the plane perpendicular to vector $(\mathbf{v}_1 - \mathbf{v})$.

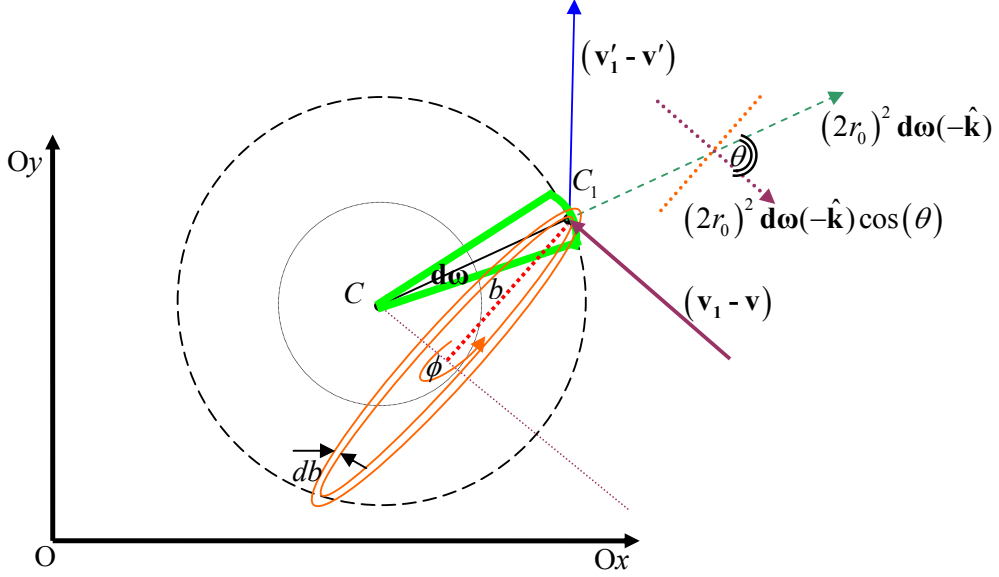


Fig. 3.2: Binary collision of two rigid spherical particles of radius r_0 whose centers are at C and C_1 . The particle at C is assumed to be at rest with respect to the reference frame.

$(2r_0)^2 d\omega$ denotes a surface element, on the sphere of radius $2r_0$ and centered at C , on which C_1 must lie at the instant of collision. The differential area $db d\phi$ is the projection of $(2r_0)^2 d\omega$ on a plane normal to $(v_1 - v)$ and θ is the angle between $(v_1 - v)$ and \hat{k} .

3.1.1 Approximation of Enskog collision operator Ω_{Enskog}

Assuming that the conditions in the dense gas are slowly varying in space, we can expand $g(\mathbf{r} \pm r_0 \hat{k})$ and $f(\mathbf{r} \pm 2r_0 \hat{k}, \mathbf{v}'_1, t)$ in a first order Taylor series as:

$$g(\mathbf{r} \pm r_0 \hat{k}) = g(\mathbf{r}) \pm r_0 \hat{k} \cdot \nabla g(\mathbf{r}) \quad (3.5)$$

$$f(\mathbf{r} \pm 2r_0 \hat{k}, \mathbf{v}'_1, t) = f(\mathbf{r}, \mathbf{v}'_1, t) \pm 2r_0 \hat{k} \cdot \nabla f(\mathbf{r}, \mathbf{v}'_1, t) \quad (3.6)$$

Substituting equations (3.5) and (3.6) in equation (3.2) and neglecting second order derivatives, we get:

$$\Omega_{\text{Enskog}} = \Omega_{\text{Enskog}}^{(0)} + \Omega_{\text{Enskog}}^{(1)} + \Omega_{\text{Enskog}}^{(2)} \quad (3.7)$$

where

$$\Omega_{\text{Enskog}}^{(0)} = g(\mathbf{r}) \int d\mathbf{u}_1 [f' f'_1 - f f_1] \quad (3.8)$$

$$\Omega_{\text{Enskog}}^{(1)} = r_0 \int d\mathbf{p}_1 [f' f'_1 + f f_1] \hat{\mathbf{k}} \cdot \nabla g(\mathbf{r}) \quad (3.9)$$

and

$$\Omega_{\text{Enskog}}^{(2)} = 2r_0 g \int d\mathbf{p}_1 \hat{\mathbf{k}} \cdot [f' \nabla f'_1 + f \nabla f_1] \quad (3.10)$$

Note that, $f \equiv f(\mathbf{r}, \mathbf{v}, t)$, $f_1 \equiv f(\mathbf{r}, \mathbf{v}_1, t)$, $f' \equiv f(\mathbf{r}, \mathbf{v}', t)$ and $f'_1 \equiv f(\mathbf{r}, \mathbf{v}'_1, t)$.

3.1.2 Evaluation of $\Omega_{\text{Enskog}}^{(0)}$

$\Omega_{\text{Enskog}}^{(0)}$ only differs from the Boltzmann collision integral Ω_{Boltz} by a factor $g(\mathbf{r})$ and thus, can be approximated by taking into account the BGK-collision approximation as:

$$\Omega_{\text{Enskog}}^{(0)} = g(\mathbf{r}) \Omega_{\text{Boltz}} = g(\mathbf{r}) \Omega_{\text{BGK}} = g(\mathbf{r}) \left[-\frac{f(\mathbf{r}, \mathbf{v}, t) - f^{eq}(\mathbf{r}, \mathbf{v}, t)}{\tau} \right] \quad (3.11)$$

where τ is the *single relaxation time* and, $f^{eq}(\mathbf{r}, \mathbf{v}, t)$ is the equilibrium distribution function given by the Maxwellian:

$$f^{eq}(\mathbf{r}, \mathbf{v}, t) = \frac{\rho}{(2\pi RT)^{d/2}} \exp\left(-\frac{(\mathbf{v} - \mathbf{u}) \cdot (\mathbf{v} - \mathbf{u})}{2RT}\right) \quad (3.12)$$

3.1.3 Evaluation of $\Omega_{\text{Enskog}}^{(1)}$

$\Omega_{\text{Enskog}}^{(1)}$ and $\Omega_{\text{Enskog}}^{(2)}$ can directly be evaluated by assuming f to be close to equilibrium, i.e. $f \approx f^{eq}$ and using the relation:

$$f^{eq'} f_1^{eq'} = f^{eq} f_1^{eq} \quad (3.13)$$

which is applicable to the Maxwell-Boltzmann form of the equilibrium distribution function (Chapman & Cowling, 1970). Note that, $f^{eq} \equiv f^{eq}(\mathbf{r}, \mathbf{v}, t)$, $f_1^{eq} \equiv f^{eq}(\mathbf{r}, \mathbf{v}_1, t)$, $f^{eq'} \equiv f^{eq}(\mathbf{r}, \mathbf{v}', t)$ and $f_1^{eq'} \equiv f^{eq}(\mathbf{r}, \mathbf{v}'_1, t)$.

From equations (3.9) and (3.13), we can write $\Omega_{\text{Enskog}}^{(1)}$ as:

$$\Omega_{\text{Enskog}}^{(1)} = 2r_0 \int d\mathbf{p}_1 [f^{eq} f_1^{eq}] (\hat{\mathbf{h}} \cos \theta) \cdot \nabla g \quad (3.14)$$

where $\hat{\mathbf{h}}$ is a unit vector in the direction of relative approach velocity $(\mathbf{v}_1 - \mathbf{v})$. Now, from equation (3.3), we can write:

$$\Omega_{\text{Enskog}}^{(1)} = 2r_0 f^{eq} \int b db \cos \theta \int d\phi \int d\mathbf{v}_1 f_1^{eq} |\mathbf{v}_1 - \mathbf{v}| \hat{\mathbf{h}} \cdot \nabla g \quad (3.15)$$

which, using equation (3.4), becomes:

$$\Omega_{\text{Enskog}}^{(1)} = 2r_0 f^{eq} \left(\int_0^{\pi/2} 4r_0^2 \sin \theta \cos^2 \theta d\theta \right) \left(\int_0^{2\pi} d\phi \right) \left(\int f_1^{eq} d\mathbf{v}_1 (\mathbf{v}_1 - \mathbf{v}) \right) \cdot \nabla g \quad (3.16)$$

The above equation simplifies to:

$$\Omega_{\text{Enskog}}^{(1)} = -f^{eq} B_2 \rho (\mathbf{v} - \mathbf{u}) \cdot \nabla g \quad (3.17)$$

where B_2 is called the *second virial coefficient* in the virial equation of state, and is equal to:

$$B_2 = \frac{16}{3} \pi r_0^3 \quad (3.18)$$

3.1.4 Evaluation of $\Omega_{\text{Enskog}}^{(2)}$

After substituting $f \approx f^{eq}$ in equation (3.10), we can write:

$$\Omega_{\text{Enskog}}^{(2)} = 2r_0 g \int d\mathbf{u}_1 (\hat{\mathbf{h}} \cos \theta) \cdot [f^{eq'} \nabla f_1^{eq'} + f^{eq} \nabla f_1^{eq}] \quad (3.19)$$

which, using equations (3.3) and (3.4), can be written as:

$$\Omega_{\text{Enskog}}^{(2)} = 2r_0 g \int b db \cos \theta \int d\phi \int d\mathbf{v}_1 |\mathbf{v}_1 - \mathbf{v}| \hat{\mathbf{h}} \cdot [f^{eq'} \nabla f_1^{eq'} + f^{eq} \nabla f_1^{eq}] \quad (3.20)$$

Using equations (3.13) and (3.18), the above equation can be simplified to:

$$\Omega_{\text{Enskog}}^{(2)} = B_2 g \int d\mathbf{v}_1 (\mathbf{v}_1 - \mathbf{v}) \cdot \left[\frac{\nabla f_1^{eq'}}{f_1^{eq'}} + \frac{\nabla f_1^{eq}}{f_1^{eq}} \right] f^{eq} f_1^{eq} \quad (3.21)$$

and can be written as:

$$\Omega_{\text{Enskog}}^{(2)} = B_2 f^{eq} g \int f_1^{eq} d\mathbf{v}_1 (\mathbf{v}_1 - \mathbf{v}) \cdot [\nabla \ln f_1^{eq} f_1^{eq'}] \quad (3.22)$$

The gradient term in equation (3.22), $\nabla \ln f_1^{eq} f_1^{eq'}$ can be written as:

$$\nabla \ln f_1^{eq} f_1^{eq'} = 2 \nabla \ln \left(\frac{\rho}{(2\pi RT)^{d/2}} \right) - \nabla \left(\frac{v_1^2 + v_1'^2}{2RT} \right) + \nabla \left(\frac{\mathbf{u} \cdot (\mathbf{v}_1 + \mathbf{v}_1')}{RT} \right) - \nabla \left(\frac{u^2}{RT} \right) \quad (3.23)$$

which after substituting relations between \mathbf{v}_1' and \mathbf{v}_1 can be integrated (details of integrations are given in Chapman and Cowling, 1970) and yields the following:

$$\Omega_{\text{Enskog}}^{(2)} = -B_2 f^{eq} g \rho \left[2(\mathbf{v} - \mathbf{u}) \cdot \nabla \ln \rho + \frac{2}{(d+2)} \frac{(v_\alpha - u_\alpha)(v_\beta - u_\beta) \partial_\alpha u_\beta}{RT} \right. \\ \left. + \left\{ \frac{1}{(d+2)} \frac{(\mathbf{v} - \mathbf{u})^2}{RT} - 1 \right\} \nabla \cdot \mathbf{u} + \frac{1}{2} \left\{ \frac{d}{(d+2)} \frac{(\mathbf{v} - \mathbf{u})^2}{RT} - 1 \right\} (\mathbf{v} - \mathbf{u}) \cdot \nabla \ln(RT) \right] \quad (3.24)$$

This equation for $\Omega_{\text{Enskog}}^{(2)}$ can be simplified for incompressible ($\nabla \cdot \mathbf{u} = 0$) and isothermal ($\nabla T = 0$) fluids by setting the last two terms on the right hand side equal to zero. Moreover, the term involving the derivative $\partial_\alpha u_\beta$ can also be neglected in order to have $\Omega_{\text{Enskog}}^{(2)}$ satisfy mass conservation i.e. $\sum \Omega_{\text{Enskog}}^{(2)} = 0$. Above simplifications, in turn, yield:

$$\Omega_{\text{Enskog}}^{(2)} = -f^{eq} B_2 \rho g (\mathbf{v} - \mathbf{u}) \cdot \nabla \ln(\rho^2) \quad (3.25)$$

3.1.5 Evaluation of Ω_{Enskog}

Now, from equations (3.7), (3.11), (3.17) and (3.25), we can write Ω_{Enskog} as:

$$\Omega_{\text{Enskog}} = -\frac{g}{\tau} (f - f^{eq}) - f^{eq} B_2 \rho g (\mathbf{v} - \mathbf{u}) \cdot \left[\frac{\nabla g}{g} + \nabla \ln(\rho^2) \right] \quad (3.26)$$

The above equation can be written as:

$$\Omega_{\text{Enskog}} = -\frac{1}{\tau_g} (f - f^{eq}) + J \quad (3.27)$$

where

$$\tau_g = \frac{\tau}{g} \quad (3.28)$$

and

$$J = -f^{eq} B_2 \rho g (\mathbf{v} - \mathbf{u}) \cdot \nabla \ln(\rho^2 g) \quad (3.29)$$

3.1.6 Lattice velocity moments of J_a

The discrete velocity counterpart of the term J in equation (3.29) can be written as follows:

$$J_a = -f_a^{eq} B_2 \rho g (\mathbf{v}_a - \mathbf{u}) \cdot \nabla \ln(\rho^2 g) \quad (3.30)$$

Zeroth lattice-velocity moment of the term J_a is:

$$\sum_a J_a = -B_2 \rho g \underbrace{\left(\sum_a \overbrace{\mathbf{v}_a f_a^{eq}}^{\rho \mathbf{u}} - \mathbf{u} \sum_a \overbrace{f_a^{eq}}^{\rho} \right)}_{=0} \partial_{r_\alpha} \left(\ln(\rho^2 g) \right) = 0 \quad (3.31)$$

First lattice-velocity moment of the term J_a is:

$$\begin{aligned} \sum_a v_{a\alpha} J_a &= -B_2 \rho g \left(\underbrace{\sum_a v_{a\alpha} v_{a\beta} f_a^{eq}}_{=\rho R T \delta_{\alpha\beta} + \rho u_\alpha u_\beta} - u_\beta \underbrace{\sum_a v_{a\alpha} f_a^{eq}}_{=\rho u_\alpha} \right) \partial_{r_\alpha} \left(\ln(\rho^2 g) \right) \\ &= -B_2 R T \delta_{\alpha\beta} \left[(\rho^2 g) \partial_{r_\alpha} \left(\ln(\rho^2 g) \right) \right] \\ &= -B_2 R T \delta_{\alpha\beta} \left[\partial_{r_\alpha} (\rho^2 g) \right] \\ &= - \left[\partial_{r_\alpha} (B_2 R T \rho^2 g) \right] \delta_{\alpha\beta} \end{aligned} \quad (3.32)$$

3.2 Enskog equation based lattice Boltzmann equation

The LBE equation for the dense gas is:

$$f_a(\mathbf{r} + \mathbf{v}_a \Delta t, t + \Delta t) = f_a(\mathbf{r}, t) - \frac{\Delta t}{\tau_g} \left[f_a(\mathbf{r}, t) - f_a^{eq}(\mathbf{r}, t) \right] + (B_a + J_a) \Delta t \quad (3.33)$$

which, following the Chapman-Enskog analysis, leads to:

$$\partial_t (u_\alpha) + \frac{\partial_{r_\beta} \Pi_{\alpha\beta}^{(0)}}{\rho} = \nu \partial_{r_\beta} \partial_{r_\beta} (u_\alpha) + F_\alpha - \frac{1}{\rho} \partial_{r_\alpha} (B_2 R T \rho^2 g) \delta_{\alpha\beta} \quad (3.34)$$

The above equation can be simplified to:

$$\partial_t (u_\alpha) + u_\beta \left(\partial_{r_\beta} u_\alpha \right) = \nu \partial_{r_\beta} \partial_{r_\beta} (u_\alpha) + F_\alpha - \frac{1}{\rho} \partial_{r_\alpha} p \quad (3.35)$$

where

$$p = \rho R T (1 + B_2 \rho g) \quad (3.36)$$

is the non-ideal equation of state for the Enskog equation based LB model and the kinematic viscosity is (Luo, 2000):

$$\nu = R T \left(\tau_g - \frac{\Delta t}{2} \right). \quad (3.37)$$

After defining the governing equation of state in equation (3.36), the sound speed can be evaluated as:

$$c_s = \sqrt{\frac{dp}{d\rho}} = \sqrt{RT \left(1 + B_2 \frac{d}{d\rho} (\rho^2 g) \right)} \quad (3.38)$$

In the Enskog equation, the radial distribution function g only accommodates the volume exclusion effects of a dense gas made of hard-spheres and has the following asymptotic form (Chapman & Cowling, 1970):

$$g = 1 + \frac{5}{8} B_2 \rho + 0.2869 (B_2 \rho)^2 + 0.1103 (B_2 \rho)^3 + \dots \quad (3.39)$$

To simulate a more realistic non-ideal behavior, g can be chosen based upon the desired non-ideal equation of state. Moreover, g also provides freedom to alter the transport coefficients, i.e. fluid viscosity (equation (3.37)) and the sound speed (equation (3.38)). For example, the van der Waals equation of state is given by:

$$p = \rho RT \left(\frac{1}{1 - \tilde{b}\rho} - \frac{\tilde{a}\rho}{RT} \right) \quad (3.40)$$

A comparison of equations (3.36) and (3.40) gives:

$$g = \frac{1}{B_2} \left[\frac{\tilde{b}}{(1 - \tilde{b}\rho)} - \frac{\tilde{a}}{RT} \right] \quad (3.41)$$

Similarly, various other non-ideal equations of state (McQuarrie & Simon, 1999) may be simulated by defining radial distributions function g accordingly.

Furthermore, for a given equation of state, the Helmholtz free energy density ϕ , defined as (Luo, 1998):

$$p = \rho \frac{d\phi}{d\rho} - \phi = \rho^2 \frac{d}{d\rho} \left(\frac{\phi}{\rho} \right) \quad (3.42)$$

can be evaluated by the following integral:

$$\phi = \rho \int \frac{p}{\rho^2} d\rho \quad (3.43)$$

3.3 A survey of two-phase models in the LB framework

The lattice-Boltzmann approach for two-phase simulation is based on a type of diffuse interface method, i.e. the phase interface spreads over several grid points. A review of diffuse interface methods can be found in Anderson et al. (1998).

In most of the two-phase LB models, phase segregation is induced via the forcing term of the standard lattice Boltzmann equation. The specifics of the forcing term, which enables one to simulate multi-phase evolution, are either determined from the kinetic models of dense fluids (for example, Enskog equation) (Luo, 1998) or by supplying a non-ideal equation of state such as van der Waals EOS or more realistic equation of states (He et al., 1998; Yuan & Schaefer, 2006) for the fluid. Some notable two-phase LB models resulted from the work of Gustensen et al. (1991), Grunau et al. (1993), Rothman & Zaleski (1997).

Below, we discuss some of the prevalent two-phase flow models (Succi, 2001):

3.3.1 Shan-Chen (S-C) model

The model proposed by Shan and Chen is one of the older LBE models for two-phase simulations. The non-ideal effects are produced via an attractive inter-particle force between nearest-neighbors, defined as (Shan & Chen, 1993; 1994):

$$\mathbf{F}_{\text{attr}} = G\psi(\mathbf{r}, t) \sum_{a=0}^b w_a \psi(\mathbf{r} + \mathbf{v}_a \Delta t, t) \mathbf{v}_a \quad (3.44)$$

where $G(> 0)$ is the strength of attraction and w_a are the lattice-specific direction-dependent weighting factors. In the above equation, ψ is called the interaction potential and is an *arbitrary* function of density ρ , empirically assumed to have the following form:

$$\psi(\mathbf{r}, t) \equiv \psi(\rho(\mathbf{r}, t)) = \psi_0 \exp\left(-\frac{\rho_0}{\rho}\right) \quad (3.45)$$

where ψ_0 and ρ_0 are arbitrary constants. This specific form of potential is designed to be a monotonically increasing and bounded function of density ρ , which is essential to have a large cohesive force for large density region (liquid) and relatively smaller cohesive force for low density region (vapor) (Sukop & Thorne, 2006).

In the S-C model, forcing effects are captured into the simulation by shifting the macroscopic velocity distribution in the equilibrium distribution function by:

$$\mathbf{u}' = \mathbf{u} + \tau \left(\frac{\mathbf{F}_{\text{attr}}}{\rho} \right) \quad (3.46)$$

The equilibrium distribution function f^{eq} is now evaluated as a function of \mathbf{u}' at each time step (replacing \mathbf{u} by \mathbf{u}' in the original f^{eq} expression). It can easily be shown that the above inclusion of forcing term into the equilibrium distribution function is accurate up to the order $O(\mathbf{u})$ and is equivalent to applying an external acceleration $\mathbf{a}_{\text{attr}} = \mathbf{F}_{\text{attr}}/\rho$ at each spatial grid point.

We can expand $\psi(\mathbf{r} + \mathbf{v}_a \Delta t, t)$ in equation (3.44) in a Taylor series:

$$\psi(\mathbf{r} + \mathbf{v}_a \Delta t, t) = \psi(\mathbf{r}, t) + \mathbf{v}_a \Delta t \nabla \psi + \frac{(\mathbf{v}_a \Delta t)^2}{2} \nabla^2 \psi + \frac{(\mathbf{v}_a \Delta t)^3}{6} \nabla^3 \psi + \dots \quad (3.47)$$

to get (Hou et al., 1997):

$$\mathbf{a}_{\text{attr}} = \nabla \left[\frac{GRT}{2} \Delta t \left(\psi^2 + RT \Delta t^2 \left(\psi \nabla^2 \psi - \frac{1}{2} (\nabla \psi)^2 \right) \right) \right] \mathbf{I} \quad (3.48)$$

Following the Chapman-Enskog expansion, in the corresponding incompressible Navier-Stokes equation, the effect of \mathbf{a}_{attr} can be combined in the pressure term as:

$$p = \rho RT + \frac{GRT}{2} \psi^2 \Delta t \quad (3.49)$$

to yield a non-ideal equation of state. Rest of the higher order derivative terms in equation (3.48) are responsible for producing the inherent surface-tension of the S-C model.

Similar to the ideas represented above, wall-fluid forces are also captured by defining a wall adhesion force as (Martys & Chen, 1996):

$$\mathbf{F}_{\text{ads}} = G_{\text{ads}} \psi(\mathbf{r}, t) \sum_{a=0}^b w_a s(\mathbf{r} + \mathbf{v}_a \Delta t, t) \mathbf{v}_a \quad (3.50)$$

where G_{ads} is the magnitude of wall adhesion force. Varying G_{ads} results in different contact angles between the fluid and the wall. s is a Boolean vector identifying the walls in the domain (1, if neighbor is a wall; 0 otherwise).

Benzi et al. (2006) proposed a methodology to simulate contact angles in the S-C model. Huang et al. (2007) proposed a technique for simulating wall contact angles in the framework of S-C multi-component model (Shan & Doolen, 1995). Markus & Hazi (2008) very recently proposed a method to analytically determine suitable pseudo-potential gradient to avoid numerical instabilities in the S-C model.

3.3.2 He-Shan-Doolen (HSD) model

To simulate a non-ideal fluid, this model combines: 1) the inter-particle attraction \mathbf{F}_{attr} ; 2) the hard-core repulsion \mathbf{F}_{rep} ; and 3) the gravitational force \mathbf{F}_{grav} into the generic forcing term of the approximate Boltzmann equation as (He et al., 1998; He et al., 1999a; Zhang & Chen, 2000, 2003; He & Doolen, 2002; Tentner et al., 2006):

$$\frac{\partial f}{\partial t} + \mathbf{v} \cdot \nabla_{\mathbf{r}} f = -\frac{f - f^{eq}}{\tau} + \frac{\mathbf{F} \cdot (\mathbf{v} - \mathbf{u})}{c_s^2} f^{eq} \quad (3.51)$$

where $\mathbf{F} = \frac{1}{\rho} (\mathbf{F}_{attr} + \mathbf{F}_{rep} + \mathbf{F}_{grav})$ is the acceleration (force per unit mass) of the particle.

In this model, \mathbf{F}_{attr} and \mathbf{F}_{rep} are defined as:

$$\mathbf{F}_{attr} = \rho \nabla (2\tilde{a}\rho + \tilde{\kappa} \nabla^2 \rho) \quad (3.52)$$

$$\mathbf{F}_{rep} = -B_2 \rho^2 R T g \nabla \ln(\rho^2 g) \quad (3.53)$$

where \tilde{a} and $\tilde{\kappa}$ are constants related to the attraction term of the inter-particle potential. Here, \mathbf{F}_{attr} represents the effective inter-particle attraction by mean-field approximation, and \mathbf{F}_{rep} represents the Enskog's exclusion volume effect.

Combining the \mathbf{F}_{attr} , \mathbf{F}_{rep} and \mathbf{F}_{grav} , we can write:

$$\mathbf{F} = \rho \nabla (2\tilde{a}\rho + \tilde{\kappa} \nabla^2 \rho) - B_2 \rho^2 R T g \nabla \ln(\rho^2 g) + \mathbf{F}_{grav} \quad (3.54)$$

The above equation can be simplified as:

$$\mathbf{F} = -\nabla U + \mathbf{F}_{\text{surf}} + \mathbf{F}_{\text{grav}} \quad (3.55)$$

where \mathbf{F}_{surf} represents the force associated with the surface tension, and is equal to:

$$\mathbf{F}_{\text{surf}} = \tilde{\kappa} \rho \nabla \nabla^2 \rho \quad (3.56)$$

and, U is defined as:

$$U = B_2 \rho^2 RTg - \tilde{a} \rho^2 \quad (3.57)$$

Furthermore, a Chapman-Enskog analysis for this model yields the non-ideal equation of state as:

$$p = \rho RT + U = \rho RT (1 + B_2 \rho g) - \tilde{a} \rho^2 \quad (3.58)$$

3.3.3 Free energy based model

Swift et al. (1995) developed a free energy based LB model to derive a more thermodynamically consistent description. In their model, the equilibrium pressure tensor for a non-ideal fluid was introduced directly into the collision operator and a connection is made between the pressure tensor and the free energy. Thermodynamic equilibrium was enforced via incorporating Cahn-Hilliard and Ginzburg-Landau models using the concepts of free-energy functional in the LB system. The model was demonstrated using the van der Waals equation of state. The scheme was tested against verification of the Laplace law. Nourgaliev et al. (1999) proposed novel numerical schemes to improve the stability of the numerics. Palmer and Rector (2000) proposed algorithm to simulate thermal two-phase flows by combining the Swift et al. (1995) model with the two-distribution model to treat the internal energy as a separate conserved scalar. Inamuro (2004) coupled the free energy base LB model with a projection method to simulate two-phase immiscible fluids with large density differences. Zheng et al. (2005, 2006) proposed a similar model in which the interface between two phases is captured by minimizing the free energy functional.

3.3.4 Pressure evolution model

The theoretical models based on the Enskog's equation and the HSD model are reported to be unstable when used directly in a numerical simulation (Lee & Lin, 2003) due to severe pressure fluctuations at the interfaces. These pressure fluctuations are claimed to be associated with the non-ideal equation of state in which the derivative of pressure with respect to density changes sign (Lee & Lin, 2003). In order to subdue these pressure fluctuations, a transformed distribution function is introduced by He et al. (1999a,b) to simulate non-ideal pressure, and the original distribution function was used to simulate an order parameter representing density of the fluid. Despite including the transformation, the model was only able to simulate very low density ratio (order $O(1)$) of the two-phases in a Rayleigh-Taylor instability problem. In an attempt to stabilize the numerical simulation of above mentioned theoretical models for larger density ratio and to make the models practically useful, Lee & Lin (2003, 2005) and Lee & Fischer (2006) proposed stable discretization schemes for the forcing terms (whose stiffness along with the use of an explicit EOS were identified as being responsible for triggering the numerical instabilities). It is claimed that using the transformation, as in He et al. (1999a,b) and the consistent discretization, as in Lee & Lin (2005), one is able to avoid the numerical instabilities which plague a large number of lattice Boltzmann simulations. Similar stabilization techniques have been proposed by Nourgaliev et al. (2003) earlier.

3.4 Summary

In this chapter, derivation of a non-ideal lattice Boltzmann equation based on the Enskog theory of dense gases is presented. Several of the two-phase models in the LB framework are also introduced. Although LB simulations based on the Enskog equation are reported to suffer from severe numerical instabilities, they are still very useful in understanding the non-ideal physics of a complex fluid. Furthermore, several of the recent two-phase LB models are proposed with an inherent Enskog component in the model, such as in the He-Shan-Doolen (HSD) and the pressure evolution model.

In the next chapter, an artificial interface lattice Boltzmann (AILB) model is proposed for the simulation of two-phase dynamics. AILB model is found to be more stable than its

earlier counterparts and is able to simulate a larger density and viscosity ratios for different phases. The wetting boundary conditions based on the Cahn's theory is also developed for the AILB model which allows simulation of different equilibrium contact angles on a wall surface.

3.5 References

Andersen, D.M., McFadden, G.B., Wheeler, A.A., 1998. Diffuse-interface in fluid mechanics. *Annu. Rev. Fluid Mech.* 30, 139–165.

Benzi, R., Biferale, L., Sbragaglia, M., Succi, S., Toschi, F., 2006. Mesoscopic modeling of a two-phase flow in the presence of boundaries: The contact angle. *Phys. Rev. E* 74, 021509.

Chapman, S., Cowling, T.G., 1970. *The Mathematical Theory of Non-Uniform Gases*. Cambridge University Press.

Grunau, D., Chen, S., Eggert, K., 1993. A lattice Boltzmann model for multiphase fluid flows. *Phys. Fluids A* 5 (10), 2557-2562.

Gustensen, A.K., Rothman, D.H., Zaleski, S., Zanetti, G., 1991. Lattice Boltzmann model of immiscible fluids. *Phys. Rev. A* 43, 4320–4327.

He, X., Chen, S., Zhang, R., 1999a. A lattice Boltzmann scheme for incompressible multiphase flow and its application in simulation of Rayleigh–Taylor instability. *J. Comput. Phys.* 152, 642–663.

He, X., Chen, S., Zhang, R., Doolen, G.D., 1999b. On the three-dimensional Rayleigh–Taylor instability. *Phys. Fluids* 11, 1143.

He, X., Doolen, G., 2002. Thermodynamic foundations of kinetic theory and lattice Boltzmann models for multiphase flows. *J. Stat. Phys.* 107, 309-328.

He, X., Shan, X., Doolen, G., 1998. Discrete Boltzmann equation model for nonideal gases. *Phys. Rev. Lett.* 57, R13–R16.

Hou, S., Shan, X., Zou, Q., Doolen, G.D., Soll, W.E., 1997. Evaluation of two lattice Boltzmann models for multiphase flows. *J. Comp. Phys.* 138, 695-713.

Huang, H., Thorne, D.T., Schaap, M.G., Sukop, M.C., 2007. Proposed approximation for contact angles in Shan-and-Chen type multicomponent multiphase lattice Boltzmann models. *Phys. Rev. E* 76, 066701.

Inamuro, T., Ogata, T., Tajima, S., Konishi, N., 2004. A lattice Boltzmann method for incompressible two-phase flows with large density differences. *J. Comp. Phys.* 198, 628-644.

Kono, K., Ishizuka, T., Tsuda, H., Kurosawa, A., 2000. Application of lattice Boltzmann model to multiphase flows with phase transition. *Comp. Phys. Comm.* 129, 110-120.

Lee, T., Lin, C.L., 2003. Pressure evolution lattice-Boltzmann-equation method for two-phase flow with phase change. *Phys. Rev. E* 67, 056703.

Lee, T., Lin, C.L., 2005. A stable discretization of the lattice Boltzmann equation for simulation of incompressible two-phase flows at high density ratio. *J. Comput. Phys.* 206, 16-47.

Lee, T., Fischer, P.F., 2006. Eliminating parasitic currents in the lattice Boltzmann equation method for nonideal gases. *Phys. Rev. E* 74, 046709.

Luo, L.S., 1998. Unified theory of lattice Boltzmann models for nonideal gases. *Phys. Rev. Lett.* 81, 1618-1621.

Luo, L.S., 2000. Theory of the lattice Boltzmann method: Lattice Boltzmann models for nonideal gases. *Phys. Rev. E* 62, 4982-4996.

Markus, A., Hazi, G., 2008. Determination of the pseudopotential gradient in multiphase lattice Boltzmann models. *Phys. Fluids* 20, 022101.

Martys, N.S., Chen, H., 1996. Simulation of multicomponent fluids in complex three-dimensional Geometries by the lattice Boltzmann method. *Phys. Rev. E* 53, 743–750.

McQuarrie, D., Simon, J.D., 1999. *Molecular Thermodynamics*, University Science, Sausalito, CA.

Nourgaliev, R.R., Dinh, T.N., Theofanous, T.G., Joseph, D., 2003. The lattice Boltzmann equation method: theoretical interpretation, numerics and implications. *Int. J. Multiphase Flow* 29, 117-169.

Nourgaliev, R.R., Dinh, T.N., Hattori, S., Sehgal, B.R., 1999. Free-energy based lattice Boltzmann model of phase transitions in an isothermal non-ideal fluid. Ninth Intl. Topical meeting on Nuclear Reactor Thermal Hydraulics (NURETH-9), San Francisco, CA, October 3-8, 1999.

Palmer, B.J., Rector, D.R., 2000. Lattice-Boltzmann algorithm for simulating thermal two-phase flow. *Phys. Rev. E* 61(5), 5295-5306.

Rothman, D.H., Zaleski, S., 1997. *Lattice-Gas Cellular Automata: Simple models of complex hydrodynamics*. Cambridge University Press.

Shan, X., Chen, H., 1993. Lattice Boltzmann model for simulation flows with multiple phases and components. *Phys. Rev. E* 47, 1815.

Shan, X., Chen, H., 1994. Simulation of nonideal gases and liquid-gas phase transitions by the lattice Boltzmann equation. *Phys. Rev. E* 49, 2941.

Shan, X., Doolen, G.D., 1995. Multicomponent lattice-Boltzmann model with interparticle interaction”, *J. Stat. Phys.* 81, 379.

Sukop, M.C., Thorne, D.T., 2006. *Lattice Boltzmann Modeling—An Introduction for Geoscientists and Engineers*. Springer-Verlag Berlin Heidelberg.

Succi, S., 2001. *The Lattice Boltzmann Equation—for Fluid Dynamics and Beyond*. Oxford Science Publications, UK.

Swift, M.R., Osborn, W.R., Yeomans, J.M., 1995. Lattice Boltzmann simulation of non-ideal fluids. *Phys. Rev. Letters* 75(5), 830-834.

Tentner, A., Chen H., Zhang, R., 2006. Simulation of two-phase flow and heat transfer phenomena in a boiling water reactor using the lattice Boltzmann method. *Physica A*, 362, 98-104.

Yuan, P., Schaefer, L., 2006. Equations of state in a lattice Boltzmann model. *Phys Fluids* 18, 042101.

Zhang, R., He, X., Chen, S., 2000. Interface and surface tension in incompressible lattice Boltzmann multiphase model. *Computer Physics Communications* 129, 121-130.

Zhang, R., Chen, H., 2003. Lattice Boltzmann method for simulation of liquid-vapor thermal flows”, *Phys. Rev. E* 67, 066711.

Zheng, H.W., Shu, C., Chew, Y.T., 2005. Lattice Boltzmann interface capturing method for incompressible flows. *Phys. Rev. E* 72, 056705.

Zheng, H.W., Shu, C., Chew, Y.T., 2006. A lattice Boltzmann model for multiphase flows with large density ratio. *J. Comp. Phys.* 218, 353-371.

Chapter 4

Artificial interface lattice Boltzmann (AILB) model

A thermodynamically consistent lattice Boltzmann (LB) model for the two-phase simulations can be obtained if one treats the chemical potential as the driving force for the phase separation. Incorporation of the Gibbs-Duhem equation, which imposes constraints on thermodynamic variables of a given system at equilibrium, into the LB model can guarantee the recovery of the equilibrium phase-thermodynamics (Wagner, 2006).

In this chapter, a new LB model, called the *artificial interface lattice Boltzmann* (AILB) model is proposed for the two-phase simulations. The model incorporates the Gibbs-Duhem equation in order to recover the equilibrium thermodynamics. In this model, a non ideal equation of state, such as the van der Waals equation of state (vdW EOS), is employed in the regions occupied by the bulk phases whereas an artificial equation of state is used in the interfacial region. The advantage of using an artificial equation of state in the interfacial regions is that the thickness of the interface can now be controlled in the two-phase simulations. Numerical experiments show that the numerical stability is also enhanced if one chooses a thicker interface which allows simulation of large density and viscosity ratios. Moreover, it is proposed to choose a suitable scaling factor for the vdW EOS. After scaling down the vdW EOS, one can simulate larger density/viscosity ratios without even making the interface thicker.

In addition, a model for the fluid-solid interactions is proposed. The model is based on the Cahn's theory of wetting and can simulate different equilibrium contact angles— ranging from 0° to 180° —on the wall surfaces.

In the following sections, the development of the proposed LB model is presented and in the chapters that follow, thermodynamic consistency and suitability of the AILB model for the general two-phase flow applications are examined.

To test and numerically analyze the proposed model, a code in Fortran-90 is developed. The code is parallelized to run on a cluster of processors. More details about the code, parallelization technique and performance are given in Appendix B.

4.1 Discrete Boltzmann (DB) equation

The discrete Boltzmann (DB) equation in the presence of forcing \mathbf{F} can be written in the following form:

$$\frac{Df_a}{Dt} = \frac{\partial f_a}{\partial t} + \mathbf{v}_a \cdot \frac{\partial f_a}{\partial \mathbf{r}} = -\frac{f_a - f_a^{eq}}{\tau} + \frac{(\mathbf{v}_a - \mathbf{u}) \cdot \mathbf{F}}{\rho R T} f_a^{eq} \quad (4.1)$$

where $f_a(\mathbf{r}, t)$ is a single-particle distribution function discretized in the microscopic velocity space, \mathbf{v}_a is the microscopic velocity of the fluid particles, $\rho(\mathbf{r}, t)$ is the fluid density, $\mathbf{u}(\mathbf{r}, t)$ is the fluid velocity, τ is a relaxation time related to the kinematic fluid viscosity, R is the ideal gas constant, T is the temperature, \mathbf{F} is the force experienced by the fluid particles, \mathbf{r} is the position vector of the fluid particles and t is time.

In the DB equation, f_a^{eq} is a single-particle equilibrium distribution function which is derived from a Maxwell-Boltzmann distribution and can be approximated to (Chen & Doolen, 1998):

$$f_a^{eq} = w_a \left[1 + \frac{\mathbf{v}_a \cdot \mathbf{u}}{RT} + \frac{1}{2} \left(\frac{\mathbf{v}_a \cdot \mathbf{u}}{RT} \right)^2 - \frac{u^2}{2RT} \right] \quad (4.2)$$

where $w_a (\equiv t_a \rho)$ are lattice constants which depend upon the chosen lattice type. For a D_2Q_9 lattice, shown in Fig. 4.1(a), we have:

$$t_a = \begin{cases} 4/9 & a = 0 \\ 1/9 & a = 1, 2, 3, 4 \\ 1/36 & a = 5, 6, 7, 8 \end{cases} \quad (4.3)$$

For a D_3Q_{19} lattice, shown in Fig. 4.1(b), we have:

$$t_a = \begin{cases} 1/3 & a = 0 \\ 1/18 & a = 1 \text{ to } 6 \\ 1/36 & a = 7 \text{ to } 18 \end{cases} \quad (4.4)$$

Lattice velocities in different directions are listed in Table 4.1 and 4.2 for the D_2Q_9 and D_3Q_{19} lattices, respectively.

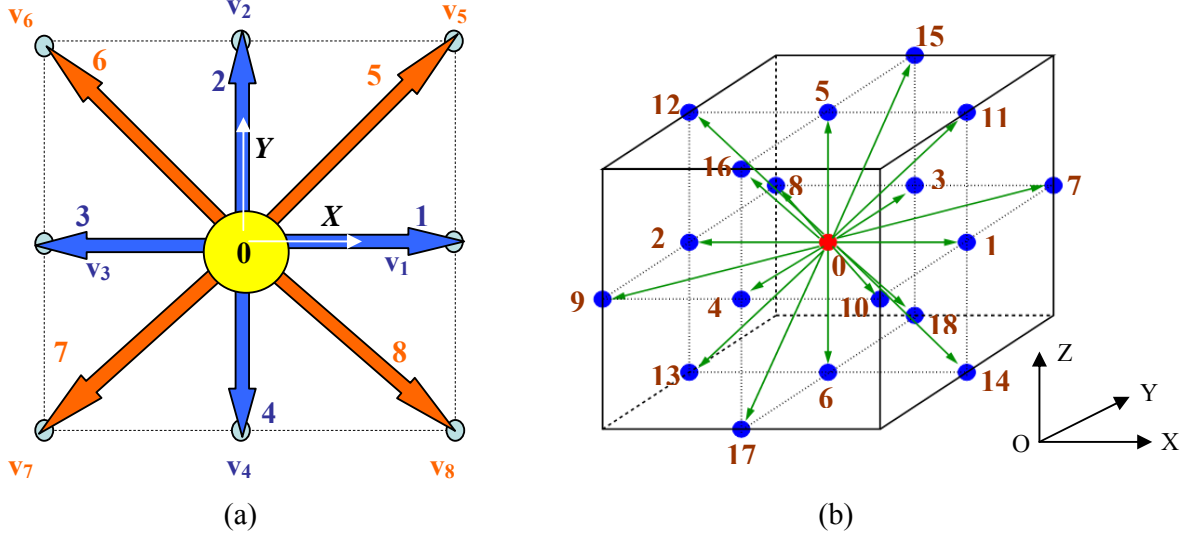


Fig. 4.1: Lattice velocity directions in (a) D_2Q_9 and (b) D_3Q_{19} lattice structures. Velocity directions are numbered accordingly in the panels.

Table 4.1: Lattice velocities in different directions for the D2Q9 lattice structure.

a	v_{ax}	v_{ay}	a	v_{ax}	v_{ay}
1	1	0	5	1	1
2	0	1	6	-1	1
3	-1	0	7	-1	-1
4	0	-1	8	1	-1

A relationship between the distribution function $f_a(\mathbf{r}, t)$ and the macroscopic hydrodynamics is established through the *BGK collision* term satisfying the conservation of collision invariants at any \mathbf{r} , and t . Fluid density $\rho(\mathbf{r}, t)$ and velocity $\mathbf{u}(\mathbf{r}, t)$ are thus evaluated as:

$$\rho(\mathbf{r}, t) = \sum_a f_a(\mathbf{r}, t) = \sum_a f_a^{eq}(\mathbf{r}, t) \quad (4.5)$$

$$\mathbf{u}(\mathbf{r}, t) = \frac{1}{\rho(\mathbf{r}, t)} \sum_a \mathbf{v}_a f_a(\mathbf{r}, t) = \frac{1}{\rho(\mathbf{r}, t)} \sum_a \mathbf{v}_a f_a^{eq}(\mathbf{r}, t) \quad (4.6)$$

Table 4.2: Lattice velocities in different directions for the D3Q19 lattice structure.

a	v_{ax}	v_{ay}	v_{az}	a	v_{ax}	v_{ay}	v_{az}
1	1	0	0	10	1	-1	0
2	-1	0	0	11	1	0	1
3	0	1	0	12	1	0	-1
4	0	-1	0	13	-1	0	-1
5	0	0	1	14	-1	0	1
6	0	0	-1	15	0	1	1
7	1	1	0	16	0	1	-1
8	-1	1	0	17	0	-1	-1
9	-1	-1	0	18	0	-1	1

4.2 Lattice Boltzmann (LB) equation

The DB equation is solved by employing a Lagrangian based discretization which essentially integrates it along the characteristics of the underlying lattice i.e.

$(\mathbf{r}, t) \rightarrow (\mathbf{r} + \mathbf{v}_a \Delta t, t + \Delta t)$. In such an integration, steps in space and time are coupled with the microscopic velocity along the characteristics such that, $\Delta \mathbf{r} = \mathbf{v}_a \Delta t$. The resulting discretized equation is called the lattice Boltzmann (LB) equation, which is:

$$f_a(\mathbf{r} + \mathbf{v}_a \Delta t, t + \Delta t) - f_a(\mathbf{r}, t) = - \int_{\mathbf{r}, t}^{\mathbf{r} + \mathbf{v}_a \Delta t, t + \Delta t} \frac{dt}{\tau} \left[f_a - f_a^{eq} \right] + \int_{\mathbf{r}, t}^{\mathbf{r} + \mathbf{v}_a \Delta t, t + \Delta t} dt \cdot \frac{(\mathbf{v}_a - \mathbf{u}) \cdot \mathbf{F}}{\rho R T} f_a^{eq} \quad (4.7)$$

After applying a trapezoidal rule of integration to evaluate the above two integrals with second-order accuracy, we get:

$$\begin{aligned} f_a(\mathbf{r} + \mathbf{v}_a \Delta t, t + \Delta t) - f_a(\mathbf{r}, t) &= -\frac{\Delta t}{2\tau} \left[f_a - f_a^{eq} \right]_{(\mathbf{r}, t)} - \frac{\Delta t}{2\tau} \left[f_a - f_a^{eq} \right]_{(\mathbf{r} + \mathbf{v}_a \Delta t, t + \Delta t)} \\ &+ \frac{\Delta t}{2} \frac{(\mathbf{v}_a - \mathbf{u}) \cdot \mathbf{F}}{\rho R T} f_a^{eq} \Big|_{(\mathbf{r}, t)} + \frac{\Delta t}{2} \frac{(\mathbf{v}_a - \mathbf{u}) \cdot \mathbf{F}}{\rho R T} f_a^{eq} \Big|_{(\mathbf{r} + \mathbf{v}_a \Delta t, t + \Delta t)} \end{aligned} \quad (4.8)$$

Note that, in the LB framework, direct numerical implementation of the above equation (as opposed to the physically more meaningful, collide-stream formulation) is difficult due to the implicit nature of the *BGK collision* and the *forcing* terms. Moreover, the direct implementation also hinders the simple physical interpretation of particles colliding and streaming which in fact is a key feature of the LB algorithm. Therefore, a modified distribution function $g_a(\mathbf{r}, t)$ is sought—in terms of the known distribution function $f_a(\mathbf{r}, t)$ and other quantities at time t —that transforms the LB equation (4.8) in a form solvable by the *collide-stream* algorithm.

4.3 Modified distribution function $g_a(\mathbf{r}, t)$

By defining the modified distribution function $g_a(\mathbf{r}, t)$ as:

$$g_a(\mathbf{r}, t) = f_a(\mathbf{r}, t) + \frac{\Delta t}{2\tau} \left[f_a - f_a^{eq} \right] \Big|_{(\mathbf{r}, t)} - \frac{\Delta t}{2} \frac{(\mathbf{v}_a - \mathbf{u}) \cdot \mathbf{F}}{\rho RT} f_a^{eq} \Big|_{(\mathbf{r}, t)} \quad (4.9)$$

the LB equation (4.8) can be transformed to the following form:

$$g_a(\mathbf{r} + \mathbf{v}_a \Delta t, t + \Delta t) = g_a(\mathbf{r}, t) - \frac{\Delta t}{\tau + 0.5\Delta t} \left[g_a - f_a^{eq} \right] \Big|_{(\mathbf{r}, t)} + \frac{0.5\tau}{\tau + 0.5\Delta t} \frac{\Delta t (\mathbf{v}_a - \mathbf{u}) \cdot \mathbf{F}}{\rho RT} f_a^{eq} \Big|_{(\mathbf{r}, t)} \quad (4.10)$$

Notice that the above transformed LB equation can be split into a set of two equations, as shown below, which clearly brings out the *collide-stream* interpretation of the LB algorithm.

- Collision

$$g_a^*(\mathbf{r}, t) = g_a(\mathbf{r}, t) - \frac{\Delta t}{\tau + 0.5\Delta t} \left[g_a - f_a^{eq} \right] \Big|_{(\mathbf{r}, t)} + \frac{0.5\tau}{\tau + 0.5\Delta t} \frac{\Delta t (\mathbf{v}_a - \mathbf{u}) \cdot \mathbf{F}}{\rho RT} f_a^{eq} \Big|_{(\mathbf{r}, t)} \quad (4.11)$$

- Streaming

$$g_a(\mathbf{r} + \mathbf{v}_a \Delta t, t + \Delta t) = g_a^*(\mathbf{r}, t) \quad (4.12)$$

Notice that the streaming equation (4.12) is responsible for the time advancement.

From the transformation equation(4.9), we can write the modified equilibrium distribution function $g_a^{eq}(\mathbf{r}, t)$ as:

$$g_a^{eq}(\mathbf{r}, t) = f_a^{eq}(\mathbf{r}, t) - \frac{\Delta t}{2} \frac{(\mathbf{v}_a - \mathbf{u}) \cdot \mathbf{F}}{\rho R T} f_a^{eq} \Big|_{(\mathbf{r}, t)} \quad (4.13)$$

The modified distribution function $g_a(\mathbf{r}, t)$ can be used to determine the macroscopic hydrodynamics using the following relations:

$$\rho(\mathbf{r}, t) = \sum_a f_a = \sum_a g_a \quad (4.14)$$

$$\mathbf{u}(\mathbf{r}, t) = \frac{1}{\rho} \left(\sum_a \mathbf{v}_a f_a \right) = \frac{1}{\rho} \left[\left(\sum_a \mathbf{v}_a g_a \right) + \frac{\Delta t}{2} \mathbf{F} \right] \quad (4.15)$$

4.4 Forcing terms to simulate phase segregation

The LB equation, with a constant forcing term (can be zero) possesses an inherent ideal gas equation of state and is not suitable for simulating the segregated phase dynamics encountered in scenarios involving two coexisting phases. In order to model the non-ideal behavior of phase segregation, inter-particle interactions have to be introduced into the forcing term of LB equation by accounting for the long range attractions \mathbf{F}_{attr} and short range repulsions \mathbf{F}_{rep} in addition to the constant body force \mathbf{F}_G . Adding those, we can define the net force \mathbf{F} as:

$$\mathbf{F} = \mathbf{F}_{attr} + \mathbf{F}_{rep} + \mathbf{F}_G \quad (4.16)$$

4.4.1 Long range attractive force \mathbf{F}_{attr}

Using a mean-field approximation for intermolecular attractions, the effective long range inter-particle forces are modeled by employing a mean field potential V_m as:

$$\mathbf{F}_{attr} = \rho \nabla V_m = \rho \nabla (2\tilde{a}\rho + \kappa \nabla^2 \rho) \quad (4.17)$$

where \tilde{a} and κ are constants related to the intermolecular attractive potential and κ is called the capillary coefficient of the fluid.

4.4.2 Short range repulsive force \mathbf{F}_{rep}

Using the Enskog theory of dense gases which accounts for the exclusion volume effect (due to the finite size of particles), the short range repulsive forces are modeled as:

$$\mathbf{F}_{rep} = -\tilde{b}\rho^2 RT \chi \nabla \ln(\rho^2 \chi) \quad (4.18)$$

where χ is a density-dependent collision probability and \tilde{b} is a constant related to the Virial equation of state.

4.4.3 Net force \mathbf{F}

Adding the long range attractive forces \mathbf{F}_{attr} , the short range repulsive forces \mathbf{F}_{rep} and the constant body force \mathbf{F}_G (which usually is the standard gravitational force ρg), we can associate the net force \mathbf{F} to the thermodynamic pressure P_0 as:

$$\mathbf{F} = -\nabla(P_0 - \rho RT) + \kappa \rho \nabla \nabla^2 \rho + \mathbf{F}_G \quad (4.19)$$

where P_0 follows a non-ideal equation of state:

$$P_0 = \rho RT \left(1 + \tilde{b} \rho \chi\right) - \tilde{a} \rho^2 \quad (4.20)$$

Notice that all the microscopic constants except κ in equations (4.19) and (4.20) are now lumped together and contribute to the non-ideal thermodynamic pressure P_0 .

4.4.4 Gibbs-Duhem (G-D) equation

For two coexisting phases of a fluid to remain in equilibrium, both the mechanical as well as the chemical equilibrium must be established. This constraint can be satisfied by enforcing the Gibbs-Duhem equation for equilibrium, which states:

$$\nabla P_0 = \rho \nabla \mu_0 \quad (4.21)$$

where μ_0 is the bulk chemical potential which is defined as the first derivative of bulk free energy density E_0 with respect to the fluid density. Combining equations (4.19) and (4.21), we get:

$$\mathbf{F} = \nabla(\rho RT) - \rho \nabla \mu + \mathbf{F}_G \quad (4.22)$$

where $\mu = \mu_0 - \kappa \nabla^2 \rho$.

4.5 Chemical potential μ_0 in the Lee-Fischer LB model

In the Lee-Fischer LB model (Lee & Fischer, 2006), the bulk free energy density E_0 of a fluid is modeled to take the following double-well form (Iwamatsu, 1993):

$$E_0 = \beta (\rho - \rho_l^{sat})^2 (\rho - \rho_v^{sat})^2 \quad (4.23)$$

where β is a constant related to the surface tension of the fluid, and ρ_l^{sat} and ρ_v^{sat} are densities of the saturated liquid and vapor phases, respectively. E_0 is plotted against density in Fig. 4.2(a). Since the above equation of state (EOS) is usually valid in the near-critical state of a fluid, i.e. at low phase-density ratios, we will refer to it as an artificial EOS.

From equation (4.23), relationship between the bulk chemical potential, $\mu_0 = \partial E_0 / \partial \rho$, and the fluid density ρ can be derived as:

$$\mu_0 = 4\beta (\rho - \rho_l^{sat}) (\rho - \rho_v^{sat}) (\rho - \rho_m^{sat}) \quad (4.24)$$

where $\rho_m^{sat} = 0.5(\rho_l^{sat} + \rho_v^{sat})$ is the mean saturation density. μ_0 is plotted against density in Fig. 4.2(b).

Using the bulk free energy density E_0 and the bulk chemical potential μ_0 , we can evaluate the thermodynamic pressure P_0 from the following thermodynamic identity

$$P_0 = \rho \mu_0 - E_0 \quad (4.25)$$

to yield:

$$P_0 = \beta (\rho - \rho_l^{sat}) (\rho - \rho_v^{sat}) [4\rho (\rho - \rho_m^{sat}) - (\rho - \rho_l^{sat}) (\rho - \rho_v^{sat})] \quad (4.26)$$

The above equation is the equation of state for the fluid being simulated in the Lee-Fischer LB model. P_0 is plotted against density in Fig. 4.3.

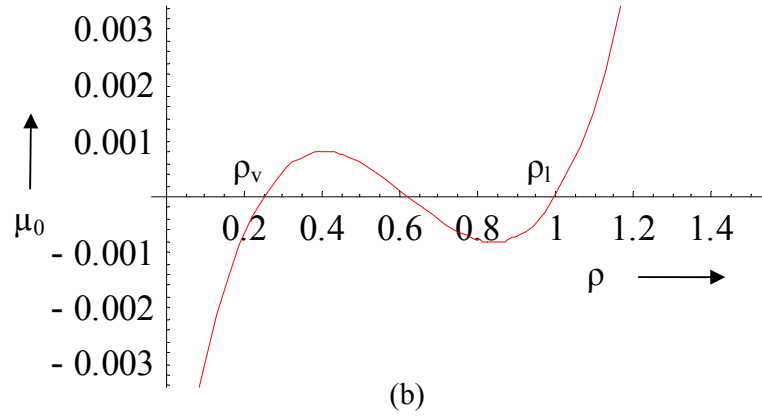
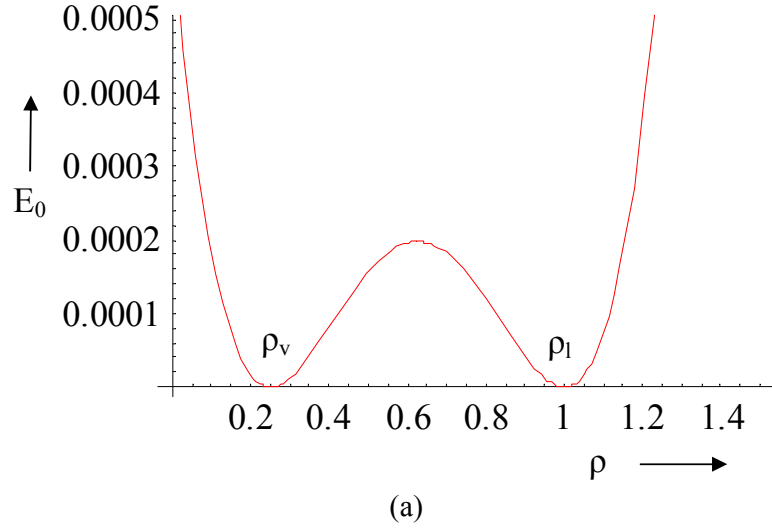


Fig. 4.2: Dependence of bulk free energy E_0 (a), and bulk chemical potential μ_0 (b), on fluid density ρ . The free energy is assumed to be in a double well form which has minimas at the bulk liquid density ρ_l^{sat} and the bulk vapor ρ_v^{sat} density. Following parameters are chosen in equation (4.23) for the above plots: $\beta = 0.01$, $\rho_l^{sat} = 1.0$ and $\rho_v^{sat} = 0.25$.

Speed of sound for the double-well EOS ($c_{s,dblW}$) can be obtained from the following equation:

$$c_{s,dblW}^2 = \frac{\partial P_0}{\partial \rho} \Big|_T = \rho \frac{\partial^2 E_0}{\partial \rho^2} \Big|_T = 4\beta\rho \left[\begin{aligned} & (\rho - \rho_l^{sat})(\rho - \rho_v^{sat}) \\ & + (\rho - \rho_l^{sat})(\rho - \rho_m^{sat}) \\ & + (\rho - \rho_v^{sat})(\rho - \rho_m^{sat}) \end{aligned} \right] \quad (4.27)$$

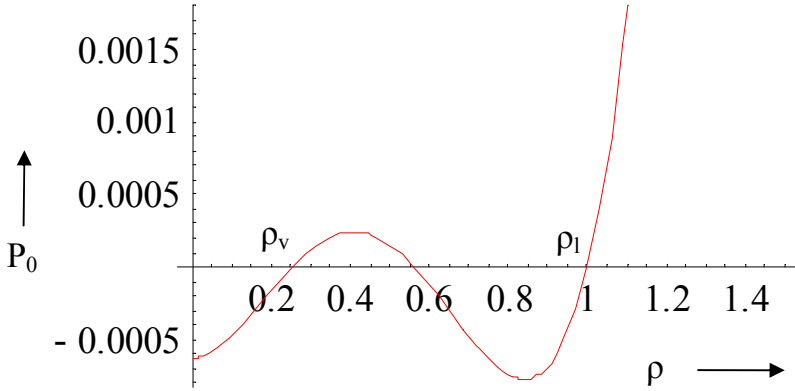


Fig. 4.3: Dependence of the bulk pressure P_0 on fluid density ρ . Theoretical Maxwell construction for the above pressure dependence on the density yields an equilibrium pressure equal to 0, and the equilibrium densities for the liquid and vapor phases equal to ρ_l^{sat} and ρ_v^{sat} , respectively. Parameters for the above plot are same as of Fig. 4.2.

Given the surface tension σ of the fluid and the densities of saturated liquid and vapor phases (ρ_l^{sat} and ρ_v^{sat}), we can evaluate the constants β and κ for an ideal one-dimensional planar interface from the following relations (derived later in the sections 4.9.3 and 4.9.4):

$$\kappa = \frac{3D\sigma}{2(\rho_l^{sat} - \rho_v^{sat})^2} \quad (4.28)$$

$$\beta = \frac{12\sigma}{D(\rho_l^{sat} - \rho_v^{sat})^4} \quad (4.29)$$

where D is the interface thickness (a numerical parameter). In the Lee-Fischer LB model, the above artificial equation of state description is used in the whole computational domain. Both the bulk as well as the interfacial regions are governed by the same density dependent free energy (double-well form) given in equation (4.23). Because of the bulk regions following an *artificial* EOS, Lee-Fischer model yields unphysical dynamics in the presence of body forces (such as gravity). Since the LB method is inherently a quasi-compressible method, the presence of body forces in the domain yields a very small density gradient in the direction of the body force. With increasing time, this small density gradient is further enhanced in the Lee-Fischer model due to the increased effective body force. The density gradient in the direction of the body force effectively provides an artificial force, which is continuously

being added to the body force as time progresses, making the system more and more compressible. Because they are governed by the artificial EOS, bulk densities are unable to correct this temporally increasing compressibility error, and the simulation ultimately becomes numerically unstable because of the unusually large density ratios produced in the simulations.

Nonetheless the Lee-Fischer LB model is proved to be thermodynamically superior (Kikkinides, 2008) and able to effectively capture two-phase dynamics in the absence of gravity. The model also works well for very low magnitudes of gravity and for body forces applied over small regions, such as the buoyancy force in a small bubble. In Chapter 6, results from both the Lee-Fisher LB model and the AILB model (proposed in the following section) are presented for several two-phase scenarios.

4.6 Chemical potential μ_0 in the AILB model

4.6.1 Bulk equation of state

For the bulk liquid ($\rho(x, y) \geq \rho_{liq}^{sat}$) and bulk vapor ($\rho(x, y) \leq \rho_{vap}^{sat}$) regions, we can choose a non-ideal equation of state, such as the van der Waals equation of state (vdW EOS), which is (McQuarrie & Simon, 1999):

$$P_0^{bulk} = \frac{\rho RT_0}{1-b\rho} - a\rho^2 \quad (4.30)$$

Bulk free energy density E_0^{bulk} for the above non-ideal pressure P_0^{bulk} is given by:

$$E_0^{bulk} = \rho \int \frac{P_0^{bulk}}{\rho^2} d\rho = \rho RT_0 \ln\left(\frac{\rho}{1-b\rho}\right) - a\rho^2 \quad (4.31)$$

Bulk chemical potential μ_0^{bulk} for the vdW EOS can be obtained from:

$$\mu_0^{bulk} = \frac{\partial E_0^{bulk}}{\partial \rho} = RT_0 \ln\left(\frac{\rho}{1-b\rho}\right) + \frac{RT_0}{1-b\rho} - 2a\rho \quad (4.32)$$

Notice that the above bulk free energy density E_0^{bulk} and the bulk chemical potential μ_0^{bulk} are related via the following identity:

$$P_0^{bulk} = \rho \mu_0^{bulk} - E_0^{bulk} \quad (4.33)$$

Speed of sound for the vdW EOS ($c_{s,vdW}$) can be obtained from the following equation:

$$c_{s,vdW}^2 = \frac{\partial P_0^{bulk}}{\partial \rho} \bigg|_T = \rho \frac{\partial^2 E_0^{bulk}}{\partial \rho^2} \bigg|_T = \frac{RT_0}{(1-b\rho)^2} - 2a\rho \quad (4.34)$$

Instead of using vdW EOS, more realistic equation of states such as the R-K or P-R equation of states (Yuan and Schaefer, 2006) may also be used in the AILB model. Note that, in this report, results are presented only for the vdW EOS in the context of AILB model. More sophisticated equation of states may be employed in future studies.

4.6.2 Interfacial equation of state

The interfacial free energy density E_0^{int} of a fluid can be modeled to take the following double well form:

$$E_0^{int} = \beta (\rho - \rho_l^{sat})^2 (\rho - \rho_v^{sat})^2 \quad (4.35)$$

where β is a constant related to the surface tension of the fluid, and ρ_l^{sat} and ρ_v^{sat} are densities of the saturated liquid and vapor phases, respectively.

A relation between the interfacial chemical potential and the fluid density ρ can be derived as:

$$\mu_0^{int} = \frac{\partial E_0^{int}}{\partial \rho} = 4\beta (\rho - \rho_l^{sat})(\rho - \rho_v^{sat})(\rho - \rho_m^{sat}) \quad (4.36)$$

where $\rho_m^{sat} = 0.5(\rho_l^{sat} + \rho_v^{sat})$ is the mean saturation density.

In order to ensure the continuity of the chemical potential at the interface boundaries, i.e. at $\rho = \rho_{liq}^{sat}$ and $\rho = \rho_{vap}^{sat}$, the interfacial chemical potential μ_0^{int} is shifted by the value of the bulk chemical potential at the interface boundary, i.e. $\mu_0^{bulk} \big|_{\rho=\rho_l^{sat}}$ to give:

$$\mu_0^{int} = \mu_0^{bulk} \bigg|_{\rho=\rho_l^{sat}} + 4\beta (\rho - \rho_l^{sat})(\rho - \rho_v^{sat})(\rho - \rho_m^{sat}) \quad (4.37)$$

Both the bulk vdW and the interfacial equation of states are graphically compared in Fig. 4.4 for the parameter values listed there. Note that the interfacial continuity of the chemical potentials is necessary in order to avoid any unwanted numerical oscillations and instabilities.

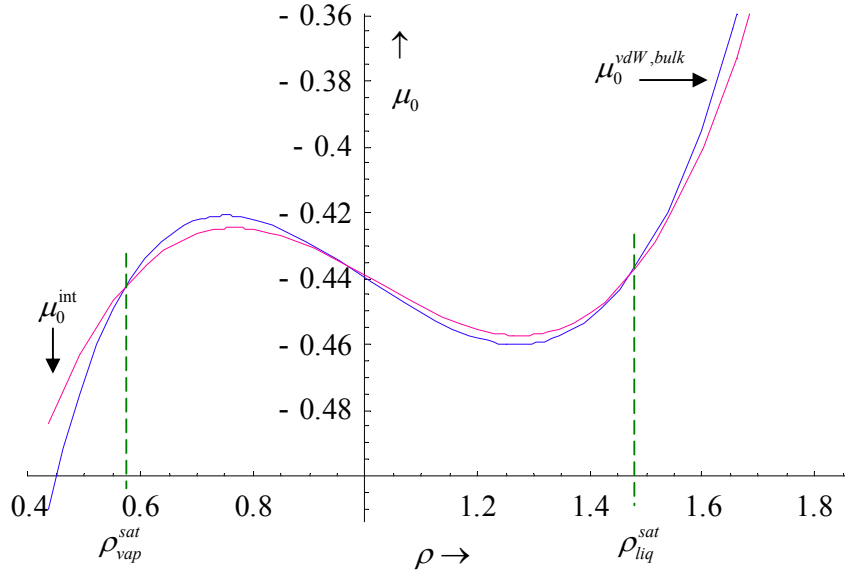
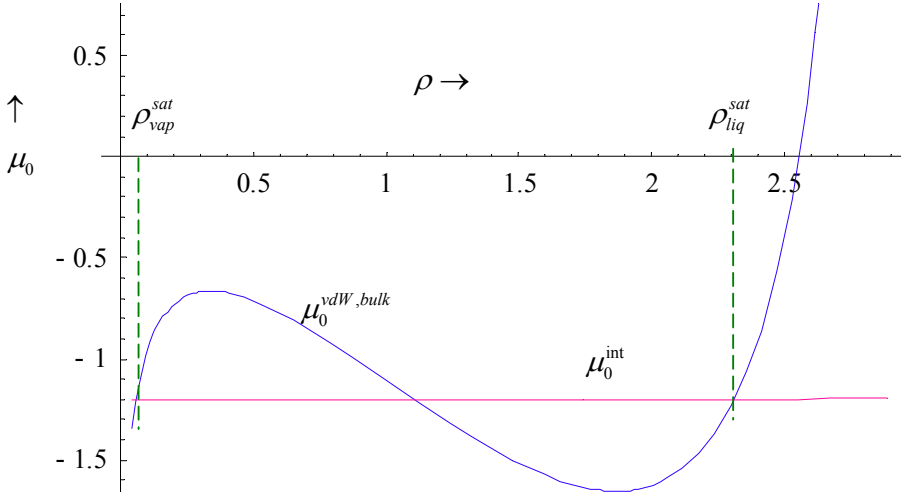


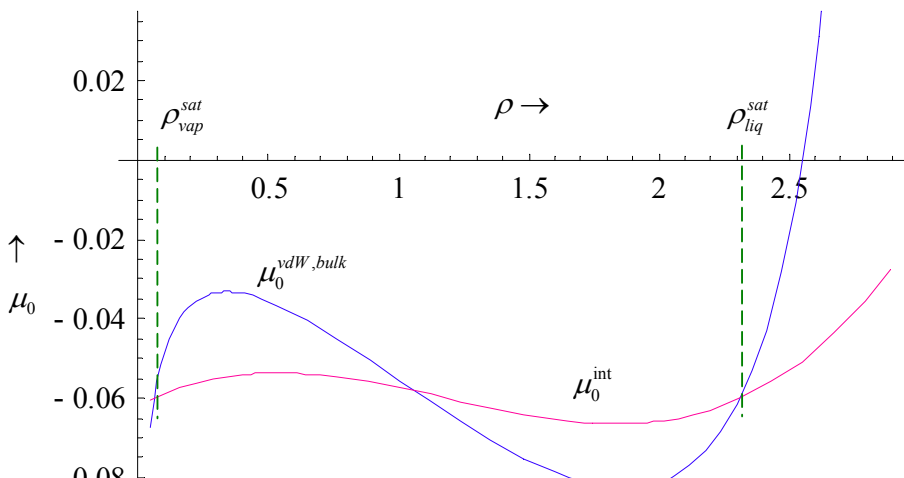
Fig. 4.4: Dependence of the chemical potential μ_0 on fluid density ρ . Parameters are: $T_R = 0.95$, $a = 9/8$, $b = 1/3$, $\rho_l^{sat} = 1.46173$, $\rho_v^{sat} = 0.579015$, $\sigma = 0.025$, $D = 4$, $\mu_0^{bulk} \Big|_{\rho=\rho_l^{sat}} = -0.440966$.

4.6.3 Proposed scaling for the van der Waals EOS in the AILB model

AILB model, as discussed in the previous section, can simulate two-phase dynamics with large density ratios only when one chooses interface thickness to be large. A thick interface spreads the interfacial gradients over a large number of lattice points and consequently, stabilizes the numerical simulation. For a thin interface, the AILB model does not converge for large density ratios. Having a thick interface impacts the computing time since one now needs to have a large number of lattice points in the domain to yield similar accuracy.



(a)



(b)

Fig. 4.5: Dependence of the chemical potential μ_0 on the fluid density ρ . Parameters are: $T_R = 0.6$, $a = 9/8$, $b = 1/3$, $\rho_l^{sat} = 2.31156$, $\rho_v^{sat} = 0.0597781$, $\sigma = 0.025$, $D = 4$, $\mu_0^{bulk} \Big|_{\rho=\rho_l^{sat}} = -1.2005$; (a) no scaling, (b) scaling factor $S_f = 0.05$

In order to avoid choosing a thick interface while retaining the numerical stability, we propose to scale down the vdW EOS, as shown in Fig. 4.5(b). Both the equations of state are graphically compared with no scaling in Fig. 4.5(a) and with scaling in Fig. 4.5(b). At a reduced temperature $T_R = 0.6$ and a density ratio of ~ 40 , a scaling factor of 0.05 was found

appropriate for stable simulations with thin interface thicknesses. Simulations are found to be stable for a range of scaling factors for the same system conditions. In this study we have treated the scaling factor to be a “free” stabilization parameter, introduced simply to help stabilize numerical simulations.

Below we present the governing equations for the scaled AILB model:

Bulk regions (saturated liquid or vapor)

$$\mu_{0,scaled}^{bulk} = \left[RT_0 \ln\left(\frac{\rho}{1-b\rho}\right) + \frac{RT_0}{1-b\rho} - 2a\rho \right] S_f \quad (4.38)$$

Interfacial regions

$$\mu_{0,scaled}^{int} = \mu_{0,scaled}^{bulk} \Big|_{\rho=\rho_l^{sat}} + 4\beta(\rho - \rho_l^{sat})(\rho - \rho_v^{sat})(\rho - \rho_m^{sat}) \quad (4.39)$$

where S_f is a “free” stability parameter chosen to stabilize the numerical simulations.

4.7 Numerical discretization schemes

Similar to use of an isotropic and compact discretization for evaluation of the gradients in the forcing term of the Lee-Fischer model, the AILB model can also be made numerically stable and applicable for large density ratios between the two phases. Numerical tests show that a proper use of second order *biased* and *central* difference scheme in evaluating gradients allows one to achieve a stable simulation while maintaining second-order accuracy of the solution (Lee & Fischer, 2006).

We can rewrite equation (4.8) to reflect the different discretization schemes of the forcing term as follows:

$$\begin{aligned} f_a(\mathbf{r} + \mathbf{v}_a \Delta t, t + \Delta t) - f_a(\mathbf{r}, t) &= -\frac{\Delta t}{2\tau} \left[f_a - f_a^{eq} \right] \Big|_{(\mathbf{r}, t)} - \frac{\Delta t}{2\tau} \left[f_a - f_a^{eq} \right] \Big|_{(\mathbf{r} + \mathbf{v}_a \Delta t, t + \Delta t)} \\ &+ \frac{\Delta t}{2} \frac{(\mathbf{v}_a - \mathbf{u}) \cdot \mathbf{F}^B}{\rho RT} f_a^{eq} \Big|_{(\mathbf{r}, t)} + \frac{\Delta t}{2} \frac{(\mathbf{v}_a - \mathbf{u}) \cdot \mathbf{F}^C}{\rho RT} f_a^{eq} \Big|_{(\mathbf{r} + \mathbf{v}_a \Delta t, t + \Delta t)} \end{aligned} \quad (4.40)$$

where

$$\mathbf{F}^B = RT \nabla^B \rho - \rho \nabla^B \mu + \mathbf{F}_G \quad (4.41)$$

$$\mathbf{F}^C = RT\nabla^C \rho - \rho \nabla^C \mu + \mathbf{F}_G \quad (4.42)$$

and superscripts B and C indicate the biased and central difference scheme of gradient evaluation, respectively.

The modified distribution function $g_a(\mathbf{r}, t)$ in equation (4.9) can now be defined as:

$$g_a(\mathbf{r}, t) = f_a(\mathbf{r}, t) + \frac{\Delta t}{2\tau} \left[f_a - f_a^{eq} \right] \Big|_{(\mathbf{r}, t)} - \frac{\Delta t}{2} \frac{(\mathbf{v}_a - \mathbf{u}) \cdot \mathbf{F}^C}{\rho RT} f_a^{eq} \Big|_{(\mathbf{r}, t)} \quad (4.43)$$

After choosing the modified equilibrium distribution function $g_a^{eq}(\mathbf{r}, t)$ to be,

$$g_a^{eq}(\mathbf{r}, t) = f_a^{eq}(\mathbf{r}, t) - \frac{\Delta t}{2} \frac{(\mathbf{v}_a - \mathbf{u}) \cdot \mathbf{F}^C}{\rho RT} f_a^{eq} \Big|_{(\mathbf{r}, t)} \quad (4.44)$$

we can write equation (4.40) as:

$$g_a(\mathbf{r} + \mathbf{v}_a \Delta t, t + \Delta t) = f_a(\mathbf{r}, t) - \frac{\Delta t}{2\tau} \left[f_a - f_a^{eq} \right] \Big|_{(\mathbf{r}, t)} + \frac{\Delta t}{2} \frac{(\mathbf{v}_a - \mathbf{u}) \cdot \mathbf{F}^B}{\rho RT} f_a^{eq} \Big|_{(\mathbf{r}, t)} \quad (4.45)$$

The above equation can be written as,

$$\begin{aligned} g_a(\mathbf{r} + \mathbf{v}_a \Delta t, t + \Delta t) = & \left\{ f_a(\mathbf{r}, t) + \frac{\Delta t}{2\tau} \left[f_a - f_a^{eq} \right] \Big|_{(\mathbf{r}, t)} - \frac{\Delta t}{2} \frac{(\mathbf{v}_a - \mathbf{u}) \cdot \mathbf{F}^C}{\rho RT} f_a^{eq} \Big|_{(\mathbf{r}, t)} \right\} \\ & - \frac{\Delta t}{\tau} \left[f_a - f_a^{eq} \right] \Big|_{(\mathbf{r}, t)} + \frac{\Delta t}{2} \frac{(\mathbf{v}_a - \mathbf{u}) \cdot (\mathbf{F}^C + \mathbf{F}^B)}{\rho RT} f_a^{eq} \Big|_{(\mathbf{r}, t)} \end{aligned} \quad (4.46)$$

which essentially is:

$$g_a(\mathbf{r} + \mathbf{v}_a \Delta t, t + \Delta t) = g_a(\mathbf{r}, t) - \frac{\Delta t}{\tau} \left[f_a - f_a^{eq} \right] \Big|_{(\mathbf{r}, t)} + \Delta t \frac{(\mathbf{v}_a - \mathbf{u}) \cdot \mathbf{F}^M}{\rho RT} f_a^{eq} \Big|_{(\mathbf{r}, t)} \quad (4.47)$$

where $\mathbf{F}^M = 0.5(\mathbf{F}^B + \mathbf{F}^C)$.

From equations (4.43) and (4.44), we can also evaluate $(f_a - f_a^{eq})$ in terms of g_a and g_a^{eq} as:

$$f_a - f_a^{eq} = \frac{\tau}{\tau + 0.5\Delta t} (g_a - g_a^{eq}) \quad (4.48)$$

Now, we can write equation (4.47) in its final solvable form as:

$$g_a(\mathbf{r} + \mathbf{v}_a \Delta t, t + \Delta t) = g_a(\mathbf{r}, t) - \frac{\Delta t}{\tau + 0.5\Delta t} (g_a - g_a^{eq}) \Big|_{(\mathbf{r}, t)} + \Delta t \frac{(\mathbf{v}_a - \mathbf{u}) \cdot \mathbf{F}^M}{\rho RT} f_a^{eq} \Big|_{(\mathbf{r}, t)} \quad (4.49)$$

The macroscopic density and velocity are now calculated from:

$$\rho(\mathbf{r}, t) = \sum_a g_a \quad (4.50)$$

$$\mathbf{u}(\mathbf{r}, t) = \frac{1}{\rho} \left[\left(\sum_a \mathbf{v}_a g_a \right) + \frac{\Delta t}{2} \mathbf{F}^c \right] \quad (4.51)$$

4.8 Numerical implementation

In this section, numerical implementation of the LB model is presented for a two-dimensional D_2Q_9 square lattice. The domain ($0 \leq x \leq L_x$, $0 \leq y \leq L_y$) is divided into a square grid ($\Delta x = \Delta y = L_x / (N_x - 1)$) of $N_x \times N_y$ grid points. The terminal grid points lie on the domain boundaries at $x = 0$, L_x and at $y = 0$, L_y . For simplicity, $\Delta x = \Delta y = \Delta t = 1$ is chosen in the present work. The LB solution algorithm may be divided into the following steps:

4.8.1 Initialization (at time $t = 0$)

Both the macroscopic state—identified by the density ρ and the fluid velocity u_x, u_y —as well as the microscopic state—identified by the distribution function g_a —of the LB fluid need to be properly initialized before the time evolution can be studied.

In the LBM simulation of two-phase dynamics, initialization of the phase densities plays an important role in governing the stability of the numerical evolution. An improper initialization may lead to large numerical fluctuations across the interfaces, may induce large spurious velocities and ultimately, turn the numerical scheme unstable. Below we present expressions—which actually are the analytical results for the equilibrium density profile across a planar interface—for initializing densities of two phases in the calculation domain.

A planar interface in the x -direction can be initialized as (illustrated in Fig. 4.6):

$$\rho(x, y, t = 0) = \rho_m^{sat} + \frac{\rho_l^{sat} - \rho_v^{sat}}{2} \tanh\left(\frac{2}{D}(x - x_{int})\right) \quad (4.52)$$

where x_{int} is the position of the interface, D is the parameter controlling the numerical interface thickness and ρ_l^{sat} , ρ_v^{sat} and ρ_m^{sat} are saturated liquid, vapor and mean densities, respectively. Note that there is no density variation in the y -direction. Moreover, at $x = x_{\text{int}}$, the density is equal to the mean density of the saturated phases ρ_m^{sat} . The numerical interface is stretched from $x_{\text{int}} - 0.5D^{\text{eff}}$ to $x_{\text{int}} + 0.5D^{\text{eff}}$ with densities ρ_v^{sat} for $0 \leq x \leq (x_{\text{int}} - 0.5D^{\text{eff}})$ and ρ_l^{sat} for $(x_{\text{int}} + 0.5D^{\text{eff}}) \leq x \leq L_x$. Note that D^{eff} is the numerical thickness of the interface and is usually larger than the parameter D . Initialization for a planar interface in the y -direction and other variations including sandwiched phase layers in either x , y or both directions can be deduced from the above equation in a straightforward manner.

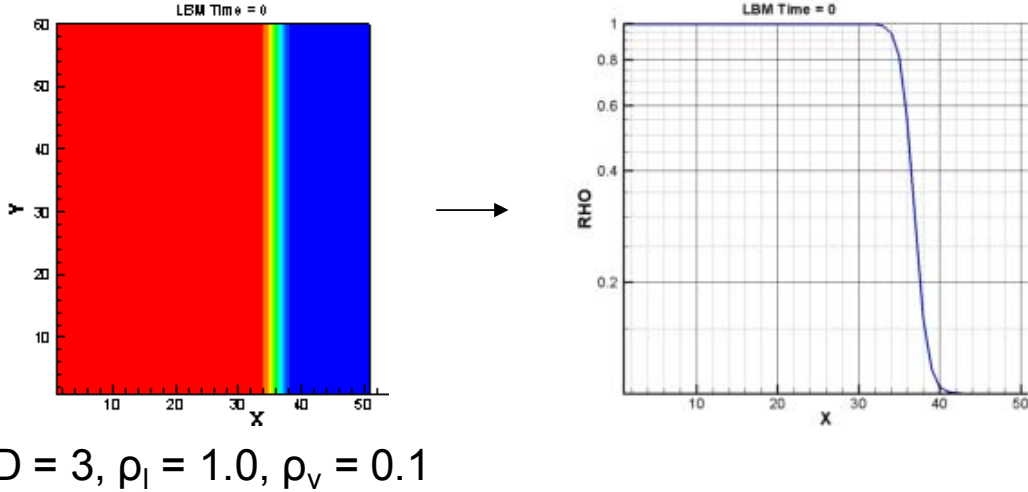


Fig. 4.6: Initialization of the densities for a two-phase (liquid-vapor) planar interface. Thickness of the density transition region is governed by a parameter D which is chosen to be 3 here. In the transition region, a continuous hyperbolic-tangent shaped variation is assumed for the fluid density which asymptotically approaches bulk liquid and vapor densities at the ends of the transition region. Red and blue color in the figure shows bulk liquid and vapor states, respectively.

Circular interface of a two dimensional vapor bubble in a liquid environment ($0 \leq x \leq L_x, 0 \leq y \leq L_y$) can be initialized as (illustrated in Fig. 4.7):

$$\rho(x, y, t=0) = \rho_m^{sat} + \frac{\rho_l^{sat} - \rho_v^{sat}}{2} \tanh\left(\frac{2}{D} \left(\sqrt{(x - x_c)^2 + (y - y_c)^2} - r \right) \right) \quad (4.53)$$

where (x_c, y_c) are coordinates of the center of the bubble and r is the radius. The annular interface is centered at (x_c, y_c) and is stretched from radius $r - 0.5D^{eff}$ to $r + 0.5D^{eff}$ with densities ρ_v^{sat} inside and ρ_l^{sat} outside the bubble. One can initialize a 2D circular droplet in a vapor environment by swapping ρ_l^{sat} and ρ_v^{sat} in the above equation.

Note that, depending upon ρ_l^{sat} and ρ_v^{sat} , the parameter D governing the (numerical) interface thickness D^{eff} has to be large enough to properly resolve the unstable region and to avoid steep gradients of density. A suitable value of D for stable numerical simulations has to be identified by conducting numerical experiments.

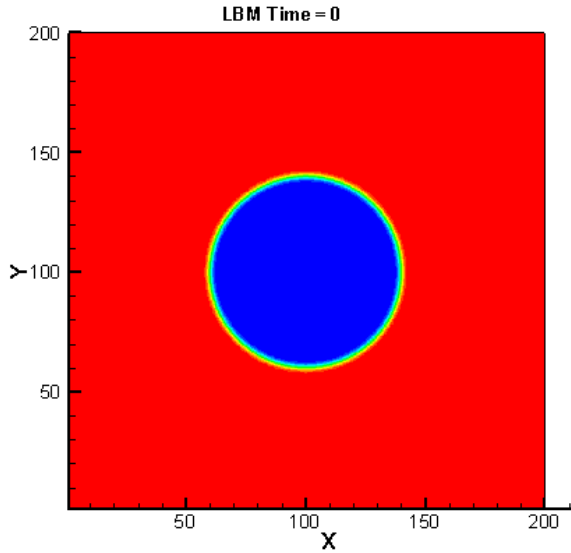


Fig. 4.7: Initialization of the densities for a two-phase (liquid-vapor) circular interface in two-dimensions. The density profile is governed by equation (4.53).

Note that the macroscopic densities $\rho(x, y, t=0)$, the macroscopic fluid velocities $u_x(x, y, t=0)$, $u_y(x, y, t=0)$ as well as the distribution function $g_a(x, y, t=0)$ should be initialized in a fashion consistent with the LB dynamics so as not to produce any large fluctuations which then leads to unstable numerical evolution. One should avoid trivial initializations of such variables. Of course, the choice of initialization may vary depending

upon the problem being simulated; however, it is always recommended to specify an initial condition which is closer to the equilibrium solution.

4.8.2 Time marching

A lattice Boltzmann solution algorithm involves implicit time marching which is performed in two steps—*collision* and *streaming* at each time step for $t \geq 0$.

Collision step:

At time t , the distribution function at each grid point $g_a(x, y, t)$ is modified using the following equation to represent *collision*:

$$g_a^*(x, y, t) = g_a(x, y, t) - \frac{1}{(\tau + 0.5\Delta t)} [g_a(x, y, t) - f_a^{eq}(x, y, t)] + \frac{0.5\tau}{(\tau + 0.5\Delta t)} \frac{\Theta_a(x, y, t)}{\rho(x, y, t)RT} f_a^{eq}(x, y, t) \quad (4.54)$$

where

$$\Theta_a(x, y, t) = RT \left(\mathbf{v}_a \Delta t \nabla^B \rho + \mathbf{v}_a \Delta t \nabla^C \rho \right) - \rho \left(\mathbf{v}_a \Delta t \nabla^B \mu + \mathbf{v}_a \Delta t \nabla^C \mu \right) + (v_{ax} F_{Gx} + v_{ay} F_{Gy} - u_x F_x^B - u_y F_y^B) \Delta t \quad (4.55)$$

$$F_x^C = RT \nabla_x^C \rho - \rho \nabla_x^C \mu + F_{Gx} \quad (4.56)$$

$$F_y^C = RT \nabla_y^C \rho - \rho \nabla_y^C \mu + F_{Gy} \quad (4.57)$$

$$F_x^B = RT \nabla_x^B \rho - \rho \nabla_x^B \mu + F_{Gx} \quad (4.58)$$

$$F_y^B = RT \nabla_y^B \rho - \rho \nabla_y^B \mu + F_{Gy} \quad (4.59)$$

and, F_{Gx} and F_{Gy} are components of the constant body force \mathbf{F}_G in the x and y directions, respectively.

Note that, $\mathbf{v}_a \Delta t \nabla^B$ and $\mathbf{v}_a \Delta t \nabla^C$ in equation (4.55) represent *lattice directional derivatives* evaluated using their indicated difference schemes, whereas, ∇_x^B , ∇_y^B , ∇_x^C and ∇_y^C in equations (4.56) to (4.59) represent *space derivatives* in x or y directions evaluated using their indicated difference schemes.

Lattice directional derivative of density $\rho(x, y, t)$ in the a^{th} direction is evaluated using the second-order central and biased finite-difference schemes as follows (Lee & Lin, 2005; Lee & Fischer, 2006):

$$\mathbf{v}_a \Delta t \nabla^C \rho \Big|_{(x, y, t)} = \frac{\rho(x + v_{ax} \Delta t, y + v_{ay} \Delta t, t) - \rho(x - v_{ax} \Delta t, y - v_{ay} \Delta t, t)}{2} \quad (4.60)$$

$$\mathbf{v}_a \Delta t \nabla^B \rho \Big|_{(x, y, t)} = \frac{-\rho(x + 2v_{ax} \Delta t, y + 2v_{ay} \Delta t, t) + 4\rho(x + v_{ax} \Delta t, y + v_{ay} \Delta t, t) - 3\rho(x, y, t)}{2} \quad (4.61)$$

Accounting for the symmetry requirements of a stable two phase LB simulation, the *space derivatives* of density $\rho(x, y, t)$ are calculated by taking velocity moments of the corresponding finite-difference discretizations along the characteristics with appropriate weights. Consequently, the derivatives in x and y directions are calculated using the following equations based on the central and biased finite difference schemes (Lee & Lin, 2005; Lee & Fischer, 2006):

$$\nabla_x^C \rho \Big|_{(x, y, t)} = \sum_{a=0}^8 \left[t_a v_{ax} \frac{\rho(x + v_{ax} \Delta t, y + v_{ay} \Delta t, t) - \rho(x - v_{ax} \Delta t, y - v_{ay} \Delta t, t)}{2RT \Delta t} \right] \quad (4.62)$$

$$\nabla_y^C \rho \Big|_{(x, y, t)} = \sum_{a=0}^8 \left[t_a v_{ay} \frac{\rho(x + v_{ax} \Delta t, y + v_{ay} \Delta t, t) - \rho(x - v_{ax} \Delta t, y - v_{ay} \Delta t, t)}{2RT \Delta t} \right] \quad (4.63)$$

$$\nabla_x^B \rho \Big|_{(x, y, t)} = \sum_{a=0}^8 \left[t_a v_{ax} \frac{-\rho(x + 2v_{ax} \Delta t, y + 2v_{ay} \Delta t, t) + 4\rho(x + v_{ax} \Delta t, y + v_{ay} \Delta t, t) - 3\rho(x, y, t)}{2RT \Delta t} \right] \quad (4.64)$$

$$\nabla_y^B \rho \Big|_{(x, y, t)} = \sum_{a=0}^8 \left[t_a v_{ay} \frac{-\rho(x + 2v_{ax} \Delta t, y + 2v_{ay} \Delta t, t) + 4\rho(x + v_{ax} \Delta t, y + v_{ay} \Delta t, t) - 3\rho(x, y, t)}{2RT \Delta t} \right] \quad (4.65)$$

where t_a are the direction dependent weighting coefficients for the equilibrium distribution function.

In 2D, for a D_2Q_9 lattice, the above derivatives can be written as follows:

$$\nabla_x^C \rho \Big|_{(x, y)} = \frac{1}{3} [\rho(x_+, y) - \rho(x_-, y)] + \frac{1}{12} [\rho(x_+, y_+) - \rho(x_-, y_-)] + \frac{1}{12} [\rho(x_+, y_-) - \rho(x_-, y_+)] \quad (4.66)$$

$$\nabla_y^C \rho \Big|_{(x,y)} = \frac{1}{3} [\rho(x, y_+) - \rho(x, y_-)] + \frac{1}{12} [\rho(x_+, y_+) - \rho(x_-, y_-)] + \frac{1}{12} [\rho(x_-, y_+) - \rho(x_+, y_-)]$$

$$\nabla_x^B \rho \Big|_{(x,y)} = A_{x1} - A_{x2} \quad (4.67)$$

$$A_{x1} = \frac{1}{6} [-\rho(x_{++}, y) + 4\rho(x_+, y) - 3\rho(x, y)] + \frac{1}{24} [-\rho(x_{++}, y_{++}) + 4\rho(x_+, y_+) - 3\rho(x, y)]$$

$$+ \frac{1}{24} [-\rho(x_{++}, y_{--}) + 4\rho(x_+, y_-) - 3\rho(x, y)]$$

$$(4.68)$$

$$A_{x2} = \frac{1}{6} [-\rho(x_{--}, y) + 4\rho(x_-, y) - 3\rho(x, y)] + \frac{1}{24} [-\rho(x_{--}, y_{--}) + 4\rho(x_-, y_-) - 3\rho(x, y)]$$

$$+ \frac{1}{24} [-\rho(x_{--}, y_{++}) + 4\rho(x_-, y_+) - 3\rho(x, y)]$$

$$(4.69)$$

$$\nabla_y^B \rho \Big|_{(x,y)} = A_{y1} - A_{y2} \quad (4.70)$$

$$A_{y1} = \frac{1}{6} [-\rho(x, y_{++}) + 4\rho(x, y_+) - 3\rho(x, y)] + \frac{1}{24} [-\rho(x_{++}, y_{++}) + 4\rho(x_+, y_+) - 3\rho(x, y)]$$

$$+ \frac{1}{24} [-\rho(x_{--}, y_{++}) + 4\rho(x_-, y_+) - 3\rho(x, y)]$$

$$(4.71)$$

$$A_{y2} = \frac{1}{6} [-\rho(x, y_{--}) + 4\rho(x, y_-) - 3\rho(x, y)] + \frac{1}{24} [-\rho(x_{--}, y_{--}) + 4\rho(x_-, y_-) - 3\rho(x, y)]$$

$$+ \frac{1}{24} [-\rho(x_{++}, y_{--}) + 4\rho(x_+, y_-) - 3\rho(x, y)]$$

$$(4.72)$$

where $x_+ \equiv x+1$, $x_- \equiv x-1$, $x_{++} \equiv x+2$ and $x_{--} \equiv x-2$ (same notation is also applicable for subscripts in y). Similarly, one can write the above derivatives for a 3D lattice (D_3Q_{19}) as well.

Note that the above equations are also valid for calculating the directional and space derivatives of μ after replacing the variable ρ with μ in the above equations. However, the scalar variable μ still needs to be calculated from the bulk chemical potential μ_0 , which requires the evaluation of second derivative of density $\rho(x, y, t)$. Following a second-order

central discretization along the characteristics and applying the appropriate weights, one can evaluate the second derivative as

$$\nabla_x^2 \rho \Big|_{(x,y,t)} = \nabla_y^2 \rho \Big|_{(x,y,t)} = \sum_{a=0}^8 \left[t_a \frac{\rho(x + v_{ax} \Delta t, y + v_{ay} \Delta t, t) - 2\rho(x, y, t) + \rho(x - v_{ax} \Delta t, y - v_{ay} \Delta t, t)}{2RT \Delta t^2} \right] \quad (4.73)$$

which gives:

$$\begin{aligned} \nabla^2 \rho \Big|_{(x,y,t)} &= \nabla_x^2 \rho \Big|_{(x,y,t)} + \nabla_y^2 \rho \Big|_{(x,y,t)} \\ &= \sum_{a=0}^8 \left[t_a \frac{\rho(x + v_{ax} \Delta t, y + v_{ay} \Delta t, t) - 2\rho(x, y, t) + \rho(x - v_{ax} \Delta t, y - v_{ay} \Delta t, t)}{RT \Delta t^2} \right] \end{aligned} \quad (4.74)$$

Notice that, the evaluation of a *biased difference* based derivative at any grid point needs information from a neighboring node located one and two grid points away in the direction of the characteristics; however, a *central difference* based derivative only requires information from its nearest neighbors in the direction of the characteristics. Therefore, for a simulation in a periodic box, *periodic boundary conditions* (for ρ and μ) should be handled in such a way that all the boundary nodes have access to the corresponding variables from as far as two grid points away.

Streaming step:

In the streaming step, the post-collision distribution function g_a^* is propagated to its neighboring node according to its directional index (similar to flowing g_a^* on the characteristics) and can be written as follows:

$$g_a(x + v_{ax} \Delta t, y + v_{ay} \Delta t, t + \Delta t) = g_a^*(x, y, t) \quad (4.75)$$

Periodic boundary conditions (for g_a^*) should be handled in such a way that each boundary node has access to g_a^* of its neighboring nodes in the direction of the characteristics. Post-streaming values of g_a at each grid point now corresponds to the time step $t + \Delta t$.

4.8.3 Calculation of macroscopic properties

At time $t + \Delta t$, the macroscopic density ρ and fluid velocities u_x, u_y at any grid point (x, y) can be calculated from:

$$\rho(x, y, t + \Delta t) = \sum_a g_a(x, y, t + \Delta t) \quad (4.76)$$

$$u_x(x, y, t + \Delta t) = \frac{1}{\rho(x, y, t + \Delta t)} \left[\left(\sum_a v_{ax} g_a(x, y, t + \Delta t) \right) + \frac{\Delta t}{2} F_x^C(x, y, t + \Delta t) \right] \quad (4.77)$$

$$u_y(x, y, t + \Delta t) = \frac{1}{\rho(x, y, t + \Delta t)} \left[\left(\sum_a v_{ay} g_a(x, y, t + \Delta t) \right) + \frac{\Delta t}{2} F_y^C(x, y, t + \Delta t) \right] \quad (4.78)$$

4.9 Simulation of equilibrium contact angles

In most engineering applications, liquid-vapor phase change (vaporization/condensation) occurs by transferring energy through the solid surfaces in/out of the system, for example, by heating or cooling the walls of a container. Therefore, the manner in which the two phases interact with the solid surface becomes important in estimating the overall heat transfer of the system.

4.9.1 Wettability and the contact angle θ_w

The behavior of a liquid in contact with a solid surface usually varies from one liquid to another and even from one surface to another. For example, liquid acetone on a flat aluminum surface spreads out to form a thin film, while liquid water on the same surface forms a bead shaped droplet. These different equilibrium shapes are due to the difference in affinities between the liquids and the solid surfaces. Usually, if a liquid has weak affinity with the solid surface, it collects itself into a bead form, whereas the liquid with strong affinity forms a film on the surface to maximize the liquid-solid contact area. The affinity of a liquid for a particular (solid) surface is called the *wettability* of that specific liquid-surface pair.

The wettability of a liquid is quantified by the *contact angle* (or wetting angle) θ_w , which is defined as the angle between the liquid-vapor interface and the solid surface, measured inside the liquid (illustrated in Fig. 4.8). The basal circle of the liquid drop is called the *contact line* where the three phases (solid, liquid and vapor) meet. As the contact angle θ_w decreases, the same quantity of liquid spreads more over the surface and yields more wetting. In the limit $\theta_w \rightarrow 0$, the liquid completely wets the surface by forming a film over it. Liquids for which $0^\circ < \theta_w < 90^\circ$ are termed as *wetting liquids* and for $90^\circ < \theta_w < 180^\circ$, liquids are called *non-wetting liquids*.

From Young's law, when a liquid-vapor interface meets a solid wall, the equilibrium contact angle θ_w can be calculated from the force balance at the contact line and written as:

$$\theta_w = \cos^{-1} \left(\frac{\sigma_{sv} - \sigma_{sl}}{\sigma_{lv}} \right) \quad (4.79)$$

where σ_{sv} , σ_{sl} and σ_{lv} are surface tensions at the solid-vapor, solid-liquid and liquid-vapor contact lines, respectively (Young, 1805).

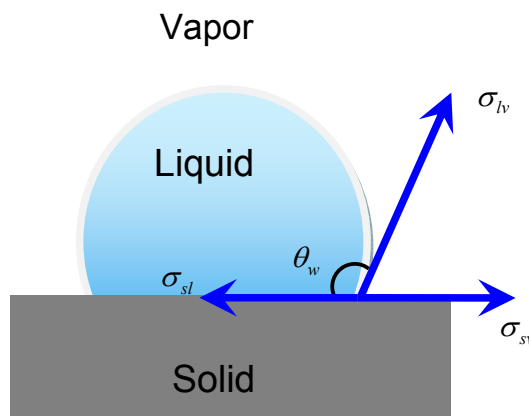


Fig. 4.8: Interfacial tensions acting on a contact line. σ_{sv} , σ_{lv} and σ_{sl} are surface tensions between the solid-liquid, liquid-vapor and solid-liquid interfaces. The solid surface is taken to be locally flat and is idealized as perfectly smooth. The *wettability* is quantified by the *contact angle* (or wetting angle) θ_w .

4.9.2 Several approaches to simulate θ_w in LBM

Contact angle between a fluid and the wall needs to be modeled accurately in order to capture the necessary surface effects of the two-phase dynamics. Since there exist several different LB approaches for two-phase simulations, the treatment of wall contact angles in those approaches also differs significantly (Fan et al., 2001; Briant et al., 2004; Niu et al., 2007; Takada et al., 2008; Lee & Liu, 2008). One of these is a model recently developed by Benzi et al. (2006), who investigated the dependency of the contact angle on “free” parameters of the Shan-Chen (S-C) two-phase model (Shan & Chen, 1993, 1994). By using such a scheme, one may simulate conditions varying from perfect hydrophobicity to perfect wettability on a wall surface. Needless to say, development and employment of a suitable wettability model is essential for any LBM based treatment of two phases.

We have developed a methodology based on the Cahn’s wetting theory (Cahn, 1977) to simulate equilibrium contact angles in the AILB model framework. Our aim is to define LB boundary conditions in order to reproduce the pre-specified contact angle θ_w under steady state conditions. In the following sections, Cahn’s theory of wetting dynamics is presented and its connection to the AILB two-phase model is derived.

4.9.3 Cahn’s theory of wetting dynamics

In the Cahn’s wetting theory (Cahn, 1977), a one-dimensional two-phase problem with planar interfaces is considered (illustrated in Fig. 4.9). The solid-liquid and the liquid-vapor interfaces are assumed to exist in the direction perpendicular to the solid surface. The fluid density $\rho(z)$ is assumed to vary smoothly in the interfacial region as a function of the distance z from the surface. [Note that the continuum assumption of density variation in the interface region is most adequate when the fluid is in its near-critical state ($T \approx T_c$), however, it may still be used for the temperatures far from the critical point.]

For the semi-infinite fluid in Fig. 4.9, which is in contact with the solid surface at $z = 0$, we can write the total free energy of the system as the sum of free energy of the bulk fluid γ_{bulk} and the free energy due to the presence of a surface at $z = 0$, i.e. γ_{surf} .

$$\gamma_{net} = \gamma_{bulk} + \gamma_{surf} \quad (4.80)$$

Using the mean-field theory, we can write the bulk free energy of the system γ_{bulk} as the “classical” gradient-square functional in the form below (Jacqmin, 1999):

$$\gamma_{bulk} = \int_{z=0}^{\infty} dz \left[E_0(\rho) + \frac{1}{2} \kappa \left(\frac{d\rho}{dz} \right)^2 \right] \quad (4.81)$$

where $E_0(\rho)$ is the bulk free energy density of the fluid and the gradient term represents the increase in system free energy due to the presence of a density gradient (Cahn, 1977).

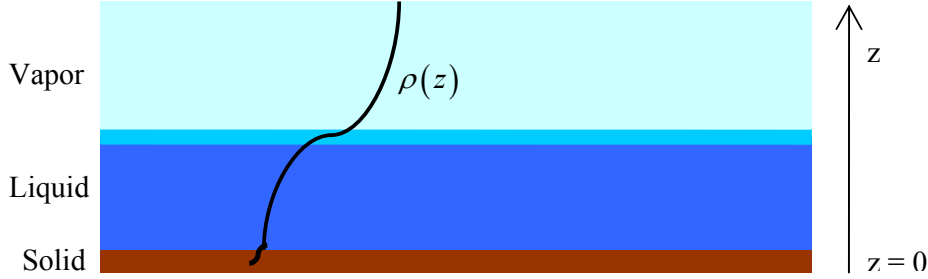


Fig. 4.9: A planar liquid-vapor interface is in contact with the solid surface situated at $z = 0$. Liquid is in direct contact with the solid surface. An equilibrium wetting model has been developed by Cahn (1977) for this interfacial configuration.

Assuming that the forces between the solid surface and the fluid are of short range, we can assume γ_{surf} to be a function of the fluid density at the surface, i.e. of $\rho_s \equiv \rho(z=0)$. In general, one can choose this functional dependence to be of any kind based on the chosen material for the surface and the fluid, however, for simplicity, we choose a linear dependence. Let us choose γ_{surf} to be:

$$\gamma_{surf} = -\lambda \rho_s \quad (4.82)$$

where a negative sign indicates the attraction of the liquid by the solid and thereby favoring of a large ρ_s (de Gennes, 1985).

In order to construct the equilibrium density profile $\rho(z)$, we need to minimize the bulk free energy of the system. From the calculus of variations, we know that the bulk free energy function in the form below

$$\gamma_{bulk} = \int_0^\infty dz \left[E_0(\rho) + \frac{1}{2} \kappa (\rho'(z))^2 \right] = \int_0^\infty dz \left[L(z, \rho(z), \rho'(z)) \right] \quad (4.83)$$

attains a minimum if $\rho(z)$ satisfies the following Euler-Lagrange equation (Sagan, 1969):

$$\frac{\partial L}{\partial \rho} = \frac{d}{dz} \left(\frac{\partial L}{\partial \rho'} \right) \quad (4.84)$$

where $\rho'(z) \equiv \frac{d\rho}{dz}$.

From equations (4.83) and (4.84),

$$\frac{\partial}{\partial \rho} \left[E_0(\rho) + \frac{1}{2} \kappa (\rho'(z))^2 \right] = \frac{d}{dz} \left(\frac{\partial}{\partial \rho'} \left[E_0(\rho) + \frac{1}{2} \kappa (\rho'(z))^2 \right] \right) \quad (4.85)$$

or,

$$\frac{dE_0}{d\rho} = \kappa \frac{d^2 \rho}{dz^2} \quad (4.86)$$

Integrating equation (4.86), we get:

$$E_0 = \frac{\kappa}{2} \left(\frac{d\rho}{dz} \right)^2 + C \quad (4.87)$$

By considering a point far into the bulk, where the fluid density $\rho(z \rightarrow \infty) = \rho_{bulk}$ (and ρ_{bulk}

can be either ρ_l or ρ_v), we have $\left. \frac{d\rho}{dz} \right|_{z \rightarrow \infty} = 0$ and $E_0(\rho = \rho_l \text{ or } \rho_v) = 0$, which yields $C = 0$.

Therefore, we get:

$$E_0 = \frac{\kappa}{2} \left(\frac{d\rho}{dz} \right)^2 \quad (4.88)$$

Now, substituting the above equation in equation (4.81), we can write the minimum bulk free energy as:

$$\gamma_{bulk, \min} = \int_{\rho_s}^{\rho_{bulk}} \kappa \left(\frac{d\rho}{dz} \right) d\rho = \int_{\rho_s}^{\rho_{bulk}} \sqrt{2\kappa E_0} d\rho \quad (4.89)$$

Notice that the density at the surface ρ_s is still not determined, which can be ascertained by minimizing the net free energy γ_{net} with respect to surface density ρ_s .

Let us write the net free energy γ_{net} by making use of $\gamma_{bulk,\min}$ to give:

$$\gamma_{net} = \gamma_{surf}(\rho_s) + \int_{\rho_s}^{\rho_{bulk}} d\rho \sqrt{2\kappa E_0(\rho)} \quad (4.90)$$

γ_{net} will have a minima with respect to ρ_s if

$$\frac{d\gamma_{net}}{d\rho_s} = 0 = \frac{d}{d\rho_s} \gamma_{surf}(\rho_s) + \frac{d}{d\rho_s} \left(\int_{\rho_s}^{\rho_{bulk}} d\rho \sqrt{2\kappa E_0(\rho)} \right) \quad (4.91)$$

Applying the Leibniz integral rule, we get:

$$\left(\frac{d\gamma_{surf}}{d\rho_s} \right) = \sqrt{2\kappa E_0(\rho_s)} \quad (4.92)$$

which from equation (4.82) gives,

$$-\lambda = \sqrt{2\kappa E_0(\rho_s)} \quad (4.93)$$

or,

$$E_0(\rho_s) = \frac{\lambda^2}{2\kappa} \quad (4.94)$$

If $-\lambda$ is smaller than the height of the function defined by $\sqrt{2\kappa E_0(\rho_s)}$, we can determine the roots of the equation above (i.e. possible values for the surface density ρ_s).

Furthermore, from equations (4.88) and (4.92), we can write an equilibrium boundary condition on the solid surface at $z = 0$ as (Briant et al., 2002, 2004; Briant & Yeomans, 2004; Yan & Zu, 2007):

$$\left(\frac{d\gamma_{surf}}{d\rho_s} \right) = \sqrt{2\kappa E_0(\rho_s)} = \kappa \frac{d\rho}{dz} \Big|_{z=0} \quad (4.95)$$

or,

$$\kappa \hat{n} \cdot \nabla \rho = \frac{d\gamma_{surf}}{d\rho_s} = -\lambda, \quad \text{at surface } z = 0 \quad (4.96)$$

where \hat{n} is a unit vector normal to the surface.

4.9.4 Implementation of Cahn's theory in the AILB model

Choosing the double-well form for $E_0(\rho)$ (from equation (4.35)), we get:

$$(\rho_s - \rho_l^{sat})^2 (\rho_s - \rho_v^{sat})^2 = \frac{\lambda^2}{2\kappa\beta} \quad (4.97)$$

The above equation has four roots i.e. four possible values for ρ_s which are:

$$\rho_{s1} = \frac{\rho_l^{sat} + \rho_v^{sat}}{2} - \frac{\rho_l^{sat} - \rho_v^{sat}}{2} \sqrt{1 + |\Omega|} \quad (4.98)$$

$$\rho_{s2} = \frac{\rho_l^{sat} + \rho_v^{sat}}{2} - \frac{\rho_l^{sat} - \rho_v^{sat}}{2} \sqrt{1 - |\Omega|} \quad (4.99)$$

$$\rho_{s3} = \frac{\rho_l^{sat} + \rho_v^{sat}}{2} + \frac{\rho_l^{sat} - \rho_v^{sat}}{2} \sqrt{1 + |\Omega|} \quad (4.100)$$

$$\rho_{s4} = \frac{\rho_l^{sat} + \rho_v^{sat}}{2} + \frac{\rho_l^{sat} - \rho_v^{sat}}{2} \sqrt{1 - |\Omega|} \quad (4.101)$$

where Ω is called the wetting potential, and is given by:

$$\Omega = \frac{4\lambda}{(\rho_l^{sat} - \rho_v^{sat})^2 \sqrt{2\kappa\beta}} \quad (4.102)$$

The formulation can now be used to calculate the surface tension force between liquid and vapor phase for an infinite one-dimensional system, in which the lower and upper parts of the system are occupied by the liquid and vapor phases, respectively. The liquid-vapor surface tension force is given by the minimum free energy (in equation (4.89), lower and upper bounds of the integral are substituted by ρ_l^{sat} and ρ_v^{sat} , respectively.).

$$\sigma_{lv} = \int_{\rho_l^{sat}}^{\rho_v^{sat}} d\rho \sqrt{2\kappa E_0(\rho)} \quad (4.103)$$

$$\sigma_{lv} = \sqrt{2\kappa\beta} \int_{\rho_l^{sat}}^{\rho_v^{sat}} d\rho (\rho - \rho_l^{sat})(\rho - \rho_v^{sat}) \quad (4.104)$$

$$\sigma_{lv} = \frac{\sqrt{2\kappa\beta}}{6} (\rho_l^{sat} - \rho_v^{sat})^3 \quad (4.105)$$

Surface tension between the solid surface and the fluid is given by:

$$\sigma_{sf} = -\lambda \rho_s + \int_{\rho_s}^{\rho_{bulk}} d\rho \sqrt{2\kappa E_0(\rho)} \quad (4.106)$$

For $\lambda > 0$, if the fluid in contact with the solid surface is vapor then the net free energy will be a minimum for $\rho_s = \rho_{s2}$ and the surface tension for the solid-vapor pair can be written as:

$$\sigma_{sv} = -\lambda \rho_{s2} + \int_{\rho_{s2}}^{\rho_v^{sat}} d\rho \sqrt{2\kappa E_0(\rho)} = -\lambda \frac{\rho_l^{sat} + \rho_v^{sat}}{2} + \frac{\sigma_{lv}}{2} - \frac{\sigma_{lv}}{2} (1-\Omega)^{\frac{3}{2}} \quad (4.107)$$

For $\lambda > 0$, if the fluid in contact with the solid surface is liquid then the net free energy will be a minimum for $\rho_s = \rho_{s4}$ and the surface tension for the solid-liquid pair can be written as:

$$\sigma_{sl} = -\lambda \rho_{s4} + \int_{\rho_{s4}}^{\rho_l^{sat}} d\rho \sqrt{2\kappa E_0(\rho)} = -\lambda \frac{\rho_l^{sat} + \rho_v^{sat}}{2} + \frac{\sigma_{lv}}{2} - \frac{\sigma_{lv}}{2} (1+\Omega)^{\frac{3}{2}} \quad (4.108)$$

For $\lambda < 0$, if the fluid in contact with the solid surface is liquid then the net free energy will be a minimum for $\rho_s = \rho_{s3}$ and the surface tension for the solid-liquid pair can be written as:

$$\sigma_{sl} = -\lambda \rho_{s3} + \int_{\rho_{s3}}^{\rho_l^{sat}} d\rho \sqrt{2\kappa E_0(\rho)} = -\lambda \frac{\rho_l^{sat} + \rho_v^{sat}}{2} + \frac{\sigma_{lv}}{2} - \frac{\sigma_{lv}}{2} (1+\Omega)^{\frac{3}{2}} \quad (4.109)$$

And finally, for $\lambda < 0$, if the fluid in contact with the solid surface is vapor then the net free energy will be a minimum for $\rho_s = \rho_{s1}$ and the surface tension for the solid-vapor pair can be written as:

$$\sigma_{sv} = -\lambda \rho_{s1} + \int_{\rho_{s1}}^{\rho_v^{sat}} d\rho \sqrt{2\kappa E_0(\rho)} = -\lambda \frac{\rho_l^{sat} + \rho_v^{sat}}{2} + \frac{\sigma_{lv}}{2} - \frac{\sigma_{lv}}{2} (1-\Omega)^{\frac{3}{2}} \quad (4.110)$$

The wetting angle θ_w is determined by substituting equations (4.105), (4.107)-(4.108) into equation (4.79),

$$\cos \theta_w = \frac{(1+\Omega)^{\frac{3}{2}} - (1-\Omega)^{\frac{3}{2}}}{2} \quad (4.111)$$

For a given wetting angle θ_w in the range of $0 < \theta_w < \pi$, we can write Ω as:

$$\Omega = 2 \operatorname{sgn} \left(\frac{\pi}{2} - \theta_w \right) \left\{ \cos \left(\frac{\omega}{3} \right) \left[1 - \cos \left(\frac{\omega}{3} \right) \right] \right\}^{\frac{1}{2}} \quad (4.112)$$

where

$$\omega = \cos^{-1} \left(\sin^2 \theta_w \right) \quad (4.113)$$

and $\text{sgn}(*)$ gives the sign of $(*)$.

Note that a desired wetting angle θ_w can be chosen for the LBM simulations and based on that the wetting potential Ω can be calculated from equation (4.112). With the wetting potential Ω known, we can now evaluate the value of λ using equation (4.102).

4.9.5 Simulation of θ_w in the AILB model

Using the approach described in the previous section, we can simulate pre-specified contact angles at the solid walls. We can simulate the specific equilibrium contact angle in the simulation algorithm by modifying the second derivative of density at the wall lattice points to include the appropriate wetting potential. Note that the second derivative of density described by equation (4.74) is still valid in the bulk region (i.e. away from the walls). One only needs to modify equation (4.74) for the lattice points at the wall sites where the specific contact angle is simulated. Details of how to modify the second gradient of density at a wall lattice point are given below.

For a two-dimensional D_2Q_9 square lattice, the second gradient of density can be evaluated in the bulk region (i.e. at the lattice points which are not part of a wall surface) using the following equation, which is essentially the expanded form of the equation(4.74):

$$\nabla^2 \rho|_{(x,y)} = \frac{1}{6} \left[\rho(x_+, y_+) + \rho(x_-, y_-) + \rho(x_-, y_+) + \rho(x_+, y_-) + 4 \{ \rho(x_+, y) + \rho(x_-, y) + \rho(x, y_+) + \rho(x, y_-) \} - 20 \rho(x, y) \right] \quad (4.114)$$

Imposing a boundary condition $\hat{n} \nabla \rho = -\lambda/\kappa$ (where \hat{n} is a unit outward normal vector) while evaluating the second gradient of density on the wall lattice points for a D_2Q_9 lattice, we get:

$$\nabla_x^2 \rho|_{(x,y)} = \frac{1}{3} [\rho(x_+, y) + \rho(x_-, y)] + \frac{1}{12} \left[\begin{matrix} \rho(x_+, y_+) + \rho(x_-, y_+, t) \\ + \rho(x_+, y_-, t) + \rho(x_-, y_-, t) \end{matrix} \right] - \rho(x, y) + \frac{\lambda}{\kappa} \quad (4.115)$$

$$\nabla_y^2 \rho \Big|_{(x,y)} = \frac{1}{3} [\rho(x, y_+) + \rho(x, y_-)] + \frac{1}{12} \left[\begin{array}{l} \rho(x_+, y_+) + \rho(x_-, y_+, t) \\ + \rho(x_+, y_-, t) + \rho(x_-, y_-, t) \end{array} \right] - \rho(x, y) + \frac{\lambda}{\kappa} \quad (4.116)$$

Combining the above two equations gives:

$$\begin{aligned} \nabla^2 \rho \Big|_{(x,y)} &= \nabla_x^2 \rho \Big|_{(x,y)} + \nabla_y^2 \rho \Big|_{(x,y)} \\ &= \frac{1}{3} \left[\begin{array}{l} \rho(x_+, y) + \rho(x_-, y) \\ + \rho(x, y_+) + \rho(x, y_-) \end{array} \right] + \frac{1}{6} \left[\begin{array}{l} \rho(x_+, y_+) + \rho(x_-, y_+, t) \\ + \rho(x_+, y_-, t) + \rho(x_-, y_-, t) \end{array} \right] - 2\rho(x, y) + \frac{2\lambda}{\kappa} \end{aligned} \quad (4.117)$$

where

$$\lambda = \frac{\Omega (\rho_l^{sat} - \rho_v^{sat})^2 \sqrt{2\kappa\beta}}{4} \quad (4.118)$$

and Ω is calculated from

$$\Omega = 2 \operatorname{sgn} \left(\frac{\pi}{2} - \theta_w \right) \left\{ \cos \left(\frac{\omega}{3} \right) \left[1 - \cos \left(\frac{\omega}{3} \right) \right] \right\}^{\frac{1}{2}}, \quad \omega = \cos^{-1} (\sin^2 \theta_w) \quad (4.119)$$

for a given contact angle θ_w .

Similarly, for a three-dimensional D_3Q_{19} lattice, the second gradient of density in the bulk region can be written as:

$$\nabla^2 \rho \Big|_{(x,y,z)} = \frac{1}{6} [2S_1 + S_2 - 24\rho(x, y, z)] \quad (4.120)$$

S_1 and S_2 are defined below in the equations (4.125) and (4.126).

Imposing the boundary condition $\hat{n} \nabla \rho = -\lambda/\kappa$ while evaluating the second gradient of density on the wall lattice points for a D_3Q_{19} lattice, we get:

$$\nabla_x^2 \rho \Big|_{(x,y,z)} = \frac{1}{6} [\rho(x_+, y, z) + \rho(x_-, y, z)] + \frac{1}{12} S_2 - \frac{4}{3} \left[\rho(x, y, z) - \frac{\lambda}{\kappa} \right] \quad (4.121)$$

$$\nabla_y^2 \rho \Big|_{(x,y,z)} = \frac{1}{6} [\rho(x, y_+, z) + \rho(x, y_-, z)] + \frac{1}{12} S_2 - \frac{4}{3} \left[\rho(x, y, z) - \frac{\lambda}{\kappa} \right] \quad (4.122)$$

$$\nabla_z^2 \rho \Big|_{(x,y,z)} = \frac{1}{6} [\rho(x, y, z_+) + \rho(x, y, z_-)] + \frac{1}{12} S_2 - \frac{4}{3} \left[\rho(x, y, z) - \frac{\lambda}{\kappa} \right] \quad (4.123)$$

Combining the above three equations, we get:

$$\begin{aligned}\nabla^2 \rho|_{(x,y,z)} &= \nabla_x^2 \rho|_{(x,y,z)} + \nabla_y^2 \rho|_{(x,y,z)} + \nabla_z^2 \rho|_{(x,y,z)} \\ &= \frac{1}{6} S_1 + \frac{1}{4} S_2 - 4 \left[\rho(x, y, z) - \frac{\lambda}{\kappa} \right]\end{aligned}\quad (4.124)$$

where

$$S_1 = \rho(x_+, y, z) + \rho(x_-, y, z) + \rho(x, y_+, z) + \rho(x, y_-, z) + \rho(x, y, z_+) + \rho(x, y, z_-) \quad (4.125)$$

$$S_2 = \begin{bmatrix} \rho(x_+, y_+, z) + \rho(x_-, y_-, z) + \rho(x_-, y_+, z) + \rho(x_+, y_-, z) \\ + \rho(x_+, y, z_+) + \rho(x_-, y, z_-) + \rho(x_+, y, z_-) + \rho(x_-, y, z_+) \\ + \rho(x, y_+, z_+) + \rho(x, y_-, z_-) + \rho(x, y_+, z_-) + \rho(x, y_-, z_+) \end{bmatrix} \quad (4.126)$$

and λ is calculated from equation (4.118).

4.10 Simulation of spatially-varying viscosities

In the LBM-BGK algorithm, the kinematic viscosity of a fluid ν is explicitly determined by the prescribed single relaxation time τ . This functional form gives a unique value for the kinematic viscosity of the fluid irrespective of the multiple phases involved. However, in order to accurately model the flow dynamics of a single-component two-phase fluid, it is essential to have different kinematic viscosities for the two phases at any given temperature.

This task may be accomplished by expressing the relaxation time τ as a linear function of the local fluid density $\rho(x, y)$ constrained by the saturation densities of both phases. Thus, $\tau(\rho)$ can be written as

$$\tau(\rho) = \left[\frac{\tau(\rho_L) - \tau(\rho_V)}{\rho_L - \rho_V} \right] \rho + \left[\frac{\tau(\rho_V) \rho_L - \tau(\rho_L) \rho_V}{\rho_L - \rho_V} \right] \quad (4.127)$$

where $\tau(\rho_L)$ and $\tau(\rho_V)$ represent, at the given temperature, the relaxation times corresponding to the saturation density of the liquid and vapor phases, respectively. These phase-specific relaxation times are calculated by knowing the kinematic viscosities of the corresponding phases.

4.11 Simulation of buoyancy effects in the LB model

Depending upon the problem being simulated, there are several ways by which one can implement buoyancy effects in the LB model. Of course, the most appropriate and physically accurate method is to apply the gravitational forces in the system and let the buoyancy effects (over the low density regions) appear from the dynamics itself. The gravitational body force corresponds to the following equation:

$$F_{\text{gravity}}(x, y) = \rho(x, y) g(-\hat{\mathbf{j}}) \quad (4.128)$$

Note that the simulation of buoyancy effects using the above equation only works when the simulation domain is not periodic in the direction of gravity i.e. there should be a solid wall present in the system resisting the downward fluid motion.

If the domain is periodic in all directions (i.e. no walls present) then application of the above equation leads to the whole fluid being continuously accelerated since there is no wall to provide any resistive drag force (Sankaranarayanan et al., 1999).

If the domain has walls in the direction parallel to the gravity then the no-slip condition on the walls provide resistive forces to the fluid motion and lead to a scenario similar to bubble motion driven by a Poiseuille flow. Since the gravity acts as the driving force for the channel flow, the bubble moves in the direction of gravity.

For simulations with periodic boundaries, one can explicitly define the buoyancy force as follows:

$$F_{\text{buo}}(x, y) = -(\rho(x, y) - \rho_l^{\text{sat}}) g \hat{\mathbf{j}} \quad (4.129)$$

where ρ_l^{sat} is the saturated density of the liquid phase. The above form corresponds to defining a body force over the low density region in the direction opposite to the gravity. Due to quasi-compressible nature of the LB simulations (Buick & Greated, 2000), one may want to explicitly define a zero force in the liquid phase, such as:

$$F_{\text{buo}}(x, y) = \begin{cases} -(\rho(x, y) - \rho_l^{\text{sat}}) g \hat{\mathbf{j}} & \rho(x, y) \leq \rho_m^{\text{sat}} \\ 0 & \text{otherwise} \end{cases} \quad (4.130)$$

where ρ_m^{sat} is the mean density of the two phases.

4.12 Similarities with the phase-field modelling technique

The Gibbs-Duhem equation based LB model is conceptually similar to the phase-field modeling technique which is quite popular in material science (Warren, 1995; Jacqmin, 1996; Anderson et al., 1998; Yue et al., 2004; Jamet et al., 2001, 2002; Badalassi et al., 2003; Acar, 2009). Hence, before closing this chapter, the phase field model is briefly reviewed here.

The phase-field method is also a fixed-grid method with a physically diffusive interface. Similar to the LB model, the interface in phase-field models is introduced via minimizing the free energy of the system. The two-components are identified by a phase-field variable (ϕ) representing the volume fraction of the two components and thereby, indicating the location of the interface. The variation in ϕ is smooth across the interface and stretches over a few grid points yielding a diffuse interface. When the thickness of the stretched interface approaches zero, results of the diffuse-interface phase-field model approximates the corresponding sharp-interface formulations (such as the level-set methods). Phase field methods have been used in studying numerous applications ranging from phase-transitions and critical phenomena, solidification and dendritic growth in alloys, interfacial tension theories, solid-state phase transformations, precipitate/grain growth (coarsening dynamics) and complex fluids (polymers etc.). Details on the phase-field methods can be found in Feng et al. (2005) and Moelans et al. (2008).

4.13 References

Acar, R., 2009. Simulation of interface dynamics: a diffuse-interface model. *Visual Comput.* 25, 101-115.

Andersen, D.M., McFadden, G.B., Wheeler, A.A., 1998. Diffuse-interface in fluid mechanics. *Annu. Rev. Fluid Mech.* 30, 139–165.

Badalassi, V.E., Ceniceros, H.D., Banerjee, S., 2003. Computation of multiphase systems with phase field models. *J. Comp. Phys.* 190, 371-397.

Benzi, R., Biferale, L., Sbragaglia, M., Succi, S., Toschi, F., 2006. Mesoscopic modeling of a two-phase flow in the presence of boundaries: The contact angle. *Phys. Rev. E* 74, 021509.

Briant, A.J., Papatzacos, P., Yeomans, J.M., 2002. Lattice Boltzmann simulations of contact line motion in a liquid-gas system. *Phil. Trans. R. Soc. Lond. A* 360, 485-495.

Briant, A.J., Wagner, A.J., Yeomans, J.M., 2004. Lattice Boltzmann simulations of contact line motion: I. Liquid-gas systems. *Phys. Rev. E* 69, 031602.

Briant, A.J., Yeomans, J.M., 2004. Lattice Boltzmann simulations of contact line motion: II. Binary fluids. *Phys. Rev. E* 69, 031603.

Buick, J.M., Created, C.A., 2000. Gravity in a lattice Boltzmann model. *Phys. Rev. E* 61(5), 5307-5320.

Cahn, J.W., 1977. Critical point wetting. *The Journal of Chemical Physics* 66(8), 3667-3672.

de Gennes, P.G., 1985. Wetting: statics and dynamics. *Reviews of modern physics*, 57(3), 827-863.

Fan, L., Fang, H., Lin, Z., 2001. Simulation of contact line dynamics in a two-dimensional capillary tube by the lattice Boltzmann model. *Phys. Rev. E* 63, 051603.

Feng, J.J., Liu, C., Shen, J., Yue, P., 2005. An Energetic Variational Formulation with Phase Field Methods for Interfacial Dynamics of Complex Fluids: Advantages and Challenges. *Modeling of soft matter*, Springer New York, 1-26.

Iwamatsu, M., 1993. A double-parabola model for the non-classical Cahn-Hilliard theory of homogenous nucleation. *J. Phys.: Condens. Matter* 5, 7537-7550.

Jacqmin, D., 1996. An energy approach to the continuum surface tension method. *American Institute of Aeronautics and Astronautics, Inc.*

Jacqmin, D., 1999. Calculation of two-phase Navier-Stokes flows using phase-field modeling. *J. Comput. Phys.* 155, 96-127.

Jamet, D., Lebaigue, O., Coutris, N., Delhaye, J.M., 2001. The second gradient method for the direct numerical simulation of liquid-vapor flows with phase change. *J. Comp. Phys.* 169, 624-651.

Jamet. D., Torres, D., Brackbill, J.U., 2002. On the theory and computation of surface tension: The elimination of parasitic currents through energy conservation in the second-gradient method. *J. Comp. Phys.* 182, 262-276.

Kikkinides, E.S., 2008. Thermodynamic consistency of liquid-gas lattice Boltzmann methods: Interfacial property issues. *Phys. Rev. E* 78, 036702.

Lee, T., Fischer, P.F., 2006. Eliminating parasitic currents in the lattice Boltzmann equation method for nonideal gases. *Phys. Rev. E* 74, 046709.

Lee, T., Lin, C.L., 2005. A stable discretization of the lattice Boltzmann equation for simulation of incompressible two-phase flows at high density ratio. *J. Comput. Phys.* 206, 16-47.

Lee, T., Liu, L., 2008. Wall boundary conditions in the lattice Boltzmann equation method for nonideal gases. *Phys. Rev. E* 78, 017702.

McQuarrie, D., Simon, J.D., 1999. *Molecular Thermodynamics*, University Science, Sausalito, CA.

Moelans, N., Blanpain, B. Wollants, P., 2008. An introduction to phase-field modeling of microstructure evolution. *Computer Coupling of Phase Diagrams and Thermochemistry* 32, 268-294.

Niu, X.D., Munekata, T., Hyodo, S.A., Suga, K., 2007. An investigation of water-gas transport processes in the gas-diffusion layer of a PEM fuel cell by a multiphase multiple-relaxation time lattice Boltzmann model. *J. Power Sources* 172, 542-552.

Sagan, H., 1969. *Introduction to calculus of variations*. McGraw Hill, New York.

Sankaranarayanan, K., Shan, X., Kevrekidis, I.G., Sundaresan, S., 1999. Bubble flow simulations with the lattice Boltzmann method. *Chem. Eng. Sci.* 54, 4817-4823.

Shan, X., Chen, H., 1993. Lattice Boltzmann model for simulation flows with multiple phases and components. *Phys. Rev. E* 47, 1815.

Shan, X., Chen, H., 1994. Simulation of nonideal gases and liquid-gas phase transitions by the lattice Boltzmann equation. *Phys. Rev. E* 49, 2941.

Takada, N., Matsumoto, J., Matsumoto, S., Ichikawa, N., 2008. Application of a phase-field method to the numerical analysis of motions of a two-phase fluid with high density ratio on a solid surface. *J. Comp. Sci. Tech.* 2(2), 318-329.

Wagner, A.J., 2006. Thermodynamic consistency of liquid-gas lattice Boltzmann simulations. *Phys. Rev. E* 74, 056703.

Warren, J.A., 1995. How does a metal freeze ? – A phase field model of alloy solidification. *IEEE Computational Science & Engineering*: Summer 1995, 38-49.

Yan, Y.Y., Zu, Y.Q., 2007. A lattice Boltzmann method for incompressible two-phase flows on partial wetting surface with large density ratio. *J. Comp. Phys.* 227, 763-775.

Young, T., 1805. An essay on the cohesion of fluids. *Phil. Trans. R. Soc. Lond.* 95, 65-87.

Yuan, P., Schaefer, L., 2006. Equations of state in a lattice Boltzmann model. *Phys Fluids* 18, 042101.

Yue, P., Feng, J.J., Liu, C., Shen, J., 2004. A diffuse-interface method for simulating two-phase flows of complex fluids. *J. Fluid Mech.* 515, 293-317.

Chapter 5

Boundary conditions for the AILB model

Dynamics of flow, whether it is in single-phase or multi-phase, depends upon the surrounding environment. This dependence is mathematically prescribed by applying the suitable boundary conditions (BCs) to the governing equations. Usually, the BCs are only available in terms of the relevant macroscopic variables (and from which not all the mesoscopic information is directly deducible). For example, on a static wall, the fluid velocity is assumed to be zero to satisfy no-slip boundary condition; however, one does not know all the particle distribution functions at the wall. Therefore, in lattice Boltzmann models, one cannot directly apply the boundary conditions to the relevant macroscopic variables since our governing equations are at a level below, i.e. on a mesoscopic scale. Consequently, one has to translate the macroscopic BCs to the scale of the governing equations and represent those in terms of the discrete distribution functions in order to proceed with the numerical solution procedure.

Depending upon the problem at hand, various types of boundary conditions including no-slip, free-slip, frictional slip, sliding walls, moving walls, in-flux, out-flux etc. (Succi, 2001) may be applied to the evolution of the distribution function. The most simple and widely used approach is the *bounce-back method*, in which, the outgoing distribution functions reflect back into the domain after streaming through any wall or solid obstacles.

There are three types of flow boundary conditions which are most commonly used in LBM simulations: (i) Periodic BCs, (ii) Velocity BCs and (iii) Pressure BCs. Periodic BCs in LBM can be applied by simply letting the outgoing distribution functions from one end of the domain to stream into the opposite end. Periodic BCs are adequate for simulating physical dynamics in which surfaces or wall effects are negligible. In addition, sliding walls, porous walls or wall flux boundaries are simulated by enforcing the fluid velocity at the walls to be equal to that of the wall. Since the pressure is not treated as an independent variable in LBM and is usually a function of density, the pressure BCs are simulated by appropriate density BCs. In the following sections, wall velocity and wall density boundary conditions are

developed for D₂Q₉ (in 2D) and D₃Q₁₉ (in 3D) lattices in the framework of the artificial interface lattice Boltzmann (AILB) model.

Before proceeding further, the governing LB equation and the conservation constraints it has to follow:

Governing LB equation:

$$g_a(\mathbf{r} + \mathbf{v}_a \Delta t, t + \Delta t) = g_a(\mathbf{r}, t) - \frac{\Delta t}{\tau + 0.5\Delta t} \left[g_a - g_a^{eq} \right]_{(\mathbf{r}, t)} + \frac{\Delta t (\mathbf{v}_a - \mathbf{u}) \cdot \mathbf{F}^M}{\rho R T} f_a^{eq} \Big|_{(\mathbf{r}, t)} \quad (5.1)$$

where

$$g_a(\mathbf{r}, t) = f_a(\mathbf{r}, t) + \frac{\Delta t}{2\tau} \left[f_a - f_a^{eq} \right]_{(\mathbf{r}, t)} - \frac{\Delta t (\mathbf{v}_a - \mathbf{u}) \cdot \mathbf{F}^C}{2 \rho R T} f_a^{eq} \Big|_{(\mathbf{r}, t)} \quad (5.2)$$

$$g_a^{eq}(\mathbf{r}, t) = f_a^{eq}(\mathbf{r}, t) - \frac{\Delta t (\mathbf{v}_a - \mathbf{u}) \cdot \mathbf{F}^C}{2 \rho R T} f_a^{eq} \Big|_{(\mathbf{r}, t)} \quad (5.3)$$

$$\mathbf{F}^M = \left(\frac{\mathbf{F}^C + \mathbf{F}^B}{2} \right) \quad (5.4)$$

$$\mathbf{F}^B = R T \nabla^B \rho - \rho \nabla^B \mu + \mathbf{F}_G \quad (5.5)$$

$$\mathbf{F}^C = R T \nabla^C \rho - \rho \nabla^C \mu + \mathbf{F}_G \quad (5.6)$$

and superscripts *B* and *C* indicate the biased and central difference scheme of gradient evaluation, respectively. Moreover, f_a^{eq} is a Maxwell-Boltzmann equilibrium distribution function, approximated as:

$$f_a^{eq} = w_a \left[1 + \frac{\mathbf{v}_a \cdot \mathbf{u}}{R T} + \frac{1}{2} \left(\frac{\mathbf{v}_a \cdot \mathbf{u}}{R T} \right)^2 - \frac{u^2}{2 R T} \right] \quad (5.7)$$

where w_a and RT are lattice constants which depend upon the chosen lattice type i.e. D₂Q₉ or D₃Q₁₉.

The distribution function at the boundaries must satisfy the following constraints of mass and momentum conservation:

Mass Conservation:

$$\rho(\mathbf{r}, t) = \sum_a g_a \quad (5.8)$$

Momentum Conservation:

$$\rho(\mathbf{r}, t) \mathbf{u}(\mathbf{r}, t) = \left(\sum_a \mathbf{v}_a g_a \right) + \frac{\Delta t}{2} \mathbf{F}^C \quad (5.9)$$

Macroscopic properties (fluid densities, velocities, forcing terms etc.) in equations (5.1) to (5.9) are known by virtue of the specific BCs being simulated, however, not all the distribution functions (g_a) are known at the boundaries in the post-streaming state. This is because the exterior of the computational domain does not take part in the solution and therefore, does not supply any distribution functions to the boundary upon streaming. These missing distribution functions at the boundaries can be determined using the relations of the mass and momentum conservation in equations (5.8) and (5.9).

5.1 Velocity boundary conditions in 2D

Let us consider a two-dimensional (2D) computational domain as shown in Fig. 5.1, in which the fluid is surrounded by the South ($y = 0$), North ($y = Ly$), East ($x = Lx$) and West ($x = 0$) boundaries. Computational grid is chosen such that there are nodes lying exactly on the physical boundaries as well as the corners. The corners are where the perpendicular boundaries meet and are named accordingly, i.e. NW denotes the intersection of the North and West boundaries, etc. Usually, there are more unknowns at the corners than at the straight boundaries, and the locally available information is not sufficient for the evaluation of those additional unknowns. Therefore, corners are treated in a special way by extrapolating unknown density from the neighboring bulk nodes (Zou & He, 1997).

For 2D simulations, we are using a D_2Q_9 lattice structure in this report (one may choose other lattice structures, for example, D_2Q_5 or D_2Q_7). As shown in Fig. 4.1(a), the D_2Q_9 lattice has 8 velocity vectors linking it with the neighboring nodes, and a null link (or rest state). Out of these 8 links, 4 are orthogonal links which point to the nearest neighbors (and have speed 1) and 4 are diagonal links which point to the next-nearest neighbors (and have speed $\sqrt{2}$). Lattice velocities in different directions are listed in Table 4.1 for the D_2Q_9

lattice. Due to the symmetry of the lattice in LBM, directional links always come in pairs i.e. each link has a partner which points into the opposite direction. Such pairs are listed in Table 5.1 for the D_2Q_9 lattice.

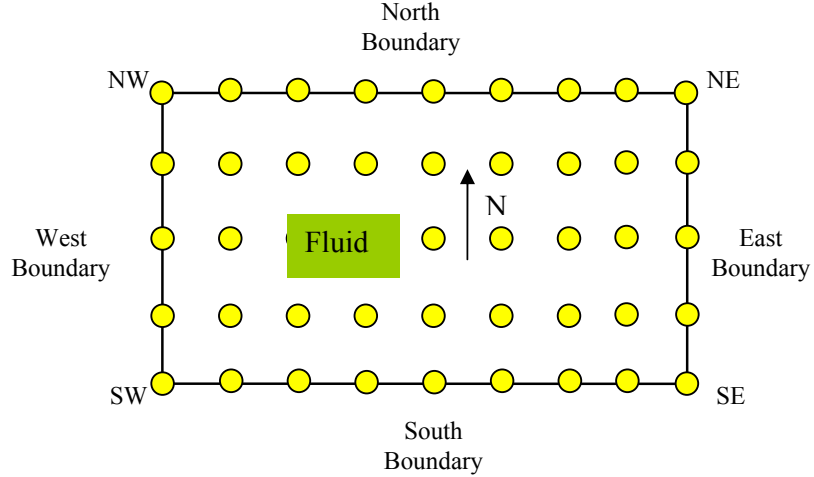


Fig. 5.1: Two-dimensional (2D) computational domain. The fluid is enclosed by North, South, East and West boundaries. Computational grid is chosen such that the nodes (depicted by yellow circles) lie on the boundaries as well as on the corners (NW, SW, NE and SE).

Table 5.1: Directional pairs having opposite lattice velocities (a, \bar{a}) for D_2Q_9 lattice.

a	\bar{a}	a	\bar{a}
1	3	5	7
2	4	6	8
3	1	7	5
4	2	8	6

In the following sections, methodology to obtain unknowns at the South boundary and the SW corner is presented. Relations for unknowns at the rest of the boundaries are provided in Appendix C.

5.1.1 South boundary

Let us consider a case in which the fluid at the South boundary has its x - and y -velocities specified and equal to U_{wx} and U_{wy} , respectively. As shown in Fig. 5.2, there are

three unknown distribution functions (g_2 , g_5 and g_6) at the boundary in the post-streaming state. In addition, the density at the boundary (ρ_w) is also an unknown. We need to determine these 4 unknowns in order to satisfy the desired velocity BC.

Mass Conservation:

$$\rho_w = g_0 + g_1 + g_2 + g_3 + g_4 + g_5 + g_6 + g_7 + g_8 \quad (5.10)$$

Momentum Conservation:

$$\rho_w U_{wx} = (g_1 + g_5 + g_8) - (g_3 + g_6 + g_7) + \frac{\Delta t}{2} F_x^C \quad (5.11)$$

$$\rho_w U_{wy} = (g_2 + g_5 + g_6) - (g_4 + g_7 + g_8) + \frac{\Delta t}{2} F_y^C \quad (5.12)$$

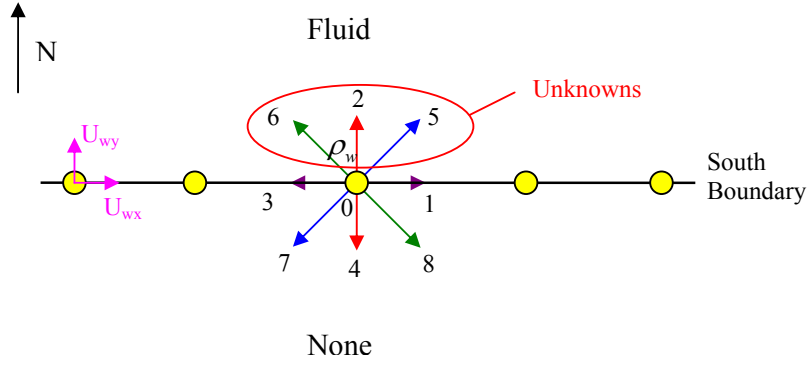


Fig. 5.2: Velocity boundary condition at the South boundary. The fluid is specified to have its x - and y -velocity equal to U_{wx} and U_{wy} , respectively. Distribution functions g_2 , g_5 , g_6 and the density ρ_w are unknown at the boundary.

Note that, in the equations (5.11) and (5.12), the forcing terms F_x^C and F_y^C depend upon gradients of the density and the chemical potential (see equation (5.6)). In order to simplify calculations, we can evaluate these forcing terms using the density at the previous LB time step and thereby, treat F_x^C and F_y^C as constants for the current LB time step.

To determine the 4 unknowns ρ_w , g_2 , g_5 and g_6 at the boundary, we are still short of one equation; we only have 3 equations: (5.10), (5.11) and (5.12). In order to close the system, we assume that upon streaming, the non-equilibrium part of the outgoing distribution

function normal to the boundary i.e. ($g_4 - g_4^{eq}$) bounces back into the domain to give the non-equilibrium part of g_2 , i.e.

$$g_2 - g_2^{eq} = g_4 - g_4^{eq} \quad (5.13)$$

This closure condition was first proposed by Zou and He (1997) for single phase flows and, as shown in this report, is also proven to be a good approximation for boundaries for two phase flows.

Now, from equations (5.10) and (5.12), we can calculate density ρ_w as:

$$\begin{aligned} \rho_w &= g_0 + g_1 + g_3 + (g_4 + g_7 + g_8) + (g_2 + g_5 + g_6) \\ \Rightarrow \rho_w &= g_0 + g_1 + g_3 + 2(g_4 + g_7 + g_8) + \rho_w U_{wy} - \frac{\Delta t}{2} F_y^C \\ \Rightarrow \rho_w &= \left\{ g_0 + g_1 + g_3 + 2(g_4 + g_7 + g_8) - \frac{\Delta t}{2} F_y^C \right\} / \left\{ 1 - U_{wy} \right\} \end{aligned} \quad (5.14)$$

With ρ_w known, the equilibrium distribution functions g_2^{eq} and g_4^{eq} in equation (5.13), can be evaluated using equations (5.3), (5.6) and (5.7) with the density ρ_w , x -velocity U_{wx} and y -velocity U_{wy} :

$$\begin{aligned} g_2 &= g_4 + (g_2^{eq} - g_4^{eq}) \\ &= g_4 + (f_2^{eq} - f_4^{eq}) - \frac{\Delta t}{2} \frac{((\mathbf{v}_2 - \mathbf{u}) f_2^{eq} - (\mathbf{v}_4 - \mathbf{u}) f_4^{eq})}{\rho_w RT} \mathbf{F}^C \end{aligned} \quad (5.15)$$

where $\mathbf{u} = U_{wx} \mathbf{i} + U_{wy} \mathbf{j}$, $f_a^{eq} \equiv f_a^{eq}(\rho_w, \mathbf{u})$ and \mathbf{F}^C is given by equation (5.6). Note that the numerical evaluation of the right hand side of the above equation requires treating the directional and non-directional derivatives differently, as discussed in Chapter 4, Sec-4.7. With ρ_w and g_2 known, g_5 and g_6 can now simply be obtained by solving equations (5.11) and (5.12).

Below we list the equations which should be solved in order to obtain the desired unknowns at the South boundary:

$$\rho_w = \left\{ g_0 + g_1 + g_3 + 2(g_4 + g_7 + g_8) - \frac{\Delta t}{2} F_y^C \right\} / \left\{ 1 - U_{wy} \right\} \quad (5.16)$$

$$g_2 = g_4 + (g_2^{eq} - g_4^{eq}) \quad (5.17)$$

$$g_5 - g_6 = (g_3 + g_7) - (g_1 + g_8) + \rho_w U_{wx} - \frac{\Delta t}{2} F_x^C \quad (5.18)$$

$$g_5 + g_6 = g_4 + g_7 + g_8 - g_2 + \rho_w U_{wy} - \frac{\Delta t}{2} F_y^C \quad (5.19)$$

$$g_5 = \frac{(g_5 + g_6) + (g_5 - g_6)}{2} \quad (5.20)$$

$$g_6 = \frac{(g_5 + g_6) - (g_5 - g_6)}{2} \quad (5.21)$$

5.1.2 South-West (SW) corner

Special treatment is required to impose and satisfy BCs at the corners. There are more unknowns at the corners than there are on the nodes on straight boundaries. For example, at the SW corner, we have 6 unknowns (ρ_w , g_1 , g_2 , g_5 , g_6 and g_8) which need to be determined (see Fig. 5.3). Since the SW node is a part of both South and West boundaries, we can choose velocity on either boundary as the fluid velocity on the SW node. In this example, we choose the West boundary's velocities U_{wx} and U_{wy} , to be the velocity on the SW corner.

Mass Conservation:

$$\rho_w = g_0 + g_1 + g_2 + g_3 + g_4 + g_5 + g_6 + g_7 + g_8 \quad (5.22)$$

Momentum Conservation:

$$\rho_w U_{wx} = (g_1 + g_5 + g_8) - (g_3 + g_6 + g_7) + \frac{\Delta t}{2} F_x^C \quad (5.23)$$

$$\rho_w U_{wy} = (g_2 + g_5 + g_6) - (g_4 + g_7 + g_8) + \frac{\Delta t}{2} F_y^C \quad (5.24)$$

Next, we assume that upon streaming, the non-equilibrium part of the outgoing distribution functions normal to the SW node, i.e. ($g_3 - g_3^{eq}$) and ($g_4 - g_4^{eq}$), bounce back into the domain to give the non-equilibrium part of g_1 and g_2 , respectively. That is

$$g_1 - g_1^{eq} = g_3 - g_3^{eq} \quad (5.25)$$

$$g_2 - g_2^{eq} = g_4 - g_4^{eq} \quad (5.26)$$

Notice that we only have 5 equations to determine the 6 unknowns. Therefore, in order to close the system, we approximate the density at the SW node ρ_w with the density at the nearest neighboring flow node ρ_{NBR} (see Fig. 5.3) i.e. $\rho_w = \rho_{NBR}$. With density ρ_w known, rest of the unknowns can now be evaluated using the aforementioned 5 equations.

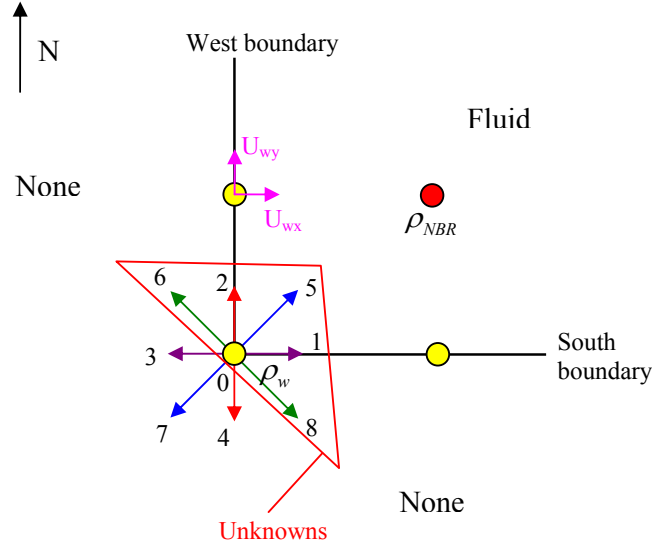


Fig. 5.3: Velocity boundary condition at the South-West (SW) corner. The x - and y -velocity of the fluid is specified to be U_{wx} and U_{wy} , respectively. Distribution functions g_1 , g_2 , g_5 , g_6 , g_8 and the density ρ_w are unknown.

Below we list the equations which should be solved in order to obtain the desired unknowns at the SW corner:

$$\rho_w = \rho_{NBR} \quad (5.27)$$

$$g_1 = g_3 + (g_1^{eq} - g_3^{eq}) \quad (5.28)$$

$$g_2 = g_4 + (g_2^{eq} - g_4^{eq}) \quad (5.29)$$

$$g_5 - g_6 + g_8 = g_3 + g_7 - g_1 + \rho_w U_{wx} - \frac{\Delta t}{2} F_x^C \quad (5.30)$$

$$g_5 + g_6 - g_8 = g_4 + g_7 - g_2 + \rho_w U_{wy} - \frac{\Delta t}{2} F_y^C \quad (5.31)$$

$$g_5 = \frac{(g_5 - g_6 + g_8) + (g_5 + g_6 - g_8)}{2} \quad (5.32)$$

$$g_6 - g_8 = (g_5 + g_6 - g_8) - g_5 \quad (5.33)$$

$$g_6 + g_8 = \rho_w - (g_0 + g_1 + g_2 + g_3 + g_4 + g_5 + g_7) \quad (5.34)$$

$$g_6 = \frac{(g_6 + g_8) + (g_6 - g_8)}{2} \quad (5.35)$$

$$g_8 = \frac{(g_6 + g_8) - (g_6 - g_8)}{2} \quad (5.36)$$

5.2 Density boundary conditions in 2D

Let us consider a 2D case in which pressure (density) is to be specified on a boundary. For example, if a flow inlet BC is specified at a boundary via pressure (density) specification, then we know the density ρ_w and the tangential velocity U_{wx} at the boundary. (Usually, the tangential velocity of the fluid at a static inlet boundary is zero.) However, the normal velocity U_{wy} at the boundary is an unknown.

In the following sections, methodology to obtain unknowns at the South boundary and the SW corner is presented. Relations for unknowns at the rest of the boundaries are provided in Appendix D.

5.2.1 South boundary

At the South boundary, we need to enforce the fluid to have its x -velocity and density equal to U_{wx} and ρ_w , respectively. As shown in Fig. 5.2, there are three unknown distribution functions (g_2 , g_5 and g_6) at each lattice site on the South boundary in the post-streaming state. In addition, the y -directional velocity of the fluid (U_{wy}) is also an unknown. Therefore, there are a total of 4 unknowns which need to be determined.

Mass Conservation:

$$\rho_w = g_0 + g_1 + g_2 + g_3 + g_4 + g_5 + g_6 + g_7 + g_8 \quad (5.37)$$

Momentum Conservation:

$$\rho_w U_{wx} = (g_1 + g_5 + g_8) - (g_3 + g_6 + g_7) + \frac{\Delta t}{2} F_x^C \quad (5.38)$$

$$\rho_w U_{wy} = (g_2 + g_5 + g_6) - (g_4 + g_7 + g_8) + \frac{\Delta t}{2} F_y^C \quad (5.39)$$

As a closure condition, we assume that upon streaming, the non-equilibrium part of the outgoing distribution functions normal to the boundary, i.e. $(g_4 - g_4^{eq})$ simply bounces back into the domain to give the non-equilibrium part of g_2 , i.e.

$$g_2 - g_2^{eq} = g_4 - g_4^{eq} \quad (5.40)$$

Below are listed all the equations which should be solved in order to obtain the desired unknowns at the South boundary:

$$U_{wy} = \left\{ g_0 + g_1 + g_3 + 2(g_4 + g_7 + g_8) - \frac{\Delta t}{2} F_y^C - \rho_w \right\} / (-\rho_w) \quad (5.41)$$

$$g_2 = g_4 + (g_2^{eq} - g_4^{eq}) \quad (5.42)$$

$$g_5 - g_6 = (g_3 + g_7) - (g_1 + g_8) + \rho_w U_{wx} - \frac{\Delta t}{2} F_x^C \quad (5.43)$$

$$g_5 + g_6 = g_4 + g_7 + g_8 - g_2 + \rho_w U_{wy} - \frac{\Delta t}{2} F_y^C \quad (5.44)$$

$$g_5 = \frac{(g_5 + g_6) + (g_5 - g_6)}{2} \quad (5.45)$$

$$g_6 = \frac{(g_5 + g_6) - (g_5 - g_6)}{2} \quad (5.46)$$

5.2.2 South-West (SW) corner

As mentioned earlier, since there are more unknowns at the corners than the nodes on the straight boundaries, a special treatment is required to handle BCs at the corners. For example, at the SW node, we have 6 unknowns (ρ_w , g_1 , g_2 , g_5 , g_6 and g_8) which need to be determined (see Fig. 5.3).

Mass Conservation:

$$\rho_w = g_0 + g_1 + g_2 + g_3 + g_4 + g_5 + g_6 + g_7 + g_8 \quad (5.47)$$

Momentum Conservation:

$$\rho_w U_{wx} = (g_1 + g_5 + g_8) - (g_3 + g_6 + g_7) + \frac{\Delta t}{2} F_x^C \quad (5.48)$$

$$\rho_w U_{wy} = (g_2 + g_5 + g_6) - (g_4 + g_7 + g_8) + \frac{\Delta t}{2} F_y^C \quad (5.49)$$

Next, we assume that upon streaming, the non-equilibrium part of the distribution function normal to the SW node and directed into the boundaries, i.e. $(g_3 - g_3^{eq})$ and $(g_4 - g_4^{eq})$ simply bounces back into the domain to give the non-equilibrium part of g_1 and g_2 , respectively, i.e.

$$g_1 - g_1^{eq} = g_3 - g_3^{eq} \quad (5.50)$$

$$g_2 - g_2^{eq} = g_4 - g_4^{eq} \quad (5.51)$$

Notice that we only have 5 equations to determine 6 unknowns. Therefore, in order to close the system, we have used Zou and He (1997) approximation, by which the density at the SW node ρ_w is assumed to be equal to the density at the nearest neighboring flow node ρ_{NBR} , i.e. $\rho_w = \rho_{NBR}$

Below are listed all the equations which should be solved in order to obtain the desired unknowns at the SW corner:

$$\rho_w = \rho_{NBR} \quad (5.52)$$

$$g_1 = g_3 + (g_1^{eq} - g_3^{eq}) \quad (5.53)$$

$$g_2 = g_4 + (g_2^{eq} - g_4^{eq}) \quad (5.54)$$

$$g_5 - g_6 + g_8 = g_3 + g_7 - g_1 + \rho_w U_{wx} - \frac{\Delta t}{2} F_x^C \quad (5.55)$$

$$g_5 + g_6 - g_8 = g_4 + g_7 - g_2 + \rho_w U_{wy} - \frac{\Delta t}{2} F_y^C \quad (5.56)$$

$$g_5 = \frac{(g_5 - g_6 + g_8) + (g_5 + g_6 - g_8)}{2} \quad (5.57)$$

$$g_6 - g_8 = (g_5 + g_6 - g_8) - g_5 \quad (5.58)$$

$$g_6 + g_8 = \rho_w - (g_0 + g_1 + g_2 + g_3 + g_4 + g_5 + g_7) \quad (5.59)$$

$$g_6 = \frac{(g_6 + g_8) + (g_6 - g_8)}{2} \quad (5.60)$$

$$g_8 = \frac{(g_6 + g_8) - (g_6 - g_8)}{2} \quad (5.61)$$

5.3 Velocity boundary conditions in 3D

In 3D, there are four macroscopic physical properties that can be specified at the boundaries of a domain: fluid density, normal velocity and two components of tangential velocity. The normal velocity is zero for solid walls and nonzero for porous walls. For no-slip boundaries, the tangential velocity is usually the same as the velocity of the moving wall. There are 6 surface boundaries, 12 edge boundaries and 8 corners in the 3D computational domain. The fluid is confined with the West ($x = 0$), East ($x = L_x$), South ($y = 0$), North ($y = L_y$), Bottom ($z = 0$) and Top ($z = 0$) surface boundaries, as shown in Fig. 5.4. Computational grid is chosen such that the nodes lie on the surface boundaries and the corners.

For 3D simulations, a D_3Q_{19} lattice structure is used in this report (one may choose other lattice structures, for example, D_3Q_{15} or D_3Q_{24}). As shown in Fig. 4.1(b), the D_3Q_{19} lattice has 18 velocity vectors linking it with the neighboring nodes, and a null link (or rest state). Out of these 18 links, 6 are orthogonal links which point to the nearest neighbors (and have speed 1) and 12 are diagonal links which point to the next-nearest neighbors (and have speed $\sqrt{2}$). Lattice velocities in different directions are listed in Table 4.2 for the D_3Q_{19} lattice. Due to the symmetry of the lattice in LBM, directional links always come in pairs i.e. each link has a partner which points into the opposite direction. Such pairs are listed in Table 5.2 for the D_3Q_{19} lattice.

In order to apply velocity BCs on the surface boundaries, 6 unknowns including the density need to be determined. However, we only have 4 equations (1 for mass conservation, 1 each for x -, y - and z -momentum). Therefore, in 3D formulation of velocity BCs, an approach different from its 2D counterpart is considered. Here, the number of unknowns is

reduced to 4 by assuming the partial bounce-back of the non-equilibrium distribution functions at the boundaries and, satisfying the mass and momentum constraints.

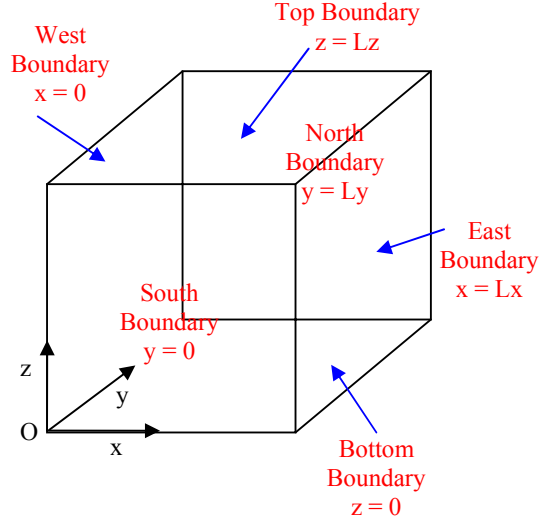


Fig. 5.4: Three-dimensional (3D) computational domain. There are 6 surface boundaries, 12 edge boundaries and 8 corners in a 3D domain. The fluid is enclosed by West ($x = 0$), East ($x = Lx$), South ($y = 0$), North ($y = Ly$), Bottom ($z = 0$) and Top ($z = Lz$) surface boundaries. Computational grid is chosen such that the nodes lie on the surface boundaries as well as on all the corners.

Table 5.2: Directional pairs having opposite lattice velocities (a, \bar{a}) for the D_3Q_{19} lattice.

a	\bar{a}	a	\bar{a}
1	2	10	8
2	1	11	13
3	4	12	14
4	3	13	11
5	6	14	12
6	5	15	17
7	9	16	18
8	10	17	15
9	7	18	16

In the following section, a methodology to obtain unknowns at the Bottom boundary is presented. Relations for unknowns at the rest of the boundaries are provided in Appendix E.

5.3.1 Bottom boundary

Unknowns:

$\rho_w, g_5, g_{11}, g_{14}, g_{15}$ and g_{18}

Mass conservation:

$$\rho_w = \sum_{a=0}^{18} g_a \quad (5.62)$$

Momentum conservation:

$$\rho_w U_{wx} = (g_1 + g_7 + g_{10} + g_{11} + g_{12}) - (g_2 + g_8 + g_9 + g_{13} + g_{14}) + \frac{\Delta t}{2} F_x^C \quad (5.63)$$

$$\rho_w U_{wy} = (g_3 + g_7 + g_8 + g_{15} + g_{16}) - (g_4 + g_9 + g_{10} + g_{17} + g_{18}) + \frac{\Delta t}{2} F_y^C \quad (5.64)$$

$$\rho_w U_{wz} = (g_5 + g_{11} + g_{14} + g_{15} + g_{18}) - (g_6 + g_{12} + g_{13} + g_{16} + g_{17}) + \frac{\Delta t}{2} F_z^C \quad (5.65)$$

From equations (5.62) and (5.65):

$$\rho_w = \frac{1}{(1 - U_{wz})} \left\{ \begin{array}{l} g_0 + g_1 + g_2 + g_3 + g_4 + g_7 + g_8 + g_9 + g_{10} \\ + 2(g_6 + g_{12} + g_{13} + g_{16} + g_{17}) - \frac{\Delta t}{2} F_z^C \end{array} \right\} \quad (5.66)$$

Now, let us assume that the outgoing non-equilibrium distribution functions $(g_{\bar{a}} - g_{\bar{a}}^{eq}, \bar{a} = 6, 12, 13, 16, 17)$ partially bounce back at the boundary to provide the corresponding incoming non-equilibrium distribution functions $(g_a - g_a^{eq}, a = 5, 14, 11, 18, 15)$ (see Table 5.4 for the number of the corresponding distribution function) with the 3 new unknowns $(\delta_x, \delta_y, \delta_z)$ as:

$$(g_5 - g_5^{eq}) = (g_6 - g_6^{eq}) + v_{5,x} \delta_x + v_{5,y} \delta_y + v_{5,z} \delta_z \quad (5.67)$$

$$(g_{11} - g_{11}^{eq}) = (g_{13} - g_{13}^{eq}) + v_{11,x} \delta_x + v_{11,y} \delta_y + v_{11,z} \delta_z \quad (5.68)$$

$$(g_{14} - g_{14}^{eq}) = (g_{12} - g_{12}^{eq}) + v_{14,x} \delta_x + v_{14,y} \delta_y + v_{14,z} \delta_z \quad (5.69)$$

$$(g_{15} - g_{15}^{eq}) = (g_{17} - g_{17}^{eq}) + v_{15,x} \delta_x + v_{15,y} \delta_y + v_{15,z} \delta_z \quad (5.70)$$

$$(g_{18} - g_{18}^{eq}) = (g_{16} - g_{16}^{eq}) + v_{18,x} \delta_x + v_{18,y} \delta_y + v_{18,z} \delta_z \quad (5.71)$$

The above equations can be rewritten after substituting corresponding lattice velocities from the Table 5.3, as:

$$g_5 = g_6 + (g_5^{eq} - g_6^{eq}) + \delta_z \quad (5.72)$$

$$g_{11} = g_{13} + (g_{11}^{eq} - g_{13}^{eq}) + \delta_x + \delta_z \quad (5.73)$$

$$g_{14} = g_{12} + (g_{14}^{eq} - g_{12}^{eq}) - \delta_x + \delta_z \quad (5.74)$$

$$g_{15} = g_{17} + (g_{15}^{eq} - g_{17}^{eq}) + \delta_y + \delta_z \quad (5.75)$$

$$g_{18} = g_{16} + (g_{18}^{eq} - g_{16}^{eq}) - \delta_y + \delta_z \quad (5.76)$$

From equations (5.73) and (5.74),

$$(g_{11} - g_{13}) - (g_{14} - g_{12}) = (g_{11}^{eq} - g_{13}^{eq}) - (g_{14}^{eq} - g_{12}^{eq}) + 2\delta_x \quad (5.77)$$

From equations (5.75) and (5.76),

$$(g_{15} - g_{17}) - (g_{18} - g_{16}) = (g_{15}^{eq} - g_{17}^{eq}) - (g_{18}^{eq} - g_{16}^{eq}) + 2\delta_y \quad (5.78)$$

From equations (5.63) and (5.77),

$$\begin{aligned} \rho_w U_{wx} = & (g_1 + g_7 + g_{10}) - (g_2 + g_8 + g_9) + \frac{\Delta t}{2} F_x^C \\ & + (g_{11}^{eq} - g_{13}^{eq}) - (g_{14}^{eq} - g_{12}^{eq}) + 2\delta_x \end{aligned} \quad (5.79)$$

From equations (5.64) and (5.78),

$$\begin{aligned} \rho_w U_{wy} = & (g_3 + g_7 + g_8) - (g_4 + g_9 + g_{10}) + \frac{\Delta t}{2} F_y^C \\ & + (g_{15}^{eq} - g_{17}^{eq}) - (g_{18}^{eq} - g_{16}^{eq}) + 2\delta_y \end{aligned} \quad (5.80)$$

From equations (5.65) and (5.72)-(5.76),

$$\begin{aligned} \rho_w U_{wz} = & (g_5^{eq} + g_{11}^{eq} + g_{14}^{eq} + g_{15}^{eq} + g_{18}^{eq}) \\ & - (g_6^{eq} + g_{12}^{eq} + g_{13}^{eq} + g_{16}^{eq} + g_{17}^{eq}) + \frac{\Delta t}{2} F_z^C + 5\delta_z \end{aligned} \quad (5.81)$$

Rearranging equations (5.79), (5.80) and (5.81), we can write the three unknowns as:

$$\delta_x = \frac{1}{2} \left\{ \begin{aligned} & \rho_w U_{wx} - (g_1 + g_7 + g_{10}) + (g_2 + g_8 + g_9) - \frac{\Delta t}{2} F_x^C \\ & - (g_{11}^{eq} - g_{13}^{eq}) + (g_{14}^{eq} - g_{12}^{eq}) \end{aligned} \right\} \quad (5.82)$$

$$\delta_y = \frac{1}{2} \left\{ \rho_w U_{wy} - (g_3 + g_7 + g_8) + (g_4 + g_9 + g_{10}) - \frac{\Delta t}{2} F_y^C \right. \\ \left. - (g_{15}^{eq} - g_{17}^{eq}) + (g_{18}^{eq} - g_{16}^{eq}) \right\} \quad (5.83)$$

$$\delta_z = \frac{1}{5} \left\{ \rho_w U_{wz} - (g_5^{eq} + g_{11}^{eq} + g_{14}^{eq} + g_{15}^{eq} + g_{18}^{eq}) \right. \\ \left. + (g_6^{eq} + g_{12}^{eq} + g_{13}^{eq} + g_{16}^{eq} + g_{17}^{eq}) - \frac{\Delta t}{2} F_z^C \right\} \quad (5.84)$$

5.4 Future directions of research

In the context of lattice Boltzmann models, a variety of “radically” different approaches are presently in use for simulating velocity and density boundary conditions for single- and two-phase flows. A consensus has not yet reached on the choice of appropriate boundary conditions. A unification of these approaches is required in order to standardize the procedure as well as for enhancing the numerical accuracy. Recently, Latt and Chopard (2008) reviewed and compared five of such different boundary treatments for different benchmark problems. They divided the boundary conditions into two broader categories, one which preserves the known particle populations (Inamuro et al. (1995), Zou & He (1997)) and the other which replaces all the particle populations (regularized, finite difference and non-linear finite difference based, see Latt & Chopard (2008)) at the boundary nodes. Moreover, many of these different boundary conditions are only tested for the single-phase flows and their applicability to different two-phase models still needs to be established.

Since most of the practical applications involve geometries which can not be fitted by a rectangular grid (such as, curved pipes and other irregular shapes), there is a need to develop boundary treatments for such non-rectangular geometries. The simplest approach to model such arbitrary boundaries is to replace the boundaries with the zigzagging contours which follow the rectangular grid in a staircase fashion. However, the accuracy of near-boundary flow may be deteriorated by the artificial staircases. An extrapolation method for treating curved boundaries is proposed in Guo et al. (2002). The distribution function at the grid point nearest to the (physical) curved boundary is decomposed into equilibrium and non-equilibrium parts. The non-equilibrium part is approximated by that of the neighboring fluid node along the link, and the equilibrium part is determined by a fictitious equilibrium

distribution function. This treatment results in second-order accuracy and good stability characteristics (Guo et al. (2002)).

5.5 References

Bao, J., Yuan, P., Schaefer, L., 2008. A mass conserving boundary condition for the lattice Boltzmann equation method. *J. Comp. Phys.* 227, 8472-8487.

Chopard, B., Dupuis, A., 2003. A mass conserving boundary condition for lattice Boltzmann models. *Int. J. Mod. Phys. B* 17, 103-107.

Guo, Z., Zheng, C., Shi., B., 2002. An extrapolation method for boundary conditions in lattice Boltzmann method, *Phys. Fluids* 14, 2007.

Ginzbourg, I., Adler, P.M., 1994. Boundary flow condition analysis for the three-dimensional lattice Boltzmann model, *J. Phys. II France* 4, 191-214.

He, X., Zou, Q., Luo, L.S., Dembo, M., 1997. Analytic solutions of simple flows and analysis of nonslip boundary conditions for the lattice Boltzmann BGK model. *J. Stat. Phys.* 87, 115-136.

Inamuro, T., Yoshino, M., Ogino, F., 1995. A non-slip boundary condition for lattice Boltzmann simulations, *Phys. Fluids* 7(12), 2928-2930.

Latt, J., Chopard, B., 2008. Straight velocity boundaries in the lattice Boltzmann method, *Phy. Rev. E* 77, 056703.

Lallemand, P., Luo, L.S., 2003. Lattice Boltzmann method for moving boundaries. *J. Comp. Phys.* 184, 406-421.

Lavallee, P., Boon, J.P., Noullez, A., 1991. Boundaries in lattice gas flows, *Physica D* 47, 233-240.

Maier, R.S., Bernard, R.S., Grunau, D.W., 1996. Boundary conditions for the lattice Boltzmann method, *Phys. Fluids* 8(7), 1788-1801.

Noble, D.R., Chen, S., Georgiadis, J.G., Buckius, R.O., 1994. A consistent hydrodynamic boundary condition for the lattice Boltzmann model, *Phys. Fluids* 7(1), 203-209.

Skordos, P.A., 1993. Initial and boundary conditions for the lattice Boltzmann method, *Phys. Rev. E* 48(6), 4823-4841.

Sofonea, V., Sekerka, R.F., 2005. Boundary conditions for the upwind finite difference lattice Boltzmann model: Evidence of slip velocity in micro-channel flow. *J. Comp. Phys.* 207, 639-659.

Sukop, M.C., Thorne, D.T., 2006. *Lattice Boltzmann Modeling—An Introduction for Geoscientists and Engineers*. Springer-Verlag Berlin Heidelberg.

Succi, S., 2001. *The Lattice Boltzmann Equation—for Fluid Dynamics and Beyond*. Oxford Science Publications, UK.

Wolf-Gladrow D.A., 2000. *Lattice-Gas Cellular Automata and Lattice Boltzmann Models. Lecture Notes in Mathematics*. Springer.

Zhang, X., Crawford, J.W., Bengough, A.G., Young, I.M., 2002. On boundary conditions in the lattice Boltzmann model for advection and anisotropic dispersion equation. *Adv. Water Resources* 25, 601-609.

Zou, Q. and He, X., 1997. On pressure and velocity boundary conditions for the lattice Boltzmann BGK model, *Phys. Fluids* 9, 1591.

Chapter 6

Results and discussions

In this chapter, simulation results for several two phase scenarios using the artificial interface lattice Boltzmann (AILB) model and the Lee-Fischer model (Lee & Fischer, 2006) are presented. An appropriate model has been chosen depending upon the problem being simulated. Simulations, in which body force (like, gravity) plays a significant role in the dynamics, AILB model is preferred to eliminate the artificial compressibility enhancements found in the Lee-Fischer model. A comparison with the available analytical and/or experimental results has also been provided.

6.1 Multi-fluid Poiseuille-Couette flow in a 2D channel

6.1.1 Analytical solution

For a three-layer Poiseuille-Couette flow in a two-dimensional (2D) channel as shown in Fig. 6.1, the governing equations and the boundary/interface conditions can be written as follows:

Governing equations:

$$\frac{d^2 u_{y1}(x)}{dx^2} = -\frac{\rho_1 g}{\mu_1} \quad (6.1)$$

$$\frac{d^2 u_{y2}(x)}{dx^2} = -\frac{\rho_2 g}{\mu_2} \quad (6.2)$$

$$\frac{d^2 u_{y3}(x)}{dx^2} = -\frac{\rho_3 g}{\mu_3} \quad (6.3)$$

where $u_{yi}(x)$, ρ_i and μ_i are the y -directional velocity, density and dynamic viscosity of the i^{th} layer respectively ($i = 1, 2$ and 3) and g represents acceleration due to gravity.

Boundary conditions:

$$u_{y1}(x = 0) = U_{w1} \quad (6.4)$$

$$u_{y3}(x = L_x) = U_{w2} \quad (6.5)$$

where U_{w1} and U_{w2} are the velocities with which the left and the right walls are moving in the direction opposite to gravity. $x = 0$ and $x = L_x$ are the domain boundaries in the x -direction. Domain is assumed to be periodic in the y -direction.

Interface conditions:

$$u_{y1}(x = x_1) = u_{y2}(x = x_1) \quad (6.6)$$

$$\mu_1 \frac{du_{y1}}{dx} \bigg|_{x=x_1} = \mu_2 \frac{du_{y2}}{dx} \bigg|_{x=x_1} \quad (6.7)$$

$$u_{y2}(x = x_2) = u_{y3}(x = x_2) \quad (6.8)$$

$$\mu_2 \frac{du_{y2}}{dx} \bigg|_{x=x_2} = \mu_3 \frac{du_{y3}}{dx} \bigg|_{x=x_2} \quad (6.9)$$

where $x = x_1$ and $x = x_2$ are the locations of the fluid interfaces.

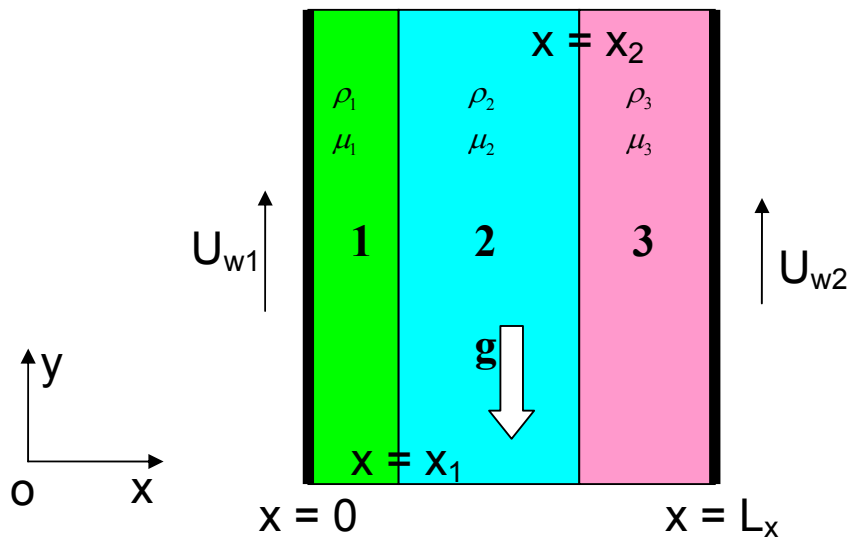


Fig. 6.1: Poiseuille-Couette flow in a two-dimensional (2D) channel. Three layers of different fluids are denoted by 1, 2 and 3, which have densities ρ_1 , ρ_2 , ρ_3 and dynamic viscosities μ_1 , μ_2 , μ_3 , respectively. The Poiseuille effect of flow is governed by the downward gravity g whose effect is equivalent to applying a constant pressure difference across y -boundaries and, the Couette effect is governed by two enclosing walls moving with the upward velocities U_{w1} and U_{w2} .

Integrating equations (6.1), (6.2) and (6.3) gives:

$$u_{y1}(x) = -\frac{\rho_1 g}{2\mu_1} x^2 + c_{11}x + c_{12} \quad (6.10)$$

$$u_{y2}(x) = -\frac{\rho_2 g}{2\mu_2} x^2 + c_{21}x + c_{22} \quad (6.11)$$

$$u_{y3}(x) = -\frac{\rho_3 g}{2\mu_3} x^2 + c_{31}x + c_{32} \quad (6.12)$$

Now, we have 6 unknowns (c_{11} , c_{12} , c_{21} , c_{22} , c_{31} and c_{32} : two for each fluid layer) and 6 equations (2 boundary conditions and 4 interface conditions).

From equation (6.4),

$$c_{12} = U_{w1} \quad (6.13)$$

From equation (6.5),

$$c_{31}L_x + c_{32} = \frac{\rho_3 g}{2\mu_3} L_x^2 + U_{w2} \quad (6.14)$$

From equation (6.7),

$$\mu_1 c_{11} - \mu_2 c_{21} = (\rho_1 - \rho_2) g x_1 \quad (6.15)$$

From equation (6.9),

$$\mu_2 c_{21} - \mu_3 c_{31} = (\rho_2 - \rho_3) g x_2 \quad (6.16)$$

From equation (6.6),

$$c_{11}x_1 + c_{12} - c_{21}x_1 - c_{22} = \left(\frac{\rho_1}{\mu_1} - \frac{\rho_2}{\mu_2} \right) \frac{gx_1^2}{2} \quad (6.17)$$

From equation (6.8),

$$c_{21}x_2 + c_{22} - c_{31}x_2 - c_{32} = \left(\frac{\rho_2}{\mu_2} - \frac{\rho_3}{\mu_3} \right) \frac{gx_2^2}{2} \quad (6.18)$$

We can determine our unknowns by solving the above equations as:

$$\begin{pmatrix} c_{11} \\ c_{12} \\ c_{21} \\ c_{22} \\ c_{31} \\ c_{32} \end{pmatrix} = \begin{pmatrix} 0 & 1 & 0 & 0 & 0 & 0 \\ 0 & 0 & 0 & 0 & L_x & 1 \\ \mu_1 & 0 & -\mu_2 & 0 & 0 & 0 \\ 0 & 0 & \mu_2 & 0 & -\mu_3 & 0 \\ x_1 & 1 & -x_1 & -1 & 0 & 0 \\ 0 & 0 & x_2 & 1 & -x_2 & -1 \end{pmatrix}^{-1} \begin{pmatrix} U_{w1} \\ 0.5(\rho_3/\mu_3)gL_x^2 + U_{w2} \\ (\rho_1 - \rho_2)gx_1 \\ (\rho_2 - \rho_3)gx_2 \\ 0.5(\rho_1/\mu_1 - \rho_2/\mu_2)gx_1^2 \\ 0.5(\rho_2/\mu_2 - \rho_3/\mu_3)gx_2^2 \end{pmatrix} \quad (6.19)$$

Above matrix equation (6.19) can easily be solved using Mathematica package for the unknowns.

6.1.2 LBM simulations

In LBM simulations, kinematic viscosities ν of different fluids are related to their corresponding relaxation times τ by:

$$\nu_1 = \frac{\mu_1}{\rho_1} = \tau_1 RT \quad (6.20)$$

$$\nu_2 = \frac{\mu_2}{\rho_2} = \tau_2 RT \quad (6.21)$$

$$\nu_3 = \frac{\mu_3}{\rho_3} = \tau_3 RT \quad (6.22)$$

where RT is a lattice constant and for the D_2Q_9 as well as the D_3Q_{19} lattices, given by:

$$RT = \frac{1}{3} \quad (6.23)$$

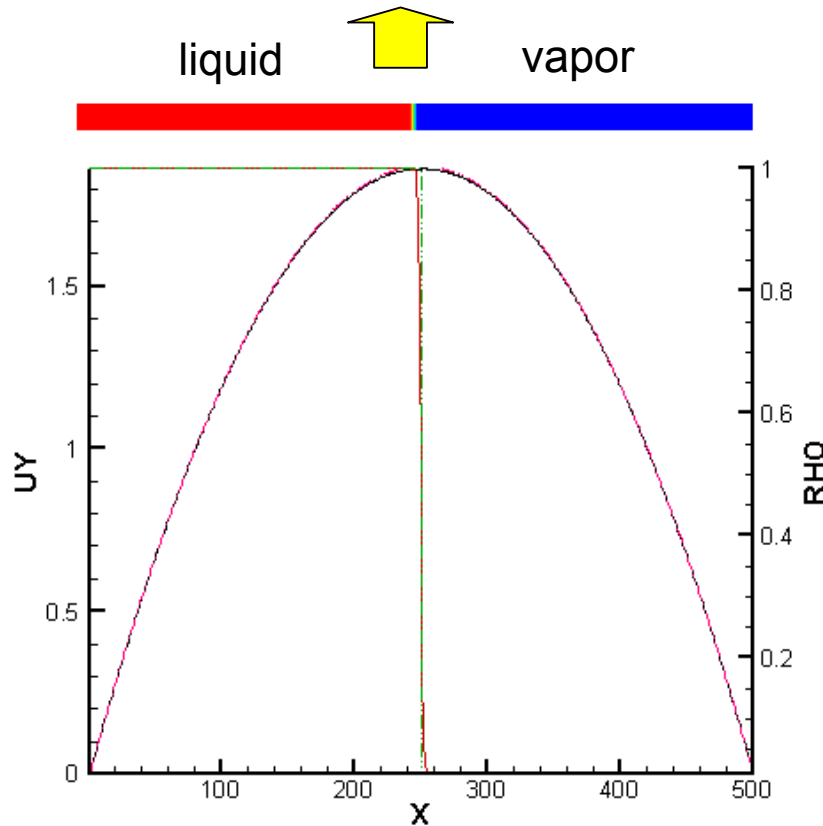
With the above relations between the relaxation time and the dynamic viscosity of a given fluid in hand, one can compare the LBM simulation results (such as, the steady state velocity profile in a 2D channel) for the Poiseuille-Couette flow with the results analytically.

6.1.3 Results obtained using the Lee-Fischer LB model

In Fig. 6.2, we compare the LBM results obtained using the Lee-Fischer model with the analytical solutions for a two-layer Poiseuille flow. Simulation parameters are given in the figure caption. Gravity is used as a buoyancy force in the simulations. A good agreement between the simulation results and the analytical solution is observed for the y -directional fluid velocity. Notice that it took about 2 million time-steps for the simulation to provide the steady state results on a LBM grid of 500 x 25 points. The grid requirement in the y -direction

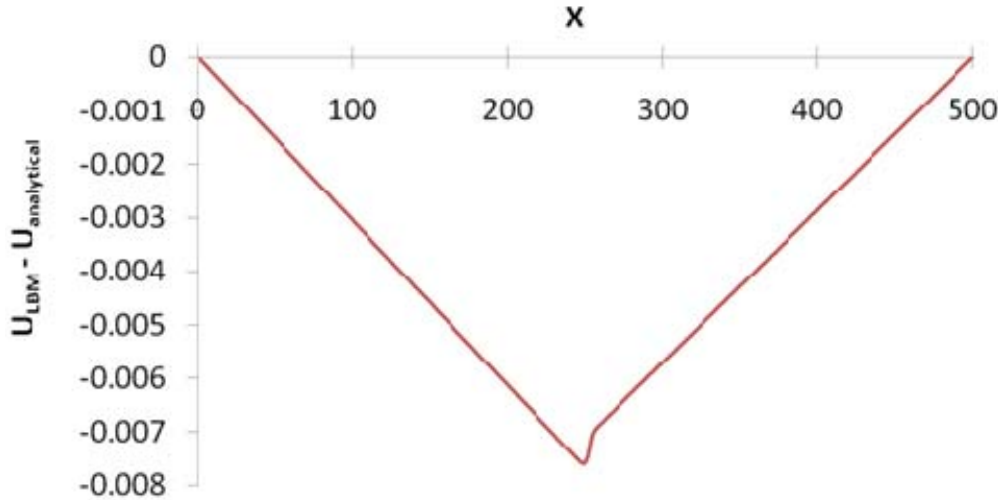
is not very restrictive since periodicity is being used in that direction. However, one should use a large number of grid points in the direction perpendicular to the interface i.e. x -direction for these simulations. From numerical experiments, it is clear that, not surprisingly, the solution accuracy depends upon the number of grid points in the direction perpendicular to the interface. Obviously using a large number of grid points make the simulation take longer to reach the steady state in a LBM simulation, however, it leads to a more accurate steady state solution.

In Fig. 6.3, the LBM results are compared against those obtained using the analytical solutions for a two-layer Couette flow problem. Simulation parameters are given in the figure caption. Gravity is assumed to be zero in the simulations. The driving force is provided by the left wall moving with an upward velocity of $U_w = 0.1$. Good agreement between the simulation results and the analytical solution is observed for the y -directional fluid velocity. 500 x 25 grid points are used in the LB simulation.

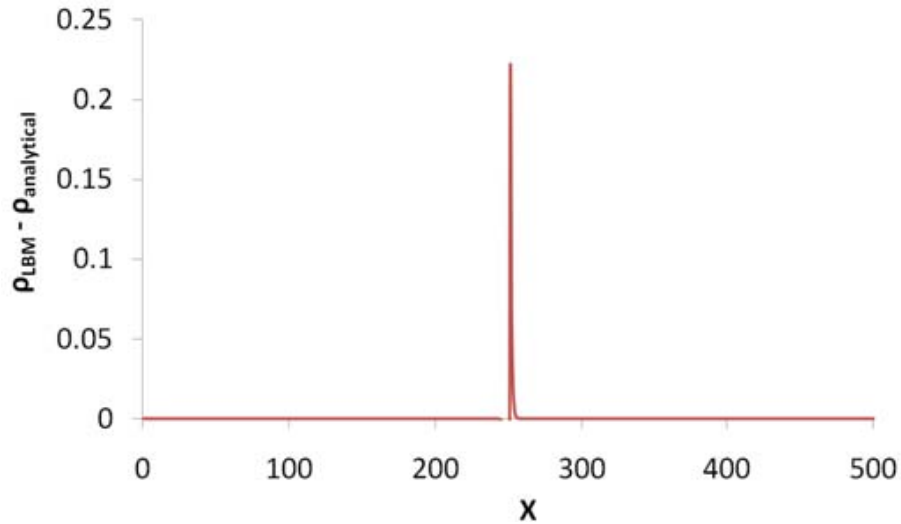


(a) A comparison of steady state LBM simulation results with the analytical solution.

Fig. 6.2 (cont. on next page)

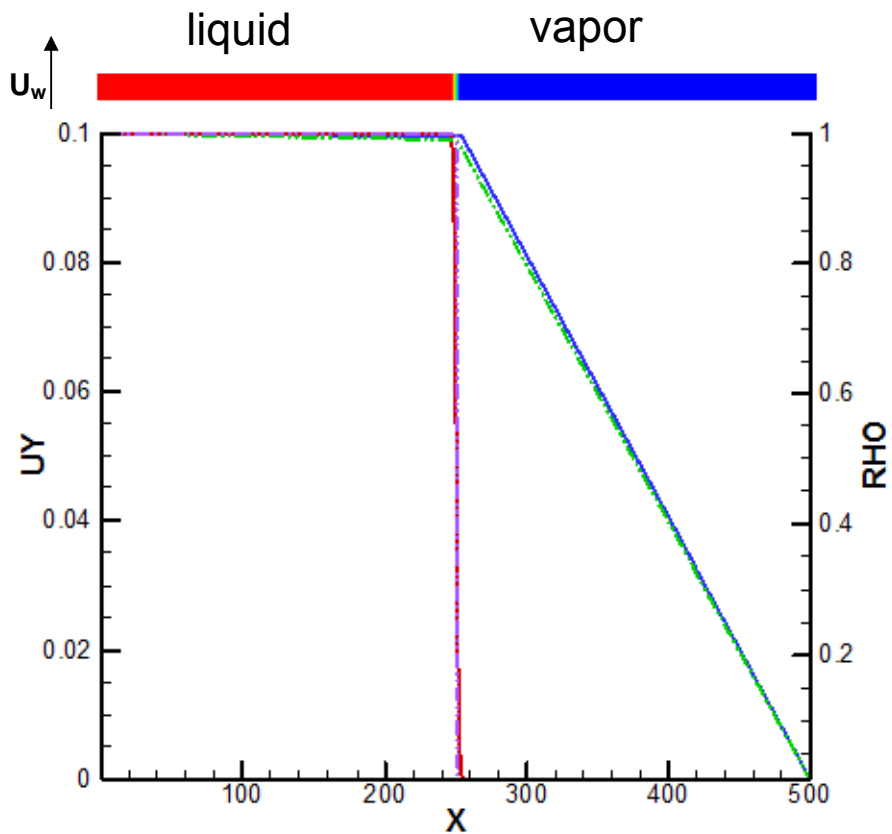


(b) Difference in LBM prediction of upward velocity compared to the exact solution.

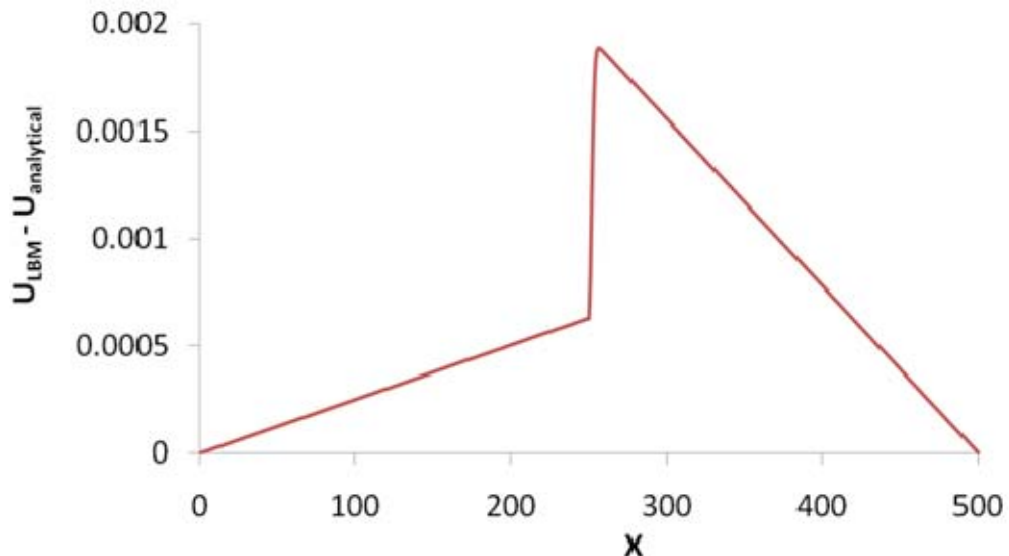


(c) LBM and exact density profiles differ due to diffuse interface in the LB simulation.

Fig. 6.2: The Poiseuille flow in a two-dimensional channel of size 500×25 . The channel is periodic in the y -direction. Layers of liquid and vapor phases are driven by a body force acting in the upward direction. No slip boundary condition is applied at the side walls in the x -direction. The simulation parameters are: $\rho_l = 1$, $\rho_v = 0.01$, body force = 10^{-5} . Kinematic viscosities of both the fluids are assumed to be equal. This is enforced by choosing the same relaxation parameter (equals to 0.5) for both the fluids. The LBM simulation (Lee-Fischer LB model) results for the steady state (at $t = 2 \times 10^6$) density ρ and upward velocity u_y are in very good agreement with the corresponding analytical solutions.

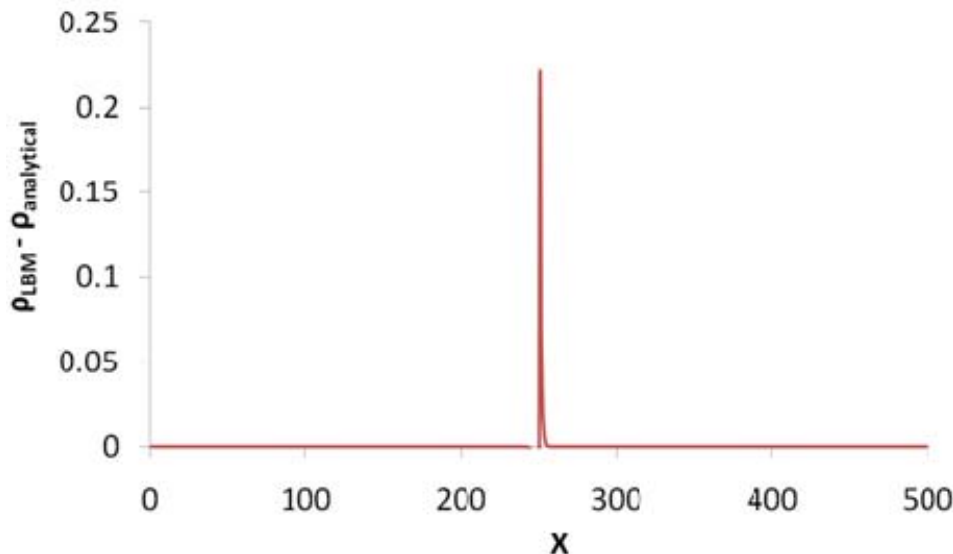


(a) A comparison of steady state LBM simulation results with the analytical solution.



(b) Difference in LBM prediction of upward velocity compared to the exact solution.

Fig. 6.3 (cont. on next page)



(c) LBM and exact density profiles differ due to diffuse interface in the LB simulation.

Fig. 6.3: The Couette flow in a two-dimensional channel of size 500 x 25. The channel is periodic in the y -direction. Layers of liquid and vapor phases are driven by moving the left wall with a velocity U_w . No slip boundary condition is applied at the side walls in the x -direction. The simulation parameters are: $\rho_l = 1$, $\rho_v = 0.01$, $U_w = 0.1$. Kinematic viscosities of both the fluids are assumed to be equal. This is enforced by choosing the same relaxation parameter (equals to 0.5) for both the fluids.

6.2 Simulation of the van der Waals coexistence curve

The van der Waals equation of state (vdW EOS) is as follows:

$$P = \frac{\rho RT}{1 - b\rho} - a\rho^2 \quad (6.24)$$

where a and b are the van der Waals constants.

In order to explicitly show the dependence on molar volume V , we can rewrite the above equation by substituting $\rho = 1/V$ as:

$$P = \frac{RT}{V - b} - \frac{a}{V^2} \quad (6.25)$$

The above equation can be written in a cubic form as:

$$V^3 - \left(b + \frac{RT}{P} \right) V^2 + \frac{a}{P} V - \frac{ab}{P} = 0 \quad (6.26)$$

Being a cubic equation, the above equation has three real roots V_1 , V_2 and V_3 for temperatures below the critical point. However, at the critical point, these three roots merge into one value called V_c . The parameters at the critical point are denoted by, $T = T_c$, $P = P_c$ and $V = V_c$.

Since the critical point is an inflection point, and the following two conditions can be used to determine the critical constants (P_c , V_c and T_c) in terms of van der Waals constants (a and b).

$$\left. \frac{\partial P}{\partial V} \right|_T = 0 \quad (6.27)$$

and

$$\left. \frac{\partial^2 P}{\partial V^2} \right|_T = 0 \quad (6.28)$$

A simpler approach to identify the critical constants is to write equation (6.26) at the critical point as:

$$(V - V_c)^3 = 0 \quad (6.29)$$

which essentially is:

$$V^3 - 3V_c V^2 + 3V_c^2 V - V_c^3 = 0 \quad (6.30)$$

Comparing coefficients in equations (6.26) and (6.30), we can write:

$$3V_c = b + \frac{RT_c}{P_c}, \quad 3V_c^2 = \frac{a}{P_c} \quad \text{and} \quad V_c^3 = \frac{ab}{P_c} \quad (6.31)$$

From the above set of equations, the critical constants (P_c , V_c and T_c) can be evaluated as:

$$V_c = 3b \quad (6.32)$$

$$P_c = \frac{a}{27b^2} \quad (6.33)$$

$$T_c = \frac{8a}{27bR} \quad (6.34)$$

From equation (6.32), the density at the critical point ρ_c can be written as:

$$\rho_c = \frac{1}{3b} \quad (6.35)$$

Substituting $a = 3P_c V_c^2$ and $b = V_c/3$ in equation(6.25), we get:

$$P = \frac{RT}{V - (V_c/3)} - \frac{3P_c}{(V/V_c)^2} \quad (6.36)$$

The above equation can be rearranged to give:

$$\left(\frac{P}{P_c}\right) = \frac{RT/P_c V_c}{(V/V_c) - (1/3)} - \frac{3}{(V/V_c)^2} \quad (6.37)$$

Now introducing reduced quantities $P_R = P/P_c$, $V_R = V/V_c$ and $T_R = T/T_c$, and substituting $P_c V_c = \frac{3}{8} RT_c$, we get the vdW equation of state in the reduced quantities:

$$P_R = \frac{(8/3)T_R}{V_R - (1/3)} - \frac{3}{V_R^2} \quad (6.38)$$

A typical van der Waals pressure-volume isotherm (variation of pressure P with volume V) is plotted in Fig. 6.4 for different values of temperature.

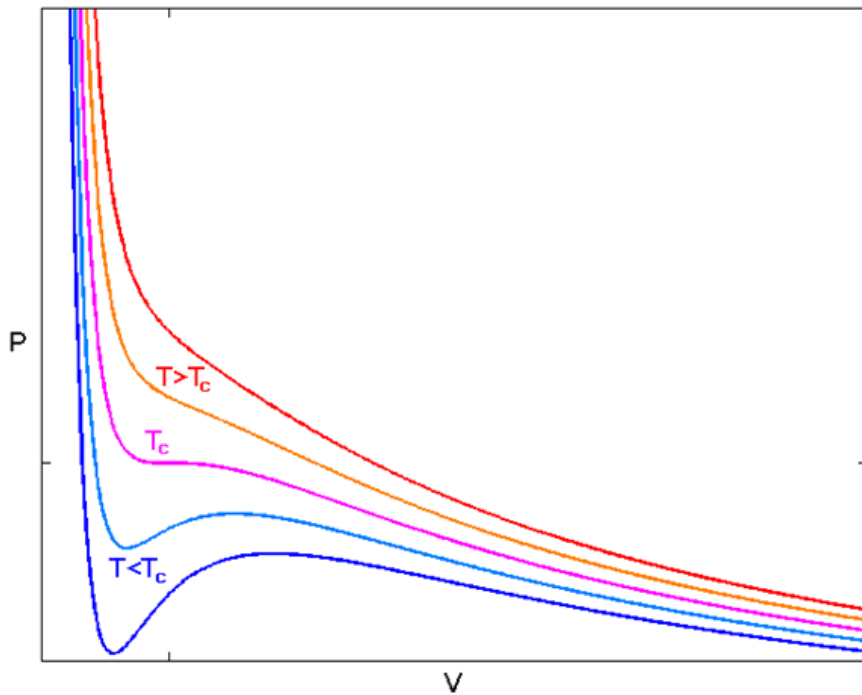


Fig. 6.4: van der Waals pressure-volume isotherms at different temperatures.

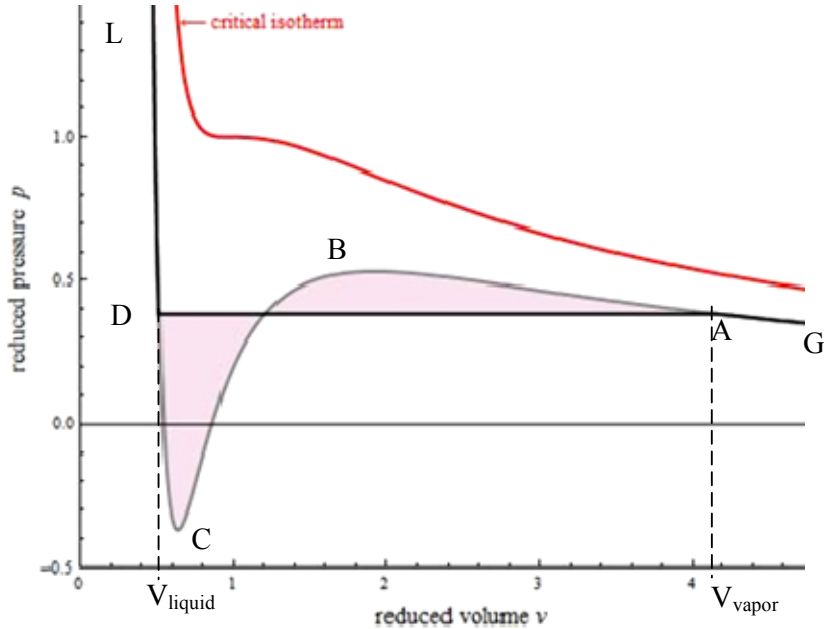


Fig. 6.5: Maxwell construction procedure. A typical van der Waals pressure-volume isotherm at a temperature less than the critical temperature is shown. The horizontal line is drawn such that the areas of the shaded part above and below the line drawn are equal. The pressure corresponding to the horizontal line is called the equilibrium pressure. Points where the ends of the horizontal line cross the P-V curve correspond to the liquid and vapor phases coexisting in equilibrium.

By choosing the following vdW constants:

$$a = \frac{9}{8}, \quad b = \frac{1}{3} \quad \text{and} \quad R = 1 \quad (6.39)$$

the critical parameters are found as:

$$\rho_c = 1, \quad T_c = 1 \quad \text{and} \quad P_c = \frac{3}{8} \quad (6.40)$$

and the vdW EOS becomes:

$$P = \frac{T}{V - (1/3)} - \frac{9}{8V^2} \quad (6.41)$$

Values of a and b given above will be used in the LBM simulations to reproduce the densities of the coexisting phases of a fluid. Having identified the governing non-ideal equation of state of a fluid, we can use Maxwell construction procedure to determine the density values at which both the phases of a fluid are in equilibrium.

6.2.1 Saturated liquid and vapour densities from Maxwell construction

A representation of the Maxwell equal-area construction procedure is shown in Fig. 6.5. On the P - V curve, an equilibrium pressure is identified by drawing a horizontal line DA such that the areas of the loops (enclosed areas) both above and below the DA line are equal. Along this line, liquid and vapor phases are in equilibrium with each other. Point A represents the coexisting vapor while point D represents the coexisting liquid. Corresponding volumes of the phases can be found by drawing vertical lines down to the x -axis from points A and D , as shown in the figure. The line DL represents the change in the volume of the liquid phase when compressed (or, increasing pressure). The steepness of this line shows the relative incompressibility of the liquid phase. The segment BC represents an unstable region, in which $(\partial P / \partial V)_T > 0$, i.e. an increase of pressure results in an increase in volume which is unphysical and not observed for equilibrium systems.

Table 6.1: Reduced variables for vdW EOS obtained via Maxwell construction.

$T_R = \frac{T}{T_C}$	$\rho_{liq,R} = \frac{\rho_{liq}}{\rho_C}$	$\rho_{vap,R} = \frac{\rho_{vap}}{\rho_C}$	$Ratio = \frac{\rho_{liq}}{\rho_{vap}}$	$P_R = \frac{P}{P_C}$
1	1	1	1	1
0.98	1.28943	0.726691	1.77	0.921912
0.95	1.46173	0.579015	2.52	0.811879
0.90	1.65727	0.425742	3.89	0.646998
0.85	1.80714	0.31973	5.65	0.504492
0.80	1.93271	0.239667	8.06	0.383362
0.75	2.04235	0.177209	11.53	0.282459
0.70	2.14044	0.128022	16.72	0.200458
0.65	2.2296	0.0894754	24.92	0.135841
0.60	2.31156	0.0597781	38.67	0.0868693
0.55	2.38755	0.03758	63.53	0.0515798
0.50	2.45849	0.0217468	113.05	0.0277887
0.45	2.5251	0.0112175	225.10	0.013134
0.40	2.58794	0.00491089	526.98	0.00517452
0.35	2.64749	0.00168746	1568.92	0.0015673
0.30	2.70416	0.000399065	6776.24	0.000318817

For the vdW EOS in reduced quantities (equation (6.38)), the Maxwell equal-area construction procedure is applied to identify the equilibrium phase densities. Results are tabulated in Table 6.1. A code has been written in Mathematica to calculate the coexisting densities and equilibrium pressure, details of which are provided in the Appendix F. Schemes for converting lattice units into physical units and vice-a-versa are discussed in the Appendix G.

6.2.2 Spinodal decomposition

If the LBM system is initialized with the densities in the unstable region of the vdW equation of state, i.e. where $(\partial P / \partial V)_T > 0$, then the temporal evolution from that state results in phase-separation. Over time, the two phases comprising the system get segregated. This process is called the spinodal decomposition. Phase-separation process is governed by the free energy minimization principle and results in minimizing interface lengths (Basagaoglu et al., 2004).

Snapshots of the spinodal decomposition process are shown in Fig. 6.6 along with the parameter values used for the simulation. As can be seen from Fig. 6.7, the mass of the individual phase remains almost constant. Interfaces merge and coalesce in order to minimize the interfacial length. Moreover, in order to reach a pressure and chemical equilibrium after starting from a random initial condition, system is seen to initially have a slight increase in mass, which later becomes constant, as shown in the Fig. 6.8. Spinodal decomposition process in 3D is shown in Fig. 6.9. Parameters for the simulations are given in the caption of the figure.

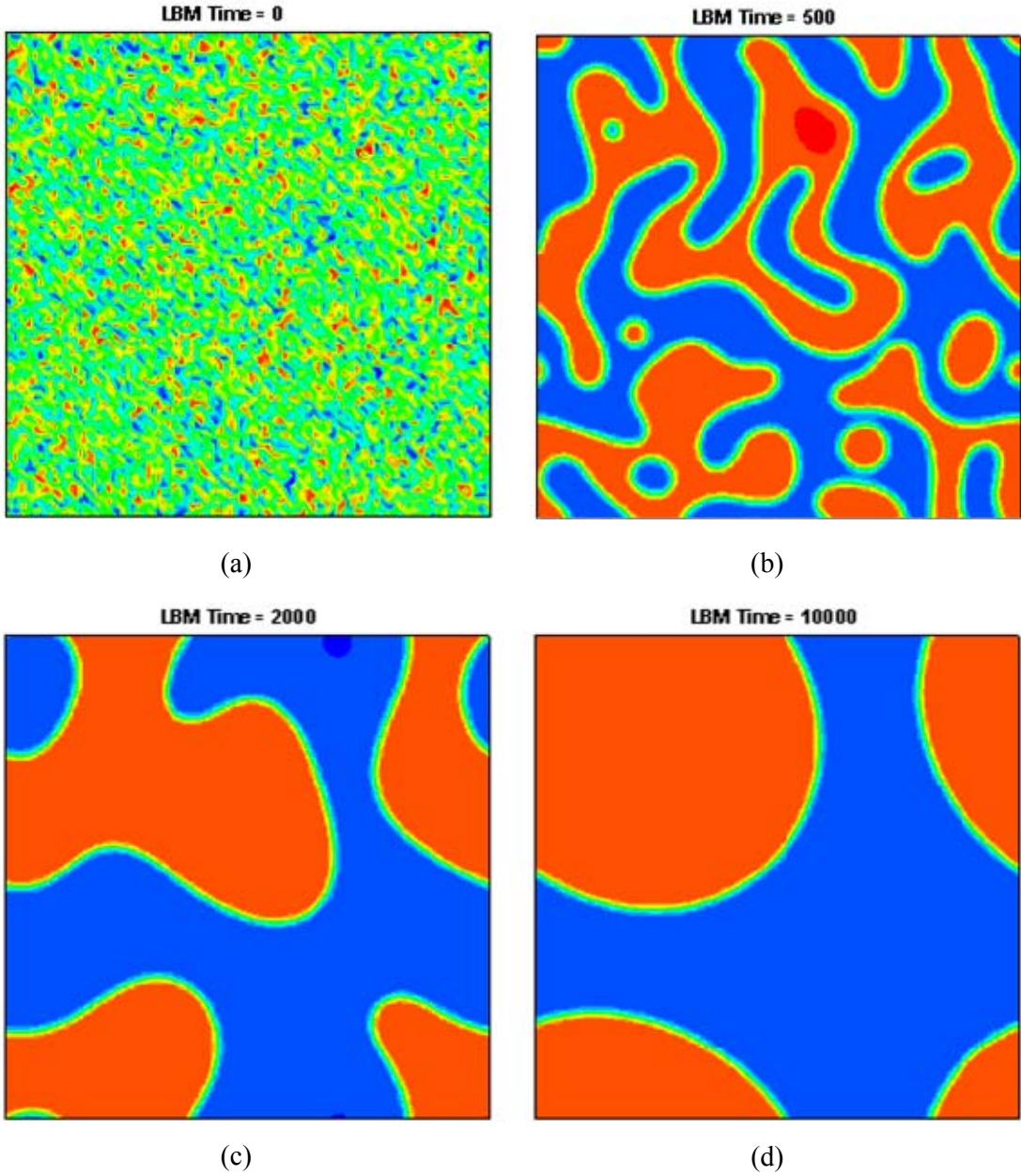


Fig. 6.6: Two-dimensional spinodal decomposition process for a van der Waals fluid. Parameters for the LBM simulation are: $\rho_l = 1.28943$, $\rho_v = 0.726691$, density ratio = 1.77 (corresponds to $T_R = 0.98$), periodic domain of size 200×200 , $\sigma = 5 \times 10^{-3}$, $\tau_l = \tau_v = 0.5$, $g = 0$, $\nu_l = \nu_v = 0.5/3 = 0.1666$, $D = 3$. At time $t = 0$, the 2D box is filled with a van der Waals fluid at critical density $\rho_c = 1$ and spatially random but small density-perturbations are introduced. Blue color in the figure represents the vapor phase and red color represents the liquid phase. (AIBL model, no scaling)

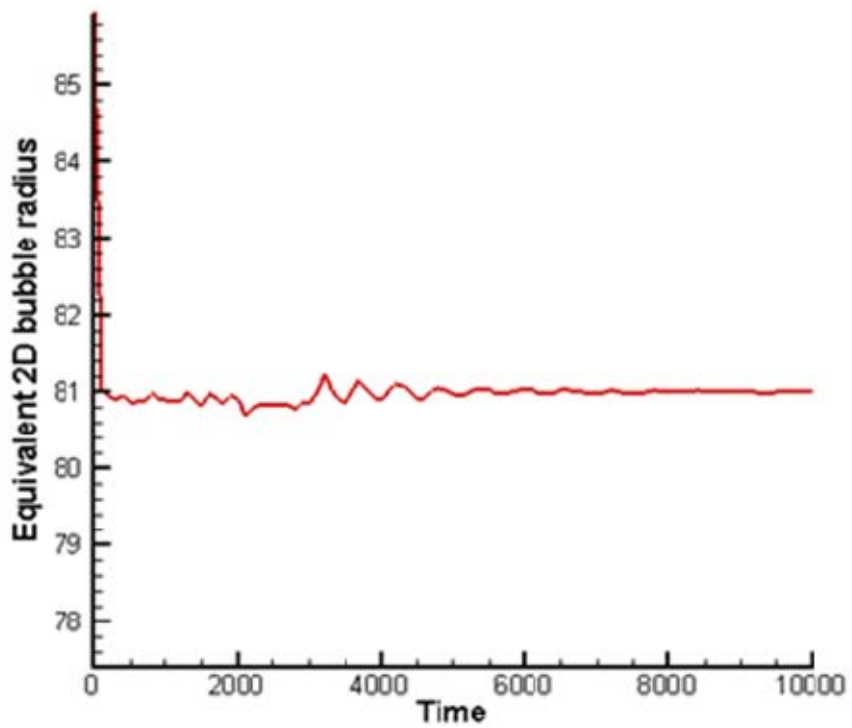


Fig. 6.7: Variation of an equivalent 2D bubble radius with time. Since bubbly region has almost constant density, the graph above also represents a variation in total density of the vapor region with time. Total mass of the bubbles remains almost constant. Bubbles and droplets merge and condense during the free energy minimization procedure; however, the net volume occupied by a particular phase does not change significantly during the process. (AILB model, no scaling)

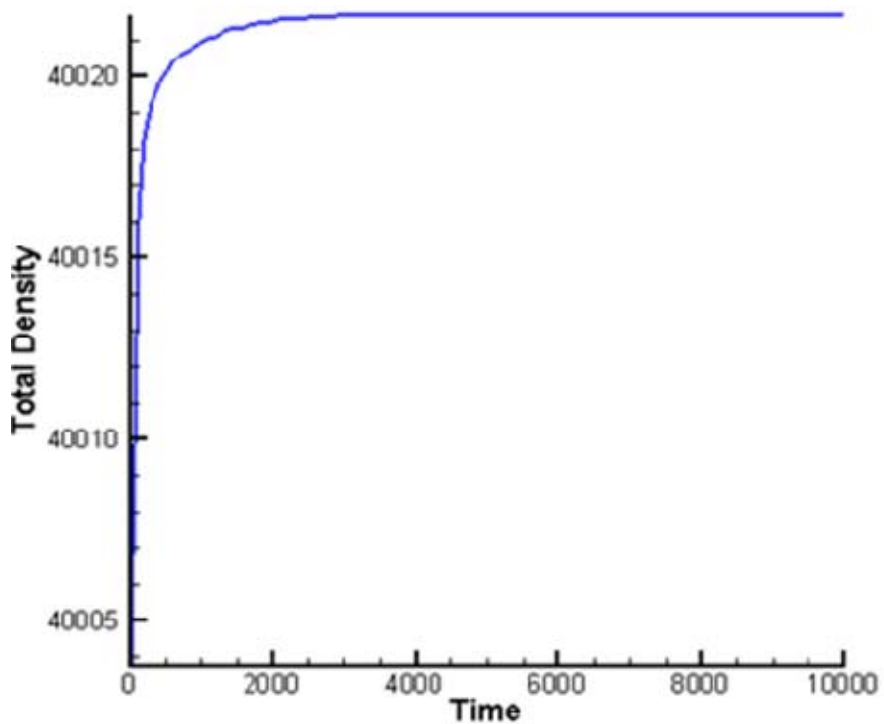


Fig. 6.8: Variation of the total density of the simulation box with time. Note that during the initial period, system attempts to reach equilibrium (pressure-equilibrium) consistent with the specified system temperature, and during that process increases its net mass. (Increase is a very small percentage of the total.) Afterwards, total system mass (density) remains conserved. (AILB model, no scaling)

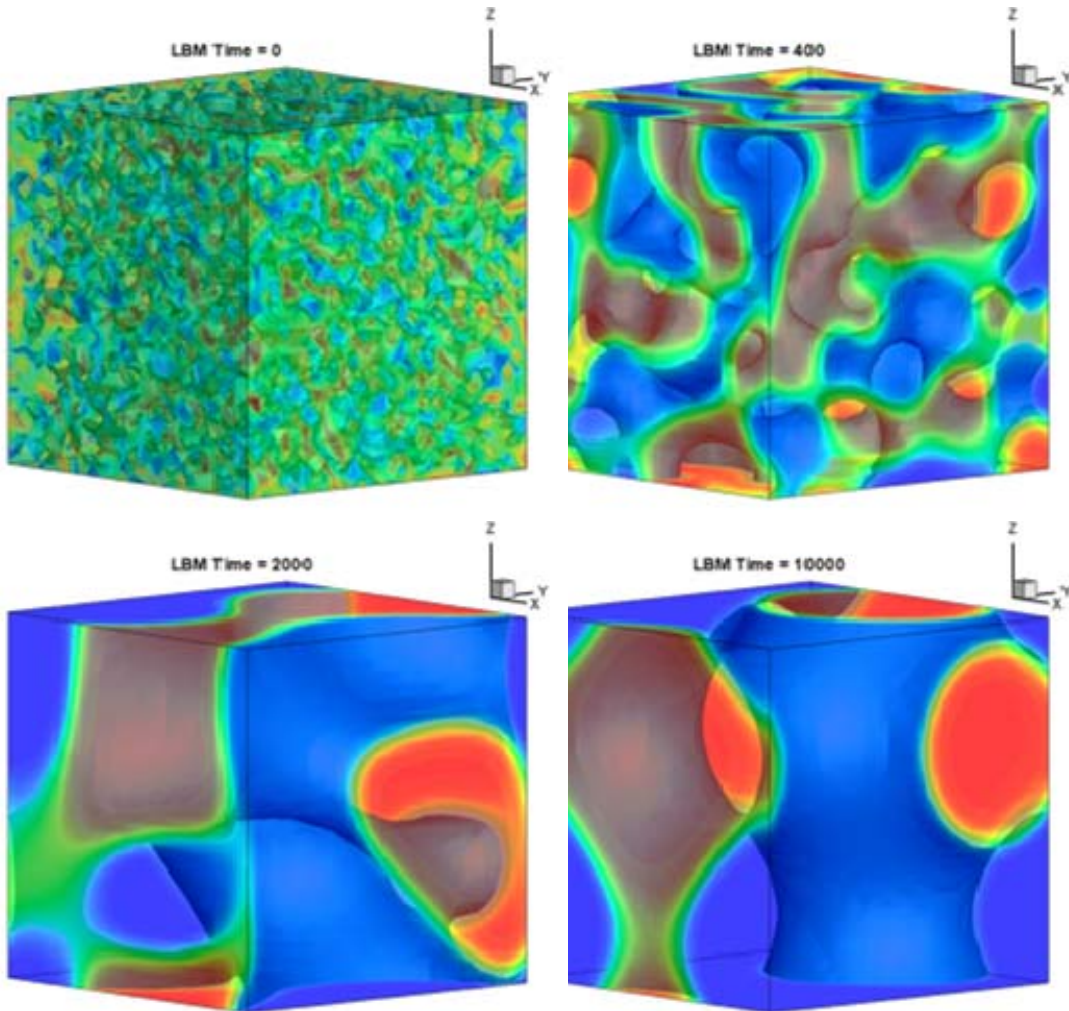


Fig. 6.9: Three-dimensional spinodal decomposition process for a van der Waals fluid. Parameters for the LBM simulation are: $\rho_l = 1.46173$, $\rho_v = 0.5790$, density ratio = 2.52 (corresponds to $T_R = 0.95$), periodic domain of size $60 \times 60 \times 60$, $\sigma = 5 \times 10^{-3}$, $\tau_l = \tau_v = 0.5$, $g = 0$, $\nu_l = \nu_v = 0.5/3 = 0.1666$, $D = 3$. At time $t = 0$, the 3D box is filled with a van der Waals fluid at critical density $\rho_c = 1$ and spatially random small density perturbations are provided. Blue color in the figure represents vapor phase and red color represents liquid phase. (AILB model, no scaling)

6.2.3 Comparison of LBM simulations with densities obtained via Maxwell construction for the vdW EOS

Several LB simulations have been performed at different system temperatures using the AILB model. Results are presented for a single bubble coexisting with the liquid phase, simulated in a zero-gravity periodic domain. Parameters for the simulations are: domain size = 200 x 200, $\sigma = 0.005$, $\tau_l = \tau_v = 0.5$, $g = 0$, $\nu_l = \nu_v = 0.5/3 = 0.1666$, $R = 50$. The bubble is centered at (100,100). Results of the simulations are given in Table 6.2. As the temperature is reduced in the simulations, interface thickness needs to be increased, as shown in Fig. 6.10.

Table 6.2: A comparison of LBM results with the theoretical densities obtained via Maxwell construction for the vdW EOS.

$T_R = \frac{T}{T_C}$	$\rho_{liq,R} = \frac{\rho_{liq}^{Th}}{\rho_C}$	$\rho_{vap,R} = \frac{\rho_{vap}^{Th}}{\rho_C}$	$\frac{\rho_{liq}^{Th}}{\rho_{vap}^{Th}}$	D	ρ_{liq}^{LBM}	ρ_{vap}^{LBM}	$\frac{\rho_{liq}^{LBM}}{\rho_{vap}^{LBM}}$
0.98	1.28943	0.726691	1.77	3	1.28803	0.72493	1.77
0.90	1.65727	0.425742	3.89	3	1.65419	0.42561	3.89
0.80	1.93271	0.239667	8.06	10	1.91809	0.23963	8.00
0.70	2.14044	0.128022	16.72	10	2.12177	0.12801	16.58
0.60	2.31156	0.0597781	38.67	10	2.29227	0.05977	38.35
0.50	2.45849	0.0217468	113.05	12	2.43775	0.02174	112.13
0.40	2.58794	0.00491089	526.98	12	2.56457	0.00491054	522.26
0.30	2.70416	0.000399065	6776.24	12	2.67819	0.000398971	6712.74

6.3 Simulation of a vapor bubble coexisting with liquid

Since LBM solution scheme is a time-marching algorithm, it is of interest to see if and when the system reaches equilibrium for very simple two-phase problems. By equilibrium, we mean a steady state where all the numerical artifacts die out and the solution becomes independent of the initial condition. Note that there have been several attempts to explain and reduce the magnitude of spurious currents in the LB simulation of two-phases (Wagner, 2002; Cristea & Sofonea, 2003; Shan, 2006).

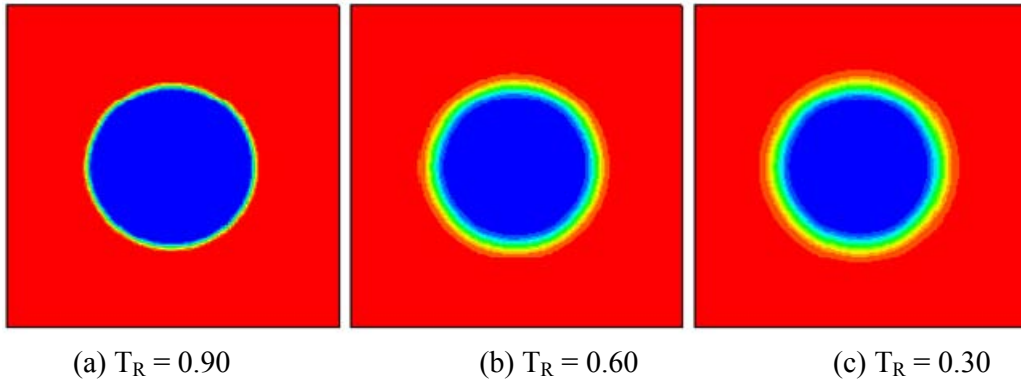


Fig. 6.10: Interfacial thickness for a single bubble in a periodic domain. With decreasing temperatures, density ratio of the two phases is increased and a thicker interface is desired for numerical stabilization. Results for the density ratios and values of the thickness controlling parameter D for several LBM simulations are given in Table 6.2. (AILB model)

One of the simplest numerical problems involving a two-dimensional (2D) circular bubble is the simulation of a single vapor bubble surrounded by liquid in gravity-free periodic box. A circular bubble can be initialized at the center of a 2D periodic box with the density in the interfacial region following the analytical result of planar interfaces in equilibrium. The evolution of such a vapor bubble is simulated in time using the Lee-Fischer LB model. In the absence of gravity, Lee-Fisher LB model is appropriate for such simulations.

Simulation results at the time step $t = 100,000$ can be assumed to have reached the steady-state since the spurious currents surrounding the bubble have died down to the order of 10^{-6} or below. Time variation of the maximum spurious velocity in the domain is shown in Fig. 6.11. It is seen that, for low density ratios of the two phases, the maximum velocity dies out to machine precision (order of 10^{-14}), however, for large density ratio a very small magnitude of spurious velocity does persist. Due to finite lattice directions and the isotropic derivatives in the LB model, these spurious currents form eight symmetric eddies, as shown in Fig. 6.12.

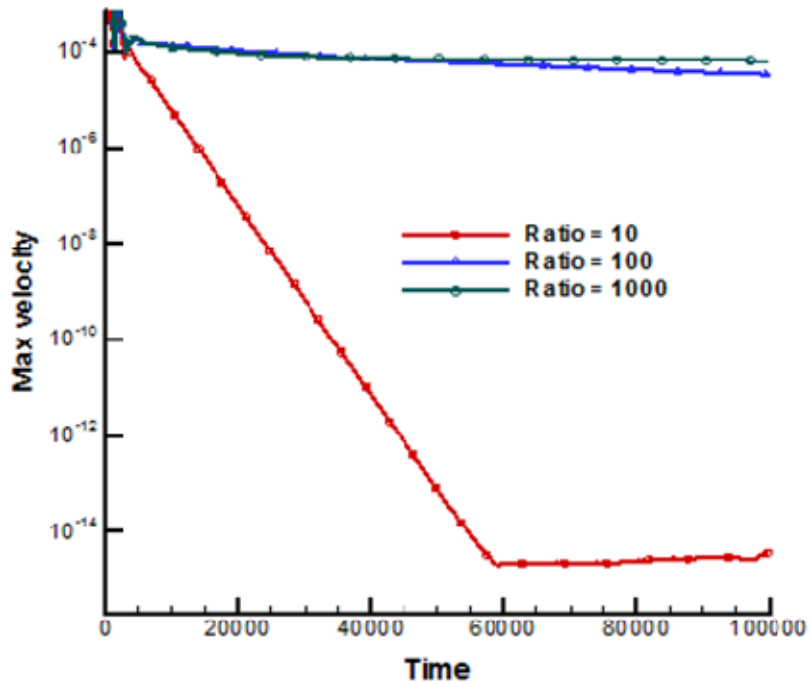


Fig. 6.11: Time evolution of maximum velocity for a single bubble coexisting with liquid in a periodic domain. The liquid density is fixed at 1.0. The vapor density is 0.1, 0.01 and 0.001 for the three curves which can be identified by different liquid to vapor density ratios in the figure. Kinematic viscosities of the two phases are the same, with relaxation time for both the liquid and the vapor phase being equal to 0.5. (Lee-Fischer LB model)

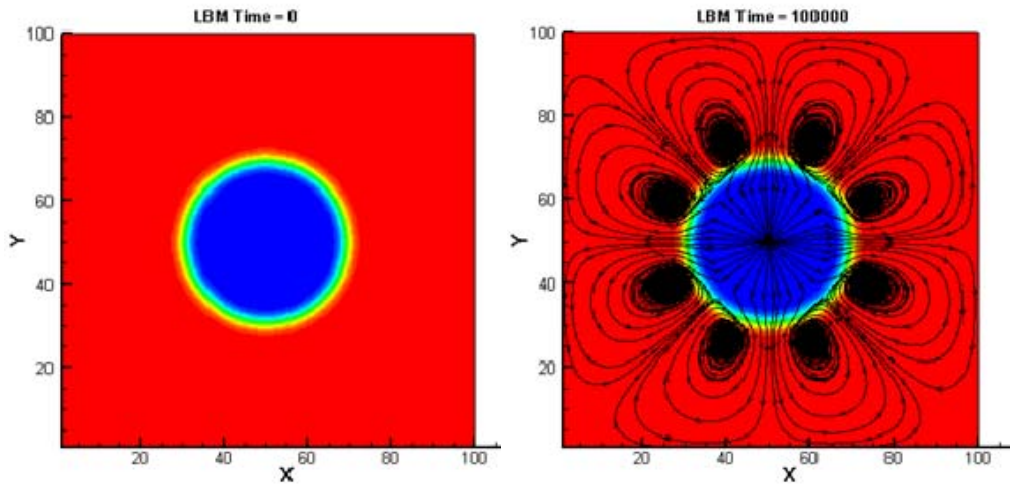


Fig. 6.12: A single bubble (of vapor density 0.001) is initialized to be in coexistence with liquid (of density 1.0) in a periodic domain. At the steady state (at $t = 100,000$), “spurious” currents are present, though of a very small magnitude (of the order of 10^{-6}), and organized in eight symmetric eddies surrounding the bubble. (Lee-Fischer LB model)

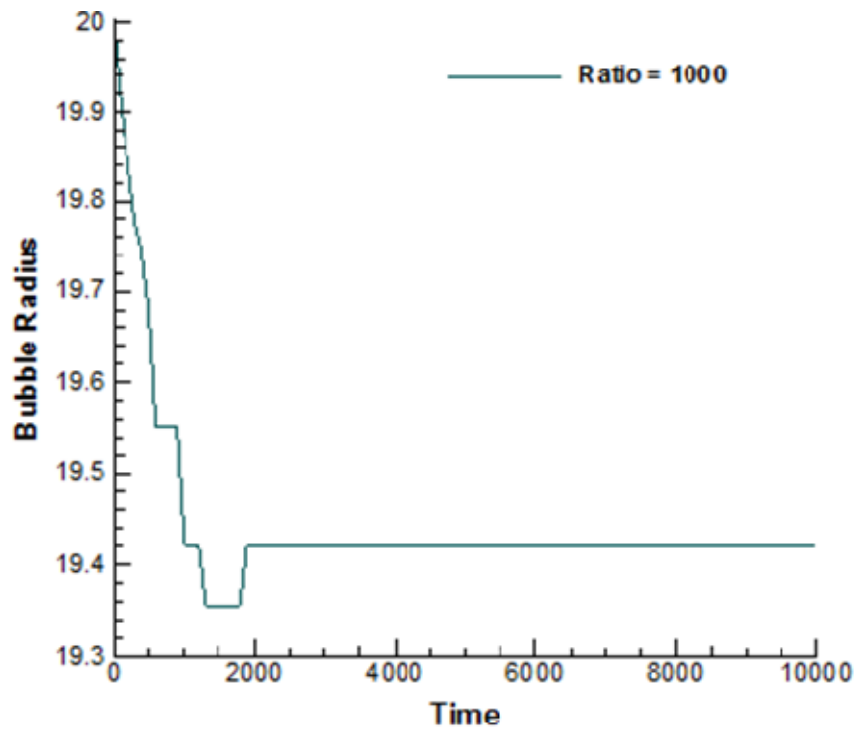


Fig. 6.13: Time evolution of the bubble radius. In the process of equilibration, radius of the bubble changes along with the densities of both the liquid as well as the vapor. At the steady state (at $t = 100,000$), the bubble radius is reduced from the initial radius of 20 lu to 19.4 lu . In the figure, the “staircase” variation of the radius is due to the applied cut-off density, which is the mean density at $t = 0$, to identify the bubble perimeter. The densities of the liquid and vapor change from their initial densities of 1.0 and 0.001 to 0.991208 and 0.00044, respectively. (Lee-Fischer LB model)

Since the initialization of the two-phase system is done by choosing equilibrium densities for a planar interface, the phase densities of both the phases as well as the radius of the bubble vary during the initial period of the evolution in order to accommodate the curvature effects. Time variation of the radius of the bubble for a density ratio of 1000 is shown in Fig. 6.13. The steady state radius and liquid/vapor densities are compared with their initialization values in Table 6.3 for three different density ratios. The spatial variation of the centerline density at the steady state is plotted against the same at $t = 0$ in Fig. 6.14.

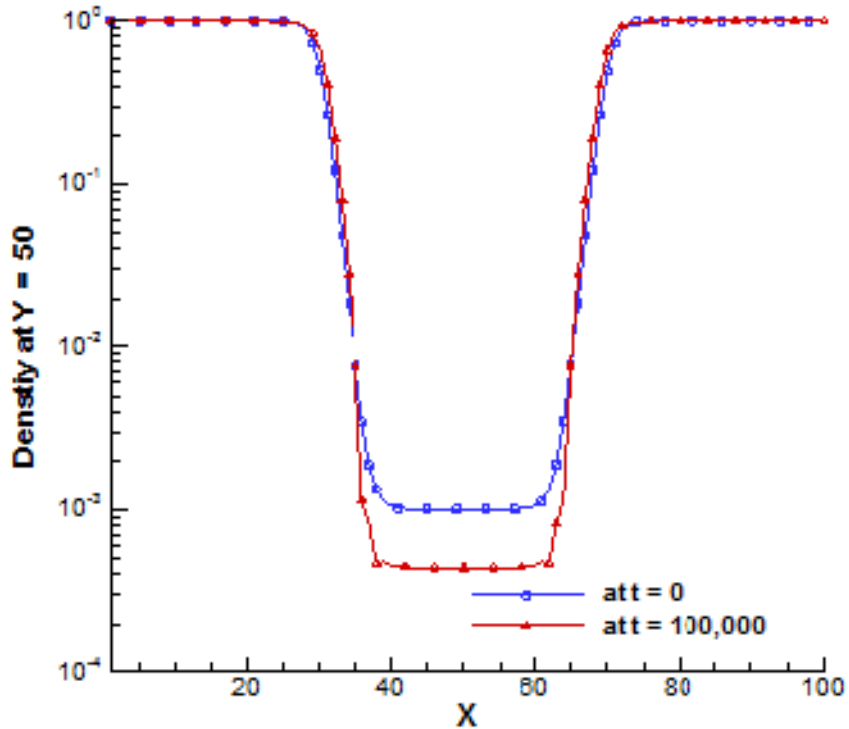


Fig. 6.14: The centerline density (at $y = 50$) of the bubble at the steady state is compared with the specified initial density. (Lee-Fischer LB model)

Table 6.3: Results for a single bubble simulation in a periodic domain

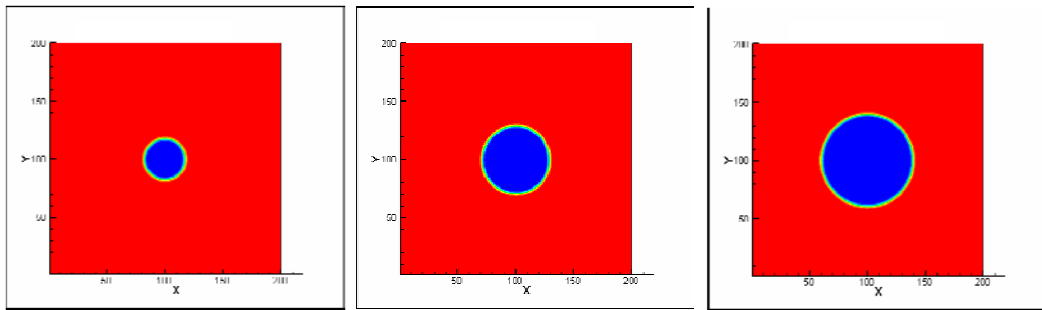
Parameters	$t = 0$	$t = 100,000$
Bubble radius	20	19.4
(a) Liquid & vapor density	{1.0, 0.1} Density ratio = 10	{0.992094, 0.0925} Density ratio = 10.725
(b) Liquid & vapor density	{1.0, 0.01} Density ratio = 100	{0.991303, 0.0348} Density ratio = 28.48
(c) Liquid & vapor density	{1.0, 0.001} Density ratio = 1000	{0.991208, 0.00044} Density ratio = 2252.74

In our LB simulations, a bubble (or droplet) is initialized using the analytical results for a planar interface. This form of initialization does not correspond to the equilibrium (or steady state) density profile due to the curvature effects. In order to quantify and analyze such curvature effects due to the radius R , several simulations are performed with increasing bubble radius R and keeping the size of the periodic computational domain fixed. It is

observed that the steady state liquid and vapor densities as well as the steady state radius R differ from their corresponding initial values. As can be seen from the Figs. 6.15-17, this difference gets reduced for larger bubble sizes in the same size computational box. Reason for this trend is that as we increase the radius R of a bubble, its curvature gets decreased and hence, the system gets closer to a system with planar interface, and therefore, the difference from the initial state gets reduced.

The results for the variation in steady state liquid and vapor densities as a function of steady state radius of bubble are shown in Fig. 6.16. As the bubble radius is increased, the densities asymptotically approach the corresponding planar interface values. Results for the effect of increasing initial bubble radius on its steady-state shrinkage are shown in Fig. 6.17. It is observed that a bubble shrinks more if it has a lower initial radius.

Note that, most of the lattice Boltzmann models for the two-phase simulation come equipped with an inherent ‘artificial’ surface tension in the model, which has to be determined from numerical experiments. Using the Lee-Fischer LB model, one can now eliminate the artificial surface tension of the LB model. Zero artificial surface tension can be tested by performing a LB simulation in which a bubble is initialized in a square shape with the surface tension parameter κ equals to zero and the parameter D equal to 3. Simulation results show that in the absence of any surface tension, the bubble does not acquire a circular shape when evolved in time. The shape and size of the bubble does not change from its initial state even after more than 100,000 LB time steps. This confirms the absence of any artificial surface tension in the Lee-Fischer LB model.



$$\rho_l = 0.993578$$

$$\rho_v = 0.0938422$$

$$R = 20 \rightarrow 17.6$$

$$\rho_l = 0.996154$$

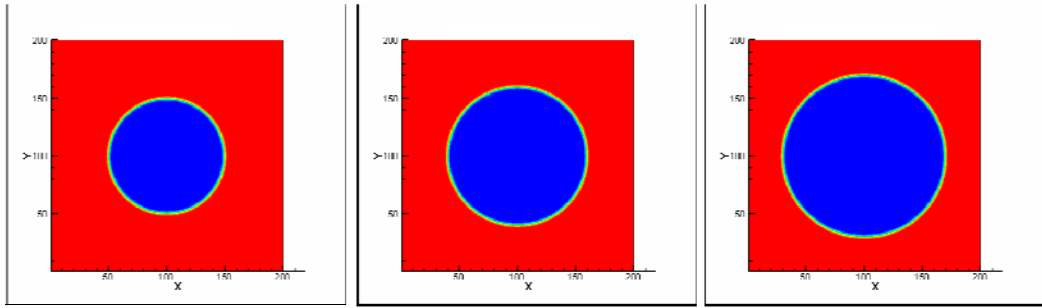
$$\rho_v = 0.0962499$$

$$R = 30 \rightarrow 29.1$$

$$\rho_l = 0.997188$$

$$\rho_v = 0.0972401$$

$$R = 40 \rightarrow 39.55$$



$$\rho_l = 0.997751$$

$$\rho_v = 0.0977844$$

$$R = 50 \rightarrow 49.75$$

$$\rho_l = 0.998124$$

$$\rho_v = 0.0981474$$

$$R = 60 \rightarrow 59.8$$

$$\rho_l = 0.998391$$

$$\rho_v = 0.0984085$$

$$R = 70 \rightarrow 69.85$$

Fig. 6.15: Effect of increasing vapor bubble size in a fixed periodic computational domain. The initial densities for liquid and vapor phases are chosen to be 1.0 and 0.1 respectively. Different panels show the steady state (at LBM $t = 500000$) shapes of vapor bubbles. The steady state liquid and vapor densities are listed below each panel. Also, the change from initial to steady-state radius of the bubble is shown for each case. Vapor and liquid phases are shown by blue and red color, respectively. (Lee-Fischer LB model)

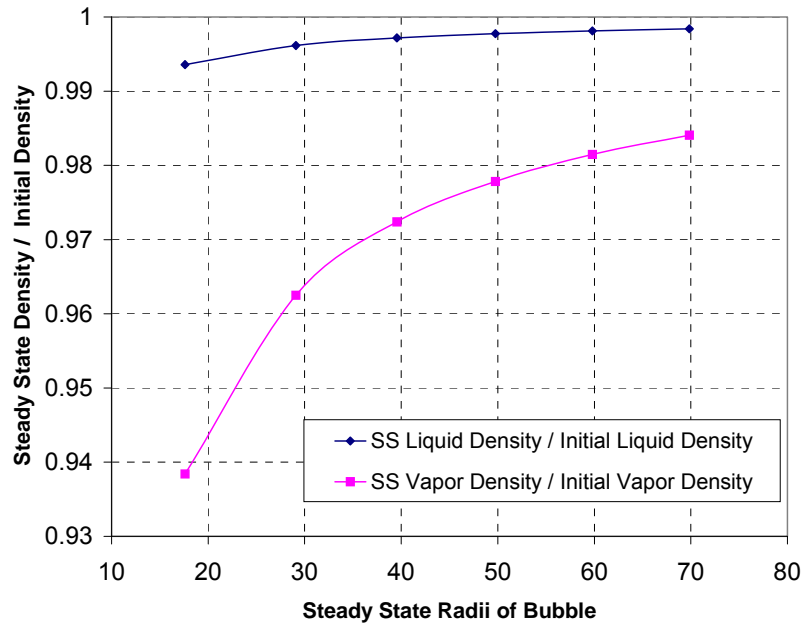


Fig. 6.16: Effect of increasing bubble radius R on steady state liquid and vapor densities. Notice that as R increases the change in steady state liquid/vapor densities from the corresponding initial densities (which are based on the planar interface results) decreases. (Lee-Fischer LB model)

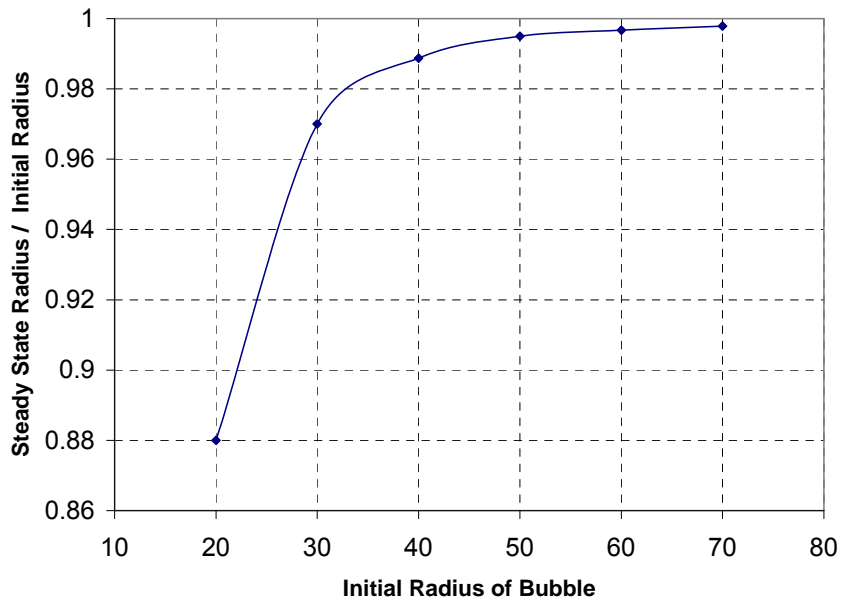


Fig. 6.17: Effect of increasing radius on the shrinkage of bubble from its initial state. Radius of a bubble shrinks less for larger bubbles in a fixed computational domain. (Lee-Fischer LB model)

6.4 Simulation of coalescence of two bubbles/droplets

Coalescence of bubbles or droplets arises in many physical situations including boiling, rain, emulsions, ink-jets and many of the two-phase scenarios. It is particularly important in Boiling Water Reactors (BWR) where vapor bubbles generated near the cladding surface coalesce to form larger bubbles and complex flow regimes, and droplets in the vapor stream coalesce with other droplets or the liquid films on the cladding. These phenomena cannot be modeled explicitly by the sub-channel or even CFD codes currently used to analyze reactor thermodynamic phenomena. In this section, we show that the LBM can be used to capture the fundamental aspects of the coalescence phenomena.

6.4.1 Experimental observations and results

When two bubbles or drops come in contact, a connecting bridge of the corresponding phase (vapor for bubbles and liquid for drops) initially forms between the two (Li, 1996; Martula et al., 2003; Ribeiro & Mewes, 2006). Experimental images for coalescence of two water droplets are shown in Fig. 6.18. This bridge then gets rapidly pulled out by the surface tension force. The speed by which the bridge widens is dictated by the competition between the capillary forces driving the coalescence and the viscous forces slowing it down (Chen & Chung, 2002).

The competition between viscous and inertial forces that govern the coalescence dynamics can be characterized by the Reynolds number:

$$\text{Re} = \frac{\rho \left(\frac{\sigma}{\mu} \right) r_b}{\mu} \quad (6.42)$$

where ρ is the density of the drops, r_b is the radius of the connecting bridge (characteristic size), σ is the surface tension and μ is the dynamic viscosity. Here, $\frac{\sigma}{\mu}$ is usually called the capillary speed (characteristic speed).

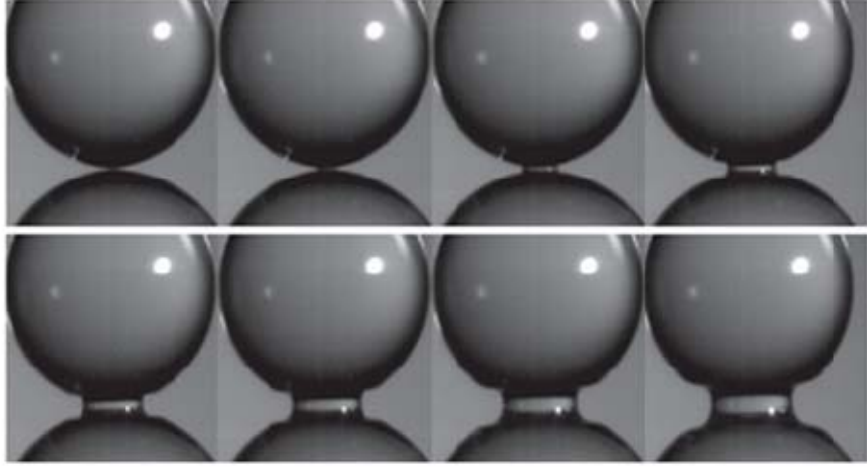


Fig. 6.18: Coalescence of two water drops. Eight consecutive images taken at 11.2 frames per second at a resolution of 256 x 256 pixels. The image size is 5.12 mm by 5.12 mm and initial radius of each drop is 2 mm. (Aarts et al., 2005)

It has been confirmed experimentally that the cross-over between viscous and inertial coalescence happens at $Re = 1$; the viscous coalescence is observed for $Re < 1$ and inertial coalescence for $Re > 1$ (Aarts et al., 2005). Cross-over junction of $Re = 1$ sets a characteristic time and length scale beyond which inertial dynamics becomes dominant. These cross-over scales are given by:

$$l_\mu = \frac{\mu^2}{\rho\sigma} \quad (6.43)$$

$$t_\mu = \frac{\mu^3}{\rho\sigma^2} \quad (6.44)$$

For water, $l_\mu \approx 15 \text{ nm}$, $t_\mu \approx 100 \text{ ns}$ and for mercury, $l_\mu \approx 0.4 \text{ nm}$ (Eggers, 1997).

In the beginning of the coalescence process, the bridge radius r_b is always small and so is the Reynolds number Re , irrespective of other fluid properties. At this stage, the viscous forces are dominant until growing r_b takes over the cross-over length scale l_μ . After that, for the rest of the dynamics, the merging process is dictated by the inertial forces.

For a pure viscous coalescence of two droplets, the radius of liquid bridge increases linearly with time, however, it varies as a square root of time for inertial coalescence (Aarts et

al., 2005; Duchemin et al., 2003; Menchaca-Rocha et al., 2001). We can observe pure viscous coalescence in experiments by either significantly increasing the viscosity or significantly decreasing the surface tension of the drops.

For merging of high viscosity drops (or drops with very low surface tension), viscous coalescence is the dominant process. To study the temporal evolution, the bridge radius r_b and the time t can be non-dimensionalized as:

$$r^* = \frac{r_b}{R_0} \quad (6.45)$$

$$t^* = \frac{t}{\tau_\nu} \quad (6.46)$$

where R_0 is the individual drop radius (which are assumed to be same for both the drops) at $t = 0$, and τ_ν is called the viscous time, given by:

$$\tau_\nu = \frac{\mu R_0}{\sigma} \quad (6.47)$$

Experimental results in Fig. 6.19 show that plotting r^* with respect to t^* gives a straight line passing through the origin with a slope of 0.55 ± 0.06 which means that the starting speed of the liquid bridge (or neck) is close to half the capillary speed (Aarts et al., 2005).

For merging of low viscosity drops (e.g., water drops in ambient conditions), inertial coalescence is the dominant process. To study the temporal evolution, bridge radius r_b and time t can be non-dimensionalized as:

$$r^* = \frac{r_b}{R_0} \quad (6.48)$$

$$t^* = \frac{t}{\tau_i} \quad (6.49)$$

where R_0 is the individual drop radius (which is assumed to be same for both the drops) at $t = 0$, and τ_i is called the inertial time, given by:

$$\tau_i = \sqrt{\frac{\rho_l R_0^3}{\sigma}} \quad (6.50)$$

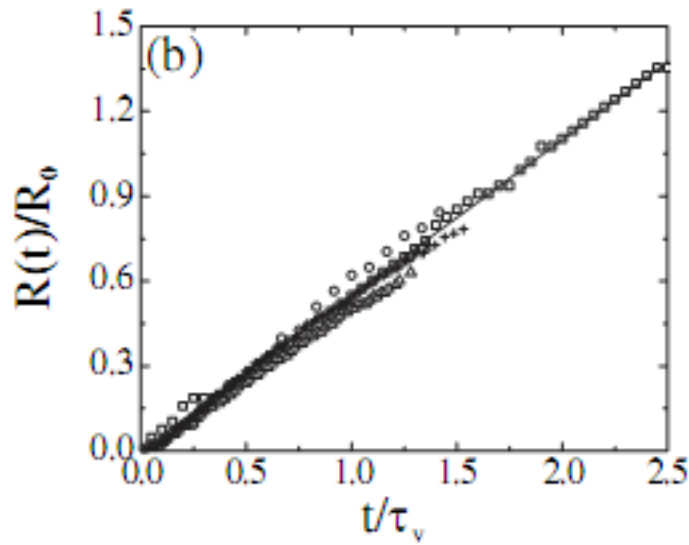


Fig. 6.19: Variation of the non-dimensional bridge radius r^* with respect to the non-dimensional time t^* for high viscosity fluids. Different symbols represent different viscosity values; squares: 100 mPa s, circles: 300 mPa s, triangles: 500 mPa s, plusses: 1 Pa s. The solid line has a slope of 0.55. (Aarts et al., 2005)

Experimental results in Fig. 6.20 show that plotting r^* with respect to $\sqrt{t^*}$ gives a straight line passing through the origin with a slope of 1.09 ± 0.08 (for water), 1.03 ± 0.07 (water-glycerol mixture) and 1.29 ± 0.05 for methanol (Wu et al., 2004). We note that, in these experimental results, $t = 0$ is the moment when both the drops started touching each other physically. In simulations, one has to consider this when comparing results with the experimental data.

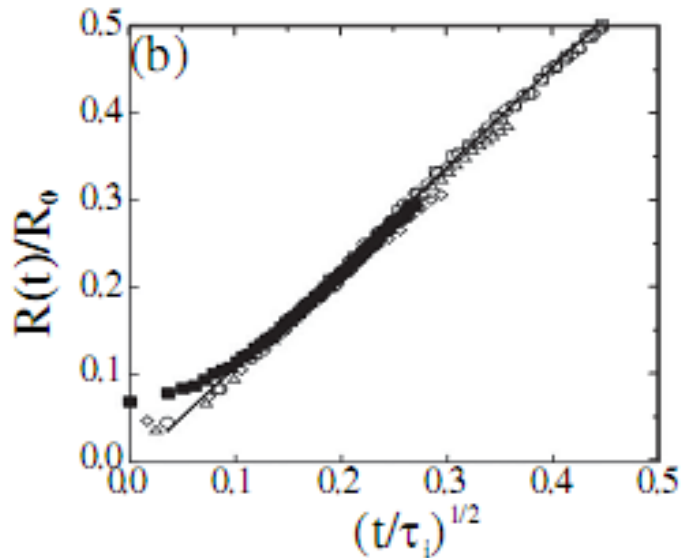


Fig. 6.20: Variation of the non-dimensional bridge radius r^* with respect to the non-dimensional time t^* for low viscosity fluids. Different symbols represent different viscosity values; Open squares: water, circles: 5 mPa s, triangles: 20 mPa s, filled squares: 50 mPa s. The solid line has a slope of 1.2. (Aarts et al., 2005)

6.4.2 LBM simulations

A 2D LBM simulation is performed using a D_2Q_9 lattice, in which, two stationary (liquid) droplets, each of density 1, are initialized such that they are in thermodynamic equilibrium with the vapor phase of density 0.0025 (see Fig. 6.23). A periodic box of size 600×1600 lu (lattice units) is chosen for the simulation. Both the droplets are assumed to be of the same radii equal to 200 lu and are separated by a minimum spacing of 4 lu . Surface tension of fluid is specified as 0.005 (in LBM units). LBM relaxation times for both the liquid and vapor are taken as 0.001 and 0.5, respectively. The interface thickness in LBM formulation is taken as equal to 4 lu initially. The kinematic viscosity ν of the liquid and vapor are related to their corresponding relaxation times τ by $\nu = \tau/3$. The temporal evolution of the above specified system of two droplets is shown in Fig. 6.21 (a) to (h).

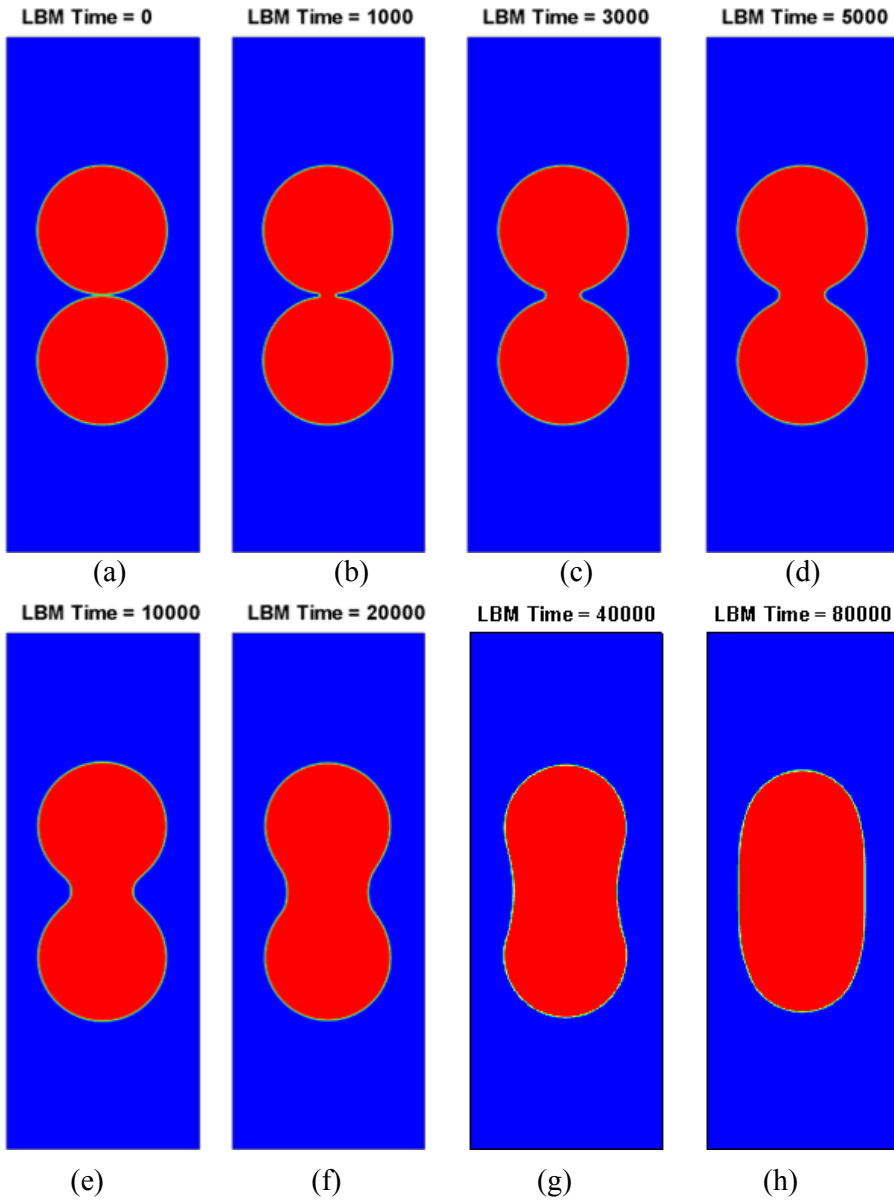


Fig. 6.21: LBM simulation of coalescence of two stationary (liquid) droplets each of radius 200 lu (lattice units) and initially separated by 4 lu (see (a)). Due to the intermolecular attraction, a liquid bridge is initially formed between the two drops (see (b)) which then widens due to the presence of surface tension (see (c) to (h)) and later minimizes its surface energy by minimizing the perimeter, for the above 2D simulation, of the liquid region to achieve the steady state in a shape of circular drop (not shown in figure). Simulations are performed in a box of size 600 x 1600 grid points. Other parameters of the simulations are: $\sigma = 0.005$, $g = 0$, $\tau_l = 0.001$, $\tau_v = 0.5$, $\rho_l = 1.0$ and $\rho_v = 0.0025$.(Lee-Fischer LB model)

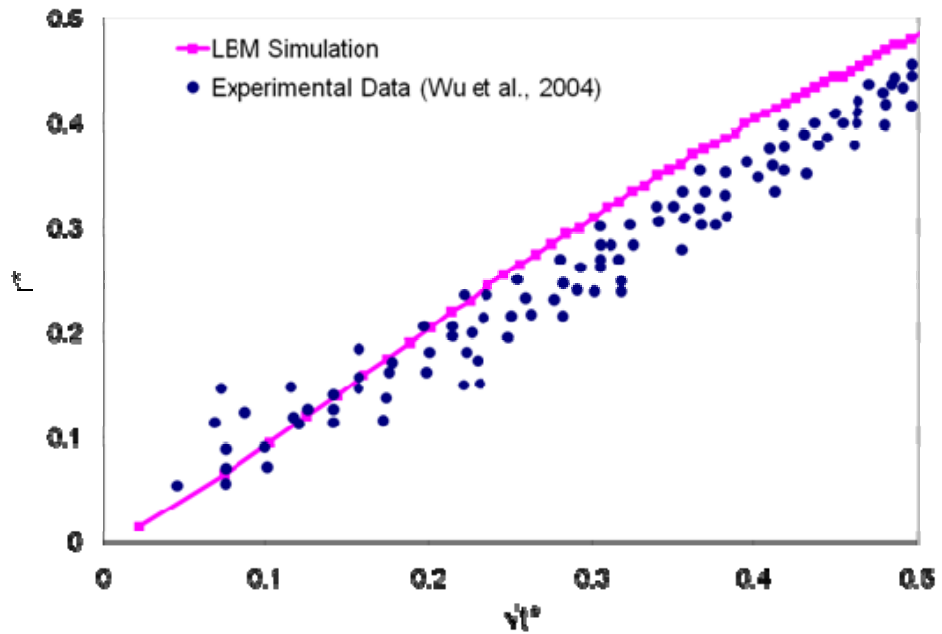


Fig. 6.22: Variation of the non-dimensional bridge radius r^* with respect to the square-root of the non-dimensional inertial time $\sqrt{t^*}$ for low viscosity fluids. Good agreement between the LBM simulation results (pink squares connected by a line) and experimental data for water drops of various radii (taken from Wu et al., 2004) is observed. (Lee-Fischer LB model)

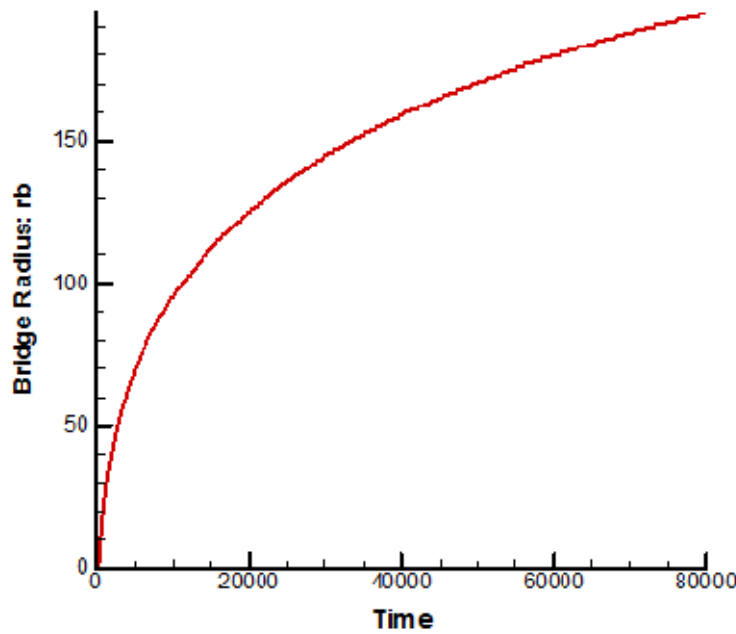


Fig. 6.23: Time evolution of the liquid bridge radius. The qualitative variation is in good agreement with the ones seen in experiments by Aarts et al. (2005) and Menchaca-Rocha et al. (2001). (Lee-Fischer LB model)

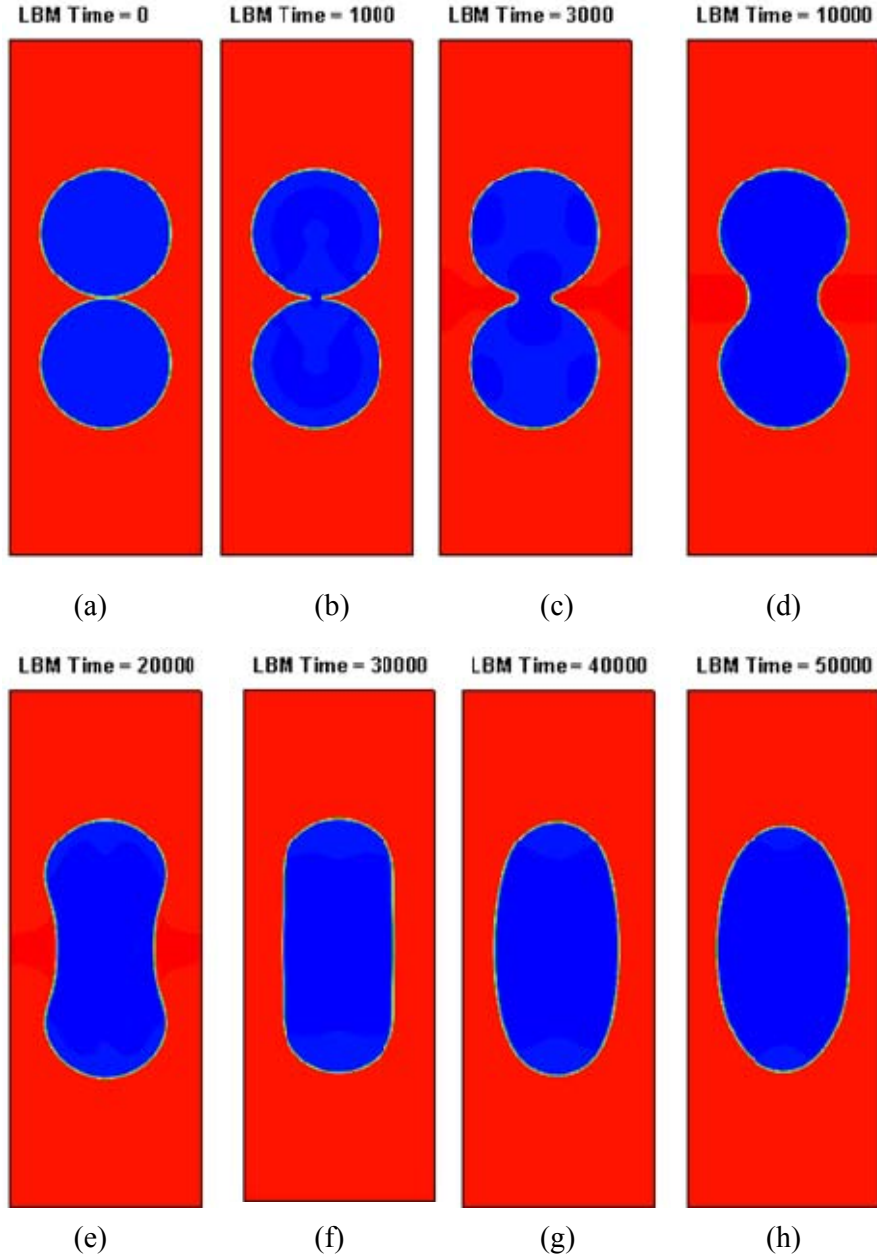


Fig. 6.24: Coalescence of two stationary (vapor) bubbles of radii $200 \text{ } lu$ which are initially separated by $4 \text{ } lu$ distance equal to the equilibrium interface thickness parameter D (see (a)). Due to the intermolecular attractions, a vapor bridge is initially formed between the duo (see (b)) which then widens due to the presence of surface tension (see (c), (d) and (e)) and later minimizes its surface energy by minimizing the perimeter of the vapor region (see (f), (g) and (h)). Simulations are performed in a box of size 600×1600 grid points. Other parameters of the simulations are: $\sigma = 0.005$, $g = 0$, $\tau_l = \tau_v = 0.5$, $\rho_l = 1.0$ and $\rho_v = 0.1$. (Lee-Fischer LB model)

The radius of the liquid bridge r_b varies proportional to $\propto \sqrt{t}$ and the corresponding variation in non-dimensional terms is shown in Fig. 6.22 for both, simulation results and experimental data for droplets of different radii. Reasonably good agreement between the two highlights the modeling capability and applicability of the LBM for such fundamental simulations. It is intended that these validation studies will be followed by more complex LBM simulations of boiling phenomena relevant for BWRs in the future. In Fig. 6.23, evolution of the liquid bridge radius is plotted in the LBM time scale. The variation shows good qualitative agreement with the results reported in the literature. In Fig. 6.24, simulation results for the coalescence of two (vapor) bubbles are presented. Parameters for the simulations are provided in the caption of the figure.

We note that 3-D calculations, which capture more accurately the geometry of the inter-phase surface and associated forces but require substantially larger computational resources, are expected to further improve the results of coalescence simulations. In Fig. 6.25, we present coalescence results for a 3D simulation on a coarse grid. Results are in good qualitative agreement; however, finer grid is necessary for better quantitative accuracy.

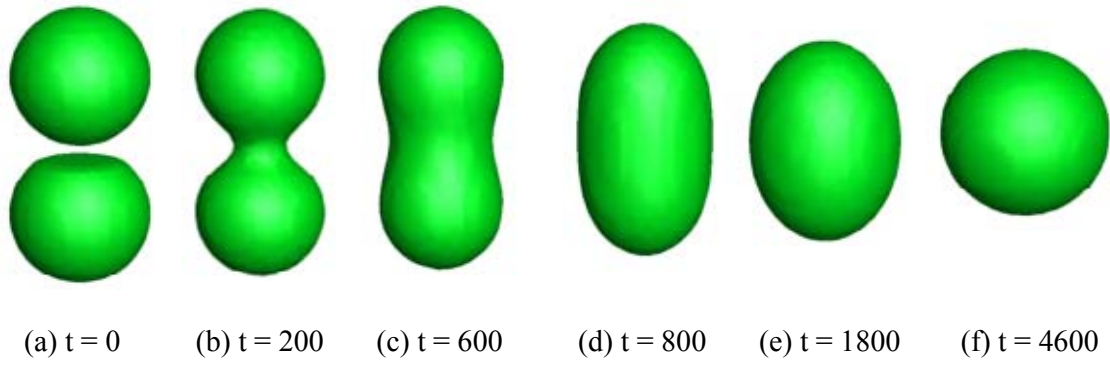


Fig. 6.25: Coalescence of two stationary bubbles of radii $15 \text{ } lu$ which are initially separated by $3 \text{ } lu$ distance equal to the equilibrium interface thickness parameter D . Simulations are performed in a periodic box of size $60 \times 60 \times 80$ grid points. Other parameters for the simulation are: $a = 9/8$, $b = 1/3$, $T_R = 0.95$, $\rho_l = 1.46173$, $\rho_v = 0.579015$, $\sigma = 0.005$, $g = 0$, $\tau_l = \tau_v = 0.5$. (AILB model with no scaling)

6.5 Simulation of the Rayleigh-Taylor instability

When a fluid of higher density is placed on top of a fluid of lower density in the presence of gravity, the interface between the two fluids is inherently unstable. Any disturbance to the interface tends to grow leading to the penetration of both fluids into each other and result in mixing. This phenomenon is called the Rayleigh-Taylor instability (Sharp, 1984; He et al., 1999a,b).

As an additional test of the capabilities of the LBM, a two-dimensional simulation of Rayleigh-Taylor instability has been carried out using LBM. Computational domain is a two-dimensional box of size 500 x 1000. No-slip boundaries are applied at the Top and the Bottom walls. Periodic boundaries are applied at the side boundaries. Kinematic viscosities of both the fluids are assumed to be same by choosing the relaxation times for both the fluids equal to 0.5. Following parameters are used in the simulation: surface tension $\sigma = 10^{-3}$, gravity $g = 10^{-5}$, heavier fluid density $\rho_l = 1.0$, lighter fluid density $\rho_v = 0.5$, channel width $W = 500$, relaxation times $\tau_l = \tau_v = 0.5$, kinematic viscosities $\nu_l = \nu_v = \tau RT = 0.16667$.

Choosing the channel width W as the length scale and $T = \sqrt{W/g}$ as the time scale, we can calculate the non-dimensional Reynolds number Re and the Atwood number A as follows:

$$Re = (\sqrt{Wg})W/\nu$$

$$A = \frac{\rho_l - \rho_v}{\rho_l + \rho_v}.$$

For the simulation parameters, we have $T = 7071$, $Re = 212$ and $A = 0.3333$.

At time $t = 0$, a single-mode y -directional perturbation is applied to the location of the interface. Initially, the perturbation grows with the heavier fluid displacing downwards in the form of a symmetrical blob. As time increases, the heavier fluid develops two side spikes and hits the Bottom wall. After hitting the Bottom wall, the heavier fluid again develops two more side spikes which ultimately gets stretched and forms very complicated dynamical patterns.

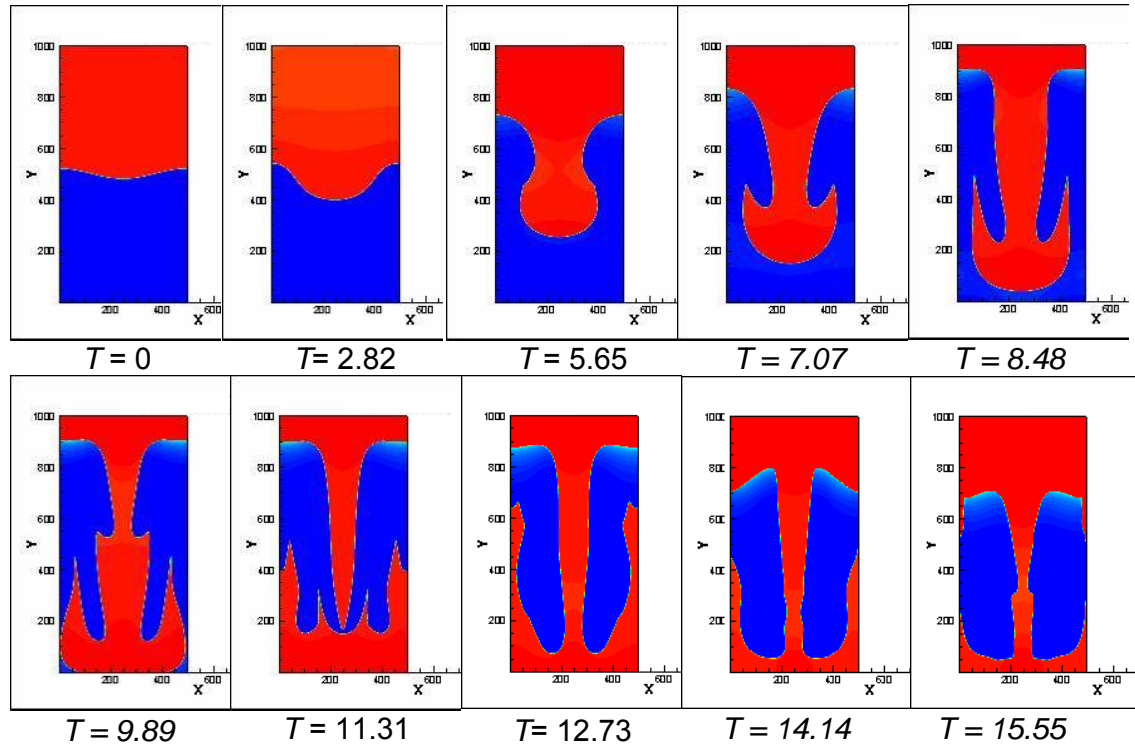


Fig. 6.26: A two-dimensional simulation of the Rayleigh-Taylor instability. Evolution of the fluid interface from a single-mode perturbation at different times is shown. Red colored fluid represents the heavier fluid and the blue represents the lighter fluid. Parameters for the simulation are: $\sigma = 0.001$, $g = 10^{-5}$, $\tau_l = \tau_v = 0.5$, $\rho_l = 1.0$ and $\rho_v = 0.5$. Time T is measured in the units of $\sqrt{W/g}$. (Lee-Fischer LB model)

6.6 Deformation and break-up of a bubble by shear forces

Flow-induced deformation of bubbles (or droplets) happens in many physical scenarios. The simplest problem to numerically study the bubble deformation is to place a 2D bubble at the center of a computational box and apply the shear forces by moving the enclosing walls of the box in the opposite directions. The box can be assumed to be periodic in one direction and surrounded by walls in the other. Due to the opposite movement of walls, the bubble at the center experiences opposite shear forces and deforms accordingly. Due to the continuing shear deformation, the bubble ultimately breaks up. The LBM simulation results are shown in the Fig. 6.27. Parameters for the simulation are listed in the caption of

the figure. Qualitatively, the results are in good agreement with the experimental observations. Simulation results using the scaled AILB model in 2D and unscaled AILB model in 3D are shown in Figs. 6.28 and 6.29, respectively.

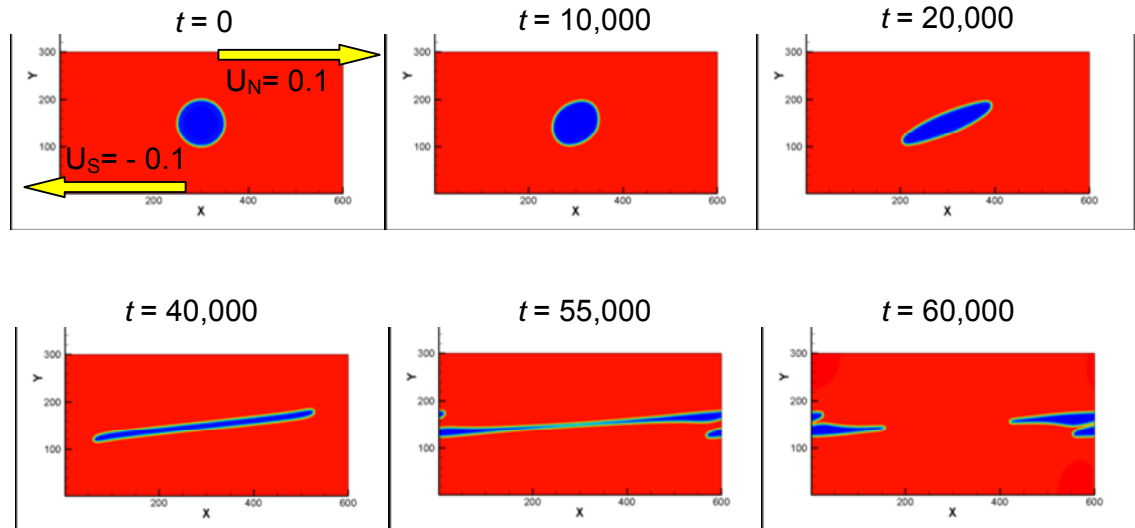
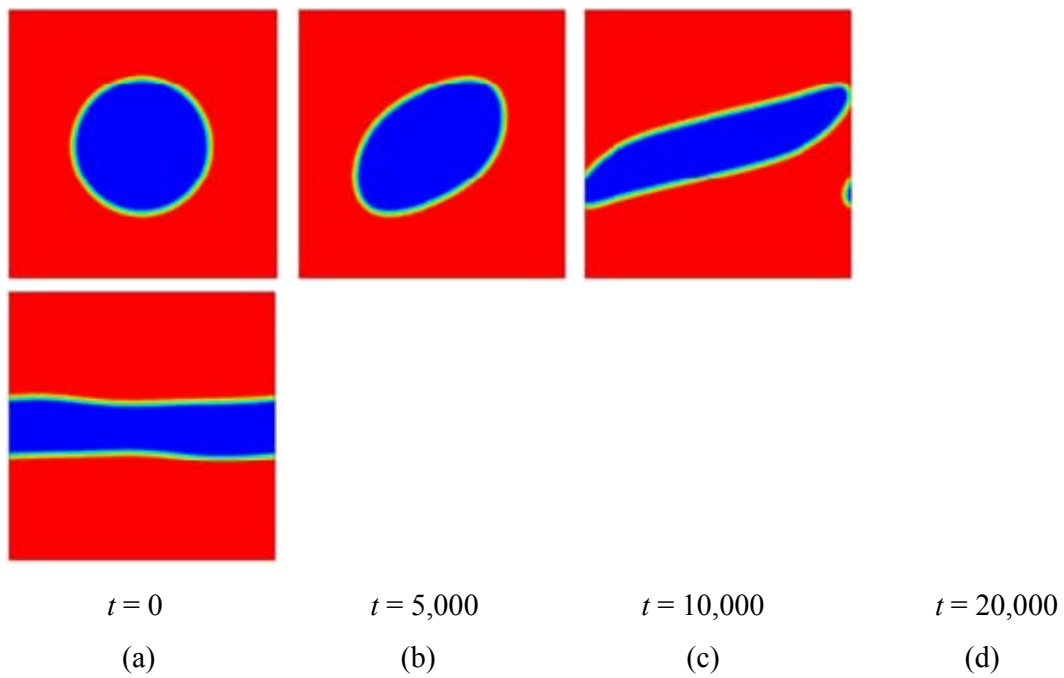


Fig. 6.27: Two-dimensional simulation for a bubble deforming (leading to break-up) in shear flow. Parameters for the simulation are: $D = 3$, $\rho_l = 1.0$, $\rho_v = 0.5$, $R = 50$, $\sigma = 10^{-3}$. (Lee-Fischer LB model)



$t = 0$

(a)

$t = 5,000$

(b)

$t = 10,000$

(c)

$t = 20,000$

(d)

Fig. 6.28: Two-dimensional simulation for a bubble deforming (leading to coalescence at its edges due to periodicity of the domain) in shear flow. Parameters are: 200×200 periodic box, $T_R = 0.6$, $a = 9/8$, $b = 1/3$, $\rho_l^{sat} = 2.31156$, $\rho_v^{sat} = 0.0597781$, $\sigma = 0.025$, $D = 3$, $S_f = 0.05$, $U_{North} = 0.05$, $U_{South} = -0.05$. (Scaled AILB model)

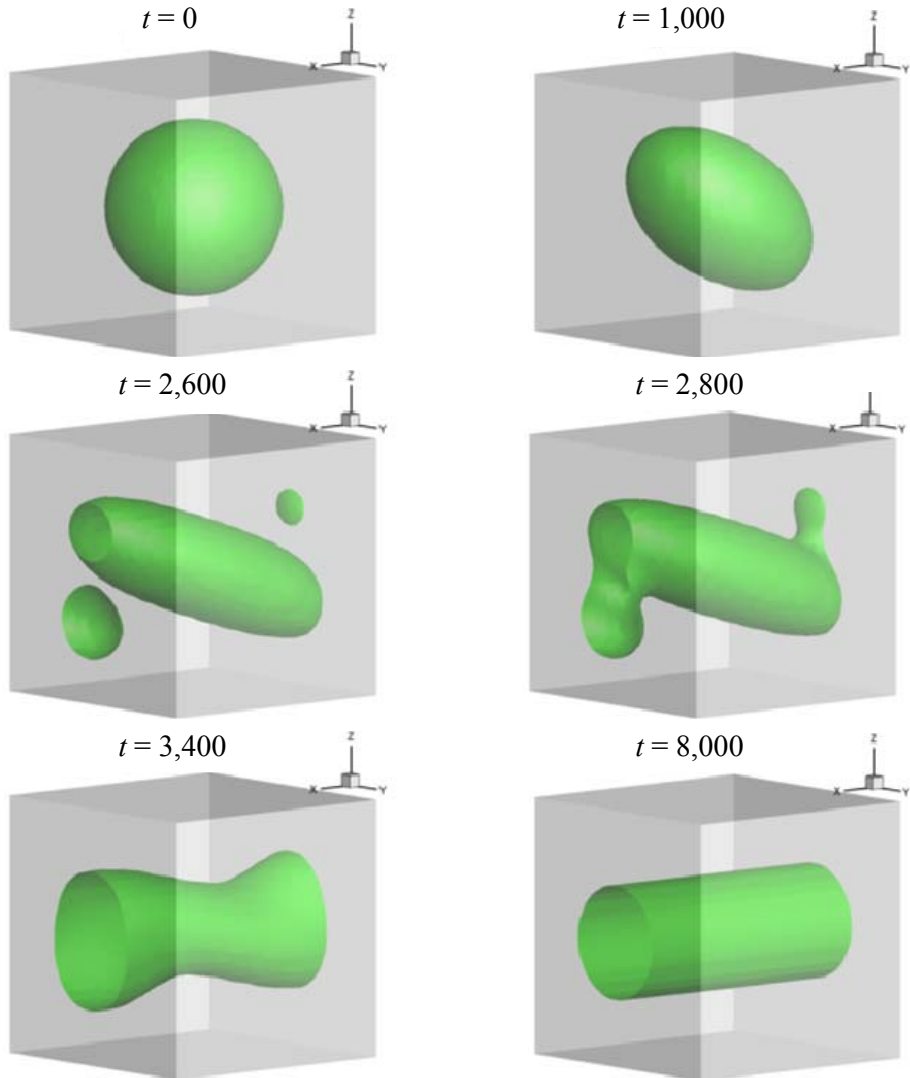


Fig. 6.29: Three-dimensional simulation for a bubble deformation (leading to coalescence at its edges due to periodicity of the domain and forming of a cylinder shape) in shear flow. Simulations are performed in a periodic box of size $60 \times 60 \times 60$ grid points. Other parameters for the simulation are: $a = 9/8$, $b = 1/3$, $T_R = 0.95$, $\rho_l = 1.46173$, $\rho_v = 0.579015$, R

$= 20 lu$, $\sigma = 0.005$, $g = 0$, $\tau_l = \tau_v = 0.5$, $D = 3$, $U_{Top} = 0.05$, $U_{Bottom} = -0.05$. (AILB model with no scaling)

6.7 Simulation of wall contact angle(s)

In this section, we show the ability of the proposed LB method to capture different contact angles in the vicinity of a wall surface. Usually the equilibrium contact angle for a given wall surface and a given fluid is known based on the experimental observations. Therefore in the LB simulations, the contact angle is pre-specified and assumed as a property of the adjoining wall.

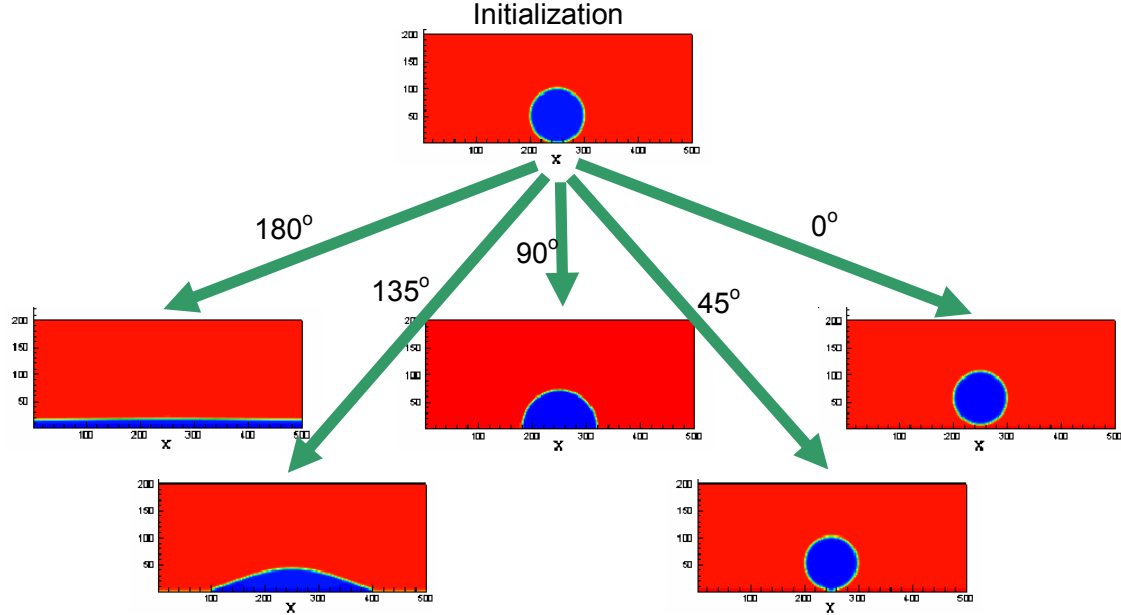


Fig. 6.30: Different equilibrium shapes and contact angles (from 0° to 180°) can be simulated for a bubble (or droplet) in the vicinity of a wall surface. The value of the equilibrium contact angle is assumed to be a property of the adjoining wall and therefore is pre-specified in the LB simulation. Other parameters for the simulation are: $\rho_l = 1.0$, $\rho_v = 0.1$, $R = 50$, $\sigma = 10^{-3}$, $g = 0$. (Lee-Fischer LB model)

Equilibrium shapes of a bubble attached on a wall surface corresponding to different equilibrium contact angles are shown in Fig. 6.30 (Lee-Fischer LB model) and Fig. 6.31 (Scaled AILB model). It can be seen that any equilibrium contact angle, ranging from 0° (complete wetting, i.e. wall has no affinity with the vapor) to 180° (complete non-wetting i.e. bubble tends to spread completely on the surface), can be simulated using the proposed LB method. Different equilibrium shapes in the figures are steady state results which evolved from the same initial condition.

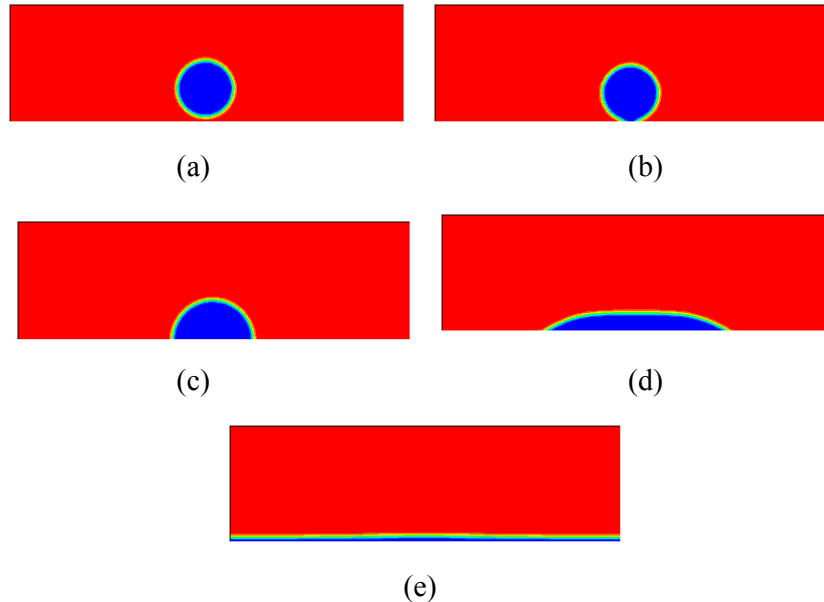


Fig. 6.31: Using the AILB model different equilibrium shapes and contact angles (from 0° to 180°) can be simulated for a bubble (or droplet) in the vicinity of a wall. Parameters for the simulation are: N-S walls, domain size = 400×120 , reduced temperature $T_R = 0.6$, $a = 9/8$, $b = 1/3$, $\rho_l^{sat} = 2.31156$, $\rho_v^{sat} = 0.0597781$, $\sigma = 0.025$, $D = 3$, scaling factor $S_f = 0.01$, initial radius $R = 30$, and density contours are at time $t = 20,000$ lu . (a) $\theta_w = 0$, (b) $\theta_w = \pi/4$, (c) $\theta_w = \pi/2$, (d) $\theta_w = 3\pi/4$, (e) $\theta_w = \pi$. (Scaled AILB model)

At time $t = 0$, a vapor bubble (vapor is shown by blue color in the figures) is initialized in a two-dimensional computational box. The vapor bubble is surrounded by a liquid (liquid is shown by red color in the figure). The interfacial region between the liquid and the vapor phase is initialized using a hyperbolic-tangent profile. [Note that a hyperbolic-tangent profile in the interfacial region comes from the analytical result for a planar interface;

however, it can still be used for the purpose of defining a suitable initial condition when the interface is non-planar (circular or spherical).]

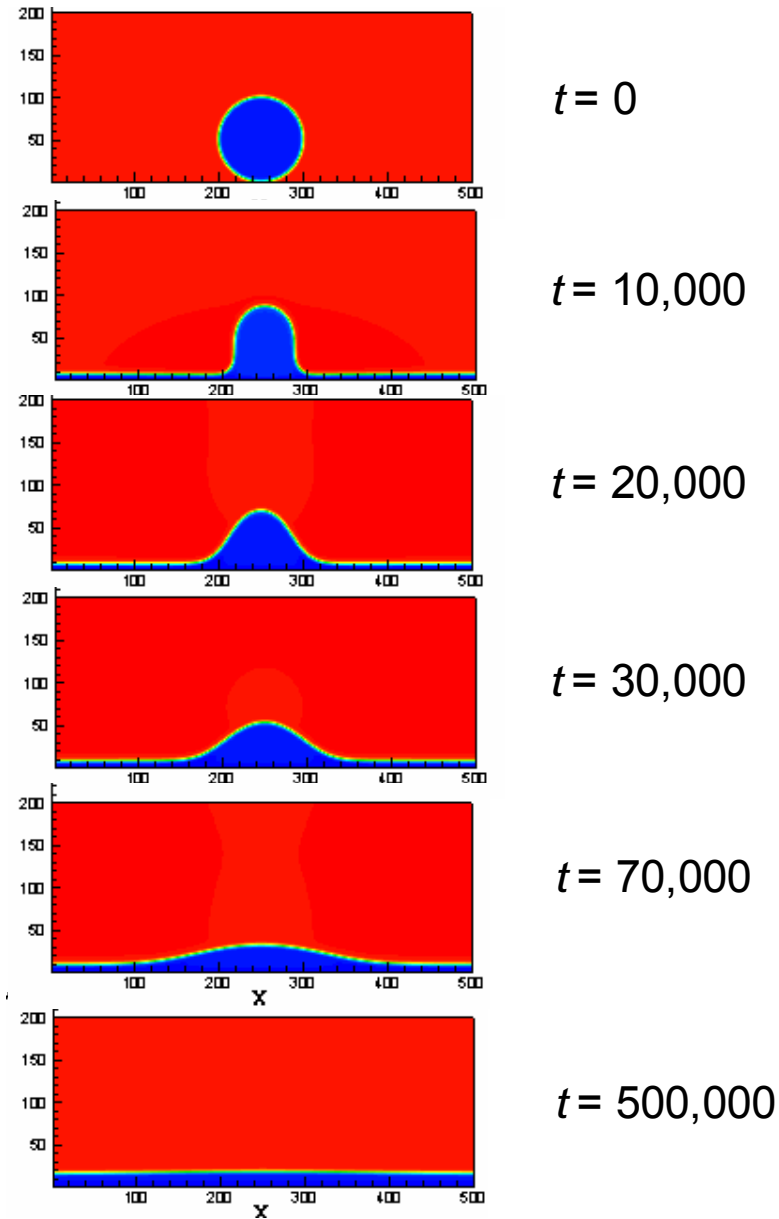


Fig. 6.32: Time sequence of topological changes in the shape of a bubble in contact with a wall surface. The equilibrium contact angle at the wall is pre-specified to be equal to 180° in the LB simulation. Other parameters for the simulation are: $\rho_l = 1.0$, $\rho_v = 0.1$, $R = 50$, $\sigma = 10^{-3}$, $g = 0$. (Lee-Fischer LB model)

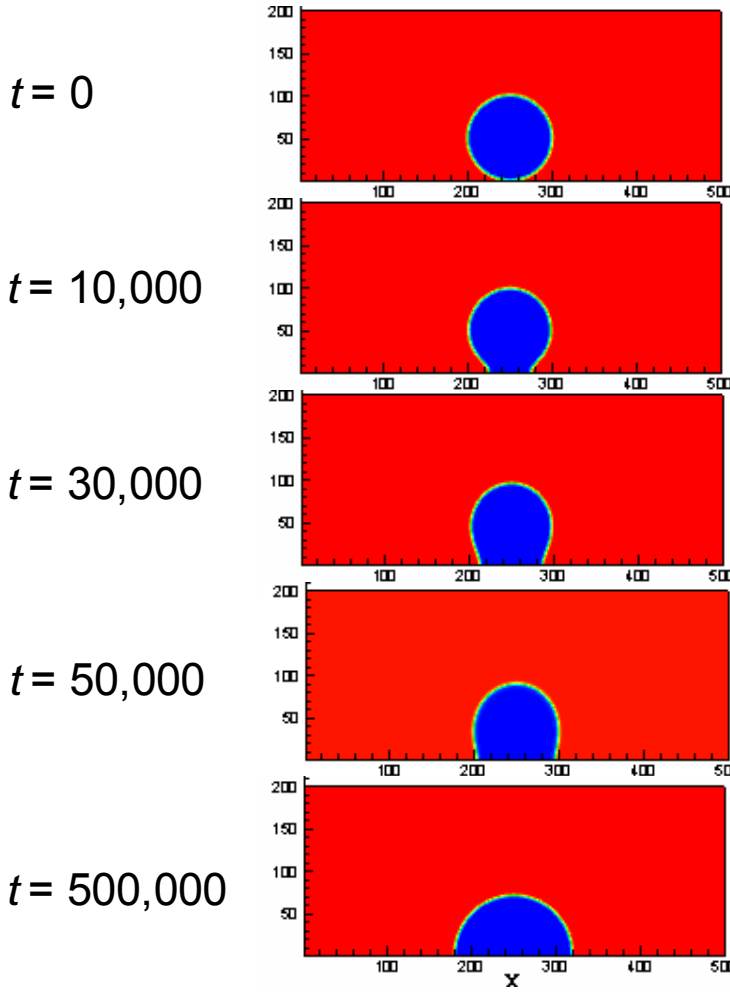


Fig. 6.33: Time sequence of topological changes in the shape of a bubble in contact with a wall surface. The equilibrium contact angle at the wall is pre-specified to be equal to 90° in the LB simulation. Other parameters for the simulation are: $\rho_l = 1.0$, $\rho_v = 0.1$, $R = 50$, $\sigma = 10^{-3}$, $g = 0$. (Lee-Fischer LB model)

Time sequence of topological changes for the equilibrium contact angles equal to 180° and 90° are shown in the Figs. 6.32 and 6.33, respectively. The vapor bubble is initialized close to the wall surface and the initial separation between the mean density contour (located inside the interfacial region) and the wall surface is kept equal to the parameter value defining the interfacial thickness, i.e. D . [Note that one may not see any interaction between the bubble and the wall surface if the bubble is not placed near the surface. The critical separation distance (below which bubble interacts with the wall and above which it does not) is usually close to the value of D .]. Of course, one can always initialize a bubble to be on the

wall surface and make any initial contact angle. The system will evolve in time such that the initial contact angle will approach the specified contact angle on the wall in the steady state. It is observed in the simulations that there is a rapid movement of contact line during the initial evolution period. Afterwards, the contact line settles down to reach its equilibrium shape by minimizing the free energy of the system and obtain the equilibrium contact angle in the steady state.

Results for the simulations of prescribed contact angles in 3D are shown in Figs. 6.34 and 6.35.

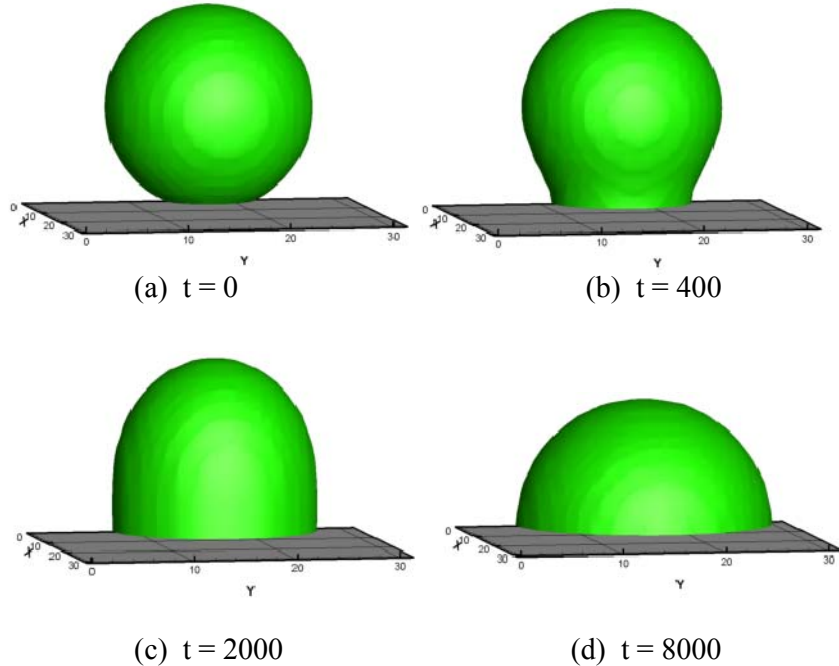


Fig. 6.34: 3D simulation of topological changes in the shape of a bubble in contact with a wall surface with a prescribed 90° contact angle. Parameters for the simulation are: Size $60 \times 60 \times 60$ (figure shown on half scale), $\sigma = 0.005$, $R = 15$, $D = 3$, $T_R = 0.95$, density ratio = 2.52, $\rho_{liq} = 1.46173$, $\rho_{vap} = 0.579015$, density contour of $\rho = 1.0$ is shown. (AILB model with no scaling).

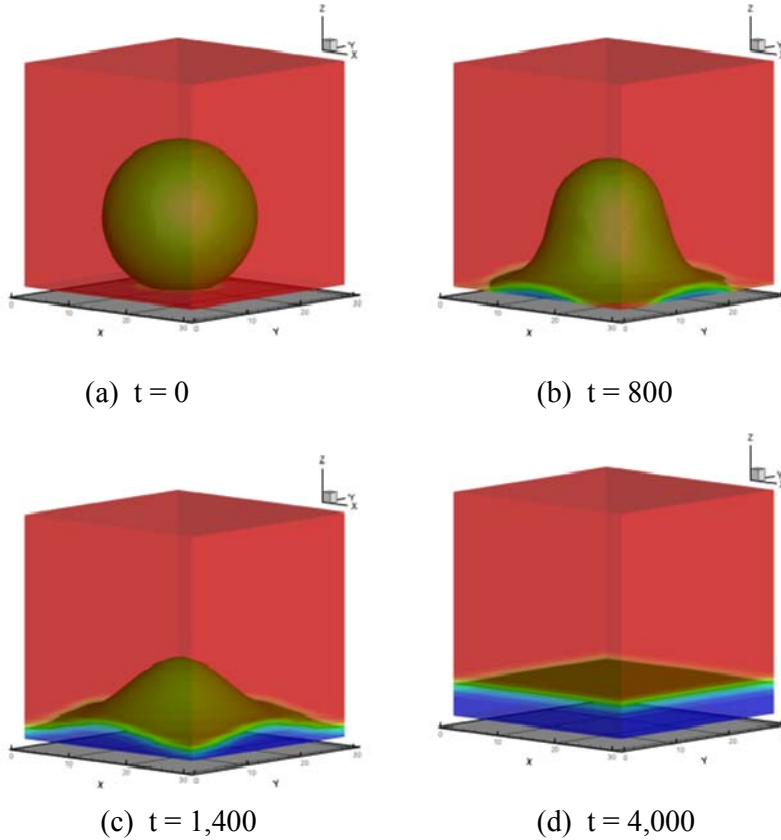


Fig. 6.35: 3D simulation of topological changes in the shape of a bubble in contact with a wall surface with a prescribed 180° contact angle. Parameters for the simulation are: Periodic domain, Size $60 \times 60 \times 60$ (figure shown on half scale), $\sigma = 0.005$, $R = 15$, $D = 3$, $TR = 0.95$, density ratio = 2.52, $\rho_{liq} = 1.46173$, $\rho_{vap} = 0.579015$, density contour of $\rho = 1.0$ is shown. (AILB model with no scaling)

6.8 Bubble detachment from a wall surface

To further test the capabilities of the scheme and code developed, a simulation of bubble detachment from a wall surface is carried out. The bubble is initialized at the Bottom wall which is specified to have an equilibrium contact angle equal to 45° . Due to the gravity and the density difference, the bubble experiences an upward buoyancy force which leads to its shape deformation and a lift-off from the wall surface. Once the bubble gets freed from the wall, its shape deforms again due to the balancing actions of the buoyancy and the viscous drag forces from the surrounding liquid. Ultimately, the bubble acquires a terminal shape and

a terminal rise velocity in the quiescent liquid. Results for the simulation are shown in Fig. 6.36. Corresponding parameter values for the simulation are shown in the caption.

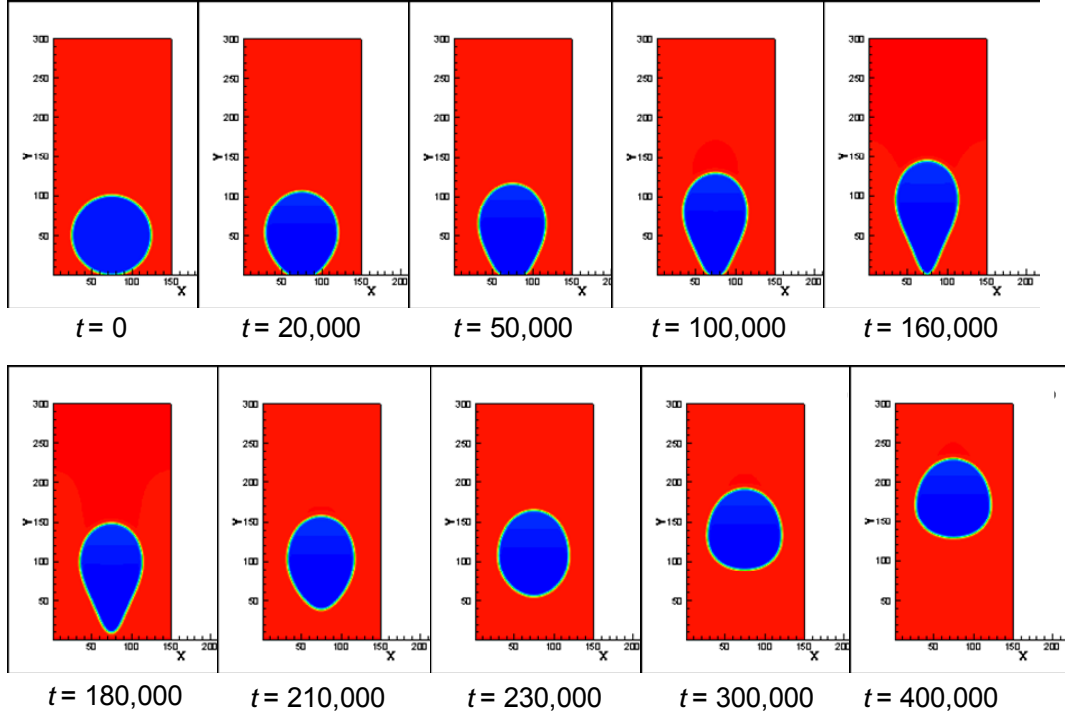


Fig. 6.36: Bubble detachment from a wall surface due to buoyancy. Parameters for the simulation are: $\rho_l = 1.0$, $\rho_v = 0.1$, $R = 50$, $\sigma = 10^{-3}$, $g = 10^{-6}$ and $\theta_s = \pi/4$. Red colored fluid represents the liquid phase and the blue represents the vapor phase. (Lee-Fischer LB model)

For a slowly growing bubble on a heated surface, the critical size of the bubble at the instant of departure is a function of buoyancy force (which attempts to detach the bubble from the surface) and the surface tension force (which prevents the bubble from detachment). Fritz (1935) proposed a relationship between the departure diameter of the bubble D_d and abovementioned forces, which is:

$$D_d \propto \theta_w \sqrt{\frac{\sigma}{g(\rho_l - \rho_v)}} \quad (6.51)$$

where θ_w is the contact angle, σ is the surface tension, g is gravity and ρ_l , ρ_v are the densities of the liquid and vapor phases, respectively. Recently, Yoon et al. (2001) found the

same dependence in their numerical simulations which uses a N-S equation based mesh-free numerical method for two-phase flows.

6.9 Single rising bubble in a quiescent liquid

Though the problem of a single rising bubble in stationary liquid has been studied for quite a while (Harmathy, 1960; Bugg et al., 1998; Sankaranarayanan et al., 1999; Chen et al., 1999; Takada et al., 2001; Yang et al., 2002; Frank et al., 2006; Kurtoglu & Lin, 2006; Hua & Lou, 2007; Mukundakrishnan et al., 2007; Li et al., 2008; Hysing et al., 2008; Gupta & Kumar, 2008), questions still remain about the flow field surrounding the bubble. There have been some experimental studies employing hydrogen tracer-bubble technique to observe the streamlines of the flow around a rising bubble. The experimental results for a single rising bubble are usually communicated through some non-dimensional parameters which characterize the rising bubble dynamics. They are:

Reynolds number:

$$Re = \frac{\rho_l D_e U_t}{\mu_l} \quad (6.52)$$

where ρ_l and μ_l are the density and the dynamic viscosity of the continuous phase (liquid) respectively, and U_t is the terminal velocity of the rising bubble. D_e is the characteristic length scale which is equivalent to the effective bubble diameter and is calculated as follows:

- Volume equivalent diameter (for experiments or in 3D simulations):

$$D_e = \left(\frac{6V}{\pi} \right)^{1/3} \quad (6.53)$$

- Area equivalent diameter (for a 2D bubble in simulations):

$$D_e = \sqrt{\frac{4A}{\pi}} \quad (6.54)$$

where V and A are the volume and the area of the bubble (dispersed phase) respectively.

Eotvos (Bond) number:

$$Eo = \frac{g \Delta \rho D_e^2}{\sigma} \quad (6.55)$$

where σ is the surface tension of the two-phase system, $\Delta\rho$ is the density difference between the continuous and the dispersed phase, i.e. $(\rho_l - \rho_v)$ and g is the gravitational acceleration.

Morton number:

$$Mo = \frac{g\mu_l^4 \Delta\rho}{\rho_l^2 \sigma^3} \quad (6.56)$$

6.9.1 Experimental observations and results

The terminal shape of a single rising bubble for a range of non-dimensional numbers, defined above, were experimentally observed by Bhaga and Weber (1981). They photographed the rising bubble using a camera that moved upward at the same speed as the bubble. The flow field surrounding the bubble was visualized using hydrogen bubbles tracing technique. Observed terminal shapes of bubble were classified into several categories (spherical, oblate ellipsoid, disk-like, spherical cap with or without wakes, skirted, etc.). Based on these observations, a shape-regime map was constructed in the space of the Reynolds, Eotvos and Morton numbers and is shown in Fig. 6.37.

From experiments of Bhaga and Weber, it was observed that small bubbles with low Reynolds and Eotvos numbers ($Re < 1$ and $Eo < 1$) remain spherical in shape and rise steadily in a straight path. Larger bubbles with intermediate Reynolds and Eotvos numbers ($1 < Re < 100$ and $1 < Eo < 100$) are deformed from their spherical shape and acquire oblate ellipsoid, disk-like, oblate ellipsoidal cap, skirt bubble, and spherical-cap type shapes during their terminal rise. Usually, the bubbles have indentation (or dimple) at their base due to the closed toroidal wake accompanying the bubble. Note that bubbles in this regime still maintain their straight rising path inside the liquid. For higher Reynolds and Eotvos numbers ($100 < Re < 1000$ and $100 < Eo < 1000$), bubble shapes become toroidal and turbulent wakes develop behind the bubble that leads to unsteady bubble motion. In this case, the bubble may rise in a wobbly path, oscillate about its mean shape and may even break-up. Several photographs of rising air bubble in aqueous sugar solutions for different Reynolds, Eotvos and Morton numbers are shown in Fig. 6.38.

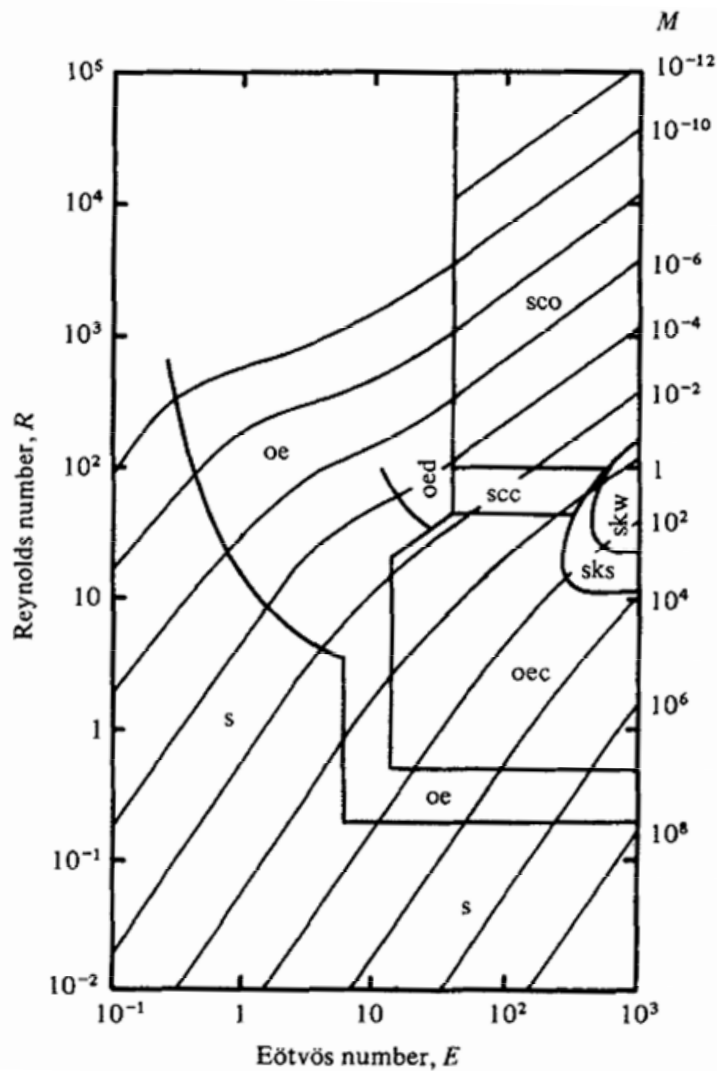


Fig. 6.37: Experimentally observed shape regime map of a single rising bubble in a quiescent liquid. s, spherical; oe, oblate ellipsoid; oed, oblate ellipsoidal (disk-like and wobbling); oec, oblate ellipsoidal cap; scc, spherical cap with closed, steady wake; sco, spherical cap with open, unsteady wake; sks, skirted with smooth, steady skirt; skw, skirted with wavy, unsteady skirt. (Bhaga and Weber, 1981)

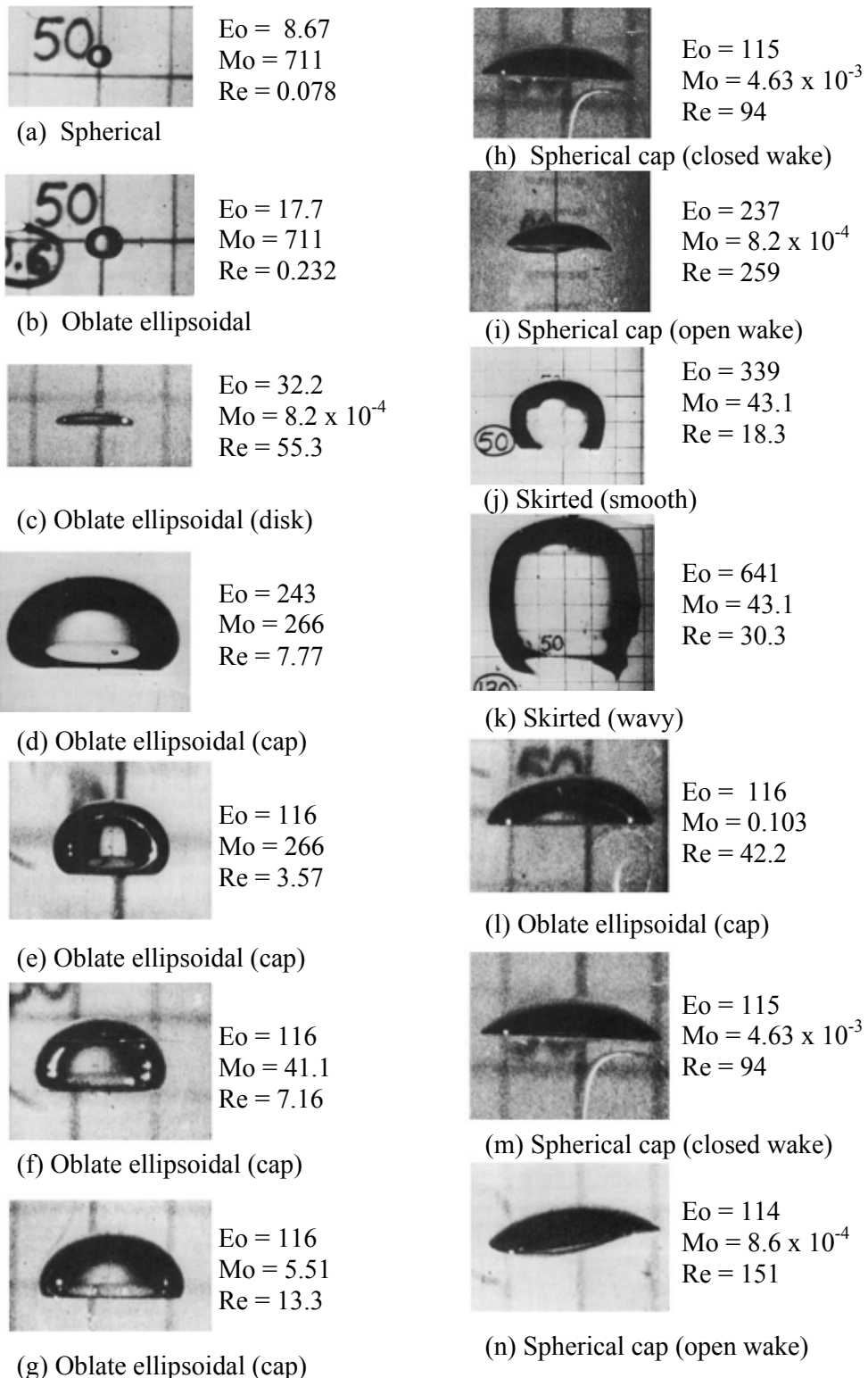


Fig. 6.38: Photographs of air bubbles from experiments conducted in aqueous sugar solutions. (Bhaga and Weber, 1981)

When a low-density fluid (gas) is inserted into a high-density fluid (liquid, $\rho_l > \rho_v$), the lighter fluid forms a bubble and the density difference between the duo builds a hydraulic pressure difference across the bubble and consequently, an upward buoyancy force is exerted on the bubble. As a result, the bubble accelerates as long as the upward buoyancy force is greater than the slowing-down drag force caused by the surrounding liquid. At the same time, the shape of the bubble also gets deformed and the bubble attains a terminal velocity once the buoyancy force (characterized by the bubble size and the density difference between two fluids) and the drag force (characterized by the bubble shape and the fluid viscosity) get balanced.

Due to initial upward acceleration of the bubble, a liquid flow field surrounding the bubble sets in and leads to a higher pressure gradient at the bottom surface of the bubble. Due to which a liquid jet forms underneath the bottom surface of the bubble. This jet pushes the bottom surface of the bubble upwards and results in the formation of a dimpled bubble. The upper surface of the bubble is pushed outward due to this jet formation and results in a nosed shape. Of course, the magnitude of bubble's deformation depends upon the density difference between the two fluids, the surface tension and viscosity of both fluids. Due to the deformation in bubble shape, the interface curvature is changed and consequently the surface tension force also changes. Since the surface tension force tends to minimize the deformation and tends to maintain the bubble in a spherical shape, there is competition between the surface tension force and the forces due to the jet formation. A high Reynolds number (large acceleration of bubble) and high Eotvos number (low surface tension) means a stronger liquid jet will form underneath the bubble and the deformation will be high. Ultimately, the relative strength between the liquid jet and the surface tension force determine whether the continuously deforming bottom surface approaches the upper surface of the bubble and results in a break-up of the bubble.

6.9.2 Results obtained using the Lee-Fischer LB model

In Fig. 6.39, results for the two-dimensional Lee-Fischer LB simulation of a single rising vapor bubble in a quiescent liquid are shown at different times. The computational domain consists of 200 x 1000 lattice points. No-slip LB boundary condition is specified on the Bottom and Top walls of the domain. Side boundaries are assumed to be periodic. A

bubble of radius $R = 50$ is initialized at $t = 0$ to be of circular shape (in 2D) and located slightly above (about two bubble diameters) the Bottom wall in order to reduce the possible wall-bubble interactions. Initially, both liquid and bubble are assumed to be stationary. Due to density difference between the vapor and the liquid phase and the presence of gravity, an upward buoyancy force acts on the lower-density bubble. The bubble moves upward and a liquid flow surrounding the bubble sets in due to the bubble's movement. This deforms the shape of the bubble from circular to 2D-oblate ellipsoidal. The deformation in bubble's shape is a natural consequence of the fluid flow fields (the wake below the lower surface and the recirculation on the sides).

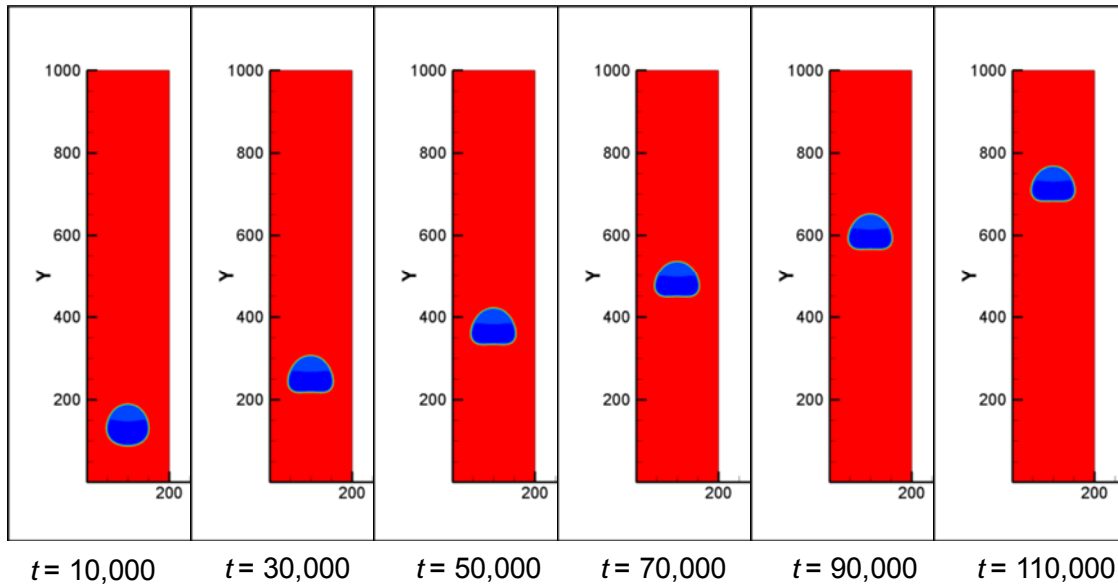


Fig. 6.39: The evolution of a single rising bubble in a quiescent liquid. Parameters for the simulation are: $\rho_l = 1.0$, $\rho_v = 0.25$, $R = 50$, $\sigma = 5 \times 10^{-3}$, $g = 10^{-5}$. (Red: liquid; blue: vapor.) (Lee-Fischer LB model)

The rising bubble is assumed to acquire a terminal shape when its area-averaged (in 2D) velocity attains a near-constant value, which for this simulation is found to be at nearly $t = 70,000$ time steps. The terminal shape and the streamlines of flow around the bubble are shown in Fig. 6.40 (a, b) in both the laboratory and the bubble's reference frame. The terminal shape from the LB simulations agrees well with the generalized shape regime map by Bhaga and Weber (1981) for the non-dimensional parameters of the simulation.

In Fig. 6.41, the variation in bubble rising velocity with time is plotted. Both the area-averaged velocity and the maximum fluid velocity in the bubble region are shown. It can be observed that bubble initially accelerates due to the dominance of the buoyancy force over the flow resistance drag. When the bubble approaches its terminal shape its rising velocity also approaches a near-constant value.

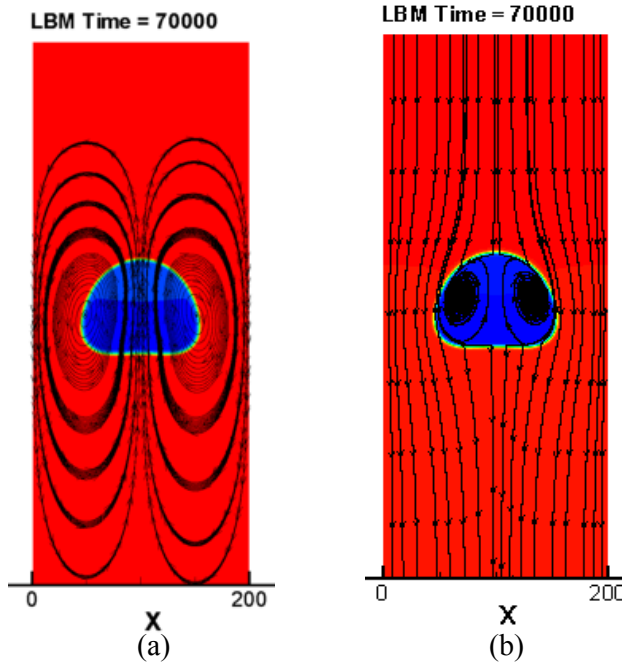


Fig. 6.40: Terminal shape (oblate ellipsoidal) of a rising bubble and corresponding velocity stream lines after 70,000 LB time steps: (a) in the laboratory reference frame; and (b) in the bubble's reference frame. Parameters for the simulation are: $\rho_l = 1.0$, $\rho_v = 0.25$, $R = 50$, $\sigma = 5 \times 10^{-3}$, $g = 10^{-5}$, $\tau_l = \tau_v = 0.5$, $Lx \times Ly = 200 \times 1000$. (Red: liquid; blue: vapor.) Non-dimensional parameters are: Reynolds number, $Re = 12.0$; Eotvos number, $Eo = 15.0$ and Morton number, $Mo = 0.046$. Terminal velocity U_t is taken to be 0.02. The predicted shape agrees well with the corresponding shape in the regime map of Bhaga and Weber (1981). (Lee-Fischer LB model)

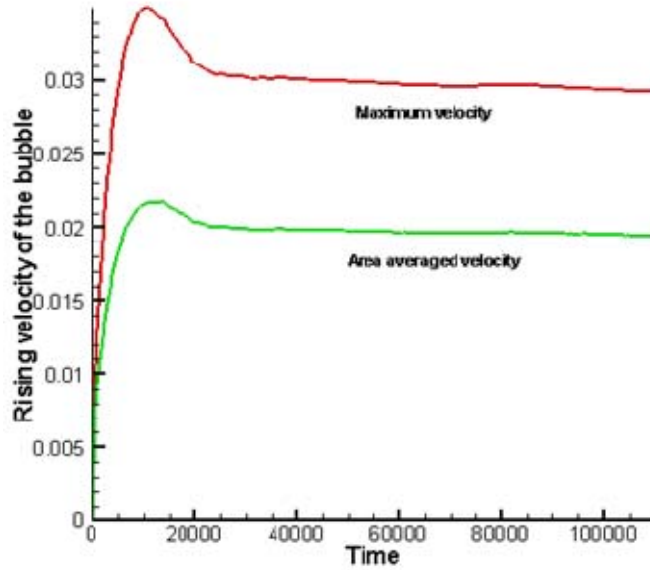
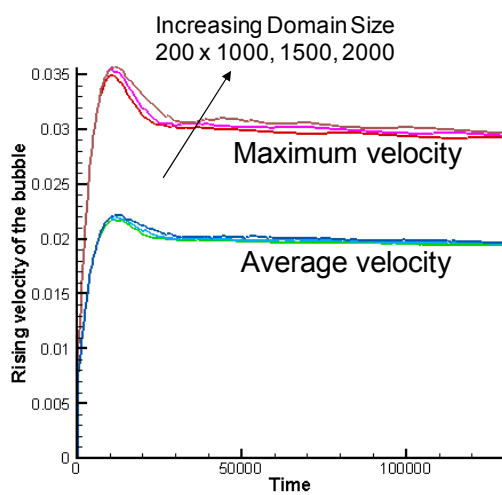


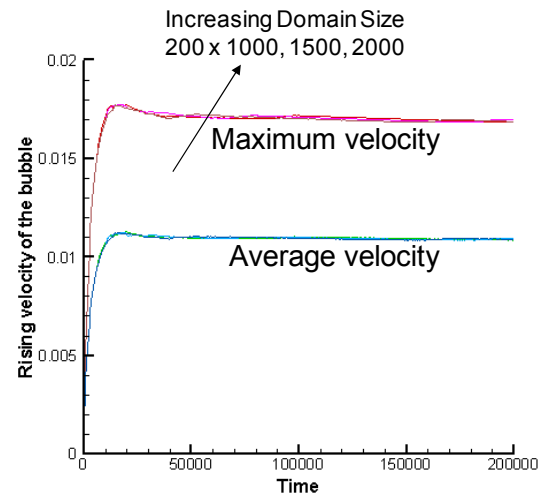
Fig. 6.41: Time variation of the upward velocity of a single vapor bubble in a quiescent liquid. Both the maximum velocity (maximum fluid velocity in the bubble region) as well as the area-averaged velocity of the bubble are shown in the figure. Simulation parameters are same as in Fig. 6.40.

In order to study the effects of the location of the Top wall on the bubble's rise and terminal velocity, several simulations have been performed with different sizes of the computational domain. Increasing the height of the domain from 1000 to 2000 grid points did not have significant effect on the bubble's rise velocity indicating that the Top wall has a minimal effect on bubble's motion when bubble is sufficiently far away from it. Upward velocity of the bubble is plotted as a function of time for three different domain sizes and two gravity values in Fig. 6.42(a, b). Other parameters of the simulation are listed below the figure.

Further simulations are performed to study the effect of increasing buoyancy force on the terminal shape and the rise velocity of the bubble. Results are presented in Fig. 6.43 which are in good qualitative agreement with the experimental observations (see Fig. 6.44). An increase in gravity corresponds to increase in buoyancy force which leads to a higher initial acceleration and a higher terminal velocity. The deformation in the shape of the bubble is also larger for higher values of gravity which may ultimately lead to break-up of a bubble into two satellite bubbles as shown in Fig. 6.45.



(a) $g = 10^{-5}$



(b) $g = 0.5 \times 10^{-5}$

Fig. 6.42: Effect of Top wall on rising velocity of a single vapor bubble in a quiescent liquid for three different domain sizes ($L_x \times L_y$). Both the maximum velocity and the area-averaged velocity of the bubble are shown in the figure. Simulation parameters are same as in Fig. 6.40.

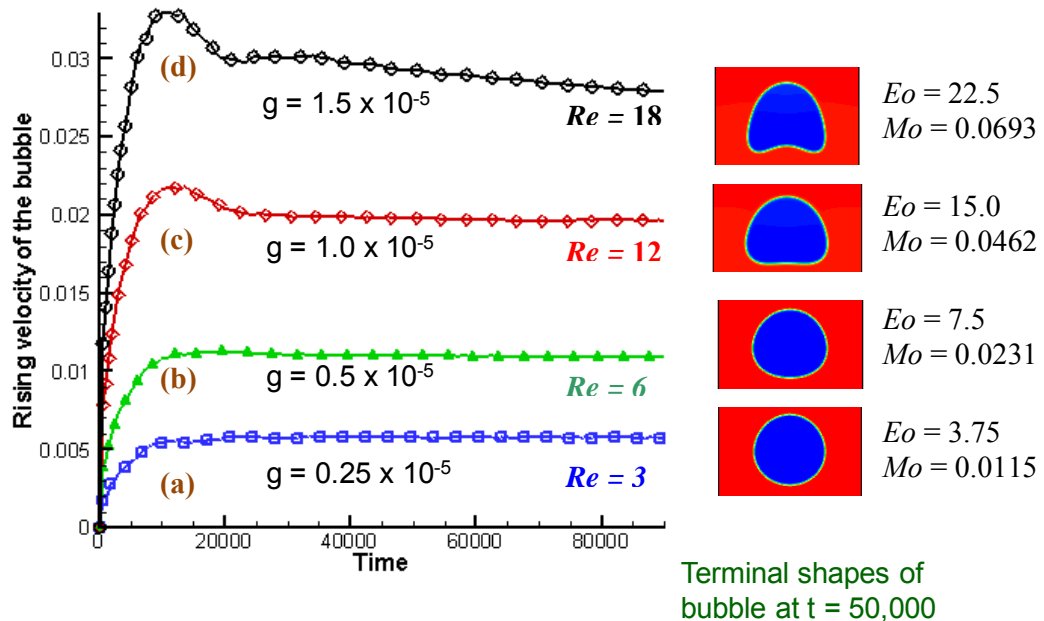


Fig. 6.43: Effect of increasing gravity (or buoyancy force) on rising velocity and terminal shape of a single vapor bubble in a quiescent liquid. Velocities are averaged over the area of the bubble. Simulation parameters are same as in Fig. 6.40. Application of gravity based

conversion between lattice and physical units (see Appendix G, section G.1.2) show that different gravity values in the figure correspond to different spatial grid sizes (in physical units), which leads to the following bubble diameters in the figure: (a) 2 mm, (b) 2.5 mm, (c) 3.19 mm and (d) 3.65 mm.

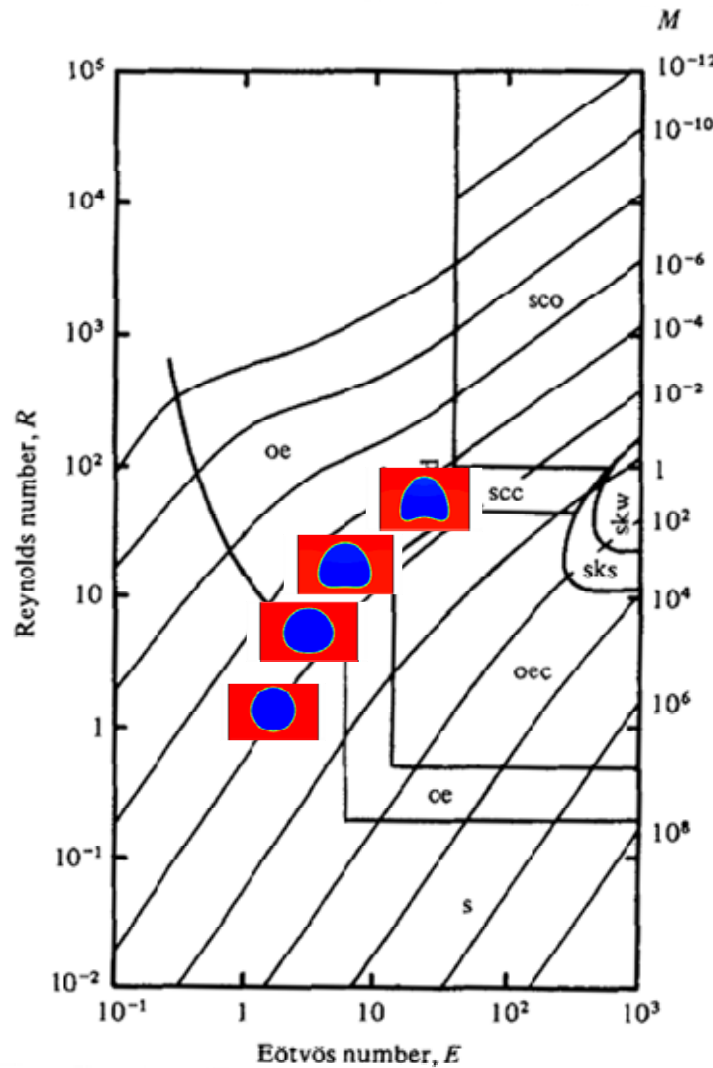


Fig. 6.44: Different bubble shapes shown in Fig. 6.43 are in good agreement with the experimental shape regime map of Bhaga and Weber (1981).

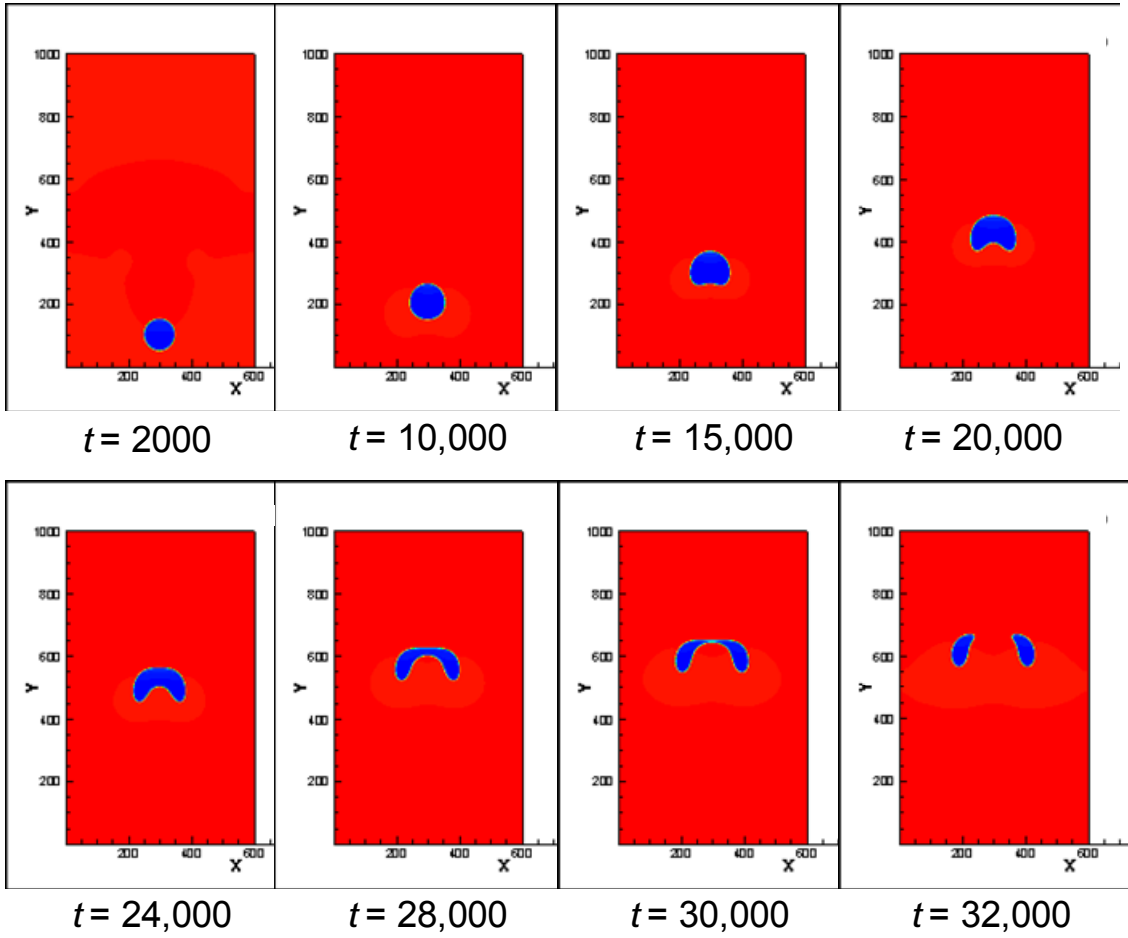


Fig. 6.45: Break up of a single rising vapor bubble in a quiescent liquid. Parameters for the simulation are: $\rho_l = 1.0$, $\rho_v = 0.25$, $R = 50$, $\sigma = 5 \times 10^{-3}$, $g = 1.5 \times 10^{-5}$, $Lx \times Ly = 600 \times 1000$. (Red: liquid; blue: vapor.) (Lee-Fischer LB model)

6.9.3 Results obtained using the AILB model

3D simulation results obtained using the AILB model are shown in Fig. 6.46 for a density ratio of 2.52. A coarse grid of $60 \times 60 \times 60$ is used in the 3D simulation. Results are in good qualitative agreement with the experimental observations. Two dimensional results at a higher density ratio of ~ 40 are shown in Fig. 6.47. As expected, deformation increases as the value of gravity is increased in the simulations (from (a) to (e)).

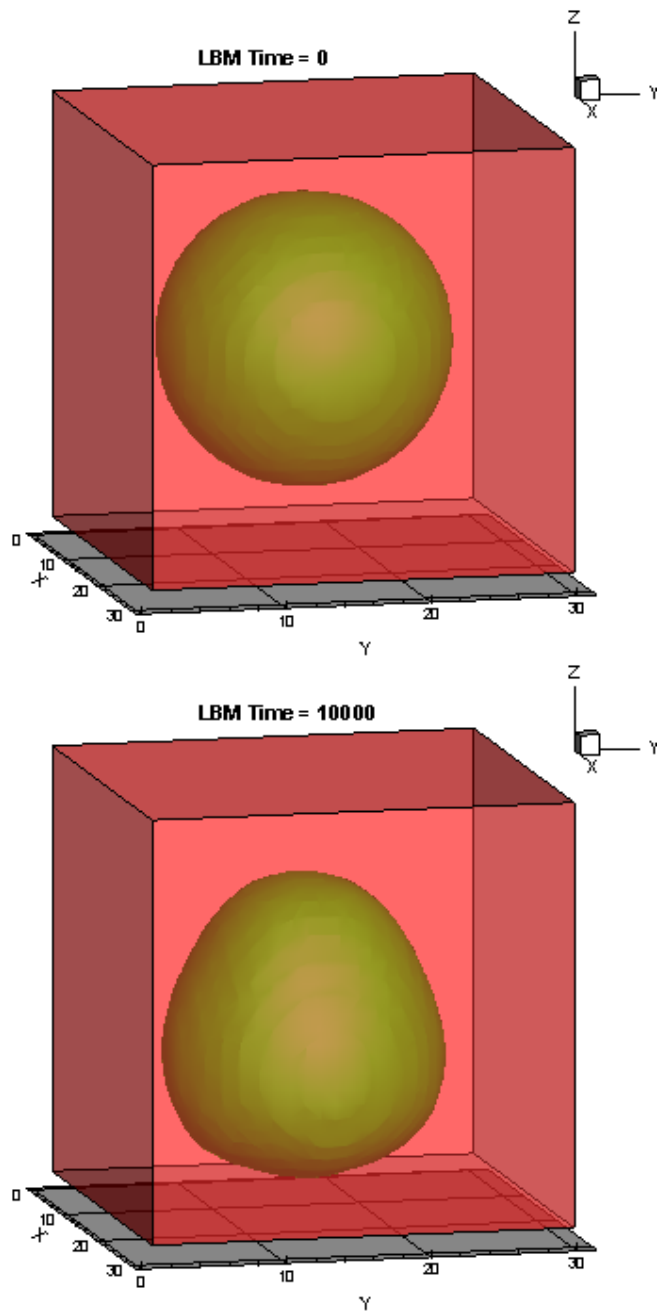


Fig. 6.46: 3D simulation of a single rising bubble. Parameters for the simulation are: Periodic domain, size $60 \times 60 \times 60$ (figure shown on half scale), $\sigma = 0.005$, $R = 15$, $D = 3$, $T_R = 0.95$, density ratio = 2.52, $\rho_{liq} = 1.46173$, $\rho_{vap} = 0.579015$, density contour of $\rho = 1$ is shown.

Result are shown at $t = 0$ and 10,000. (AILB model with no scaling).

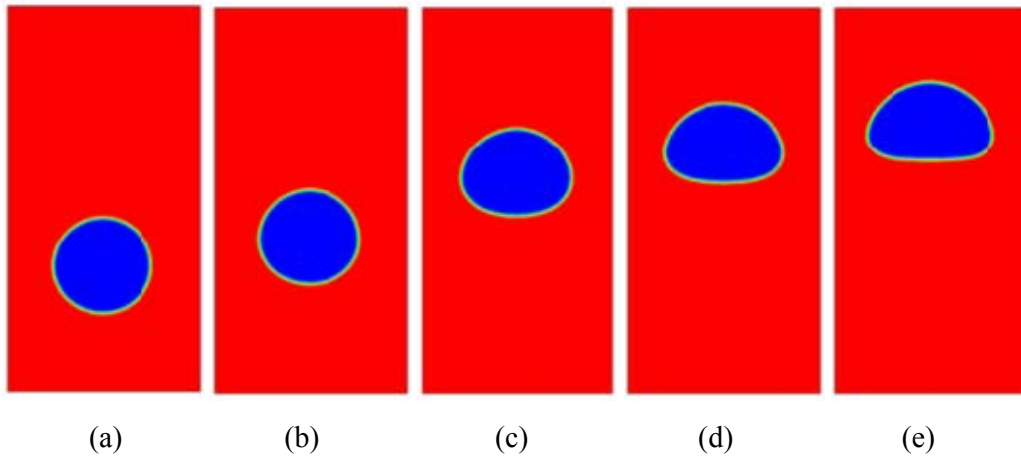


Fig. 6.47: Simulation of a rising bubble in a quiescent liquid. Parameters for the simulation are: North-South walls, 200×400 , $T_R = 0.6$, $a = 9/8$, $b = 1/3$, $\rho_l^{sat} = 2.31156$, $\rho_v^{sat} = 0.0597781$, $\tau_l = 0.5$, $\tau_v = 0.1$, $\sigma = 0.025$, $D = 3$, $S_f = 0.05$, shapes at $t = 20,000$, $R = 50$; (a) $g = 0.1 \times 10^{-5}$, (b) $g = 0.2 \times 10^{-5}$, (c) $g = 0.5 \times 10^{-5}$, (d) $g = 0.75 \times 10^{-5}$, (e) $g = 1 \times 10^{-5}$. (Scaled AILB model)

6.10 Some guidelines to avoid shrinkage of the dispersed phase

Approach to equilibrium in the Gibbs-Duhem equation based LB models is driven by the gradient of chemical potential which is similar to the Cahn-Hilliard diffusion in the phase-field based methods. Since the LB model is governed by an overall optimization of free energy, it is susceptible to violate mass conservation of the two phases. For example, in a simulation of single bubble (or droplet), it is possible that the total free energy of the system is reduced if the bubble shrinks while simultaneously drifting the bulk densities away from their initialized values. In the shrinking process, the interfacial energy is reduced at the expense of an increase in the bulk energy which is permissible in the Cahn-Hilliard framework. This, however, could result in violating mass conservation for the bubble. Theoretical analysis of the drops' spontaneous shrinkage and its impact on mass conservation in phase-field simulations are discussed in Yue et al. (2007).

Based on the observations from the numerical experiments and the phase-field two-phase models, some guidelines to avoid significant mass loss from the LB system are suggested below:

- In the simulations, use of a very large computational domain relative to the dispersed phase should be avoided. If the volume ratio (volume of computational box divided by the volume of bubble) is very high, the bubble is susceptible to significant shrinking. Bubbles below a certain critical radius may even disappear when evolved in time due to this reason.
- The Cahn number should be small (i.e. $Cn < < 1$). Cahn number is defined as

$$Cn \equiv \frac{D}{r_0}, \text{ where } D \text{ is the interface thickness parameter and } r_0 \text{ is the radius of a}$$

bubble (or drop). Usually, choosing a value of D below 3 results in deformed interfaces, therefore, one should avoid choosing a very small number for D . Therefore, a larger radius of the bubble should be chosen in order to have a small Cahn number.

6.11 References

Aarts, D. G. A. L., Lekkerkerker, H. N. W., Guo, H., Wegdam, G. H., Bonn, D., 2005. Hydrodynamics of droplet coalescence. *Phy. Rev. Lett.* 95, 164503.

Basagaoglu, H., Green, C.T., Meakin, P., McCoy, B.J., 2004. Lattice-Boltzmann simulation of coalescence-driven island coarsening. *J. Chem. Phys.* 121(16), 7987-7995.

Bhaga, D., Weber, M.E., 1981. Bubbles in viscous liquids: shapes, wakes and velocities. *J. Fluid Mech.* 105, 61-85.

Bugg, J.D., Mack, K., Rezkallah, K.S., 1998. A numerical model of Taylor bubbles rising through stagnant liquids in vertical tubes. *Int. J. Multiphase Flow* 24, 271-281.

Chen, L., Garimella, S.V., Reizes, J.A., Leonardi, E., 1999. The development of a bubble rising in a viscous liquid. *J. Fluid Mech.* 387, 61-96.

Chen, T., Chung, J.N., 2002. Coalescence of bubbles in nucleate boiling on microheaters. *Int. J. Heat Mass Transfer* 45, 2329-2341.

Cristea, A., Sofonea, V., 2003. Reduction of spurious velocity in finite difference lattice Boltzmann models for liquid-vapor systems. *Int. J. Mod. Phys.* 14, 1251-1266.

Duchemin, L., Eggers, J. Josserand, C., 2003. Inviscid coalescence of drops. *J. Fluid Mech.*, 487, 167-178.

Eggers, J., 1997. Nonlinear dynamics and breakup of free surface flows. *Rev. Mod. Phys.* 69, 865-929.

Frank, X., Funfschilling, D., Midoux, N., Li, H.Z., 2006. Bubbles in a viscous liquid: lattice Boltzmann simulation and experimental validation. *J. Fluid Mech.* 546, 113-122.

Fritz, W., 1935. Maximum volume of vapor bubbles. *Physik Zeitschr.* 36, 379-384.

Gupta, A., Kumar, R., 2008. Lattice Boltzmann simulation to study multiple bubble dynamics, *Int. J. Heat Mass Transfer* 51, 5192-5203.

Harmathy, T.Z., 1960. Velocity of large drops and bubbles in media of infinite or restricted extent. *A.I.Ch.E. Journal* 6, 281-288.

He, X., Chen, S., Zhang, R., 1999a. A lattice Boltzmann scheme for incompressible multiphase flow and its application in simulation of Rayleigh-Taylor instability. *J. Comp. Phys.* 152, 642-663.

He, X., Chen, S., Zhang, R., Doolen, G.D., 1999b. On the three-dimensional Rayleigh-Taylor instability. *Phys. Fluids* 11, 1143.

Hysing, S., Turek, S., Kuzmin, D., Parolini, N., Burman, E., Ganesan, S., Tobiska, L., 2008. Quantitative benchmark computations of two-dimensional bubble dynamics. *Int. J. Numer. Meth. Fluids*, DOI: 10.1002/fld.1934.

Hua, J., Lou, J., 2007. Numerical simulation of bubble rising in viscous liquid. *J. Comp. Phys.* 222, 769-795.

Kurtoglu, I.O., Lin, C.L., 2006. Lattice Boltzmann study of bubble dynamics. *Numerical Heat Transfer B* 50, 333-351.

Li, D., 1996. Coalescence between small bubbles: effects of surface tension gradient and surface viscosities. *J. Colloid & Interface Sci.* 181, 34-44.

Li, J., Bulusu, V., Gupta, N.R., 2008. Buoyancy-driven motion of bubbles in square channels. *Chem. Engg. Sci.* 63, 3766-3774.

Martula, D.S., Bonnecaze, R.T., Lloyd, D.R., 2003. The effects of viscosity on coalescence-induced coalescence. *Int. J. Multiphase Flow* 29, 1265-1282.

Menchaca-Rocha, A., Martinez-Davalos, A., Nunez, R., 2001. Coalescence of liquid drops by surface tension, *Phy. Rev. E* 63, 046309.

Mukundakrishnan, K., Quan, S., Eckmann, D.M., Ayyaswamy, P.S., 2007. Numerical study of wall effects on buoyant gas-bubble rise in a liquid-filled finite cylinder. *Phy. Rev. E* 76, 036308.

Ribeiro P.C., Mewes, D., 2006. On the effect of liquid temperature upon bubble coalescence. *Chem. Engg. Sci.* 61, 5704-5716.

Sankaranarayanan, K., Shan, X., Kevrekidis, I.G., Sundaresan, S., 1999. Bubble flow simulations with the lattice Boltzmann method. *Chem. Engg. Sci.* 54, 4817-4823.

Shan, X., 2006. Analysis and reduction of the spurious current in a class of multiphase lattice Boltzmann models. *Phys. Rev. E* 73, 047701.

Sharp, D.H., 1984. An overview of Rayleigh-Taylor instability. *Physica 12D*, 3-8.

Takada, N., Misawa, M., Tomiyama, A., Hosokawa, S., 2001. Simulation of bubble motion under gravity by lattice Boltzmann method. *J. Nuc. Sci. Tech.* 38(5), 330-341.

Wagner, A.J., 2002. The origin of spurious velocities in lattice Boltzmann. *Int. J. Mod. Phys. B*, 1-4.

Wu, M., Cubaud, T., Ho, C.M., 2004. Scaling law in liquid drop coalescence driven by surface tension. *Phys. Fluids* 16, L51-L54.

Yang, Z.L., Palm, B., Sehgal, B.R., 2002. Numerical simulation of bubbly two-phase flow in a narrow channel. *Int. J. Heat Mass Transfer* 45, 631-639.

Yue, P., Zhou, C., Feng, J.J., 2007. Spontaneous shrinkage of drops and mass conservation in phase-field simulations. *Short note in J. Comp. Phys.* 223, 1-9.

Chapter 7

Peng-Robinson Equation of State (P-R EOS) based two-phase model

A consistent LBM formulation for the simulation of a two-phase water-steam system is presented in this chapter. Results of initial model validation over a range of thermodynamic conditions typical of Boiling Water Reactors (BWRs) are also shown. The interface between the two coexisting phases is captured from the dynamics of the model itself, i.e., no interface tracking is needed. An inter-particle potential model proposed by Zhang & Chen (2003) is used in this study to segregate the two coexisting phases. The Exact Difference Method (EDM) proposed by Kupershtokh (2004) is employed to account for body forces in the LBM algorithm. The developed model is based on the Peng-Robinson (P-R) non-ideal equation of state and can quantitatively approximate the phase-coexistence curve for water at different temperatures ranging from 125 to 325 °C. Consequently, coexisting phases with large density ratios (up to ~ 1000) may be simulated. Two-phase models in the 200-300 °C temperature range are of significant importance to nuclear engineers since most BWRs operate under similar thermodynamic conditions. Simulation of bubbles and droplets in a gravity-free environment of the corresponding coexisting phase until steady state is reached satisfies Laplace law at different temperatures and thus, yield the surface tension of the fluid. Comparing the surface tension thus calculated using the LBM to the corresponding experimental values for water, the LBM lattice unit (lu) can be scaled to the physical units. Using this approach, spatial scaling of the LBM emerges from the model itself and is not imposed externally.

7.1 D₂Q₉ scheme with LBGK approximation

The Lattice Boltzmann equation with streaming and single relaxation time collision operator (often known as BGK approximation, Bhatnagar et al. (1954)) is

$$f_a(\mathbf{x} + \mathbf{e}_a \Delta t, t + \Delta t) = f_a(\mathbf{x}, t) + \frac{[f_a^{eq}(\mathbf{x}, t) - f_a(\mathbf{x}, t)]}{\tau} \quad (7.1)$$

where $f_a(\mathbf{x}, t)$ is the streaming part and $\frac{[f_a^{eq}(\mathbf{x}, t) - f_a(\mathbf{x}, t)]}{\tau}$ is the collision part. Here, f_a is the density of particles in the “ a ” direction, and f_a^{eq} is the equilibrium distribution function. Moreover, \mathbf{x} is position vector, \mathbf{e}_a are velocity vectors, t is time, Δt is the time step, and τ is the relaxation time that captures the kinematic viscosity ν of the fluid given by $\nu = \frac{2\tau-1}{6}$.

On a simple D₂Q₉ lattice (two-dimensional lattice with 8 velocity directions and 1 rest state), the equilibrium distribution function f_a^{eq} is defined as,

$$f_a^{eq}(\mathbf{x}, t) = f_a^{eq}(\rho(\mathbf{x}, t), \mathbf{u}(\mathbf{x}, t)) = w_a \rho(\mathbf{x}, t) \left[1 + 3 \frac{\mathbf{e}_a \cdot \mathbf{u}}{c^2} + \frac{9}{2} \frac{(\mathbf{e}_a \cdot \mathbf{u})^2}{c^4} - \frac{3}{2} \frac{\mathbf{u}^2}{c^2} \right] \quad (7.2)$$

where the weights w_a are 4/9 for the rest particles ($a = 0$), 1/9 for $a = 1, 2, 3, 4$, and 1/36 for $a = 5, 6, 7, 8$, and $\sqrt{2}c$ is the maximum attainable macroscopic speed on the lattice.

Macroscopic variables such as the fluid density ρ and velocity \mathbf{u} are obtained in terms of

$f_a(\mathbf{x}, t)$:

$$\rho = \sum_a f_a \quad (7.3)$$

$$\mathbf{u} = \frac{1}{\rho} \sum_a f_a \quad (7.4)$$

7.2 Particle interaction potential and force

In order to simulate two coexisting phases in equilibrium, an inter-particle potential model proposed by Zhang & Chen (2003) is implemented. A non-ideal equation of state $p(\rho, T)$ (such as the Peng-Robinson equation of state for water and steam) is incorporated in this model by expressing the particle interaction force as the spatial gradient of a scalar function $U(\mathbf{x}, t)$,

$$\mathbf{F}_{\text{int}}(\mathbf{x}, t) = -\nabla U(\mathbf{x}, t) \quad (7.5)$$

$U(\mathbf{x}, t)$ is chosen to satisfy

$$U(\mathbf{x}, t) = p(\rho(\mathbf{x}, t), T(\mathbf{x}, t)) - \rho(\mathbf{x}, t) c_s^2 \quad (7.6)$$

in order to yield global momentum conservation. Here c_s^2 is the *lattice sound speed* and is equal to $c^2/3$ for the D₂Q₉ scheme. Now, by introducing interaction potential $\psi(\mathbf{x}, t)$ as

$$\psi^2(\mathbf{x}, t) = |U(\mathbf{x}, t)| \quad (7.7)$$

the interaction force $F_{\text{int}}(\mathbf{x}, t)$ can be written as

$$F_{\text{int}}(\mathbf{x}, t) = 2\psi(\mathbf{x}, t)\nabla\psi(\mathbf{x}, t) \quad (7.8)$$

In the above equations, the interaction potential (and force) depends upon the spatial and temporal grid via local density and local temperature governed by the non-ideal equation of state.

7.3 Numerical implementation on a D₂Q₉ lattice

For a grid point (i, j) of a D₂Q₉ lattice, the equation (7.8) can be numerically evaluated by taking account of the interaction potentials at its nearest— $(i+1, j)$, $(i-1, j)$, $(i, j+1)$, $(i, j-1)$ —and the next-nearest— $(i+1, j+1)$, $(i-1, j-1)$, $(i+1, j-1)$, $(i-1, j+1)$ —neighbor sites. This leads to a six point scheme for the potential gradient in the x - and y -directions, and may be written as,

$$\begin{aligned} \frac{\partial\psi}{\partial x}(i, j) &= w_{\text{near}}[\psi(i+1, j) - \psi(i-1, j)] \\ &\quad + w_{\text{next-near}}[\psi(i+1, j+1) - \psi(i-1, j+1) + \psi(i+1, j-1) - \psi(i-1, j-1)] \end{aligned} \quad (7.9)$$

$$\begin{aligned} \frac{\partial\psi}{\partial y}(i, j) &= w_{\text{near}}[\psi(i, j+1) - \psi(i, j-1)] \\ &\quad + w_{\text{next-near}}[\psi(i+1, j+1) - \psi(i+1, j-1) + \psi(i-1, j+1) - \psi(i-1, j-1)] \end{aligned} \quad (7.10)$$

To find the weighting coefficients w_{near} and $w_{\text{next-near}}$, the potential gradient may be approximated by using the method of finite difference in the x -direction (assuming $\Delta x = \Delta y = 1$),

$$\begin{aligned} \frac{\partial\psi}{\partial x}(i, j) &= \frac{1}{2}[\psi(i+1, j) - \psi(i-1, j)] \\ &= \frac{1}{4}[(\psi(i+1, j+1) + \psi(i+1, j-1)) - (\psi(i-1, j+1) + \psi(i-1, j-1))] \end{aligned} \quad (7.11)$$

In the above equation, a second order central finite-difference scheme is used in the x -direction to evaluate the potential gradient at (i, j) in terms of potential values at $(i-1, j)$ and $(i+1, j)$. These neighboring node potentials are further approximated by averaging the

corresponding potential values of the neighboring nodes in the y -direction. The equation for the potential gradient in the y -direction can also be written in a similar way. From equations (7.9) and (7.11), it is clear that the correct determination of the weighting coefficients requires,

$$w_{near} + 2w_{next-near} = \frac{1}{2} \quad (7.12)$$

and $w_{near} > w_{next-near}$ since nearest neighbors should have more influence when compared to the next-nearest neighbors. For the LBM simulations reported here, w_{near} and $w_{next-near}$ are chosen to be $w_{near} = 4w_{next-near} = \frac{1}{3}$.

There is a need for some flexibility in predicting the same coexistence curve from the LBM simulations when using different equations of state. To provide this flexibility, a parameter ξ is inserted into the expression for the interaction force by approximating $\psi(\mathbf{x}, t)$ that appears in equation (7.8), for example, in the x -direction as

$$\psi_{approx}(i, j) = \xi(\psi(i+1, j) + \psi(i-1, j)) + (1-2\xi)\psi(i, j) \quad (7.13)$$

Depending upon the equation of state being modeled, a ξ value may be determined that leads to LBM results that accurately match the theoretical saturated densities for both the phases (Medvedev et al., 2007). Several numerical experiments of spinodal decomposition phase-segregation are carried out at the same temperature using different ξ values in the simulations. A ξ value of -0.088 is found to yield good agreement with the theoretical coexistence curve constructed using the Peng-Robinson (P-R) equation of state (described later in Sec. 7.5), and for which the resulted saturated densities are in close agreement with the theoretically obtained (using the Maxwell construction on the P-R equation of state) saturated densities of liquid and vapor phases. While performing numerical experiments it is observed that the parameter ξ only needs to be tuned once for any selected temperature in the coexistence region and then may be used for other temperatures as a constant to yield results in fairly good agreement with the theoretical ones.

7.4 Simulation of the body forces

In the LBM, the incorporation of body forces (particle interaction, gravitational or externally applied forces) usually affects the stability of multi-phase simulations. Numerical

instability is caused by the large changes in velocity in the interface region during each time step. In order to increase the stability of the LBM simulations, an Exact Difference Method (EDM) is proposed by Kupershtokh (2004) which combined with the general approximation of forcing functions results in reduced spurious currents at the interfaces and accurate reproduction of the phase-coexistence curve. In EDM, a term Δf_a representing the change in the distribution function is added to the collision term to account for the change in momentum due to body forces. Thus, at the time step $(t + \Delta t)$

$$f_a(\mathbf{x} + \mathbf{e}_a \Delta t, t + \Delta t) = f_a(\mathbf{x}, t) + \frac{[f_a^{eq}(\mathbf{x}, t) - f_a(\mathbf{x}, t)]}{\tau} + \Delta f_a \quad (7.14)$$

where Δf_a equals to the difference in the equilibrium distribution function evaluated at the constant density as the velocity is varied for each time-step Δt , and is given by,

$$\Delta f_a = f_a^{eq}(\rho, \mathbf{u} + \Delta \mathbf{u}) - f_a^{eq}(\rho, \mathbf{u}) \quad (7.15)$$

Here, change in velocity $\Delta \mathbf{u}$ is evaluated by computing the change in momentum $\Delta \mathbf{p}$ at each time-step due to body forces, and is given by

$$\Delta \mathbf{u} = \frac{\Delta \mathbf{p}}{\rho} = \frac{\mathbf{F}(\mathbf{x}, t) \Delta t}{\rho} \quad (7.16)$$

7.5 Peng-Robinson (P-R) equation of state

An equation of state (EOS) describes the relationship between temperature, pressure and density (volume) of a fluid. One such EOS is the Peng-Robinson (P-R) equation of state (McQuarrie & Simon (1998)). It is widely used for determining the state of various fluids categorized by different accentric factors. The *accentric factor* (ω) depends on the molecular structure of the fluid and is determined from its critical properties. Values of ω are tabulated in thermodynamic tables for various fluids. P-R EOS, which is a three-parameter (T_c , p_c and ω , defined below) cubic equation, fairly accurately captures the saturated densities over most of the liquid-vapor equilibrium curve. For water and steam, the accentric factor $\omega = 0.3443$ leads to predicted values of saturated densities that agree very well with experimental data. This comparison is shown in Fig. 7.1. Although more sophisticated equations of state — fitted to experimental data — can be developed and implemented in the LBM model, the P-R EOS is chosen due to its flexibility in changing the type of fluid by varying the accentric factor ω .

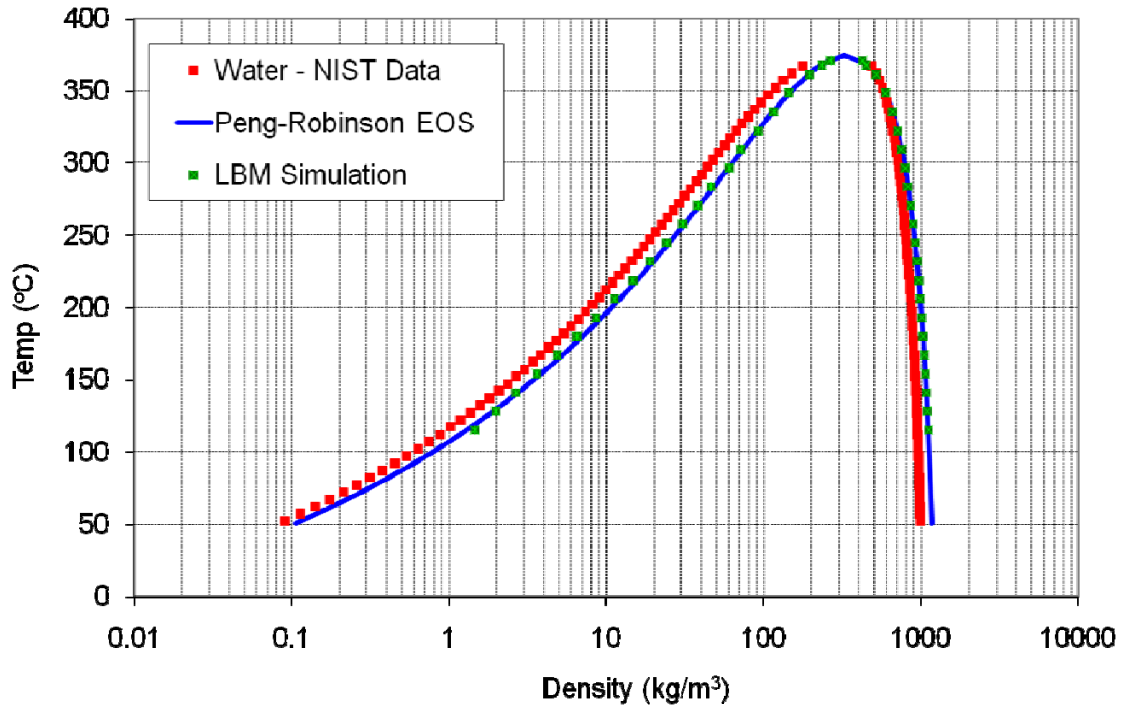


Fig. 7.1: Comparison of the theoretical coexistence curve (Maxwell construction) and the corresponding LBM simulation for Peng-Robinson (P-R) equation of state. Saturated water and vapor densities from NIST tables are also shown.

The P-R equation of state is:

$$p = \frac{\rho RT}{1-b\rho} - \frac{a\alpha(T)\rho^2}{1+2b\rho-b^2\rho^2} \quad (7.17)$$

where $\alpha(T) = [1 + (0.37464 + 1.54226\omega - 0.26992\omega^2)(1 - \sqrt{T/T_c})]^2$ and $a = 0.45724R^2T_c^2/p_c$, $b = 0.0778RT_c/p_c$. Here, T_c and p_c represent critical temperature and critical pressure of the fluid under consideration, respectively. For water, T_c is 647.1 K and p_c is 22.064 MPa. In simulations reported here, the constants a , b and R are set to be 2/49, 2/21 and 1, respectively. The critical properties of the LBM fluid are then evaluated in terms of these constants. Using the law of corresponding states (McQuarrie & Simon (1998)), the reduced properties of lattice fluid can then be converted to real fluid properties.

Table 7.1: Comparison of saturated properties of water obtained from NIST tables and LBM simulations at various temperatures.

T / T_c	T (°C)	$\rho_{\text{sat, liquid}}$ (kg / m³)		$\rho_{\text{sat, vapor}}$ (kg / m³)		p_{sat} (MPa)	
		NIST	LBM	NIST	LBM	NIST	LBM
0.60	115.11	945.62	1117.36	1.02	1.46	0.18	0.18
0.62	128.05	937.49	1093.01	1.37	1.98	0.25	0.26
0.64	140.99	924.48	1077.74	2.07	2.66	0.38	0.35
0.66	153.94	915.27	1061.57	2.67	3.60	0.50	0.49
0.68	166.88	900.65	1044.51	3.83	4.85	0.73	0.68
0.70	179.82	885.01	1026.35	5.37	6.49	1.05	0.92
0.72	192.76	874.00	1007.07	6.65	8.61	1.31	1.24
0.74	205.70	856.54	986.53	9.01	11.31	1.79	1.65
0.76	218.65	837.84	964.56	12.03	14.70	2.40	2.16
0.78	231.59	824.63	941.06	14.47	18.91	2.89	2.79
0.80	244.53	803.53	915.81	18.90	24.11	3.77	3.56
0.82	257.47	788.53	888.55	22.47	30.49	4.46	4.47
0.84	270.41	764.36	859.00	28.96	38.28	5.66	5.56
0.86	283.36	746.97	822.79	34.20	46.15	6.60	6.64
0.88	296.30	718.53	793.43	43.82	60.33	8.21	8.36
0.90	309.24	686.48	747.75	56.27	71.51	10.12	9.74
0.92	322.18	662.45	707.96	66.74	92.21	11.56	11.86
0.94	335.12	620.65	657.16	87.37	115.75	14.03	14.01
0.96	348.07	586.88	591.89	106.31	144.42	15.90	16.28
0.98	361.01	516.71	518.09	151.35	195.95	19.09	19.10
0.99	367.48	481.53	445.58	177.15	234.35	20.27	20.55

P-R EOS can be written as a cubic equation in V (replace ρ by $1/V$ in Eq. (17)) and thus, has three real roots for $T < T_c$. The benefit of the cubic nature is that it can describe both the gaseous and the liquid phases of a fluid. Plotting p vs. V at constant T and then applying the so-called *Maxwell equal-area construction* (McQuarrie & Simon (1998)), yields the phase-coexistence curve. Fig. 7.1 compares the theoretical coexistence curve with the one obtained using the LBM simulations. It can be seen that the LBM results agree well with the theoretical results. Moreover, in Fig. 7.1, the saturated water and vapor densities from NIST tables (Harvey et al. (2004)) are also plotted for comparison. It is observed that, when compared to the water-steam data at a selected temperature, P-R EOS slightly over-predicts the saturated vapor and water densities. However, the calculated density ratio of saturated liquid and vapor matches very well with the water-steam data at different temperatures as shown in Fig. 7.2. The saturated properties obtained from NIST data and LBM simulations are compared in Table 7.1 for different temperatures.

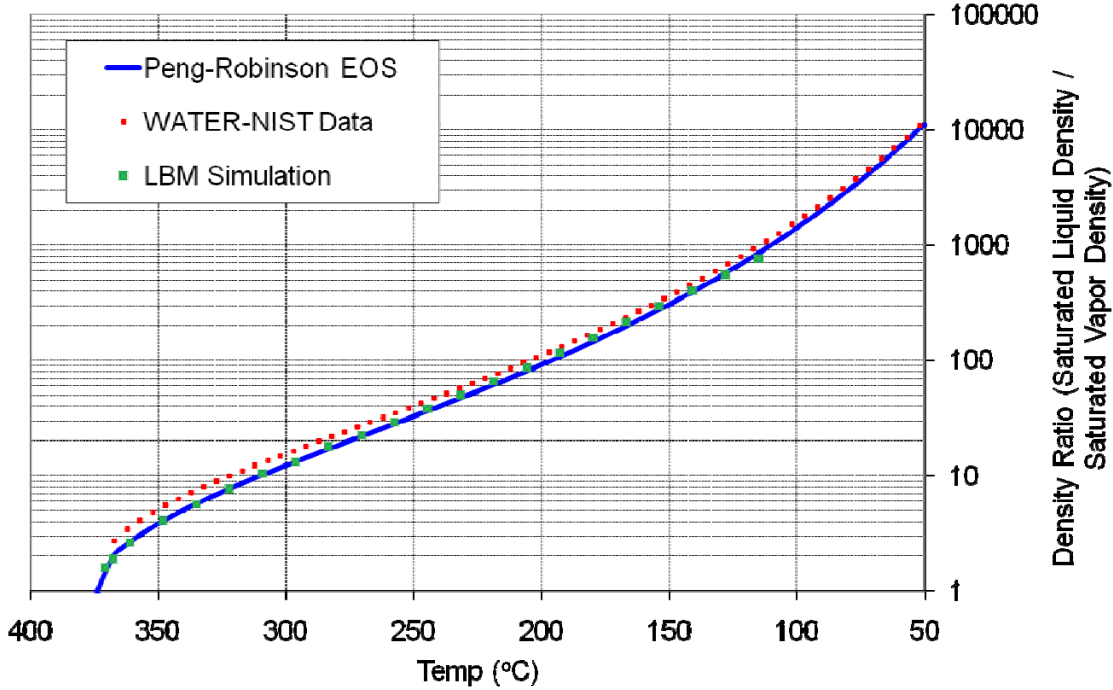


Fig. 7.2: Comparison of density ratios (saturated water / saturated vapor) obtained from Peng-Robinson EOS, NIST saturated property tables, and from corresponding LBM simulations at different temperatures.

7.6 Kinematic viscosities of liquid and vapor phases

In the LBM-BGK algorithm, the kinematic viscosity of a fluid ν is explicitly determined by the prescribed single relaxation time τ from the relationship, $\nu = \frac{2\tau - 1}{6}$. This functional form gives a unique value for the kinematic viscosity of the fluid irrespective of the multiple phases involved. However, in order to accurately model the flow dynamics of a single-component two-phase fluid, it is essential to have different kinematic viscosities for the two phases at any given temperature. This can be accomplished by expressing the relaxation time τ as a linear function of the local fluid density $\rho(x, y)$ constrained by the saturation densities of both phases. Thus, $\tau(\rho)$ can be written as (Angelopoulos et al. (1998)),

$$\tau(\rho) = \left[\frac{\tau(\rho_L) - \tau(\rho_V)}{\rho_L - \rho_V} \right] \rho + \left[\frac{\tau(\rho_V)\rho_L - \tau(\rho_L)\rho_V}{\rho_L - \rho_V} \right] \quad (7.18)$$

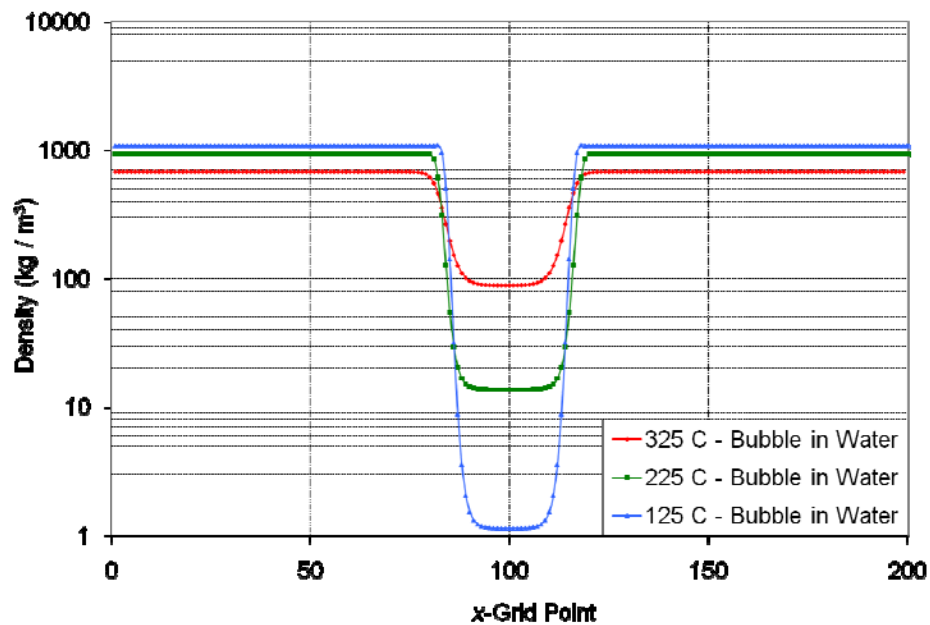
where $\tau(\rho_L)$ and $\tau(\rho_V)$ represent, at the given temperature, the relaxation times corresponding to the saturation density of the liquid and vapor phases, respectively. These phase-specific relaxation times are calculated by knowing the corresponding phase kinematic viscosities.

7.7 Results and discussions

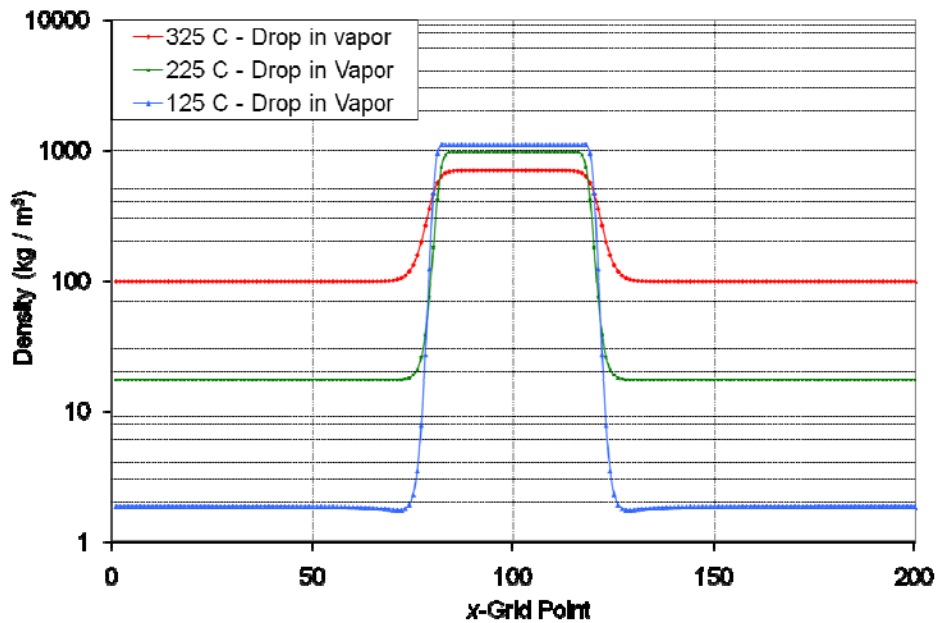
The LBM simulations are performed for a xy -periodic domain of size 200×200 lattice-units (lu). Initially, a water drop (or vapor bubble) of $20 \times 20 lu$ radius is placed at the center of the domain surrounded by the corresponding coexisting phase (saturated vapor for liquid *drop at the centre* and saturated liquid for vapor *bubble in the centre*). The simulation is evolved in time till the steady state is reached. After 40,000 time-steps, the difference in simulated observed variables (velocities, densities etc.) for each consecutive 1000 time-steps reaches below 10^{-6} units. This is taken as the criterion for the steady-state. Fig. 7.3 shows the steady-state density variation along a line passing through the center of the drop (or bubble) for different temperatures. It is observed that the interface between the two phases becomes thicker as temperature increases for both the drop and the bubble.

Using the Laplace law, the surface tension of water-steam system may be estimated. A series of bubbles of various sizes (20 to 50 lu radius) are simulated at different temperatures. After 40,000 time steps, the steady-state radii and inside/outside densities of the bubble are evaluated. Densities are then converted to the corresponding pressures using P-R EOS and the difference between the inside and the outside pressure ΔP of the bubble is computed. According to the Laplace law, for a 2D droplet/bubble, the pressure difference is given by

$$\Delta P = \frac{\sigma}{R} \quad (7.19)$$



(a)



(b)

Fig. 7.3: The LBM simulation of a stationary saturated vapor bubble (saturated liquid drop) in equilibrium with its saturated liquid (saturated vapor) environment at different temperatures. A periodic domain of 200×200 grid size is initialized with one phase over a circular shape (of 20 grid-point radius) surrounded by another phase in the remaining space. A total of 40,000 time-steps are simulated to achieve steady state for both cases: (a) *vapor bubble in liquid*; and (b) *liquid drop in vapor*.

In Fig. 7.4, ΔP is plotted against the inverse of the bubble radius ($1/R$) which yields straight lines of different slopes at different temperatures. As can be seen from Fig. 7.4, the spatial grid resolution of the LBM fluid is still in the lattice units (lu). Therefore, comparing the LBM surface tension (slope of ΔP vs. $1/R$) with experimental surface tension of water may give an approximate measure of the LBM grid size in physical units. Thus, we can write

$$\sigma_{LBM,lu} (MPa.lu) = f \sigma_{Water} (Pa.m) \quad (7.20)$$

where $\sigma_{LBM,lu}$ is the LBM surface tension in $MPa\text{-}lu$ units and σ_{Water} is the water surface tension in $Pa\text{-}m$ units, for example, as given by NIST. Here, f is a scaling factor with appropriate units to relate both the surface tensions. From Eq. (20), the estimate for 1 lattice unit in LBM is obtained as:

$$1 lu = f \times 10^{-6} m \quad (7.21)$$

With f close to 1/3000, the LBM surface tension when converted to physical units well predicts the surface tension values in NIST tables for water for different temperatures ranging from 125 °C to 325 °C. For water, 1 lattice unit is hence estimated to be close to 0.33 nm. Fig. 7.5 and Table 7.2 show comparison of the surface tensions of the LBM fluid and the values tabulated in NIST water property table (after the spatial scaling). Good agreement with macroscopic values suggests that the LBM approach is able to capture the surface tension phenomenon rather well at this scale. However, such a small lattice size is a concern for the computational viability of any realistic simulation and future work will refine the LBM model to allow capturing the correct surface tension while using a coarser lattice.

Next, some qualitative results for the two-phase test simulations performed in a zero-gravity periodic domain of 200 x 200 lattice dimension are presented. The local densities are allowed to evolve according to the LBM algorithm at a specified temperature until the steady state is reached. Simulations are performed at a temperature of 250 °C at which the coexisting phase density ratio equals to ~40. This temperature and the corresponding density ratio are of prime interest to nuclear engineers since most of the Boiling Water Reactors (BWRs) operate at this mean temperature. In Fig. 7.6, different stages of a coalescence process of two vapor bubbles (2D) are shown. Initially, at $t = 0$, the bubbles are separated by a very thin liquid layer of 1 lu thickness. As time evolves, the bubbles start coalescing with each other to

minimize the net interfacial energy and finally, leading to a single large bubble of area *approximately* equal to the sum of the areas of initial bubbles.

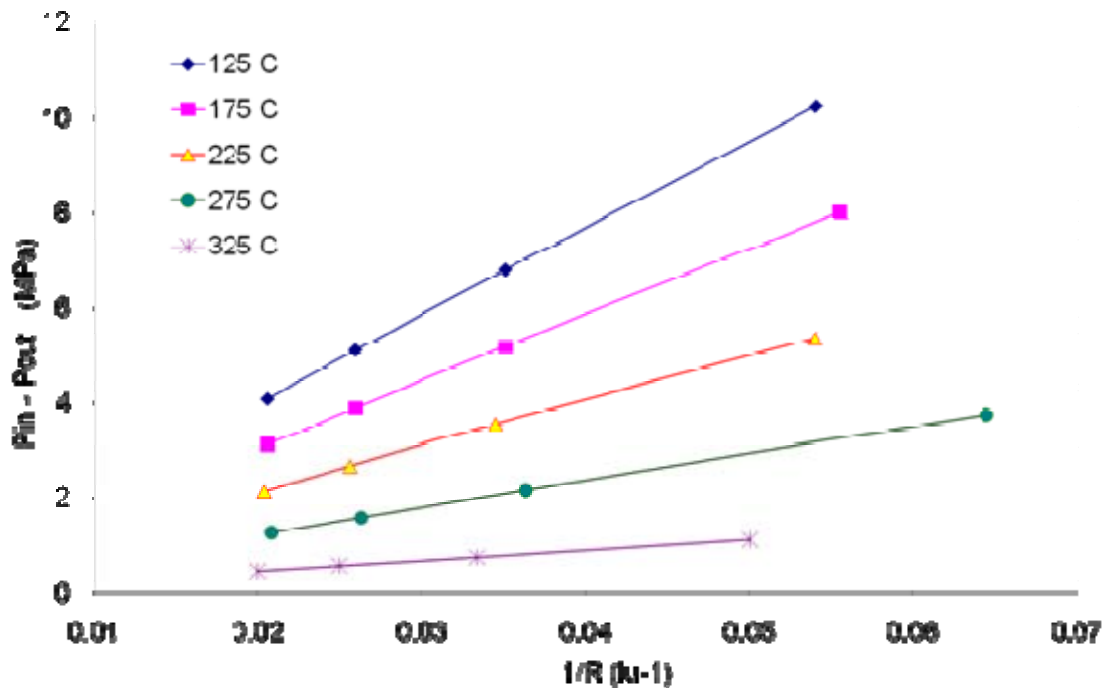


Fig. 7.4: Plot of pressure difference across bubble vs. inverse radius simulated at different temperatures. Results of the LBM simulations satisfy Laplace law and the slope of curves gives surface tension of the fluid at the corresponding temperature. Simulation domain is xy -periodic, and of 200×200 lattice unit size.

Table 7.2: Comparison of surface tension of water obtained from NIST tables and LBM simulations at various temperatures.

T (°C)	σ (N/m)	
	NIST	LBM
125	0.053955	0.059265
175	0.043302	0.045139
225	0.031903	0.030836
275	0.020163	0.018221
325	0.008774	0.006924

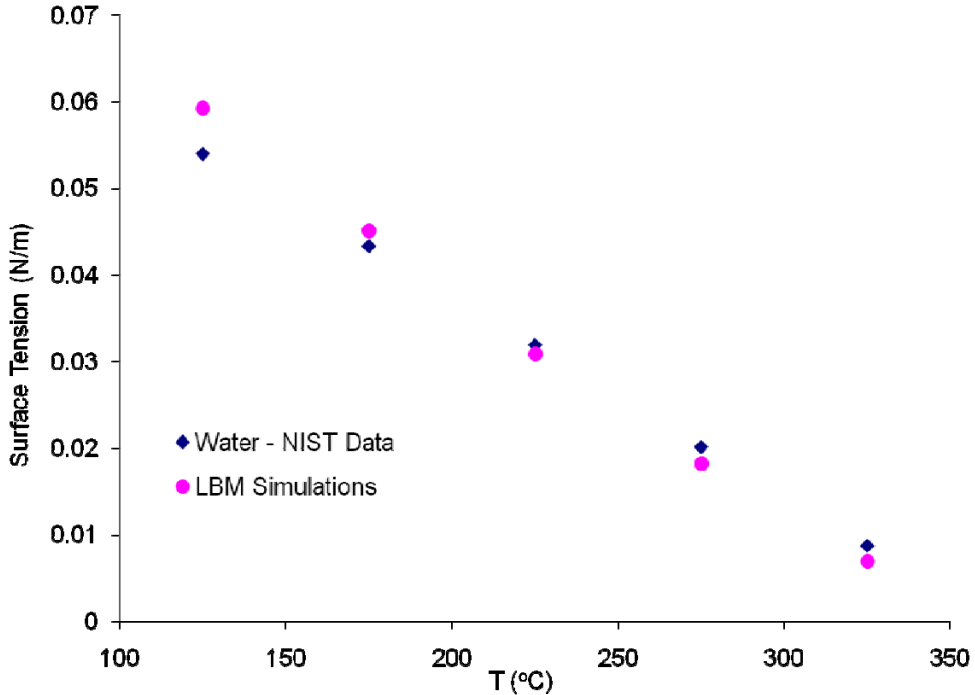


Fig. 7.5: A comparison of surface tension of water (NIST data) with the surface tension values obtained from the LBM simulations, after lattice scaling.

In Fig. 7.7, results of a simulation that models the interaction between a liquid film and a liquid droplet are shown. Initially, at $t = 0$, there exists a thin vapor film between the liquid film and the droplet. As time evolves, the drop experiences a cohesive force from the film and attaches to it. Now, the combined liquid chunk oscillates and reorganizes itself to minimize the net interfacial energy by minimizing its surface area. Finally, it leads to a thick liquid film of volume equal to the sum of the volumes of the liquid film and the droplet. In Figs. 7.8 and 7.9, results are shown for a thin liquid film of sinusoidal shape as it evolves after a sudden relaxation in the absence of any external force. By prescribing the sinusoidal shape as an initial condition, the system contains very high interfacial energy and tries to minimize it during relaxation to equilibrium over time. The evolution scenario is simulated for two different cases with equal film thickness and different amplitudes of the sinusoidal initial shape. In the case of a large amplitude sinusoidal wave, the film breaks up into several circular droplets (Fig. 7.8), while a relatively small amplitude wave damps out and evolves into a liquid film of uniform thickness (Fig. 7.9).

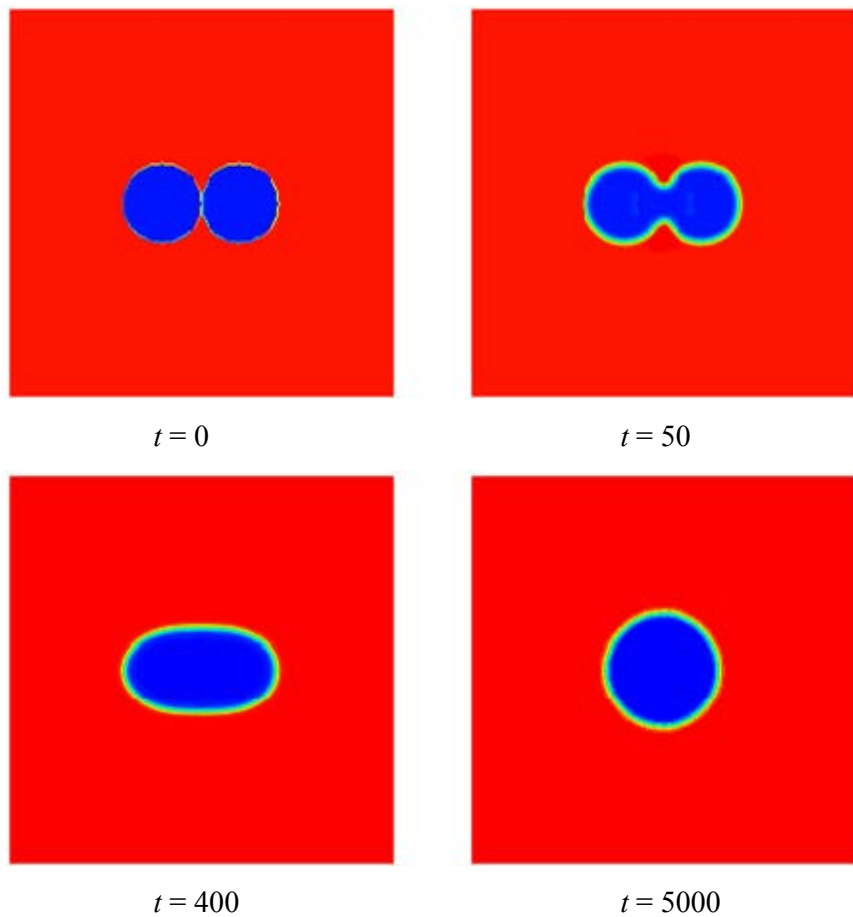


Fig. 7.6: Snapshots showing coalescence of 2D vapor bubbles at $T = 250$ °C. Densities of bubble (shown in blue) and liquid (shown in red) are 23.093 and 896.214 kg/m³, respectively. Ratio of kinematic viscosity of vapor and liquid is 6.5.

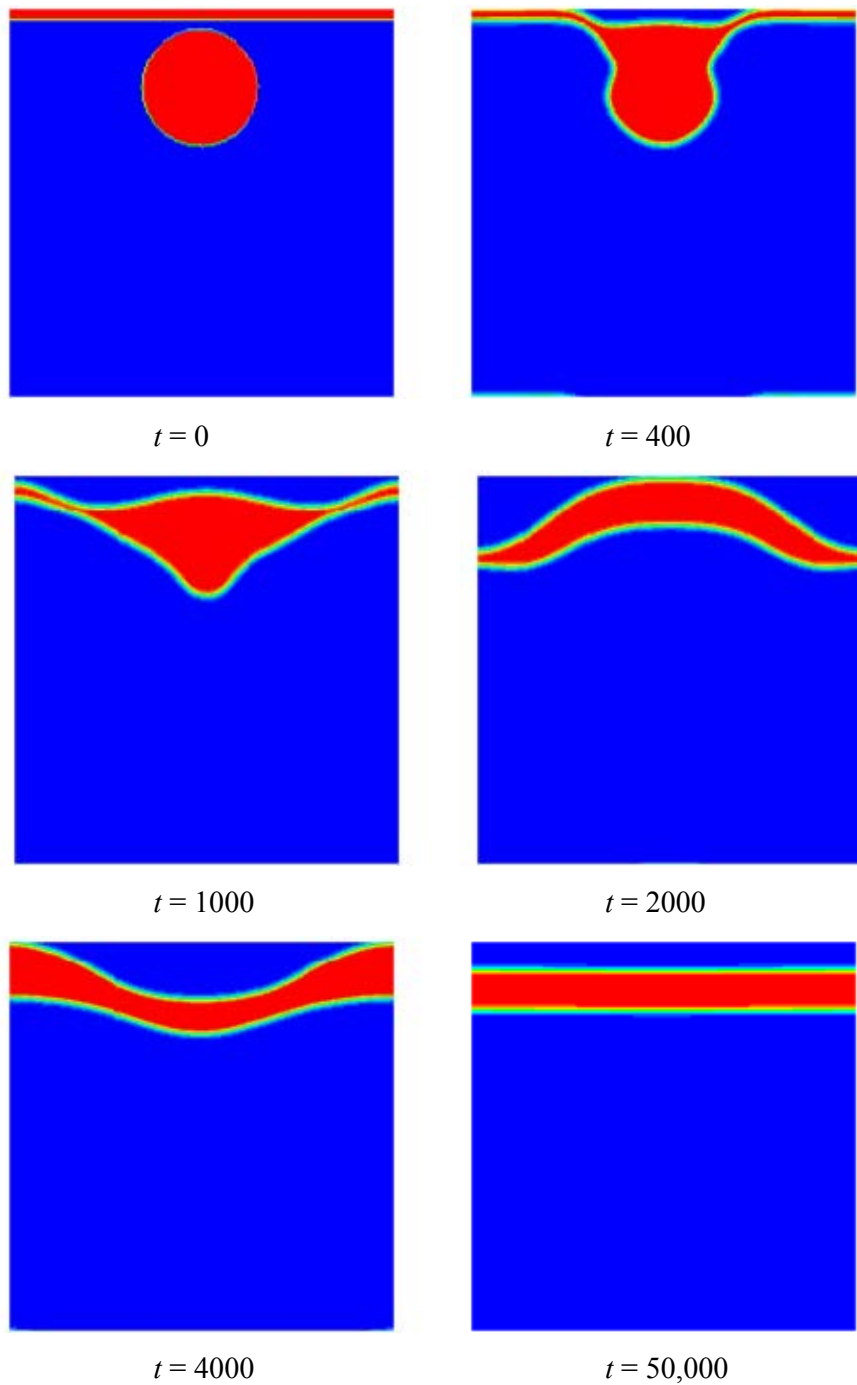


Fig. 7.7: Snapshots showing coalescence of a thin liquid film with a liquid droplet at different LBM time-steps for $T = 250$ °C. Densities of vapor (shown in blue) and liquid drop or film (shown in red) are 23.093 and 896.214 kg/m³, respectively. Ratio of kinematic viscosity of vapor and liquid is 6.5.

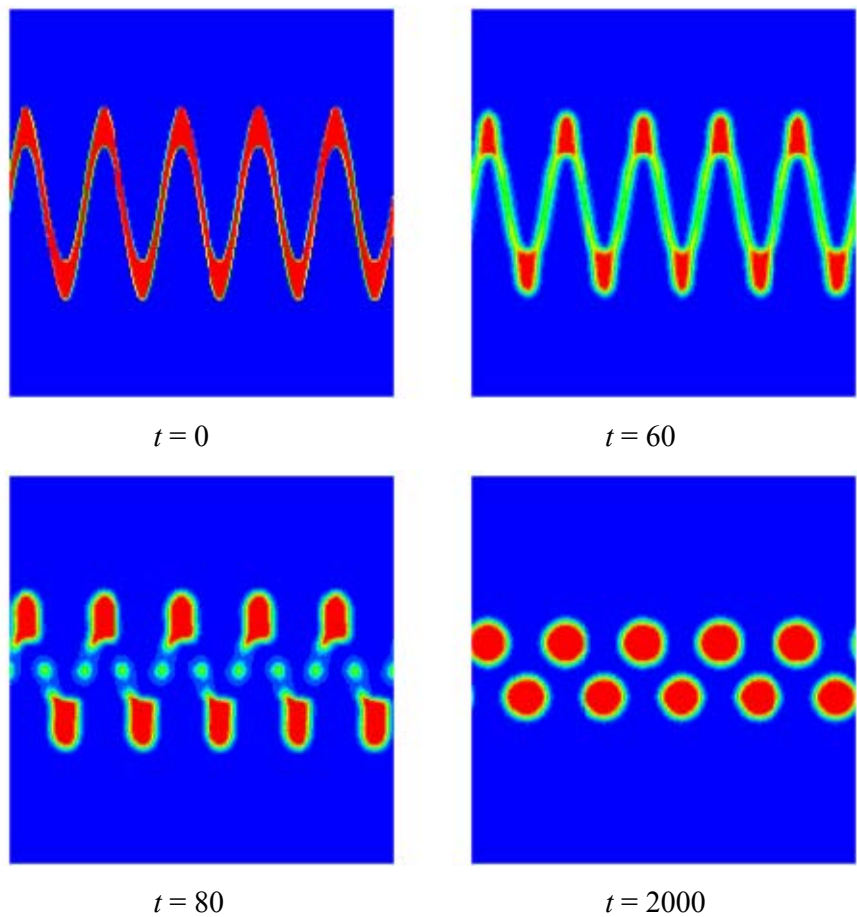


Fig. 7.8: Snapshots showing break-up of a sinusoidal thin liquid film of large wave amplitude into several circular droplets ($T = 250$ °C). Densities for vapor (shown in blue) and liquid (shown in red) are 23.093 and 896.214 kg/m³, respectively. Ratio of kinematic viscosity of vapor and liquid is 6.5.

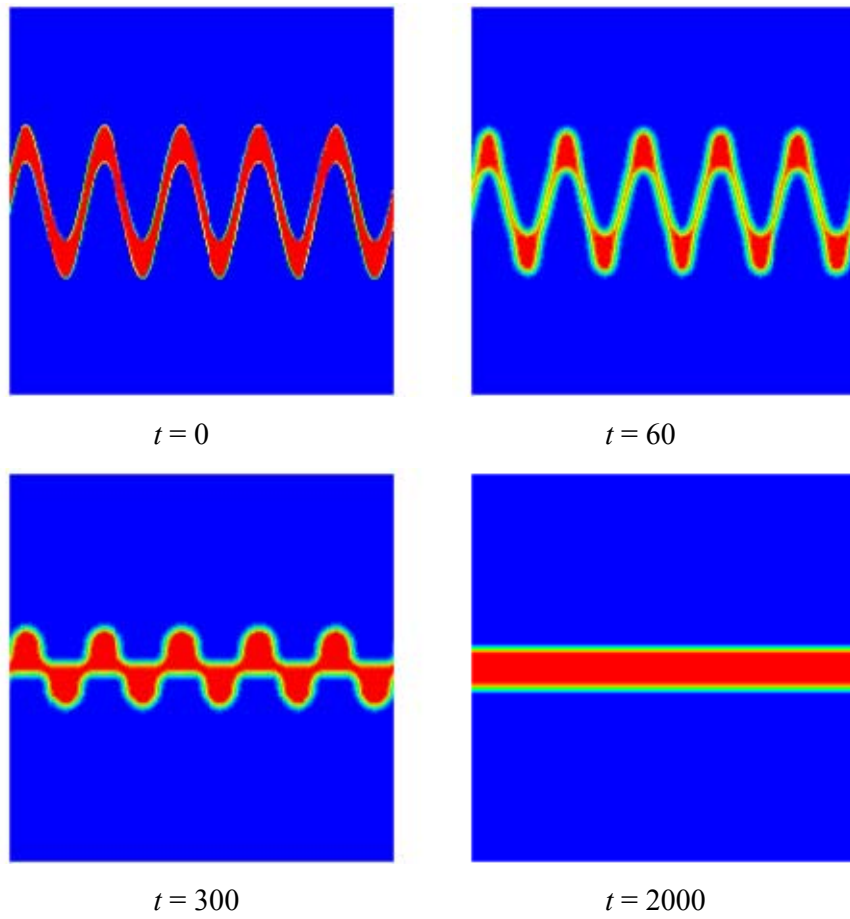


Fig. 7.9: Snapshots showing relaxation of a sinusoidal thin liquid film of small wave amplitude into a thick liquid film ($T = 250$ °C). Densities for vapor (shown in blue) and liquid (shown in red) are 23.093 and 896.214 kg/m^3 , respectively. Ratio of kinematic viscosity of vapor and liquid is 6.5.

7.8 Conclusions

It is shown that a non-ideal equation of state, such as the Peng-Robinson EOS, may be coupled with the LBGK scheme with a single density-dependent relaxation time to capture the phase-coexistence curve for water and steam over a wide range of temperatures. Simulating a series of isothermal bubbles and droplets suspended in their coexisting phase predicts the surface tension of the LBM fluid. Comparing this to the experimental data for water provides a way to scale the spatial grid of the LBM in physical units so that the

predicted surface tension in physical units accurately matches the measured surface tension data.

7.9 References

Angelopoulos, A.D., Paunov, V.N., Burganos, V.N., Payatakes, A.C, 1998. Lattice Boltzmann simulation of nonideal vapor-liquid flow in porous media, *Phys. Rev. E*, 57 (3), 3237-3245.

Bhatnagar, P.L., Gross, E.P., Krook, M.K., 1954. A model for collision process in gases. I. Small amplitude process in charged and neutral one-component system, *Phys. Rev.*, 94 (3), 511-525.

Harvey, A.H., Peskin, A.P., Klien, S.A., 2004. NIST/ASME Steam Properties, version 2.21. US Department of Commerce, Technology Administration, National Institute of Standards and Technology.

Kupershtokh, A.L, 2004. New method of incorporating a body force term into the lattice Boltzmann equation, *Proceedings of the 5th International EHD Workshop*, Aug 30-31, Poitiers-France, 241-246.

McQuarrie, D., Simon, J.D., 1999. *Molecular Thermodynamics*, University Science, Sausalito, CA.

Medvedev, D., Kupershtokh, A., Karpov, D., 2007. On equations of state in a lattice Boltzmann method, Talk at: *Fourth International Conference for Mesoscopic Methods in Engineering and Science (ICMMES)*, July 16-20, Munich, Germany.

Yuan, P., Schaefer, L., 2006. Equations of state in a lattice Boltzmann model, *Phys. Fluids* 18, 042101.

Zhang, R., Chen, H., 2003. Lattice Boltzmann method for simulation of liquid-vapor thermal flows, *Phys. Rev E* 67, 066711.

Chapter 8

Simulation of thermal effects

In general, thermal lattice Boltzmann models fall into three categories, 1) the multispeed approach, 2) the passive-scalar approach and 3) the thermal energy distribution approach.

Multispeed LB models are developed by extending corresponding isothermal models by using additional lattice speeds and higher-order velocity terms in the equilibrium distribution functions. Although this approach is based on a rigorous theoretical foundation, numerical simulations using the multispeed thermal model usually suffer from severe numerical instabilities, and applicability is often restricted to a narrow temperature range (Alexander et al., 1993; Chen et al., 1994; McNamara et al., 1995).

In passive scalar based LB models, temperature dynamics is simulated by a separate distribution function which is independent of the density distribution function. Numerical stability is significantly enhanced in these models compared with the multispeed thermal models. However, the viscous heat dissipation and the compression work done by pressure are assumed to be negligible in these models. Shan (1997) used the passive scalar LB approach to simulate Rayleigh-Benard convection. Boussinesq approximation was used in the body force term. Palmer & Rector (2000) used a similar approach to solve the following flow problems: 1) flow with non-uniform conductivity between two plates, 2) entry length behavior for flow in a channel between two parallel plates, and 3) Rayleigh-Benard convection. Similarly, Guo et al. (2002) also used the passive scalar thermal LB model for the Boussinesq incompressible fluids. A porous plate problem with a temperature gradient and the problem of natural convection in a square cavity were solved. Kao & Yang (2007) and Kuznik (2007) also simulated the same Rayleigh-Benard convection problem using the passive scalar approach.

The thermal energy distribution approach is derived by discretizing the continuous evolution Boltzmann equation for the internal energy distribution function and was first proposed by He et al. (1998). This scheme is similar to the passive scalar approach since it

also uses a separate distribution function to simulate the temperature evolution. Its numerical stability is also comparable with the passive scalar approach. Moreover, this scheme also incorporates the viscous heat dissipation and the compression work done by pressure. Peng et al. (2003a,b) simplified the thermal LB model by He et al. (1998) to neglect the compression work done by pressure and the viscous heat dissipation, and simulated the natural convection in 2D and 3D cavities. Dixit & Babu (2006) used the thermal energy distribution LB approach to simulate natural convection in a square cavity for high Rayleigh numbers (up to 10^{10}). They implemented the LB model on to non-uniform grids in order to achieve high Rayleigh numbers. No turbulence model was invoked in their simulations. Niu et al. (2007) used the thermal energy distribution LB approach to simulate micro-thermal flows by relating the thermal relaxation time to the Knudsen number of the fluid. Results for the thermal Couette flow problem in a micro-channel was compared against those from the direct simulation Monte Carlo (DSMC) and the molecular dynamics (MD) approaches.

Recently, thermal models based on LBM were extended for some novel applications. Mishra et al. (2005) and Mishra & Roy (2007) developed the LB method to solve the energy equation of a two-dimensional transient conduction-radiation problem. Results of the LBM simulations were compared against results obtained using the finite volume method (FVM) . Wang et al. (2007) applied the thermal LB approach to simulate the fluid-solid conjugate heat transfer. Hazi & Markus (2008) extended the LBM to model heat transfer in supercritical fluids. Their model was able to qualitatively capture the *piston effect* which is responsible for increased heat transfer in a microgravity environment. Onset of convection in a Rayleigh-Benard configuration was also studied.

Note that most of the thermal LB models proposed in the past are for the single phase fluids and do not really account for the thermodynamic phase change in a system. In Yuan & Schaefer (2006a,b), Shan-Chen (S-C) model is coupled with a passive-scalar based temperature solver. The nature of the thermal and momentum coupling was essentially through the body force term similar to the approach popularly being used in the simulation of Rayleigh-Benard convection problems. Chatterjee & Chakraborty (2007) developed an enthalpy-source based LBM to simulate conduction dominated phase change (such as, melting of ice) problem. Very recently, Dong et al. (2009) introduced a phase-change

coupling between the LB momentum and energy solvers. The problem of growth and deformation of a rising bubble in a superheated liquid was simulated.

In this chapter, a simplified thermal LB model, based on the thermal energy distribution approach, is presented. The simplifications are made after neglecting the viscous heat dissipation and the work done by pressure in the original thermal energy distribution model. Details of the model are presented in the next section, followed by a discussion of the boundary conditions, and then results for some two-phase thermal problems.

8.1 Thermal energy distribution LB model

The governing equation for the thermal energy distribution function is (Peng et al., 2003a):

$$h_a(\mathbf{r} + \mathbf{v}_a \Delta t, t + \Delta t) = h_a(\mathbf{r}, t) - \frac{\Delta t}{\tau_T} [h_a(\mathbf{r}, t) - h_a^{eq}(\mathbf{r}, t)] \quad (8.1)$$

where τ_T is the thermal relaxation time and is related to the thermal diffusivity α_T by:

$$\alpha_T = \frac{2}{3} \left(\tau_T - \frac{1}{2} \right) c^2 \Delta t \quad (8.2)$$

[In the above, c is taken to be unity for a uniform square lattice (D_2Q_9 or D_3Q_{19}), i.e. for $\Delta x = \Delta t$. For numerical stability reasons, τ_T is usually chosen well above 0.5.]

The above governing equation may be split into the following two equations:

- Collision

$$h_a^*(\mathbf{r}, t) = h_a(\mathbf{r}, t) - \frac{\Delta t}{\tau_T} [h_a(\mathbf{r}, t) - h_a^{eq}(\mathbf{r}, t)] \quad (8.3)$$

- Streaming

$$h_a(\mathbf{r} + \mathbf{v}_a \Delta t, t + \Delta t) = h_a^*(\mathbf{r}, t) \quad (8.4)$$

For a D_2Q_9 lattice, which is defined as:

$$\mathbf{v}_a = \begin{cases} 0, & a = 0 \\ \{\cos[(a-1)\pi/2], \sin[(a-1)\pi/2]\}c, & a = 1, 2, 3, 4 \\ \sqrt{2}\{\cos[(a-5)\pi/2 + \pi/4], \sin[(a-5)\pi/2 + \pi/4]\}c, & a = 5, 6, 7, 8 \end{cases} \quad (8.5)$$

the equilibrium distribution function h_a^{eq} is given by (He et al., 1998):

$$h_0^{eq} = -\frac{2\rho\varepsilon}{3} \frac{\mathbf{u}^2}{c^2} \quad (8.6)$$

$$h_{1,2,3,4}^{eq} = \frac{\rho\varepsilon}{9} \left[1.5 + 1.5 \frac{\mathbf{v}_a \cdot \mathbf{u}}{c^2} + 4.5 \left(\frac{\mathbf{v}_a \cdot \mathbf{u}}{c^2} \right)^2 - 1.5 \frac{u^2}{c^2} \right] \quad (8.7)$$

$$h_{5,6,7,8}^{eq} = \frac{\rho\varepsilon}{36} \left[3 + 6 \frac{\mathbf{v}_a \cdot \mathbf{u}}{c^2} + 4.5 \left(\frac{\mathbf{v}_a \cdot \mathbf{u}}{c^2} \right)^2 - 1.5 \frac{u^2}{c^2} \right] \quad (8.8)$$

where $\varepsilon = DRT/2$ and D is the number of dimensions.

Note that the above equilibrium distribution function h_a^{eq} , given by equations (8.6) to (8.8), simulates the convection-diffusion equation for the energy transport. In order to only simulate the heat conduction effects, which might be dominant in several physical scenarios, following distribution function can be used:

$$h_0^{eq} = 0 \quad (8.9)$$

$$h_{1,2,3,4}^{eq} = \frac{\rho\varepsilon}{6} \quad (8.10)$$

$$h_{5,6,7,8}^{eq} = \frac{\rho\varepsilon}{12} \quad (8.11)$$

Macroscopic temperature $T(\mathbf{r}, t)$ can be calculated from the following equation:

$$\varepsilon(\mathbf{r}, t) = \frac{1}{\rho(\mathbf{r}, t)} \sum_a h_a(\mathbf{r}, t) \quad (8.12)$$

Note that a Chapman-Enskog expansion of equation (8.1) with the equilibrium distribution function given by equations (8.6) to (8.8) leads to the following energy equation (Peng et al., 2003a):

$$\partial_t(\rho\varepsilon) + \nabla \cdot (\rho \mathbf{u} \varepsilon) = \alpha_T \nabla^2(\rho\varepsilon) \quad (8.13)$$

8.2 Density dependent thermal diffusivities: $\alpha_T(\rho)$

In the thermal LB algorithm described earlier, the thermal diffusivity of a fluid α_T is explicitly determined by the prescribed thermal relaxation time τ_T using equation (8.2). This

functional form gives a unique value for the thermal diffusivity of the fluid irrespective of the multiple phases involved. However, in order to accurately model the temperature dynamics of a single-component two-phase fluid, it is essential to have different thermal diffusivities for the two phases and incorporation of density-dependent variation in the interfacial regions.

This task may be accomplished by expressing the thermal relaxation time τ_T as a linear function of the local fluid density $\rho(x, y)$ constrained by the saturation densities of both phases. Thus, $\tau_T(\rho)$ can be written as

$$\tau_T(\rho) = \left[\frac{\tau_T(\rho_L) - \tau_T(\rho_V)}{\rho_L - \rho_V} \right] \rho + \left[\frac{\tau_T(\rho_V) \rho_L - \tau_T(\rho_L) \rho_V}{\rho_L - \rho_V} \right] \quad (8.14)$$

where $\tau_T(\rho_L)$ and $\tau_T(\rho_V)$ represent, at the given temperature, the relaxation times corresponding to the saturation density of the liquid and vapor phases, respectively. These phase-specific thermal relaxation times are calculated using the thermal diffusivities of the corresponding phases.

8.3 Wall Temperature BCs (Dirichlet type)

For a D₂Q₉ lattice, unknown thermal distribution functions at the walls can be approximated to be the equilibrium distribution functions with an additional counter-slip thermal energy $\rho\varepsilon'$ determined to satisfy the fixed temperature constraint at the walls (D'Orazio and Succi, 2003, 2004; D'Orazio et al., 2004).

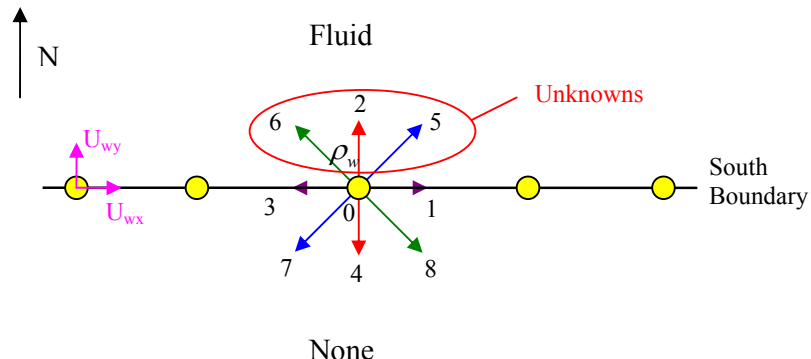


Fig. 8.1: Unknown distribution functions at the South boundary for application of a thermal boundary condition.

For example, if the temperature is specified on a South boundary which is moving with a velocity $\mathbf{U}_w \equiv (U_{wx}, U_{wy})$ then the unknowns h_2 , h_5 and h_6 can be assumed to be the equivalent equilibrium distribution functions with a total thermal energy $\rho(\varepsilon_s + \varepsilon')$, i.e.

$$h_2 = \frac{\rho(\varepsilon_s + \varepsilon')}{9} \Gamma_2 \quad (8.15)$$

where

$$\Gamma_2 = 1.5 + 1.5 \frac{\mathbf{v}_a \cdot \mathbf{U}_w}{c^2} + 4.5 \left(\frac{\mathbf{v}_a \cdot \mathbf{U}_w}{c^2} \right)^2 - 1.5 \frac{U_w^2}{c^2} \quad (8.16)$$

and

$$h_5 = \frac{\rho(\varepsilon_s + \varepsilon')}{36} \Gamma_5 \quad (8.17)$$

$$h_6 = \frac{\rho(\varepsilon_s + \varepsilon')}{36} \Gamma_6 \quad (8.18)$$

where

$$\Gamma_5 = \Gamma_6 = 3 + 6 \frac{\mathbf{v}_a \cdot \mathbf{u}}{c^2} + 4.5 \left(\frac{\mathbf{v}_a \cdot \mathbf{u}}{c^2} \right)^2 - 1.5 \frac{u^2}{c^2} \quad (8.19)$$

Now, applying the conservation equation (8.12), we have:

$$\rho \varepsilon_s = \sum_a h_a = (h_0 + h_1 + h_3 + h_4 + h_7 + h_8) + (h_2 + h_5 + h_6) \quad (8.20)$$

Using equations (8.15) to (8.19), we can write the above equation as:

$$\rho \varepsilon_s = G_{known} + \frac{\rho(\varepsilon_s + \varepsilon')}{9} \Gamma_2 + \frac{\rho(\varepsilon_s + \varepsilon')}{36} \Gamma_5 + \frac{\rho(\varepsilon_s + \varepsilon')}{36} \Gamma_6 \quad (8.21)$$

where

$$G_{known} = h_0 + h_1 + h_3 + h_4 + h_7 + h_8 \quad (8.22)$$

Now, $\rho(\varepsilon + \varepsilon')$ can be determined as:

$$\rho(\varepsilon_s + \varepsilon') = \frac{36(\rho \varepsilon_s - G_{known})}{(4\Gamma_2 + \Gamma_5 + \Gamma_6)} \quad (8.23)$$

Now, using equations (8.15), (8.17) and (8.18), the unknown distribution functions at the South boundary can be determined.

Using the same approach described above, the temperature boundary conditions at the other wall orientations (i.e., the North, West and East walls) can be developed.

8.4 Wall Heat Flux BCs (Neumann type)

In order to apply the wall heat flux boundary conditions, one can use an approach similar to the one described in the previous section. The specified heat flux condition (Neumann boundary condition) at the wall has to be first converted into a Dirichlet-type condition. This can be done by using the conventional second-order finite difference approximation for the temperature gradient and identifying the unknown temperature value at the wall. Once the corresponding temperature at the wall is known, the scheme described in previous section to determine the unknowns can be used.

For example, if the heat flux on the South boundary is specified, then the temperature on the South boundary can be obtained from:

$$\left. \frac{\partial T}{\partial y} \right|_{(i,1)} = \frac{4T_{(i,2)} - T_{(i,3)} - 3T_{(i,1)}}{2\Delta y} = q_s \quad (8.24)$$

which is:

$$T_s = \frac{4T_{(i,2)} - T_{(i,3)} - 2q_s \Delta y}{3} \quad (8.25)$$

Once T_s is known, we can use the relations in the previous section to determine the unknown distribution functions. Here, q_s denotes the outward heat flux (heat being taken away from the boundary), a positive increase in which yields a subsequent decrease in T_s .

Using the same approach described above, the heat flux boundary conditions can be developed and applied for the other orientations as well (North, West and East walls).

8.5 Simulation of evaporation and condensation

For bubbles in liquid scenarios, one can qualitatively simulate evaporation and condensation effects by making the interfacial (i.e. for $\rho_{vap} < \rho < \rho_{liq}$) *rest-state* particle

distribution function depend upon the local superheat (or local sub-cooling) and the local temperature gradient.

Evaporation effects:

For a D₂Q₉ lattice, the *rest-state* particle distribution functions at the interfacial lattice nodes ($x_{\text{int}}, y_{\text{int}}$) are modified by the following equation at each time step in the post-collision stage to simulate evaporation effects:

$$g_9^{\text{new}}(x_{\text{int}}, y_{\text{int}}) = g_9^{\text{old}}(x_{\text{int}}, y_{\text{int}}) - \chi \Delta T_{\text{Super}} \sum_{a=1}^9 w_a \left[T(x_{\text{int}} + v_{ax} \Delta t, y_{\text{int}} + v_{ay} \Delta t) - T(x_{\text{int}}, y_{\text{int}}) \right] \quad (8.26)$$

where ($x_{\text{int}}, y_{\text{int}}$) are the lattice coordinates that fall into the interfacial regions (i.e. $\rho_{\text{vap}} < \rho < \rho_{\text{liq}}$), g_a is the particle distribution function, T^{sat} is the saturation temperature of the fluid, $\Delta T_{\text{Super}} = T(x_{\text{int}}, y_{\text{int}}) - T^{\text{sat}}$ is the local superheat and χ is the temperature sensitivity coefficient quantifying the evaporation of the LB fluid.

Note that the above modification is only applied for the lattice directions, for which the following three conditions are met:

$$\rho(x_{\text{int}} + v_{ax} \Delta t, y_{\text{int}} + v_{ay} \Delta t) > \rho(x_{\text{int}}, y_{\text{int}}) \quad (8.27)$$

$$T(x_{\text{int}} + v_{ax} \Delta t, y_{\text{int}} + v_{ay} \Delta t) > T(x_{\text{int}}, y_{\text{int}}) \quad (8.28)$$

$$\Delta T_{\text{Super}} = T(x_{\text{int}}, y_{\text{int}}) - T^{\text{sat}} > 0 \quad (8.29)$$

Above conditions ensure that only the liquid particles (surrounding the vapor region) which have higher temperature than the interfacial lattice points transfer their energy to the bubble and yield evaporation.

Condensation effects:

For a D₂Q₉ lattice, the *rest-state* particle distribution functions at the interfacial lattice nodes ($x_{\text{int}}, y_{\text{int}}$) are modified by the following equation at each time step in the post-collision stage to simulate condensation effects:

$$g_9^{new}(x_{int}, y_{int}) = g_9^{old}(x_{int}, y_{int}) + \chi \Delta T_{Sub} \sum_{a=1}^9 w_a \left[T(x_{int}, y_{int}) - T(x_{int} + v_{ax} \Delta t, y_{int} + v_{ay} \Delta t) \right] \quad (8.30)$$

where (x_{int}, y_{int}) are the lattice coordinates that fall into the interfacial regions (i.e. $\rho_{vap} < \rho < \rho_{liq}$), g_a is the particle distribution function, T^{sat} is the saturation temperature of the fluid, $\Delta T_{Sub} = T^{sat} - T(x_{int}, y_{int})$ is the local sub-cooling and χ is the temperature sensitivity coefficient quantifying the condensation of the LB fluid.

Note that, as in the evaporation case, the above modification is only applied for the lattice directions, for which the following three conditions are met:

$$\rho(x_{int} + v_{ax} \Delta t, y_{int} + v_{ay} \Delta t) > \rho(x_{int}, y_{int}) \quad (8.31)$$

$$T(x_{int} + v_{ax} \Delta t, y_{int} + v_{ay} \Delta t) < T(x_{int}, y_{int}) \quad (8.32)$$

$$\Delta T_{Sub} = T^{sat} - T(x_{int}, y_{int}) > 0 \quad (8.33)$$

Above conditions ensure that only the liquid particles (surrounding the vapor region) which have lower temperature than the interfacial lattice points are allowed to accept energy and mass transfer (condensation) from the bubble interface.

By changing the rest-state particle distribution functions to simulate evaporation or condensation effects, we are essentially changing the pressure in the interfacial region of the bubble. Depending upon the local superheat/sub-cooling and temperature gradient from the neighboring lattice points, the change in interfacial pressure leads to the growth or shrinkage of the bubble.

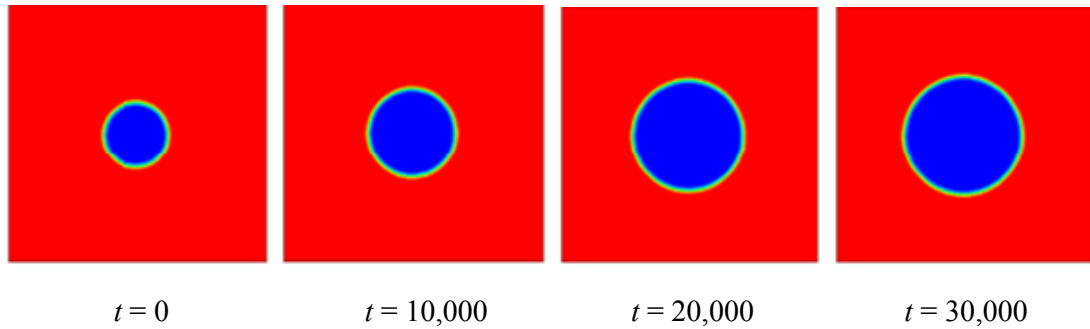
8.6 Results and discussions

In Fig. 8.2, results for the growth of a bubble due to thermal diffusion from the superheated walls are presented. A single bubble is initialized in the two-dimensional domain using the simulation parameters listed in the figure. At time $t = 0$, the bubble is at its saturated temperature and the walls surrounding the domain are at a higher temperature. As time is increased, higher temperature from the walls causes heat to diffuse to the bubble and

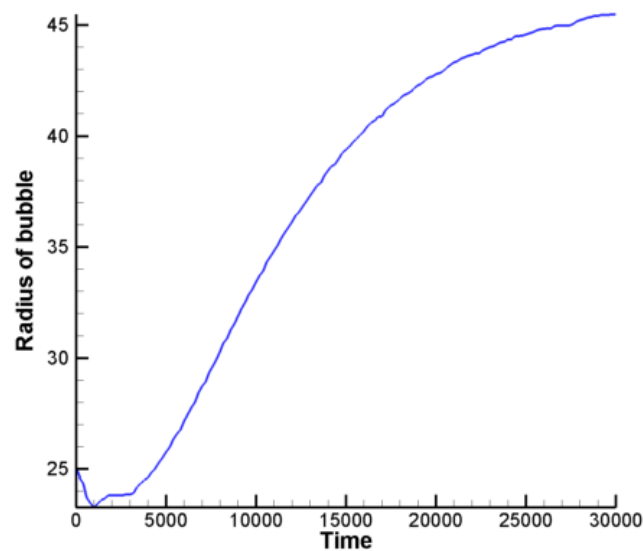
contributes in its temporal growth as shown in Fig. 8.2 (b). Note that the heat conduction is assumed to be the dominant mode of heat transfer in the simulations. Resulting growth of the bubble is in close agreement with the theoretical model of $R \propto \sqrt{t}$ (Zuber, 1961).

In Fig. 8.3, simulation results for the shrinkage, due to condensation, of a single bubble in a sub-cooled domain are presented. The bubble is initially at the saturated temperature and as time proceeds, gets condensed due to the temperature diffusion from the sub-cooled walls. Here again, the conduction is assumed to be the dominant mode of heat transfer.

In Fig. 8.4, simulation results for the *temperature coupled AILB model* are presented for the growth and rise of a vapor bubble away from a heated wall. Temperature boundary conditions are applied at the South ($T_S = 1.0$) and the North wall ($T_N = 0.8$) of the 2D domain, whereas both the fluid phases are initialized at a reduced temperature equal to 0.95. The vapor bubble is initialized at $t = 0$ away from the South wall which grows due to evaporation at the interface because of the higher temperature in the interfacial region. The bubble rises because of the buoyancy forces, resulting in the shape deformation of the bubble. Parameters for the simulation are listed in the figures. Since the temperature in the vicinity of the North wall is less than the bulk fluid temperature, condensation happens at the interface when bubble approaches the North wall. Bubble disappears due to condensation as time increases.

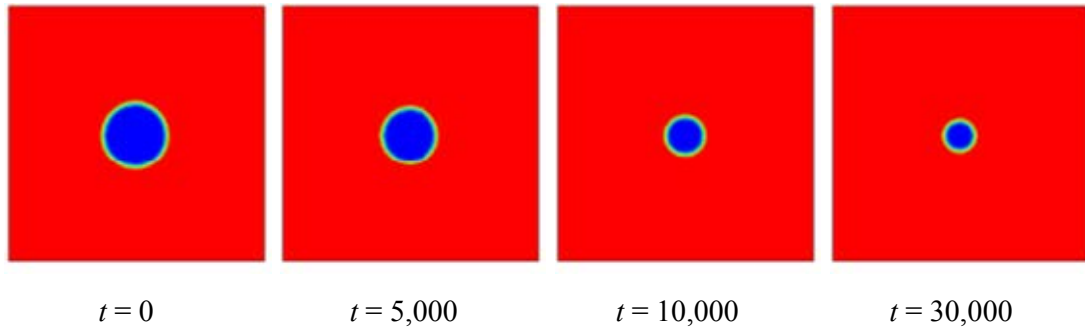


(a) Growth of a two-dimensional bubble

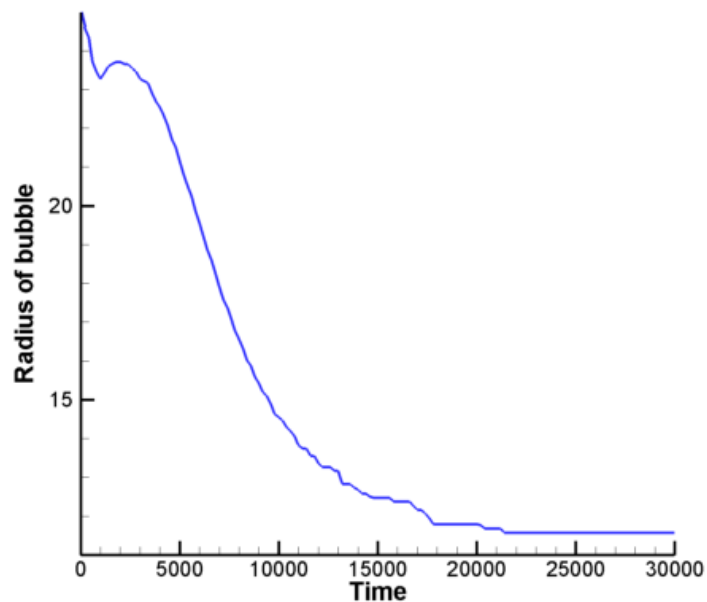


(b) Temporal variation in the radius of the growing bubble

Fig. 8.2: Two-dimensional simulation of the growth of a single vapor bubble due to temperature dynamics. The initial temperature of the bulk fluid at $t = 0$ equals to $T_R = 0.95$ and all the walls of the domain are kept at a higher temperature ($T_{wall} = 1.0$). Heat conduction is assumed to be the dominant mode of heat transfer in the system. Simulations are performed in a 2D box of size 200×200 grid points. Other parameters for the simulation are: N-S-E-W walls, $a = 9/8$, $b = 1/3$, $T_R = 0.95$, $\rho_l = 1.46173$, $\rho_v = 0.579015$, $R = 25$ lu , $\sigma = 0.005$, $g = 0$, $\tau_l = \tau_v = 0.5$, $D = 3$, $\chi = 50$, $\tau_{T,l} = 1.2$, $\tau_{T,v} = 0.6$. (AILB model with no scaling)



(a) Shrinkage of a two-dimensional bubble



(b) Temporal variation in the radius of the shrinking bubble

Fig. 8.3: Two-dimensional simulation of the shrinking of a single vapor bubble due to condensation. The initial temperature of the bulk fluid at $t = 0$ equals to $T_R = 0.95$ and all the walls of the domain are kept at a lower temperature ($T_{\text{wall}} = 0.9$). Heat conduction is assumed to be the dominant mode of heat transfer in the system. Simulations are performed in a 2D box of size 200×200 grid points. Other parameters for the simulation are: N-S-E-W walls, $a = 9/8$, $b = 1/3$, $T_R = 0.95$, $\rho_l = 1.46173$, $\rho_v = 0.579015$, $R = 25 \text{ lu}$, $\sigma = 0.005$, $g = 0$, $\tau_l = \tau_v = 0.5$, $D = 3$, $\chi = 50$, $\tau_{T,l} = 1.2$, $\tau_{T,v} = 0.6$. (AILB model with no scaling)

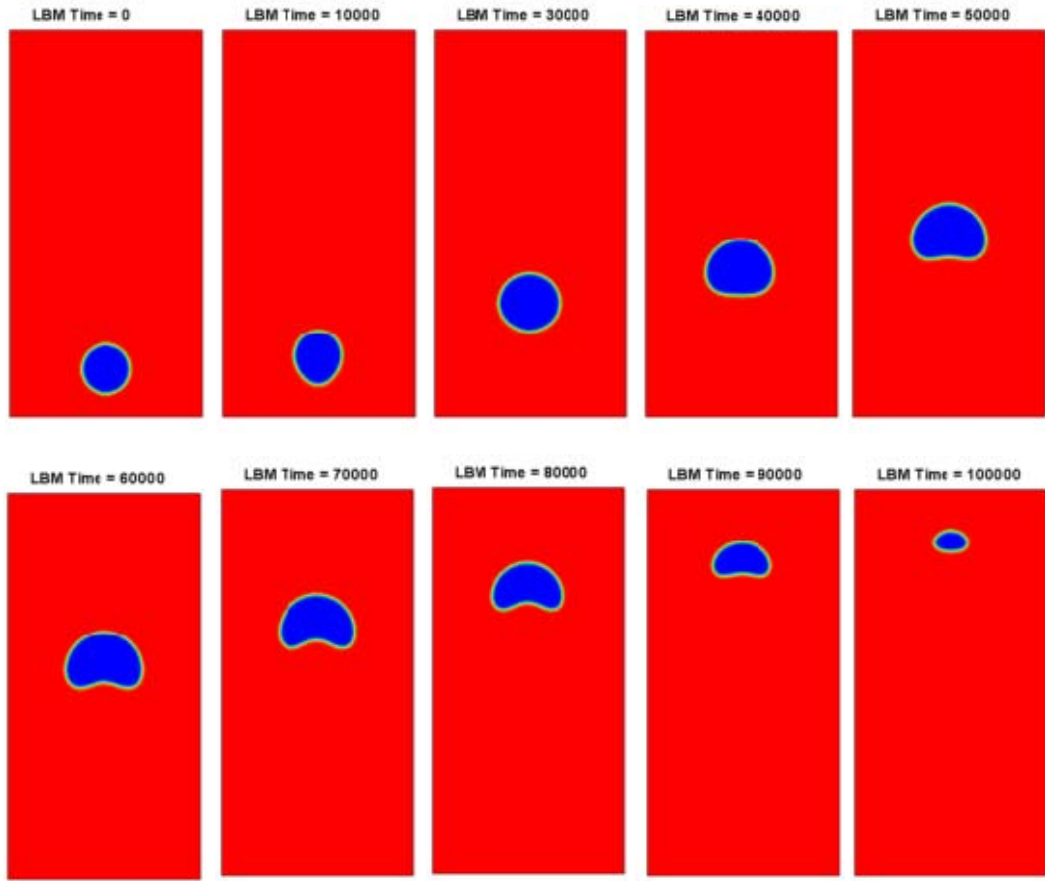


Fig. 8.4: Two-dimensional simulation of a single rising vapor bubble with heat transfer. South wall of the domain is at higher temperature ($T_S = 1.0$) and the North wall of the domain is at a lower temperature ($T_N = 0.8$) than the bulk fluid temperature which is at a temperature equal to $T_R = 0.95$. Simulations are performed in a 2D box of size 240×480 grid points. Other parameters for the simulation are: N-S walls, E-W periodic, $a = 9/8$, $b = 1/3$, $T_R = 0.95$, $\rho_l = 1.46173$, $\rho_v = 0.579015$, $R = 30 \text{ lu}$, $\sigma = 0.005$, $g = 5 \times 10^{-6}$, $\tau_l = \tau_v = 0.5$, $D = 3$, $\chi = 10$, $\tau_{T,l} = 1$, $\tau_{T,v} = 0.6$. (AILB model with no scaling)

8.7 References

Alexander, F.J., Chen, S., Sterling, J.D., 1993. Lattice Boltzmann thermohydrodynamics. *Phys. Rev. E* 47, R2249.

Chatterjee, D., Chakraborty, S., 2007. An enthalpy-source based lattice Boltzmann model for conduction dominated phase change of pure substances. *Int. J. Thermal Sci.* 47, 552-559.

Chen, Y., Ohashi, H., Akiyama, M., 1994. Thermal lattice BGK model without nonlinear deviations in macrodynamic equations. *Phys. Rev. E* 50, 2776.

Dixit, H.N., Babu, V., 2006. Simulation of high Rayleigh number natural convection in a square cavity using the lattice Boltzmann method. *Int. J. Heat Mass Transfer* 49, 727-739.

Dong, Z., Li, W., Song, Y., 2009. Lattice Boltzmann simulation of growth and deformation for a rising vapor bubble through superheated liquid. *Numerical Heat Transfer A* 55, 381-400.

D’Orazio, A., Succi, S., 2003. Boundary conditions for thermal lattice Boltzmann simulations. *ICCS 2003, LNCS* 2657, 977-986.

D’Orazio, A., Succi, S., 2004. Simulating two-dimensional thermal channel flows by means of a lattice-Boltzmann method with new boundary conditions. *Future Generation Computer Systems* 20, 935-944.

D’Orazio, A., Corcione, M., Celata, G.P., 2004. Application to natural convection enclosed flows of a lattice Boltzmann BGK model coupled with a general purpose thermal boundary condition. *Int. J. Thermal Sci.* 43, 575-586.

Guo, Z., Shi, B., Zheng, C., 2002. A coupled lattice BGK model for the Boussinesq equations. *Int. J. Num. Methods in Fluids* 39, 325-342.

Hazi, G., Markus, A., 2008. Modeling heat transfer in supercritical fluid using the lattice

Boltzmann method. *Phys. Rev. E* 77, 026305.

He, X., Chen, S., Doolen, G.D., 1998. A novel thermal model for the lattice Boltzmann method in incompressible limit. *J. Comp. Phys.* 146, 282-300.

Kao, P.H., Yang, R.J., 2007. Simulating oscillatory flows in Rayleigh-Benard convection using the lattice Boltzmann method. *Int. J. Heat Mass Transfer* 50, 3315-3328.

Kuznik, F., Vareilles, J., Rusaouen, G., Krauss, G., 2007. A double-population lattice Boltzmann method with non-uniform mesh for the simulation of natural convection in a square cavity. *Int. J. Heat Fluid Flow* 28, 862-870.

McNamara, G., Garcia, A.L., Alder, B.J., 1995. Stabilization of thermal lattice Boltzmann models. *J. Stat. Phys.* 81, 395.

Mishra, S.C., Lankadasu, A., Beronov, K.N., 2005. Application of the lattice Boltzmann method for solving the energy equation of a 2-D transient conduction-radiation problem. *Int. J. Heat Mass Transfer* 48, 3648-3659.

Mishra, S.C., Roy, H.K., 2007. Solving transient conduction and radiation heat transfer problems using the lattice Boltzmann method and the finite volume method. *J. Comp. Phys.* 223, 89-107.

Niu, X.D., Shu, C., Chew, Y.T., 2007. A thermal lattice Boltzmann model with diffuse scattering boundary condition for micro thermal flows. *Computers & Fluids* 36, 273-281.

Palmer, B.J., Rector, D.R., 2000. Lattice Boltzmann algorithm for simulating thermal flows in compressible fluids. *J. Comp. Phys.* 161, 1-20.

Peng, Y., Shu, C., Chew, Y.T., 2003a. Simplified thermal lattice Boltzmann model for incompressible thermal flows. *Phys. Rev. E* 68, 026701.

Peng, Y., Shu, C., Chew, Y.T., 2003b. A 3D incompressible thermal lattice Boltzmann model

and its application to simulate natural convection in a cubic cavity. *J. Comp. Phys.* 193, 260-274.

Shan, X., 1997. Simulation of Rayleigh-Benard convection using a lattice Boltzmann method. *Phys. Rev. E* 55 (3), 2780-2788.

Wang, J., Wang, M., Li, Z., 2007. A lattice-Boltzmann algorithm for fluid-solid conjugate heat transfer. *Int. J. Thermal Sci.* 46, 228-234.

Yuan, P., Schaefer, L., 2006a. A thermal lattice Boltzmann two-phase flow model and its application to heat transfer problems-Part 1. Theoretical foundation. *J. Fluid Eng.* 128, 142-150.

Yuan, P., Schaefer, L., 2006b. A thermal lattice Boltzmann two-phase flow model and its application to heat transfer problems-Part 2. Integration and validation. *J. Fluid Eng.* 128, 151-156.

Zhang, R., Chen, H., 2003. Lattice Boltzmann method for simulation of liquid-vapor thermal flows, *Phys. Rev E* 67, 066711.

Zuber, N., 1961. The dynamics of vapor bubbles in nonuniform temperature fields. *Int. J. Heat Mass Transfer* 2, 83-98.

Chapter 9

Summary and Conclusions

In the boiling water reactors (BWRs), the two-phase interactions play an important role in the design, operation and accident scenarios. Sub-cooled boiling and critical heat flux play an important role even in pressurized water reactors (PWRs). The two fluid phases and their different flow patterns make the fluid dynamics highly complex and therefore, the predictive modeling of such a system becomes very difficult. In order to circumvent these modeling difficulties, experiments have been performed in the past which employ relatively simpler geometries, and empirical results from those studies have been extrapolated to the reactor system conditions. Of course, most of the empirical correlations may not be applicable in a wide range of system conditions and the reactor system analyses codes employing those correlations suffer from a large error margin in their predictions.

One should note that the physics of two-phase (or two-fluid) interactions, with or without temperature variations, is still not very clear and simple experiments (such as, rising of a single air (or vapor) bubble or two bubble coalescence) are still being performed and analyzed. Therefore, the path to successfully model the two-phase dynamics would be to develop a simulation tool which can simulate, in the order of increasing complexity, single bubble/droplet coexisting with the inverse phase, interaction of two phases with system walls having different contact angles, suitable boundary conditions to simulate moving walls and walls at rest effects, existence of a body force such as gravity, topological shape changes due to fluid dynamics which may result in break-up or coalescence of a fluid phase, and multiple bubbles/droplets interactions for different system conditions. Once all these scenarios have been independently tested and validated with experiments and/or other available data in the literature, one will have more faith and of course, more understanding of the physics being simulated when simulations are performed for more complicated scenarios. All of the above mentioned scenarios should be first validated for isothermal cases and then, with the inclusion of temperature effects. More experimental studies would become a necessity in order to fine tune the models. In this report, a successful attempt has been made to address the above mentioned goals in the order described in the framework of the lattice Boltzmann (LB) model. Obviously, additional refinements to the model and validation studies are still

needed to develop a predictive capability to model two-phase flow dynamics in, say, BWRs.

The lattice Boltzmann method (LBM) is an alternative numerical scheme for solving incompressible fluid flow behavior. The scheme has its roots in kinetic theory and can serve as an efficient solver for incompressible low-*Re* number flows in complex geometries — including porous media and for the simulation of complex fluids. Since the incompressibility criterion is not strictly enforced in the LB models, therefore it belongs to a class of pseudo-compressible solvers of fluid dynamics. The LB method inherited most of the advantages from the LGCA and eliminated excessive statistical noise, lattice artifacts such as the lack of Galilean invariance and the dependence of pressure on the fluid velocity. The advantage with LBM lies in the fact that the computational algorithm is simple and efficient; and there is no need to solve the Poisson equation for pressure distribution. Moreover, the LB method allows the implementation of phenomenological terms and rules on the kinetic motion of fictive particle-clusters and thereby, allows the more complex macroscopic dynamics to evolve.

An artificial interface lattice Boltzmann (AILB) model is proposed in this report for the analysis of liquid-vapor two phase flows. Interface between the two fluid phases in the AILB model stretches across several grid points. Because of the diffuse interface description and the lattice Boltzmann evolution algorithm, moving interfaces are handled with a relative ease compared with the corresponding sharp-interface approaches. In the AILB algorithm, there is no need to explicitly track the phase-interface (i.e. to explicitly follow the position of the interfaces) or apply any interface conditions (such as, the continuity of shear stress etc.). Therefore, the overall computational complexity is reduced. The AILB model is able to handle singular topological events (such as, break-up and coalescence) without any need to introduce separate models for them. Simulation of such events in existing two-phase models usually requires special treatment in the solution algorithm. For example, in several other models, a threshold on the thickness has to be prescribed in order to remove any thinning neck (or film) during the simulation of a break-up event. In the AILB model, no artificial trigger is needed to simulate bubble/drop breakup and coalescence. Due to the free-energy minimization principal of the AILB model, it could easily be extended to incorporate complex fluids (such as, polymers, colloids etc.). Several other interaction models could be included in composing the net free energy of the system, which upon minimization could produce desired interfacial events.

The artificial interface LB model (AILB) model, proposed in this report, differs from the earlier proposed Lee-Fischer LB model in the fact that the AILB model employs two equations of states, one for the bulk phase and another for the interfacial region. Artificial equation of state in the interfacial region allows one to have some control over the interfacial thickness, and use of which also facilitates stable numerical simulations for the fluid phases with large density and viscosity ratios. Use of the van der Waals or other similar non-ideal equation of state in the bulk phases allows one to maintain the near-constant bulk densities in the presence of body forces (such as gravity). Lee-Fischer LB model fails to maintain the near-constant density ratio in the presence of gravity, and the time-dependent increase in the density ratio of bulk phases in a Lee-Fischer LB simulation makes them numerically unstable. The cause of artificial enhancement of the numerical compressibility effects due to gravity in a Lee-Fischer LB simulation was identified in this report and the above artifact is cured in the AILB model.

Based on the Cahn's wetting theory, a model is proposed in the context of AILB framework to simulate different contact angles at the wall sites. Moreover, boundary conditions for the AILB model are developed in both the two as well as three dimensional domains. Several simulation scenarios are presented and the results are compared with some of the existing data. For example, in an isothermal flow, rising of a vapor bubble in viscous liquid is numerically simulated and the results are compared with the empirical data. Numerical results are provided for the shape and terminal speed of the rising bubble which shows good agreement with the experimental observations. Similarly, LB simulation of coalescence of two droplets provided good agreement with experimental studies.

A thermal model, based on the two-distribution function approach, is also developed in the AILB model framework. The temperature effects are simulated by using a separate particle distribution function. A phenomenological model is also developed for the simulation of evaporation and condensation effects on a bubble. Additional work is needed to develop a physical model to couple the momentum and thermal energy dynamics of the LB system to effectively simulate boiling and other thermal effects.

It is hoped that these developments will lead to a better understanding of multi-phase interactions, formation of various flow patterns and thus, will pave the way towards a

simulation-based capability to predict critical heat flux (CHF) and flow regime maps with an ultimate goal to improve reactor safety calculations.

Appendix A

Lattice Boltzmann equation to Navier-Stokes (N-S) equations

To derive the hydrodynamic equations from the generic LBE, the truncated Taylor series expansion and the Chapman-Enskog two-time scale separation techniques is adopted. Resulting partial differential equations in the two separated time scales describe advective ‘fast’ dynamics in the faster time scale, and diffusive ‘slow’ dynamics in the slower time scale. These two different PDEs are combined to yield the compressible Navier-Stokes (N-S) equation, from which, the incompressible N-S equation is obtained in the limit of constant density. The derivation given below is based on material from Wolf-Gladrow (2000).

A.1 Multi-scale expansion

Hydrodynamic description of the collective motion of particles requires defining a *hydrodynamic limit*, in which, the smallest macroscopic length scale L is large compared to the characteristic microscopic length scale (for example, lattice mean free path λ which is of the order of the distance between two neighboring lattice points), i.e. $L \gg \lambda$. Ratio of λ and L can be defined as the lattice Knudsen number, ε :

$$\varepsilon \equiv \frac{\lambda}{L} \quad \varepsilon \ll 1 \quad (\text{A.1})$$

which, being a small number ($\varepsilon \ll 1$), can be used as an expansion parameter in the Chapman-Enskog multi-scale expansion procedure.

Using ε as an expansion parameter, the discrete velocity distribution function $f_a(\mathbf{r}, t)$ can be expanded about the discrete equilibrium distribution function $f_a^{eq}(\mathbf{r}, t)$ [This is valid since the system is assumed to be in a near-equilibrium state.]:

$$f_a = f_a^{eq} + \varepsilon f_a^{(1)} + \varepsilon^2 f_a^{(2)} + \dots \quad (\text{A.2})$$

where the lattice Knudsen number (ε) acts as a small parameter used to distinguish *relative* orders of magnitude of the terms in the series. In addition, to satisfy the conservation of collision invariants, we must have:

$$\sum_a f_a^{(k)} = \sum_a \mathbf{v}_a f_a^{(k)} = 0 \quad k \geq 1 \quad (\text{A.3})$$

Since smallest macroscopic length scale L is of order ε^{-1} (see equation (A.1)), we can introduce a new space variable \mathbf{r}_1 , which in the units of ε^{-1} , is defined by:

$$\mathbf{r}_1 = \frac{\mathbf{r}}{\varepsilon^{-1}} = \varepsilon \mathbf{r} \quad (\text{A.4})$$

Based on experience with real fluids, we may anticipate two time-scales (fast and slow) for any macroscopic inhomogeneity to propagate in a fluid. For example, (i) non-linear and pressure effects advect ‘*fast*’ and are represented by first-order space derivatives in a partial differential equation. Therefore, such an inhomogeneity will traverse a length scale of order ε^{-1} in a time scale of order ε^{-1} , i.e. $\Delta t \ll O(\Delta x)$. However, (ii) linear diffusive effects (e.g., viscous damping of sound waves) occur ‘*slowly*’ and are represented by second-order space derivatives in a partial differential equation. Therefore, such an inhomogeneity will traverse a length scale of order ε^{-1} in a time scale of order ε^{-2} i.e. $\Delta t \ll O(\Delta x^2)$. Relying on these physical arguments, we may assume two new time scales, fast t_1 and slow t_2 , in the units of ε^{-1} and ε^{-2} , respectively:

$$t_1 \ll \frac{t}{\varepsilon^{-1}} \quad \text{and} \quad t_2 \ll \frac{t}{\varepsilon^{-2}} \quad (\text{A.5})$$

Note that t_1 and t_2 are not independent variables. They are related to t by:

$$t = \varepsilon^{-1} t_1 + \varepsilon^{-2} t_2 \quad (\text{A.6})$$

As a consequence, the time derivative ∂_t becomes:

$$\partial_t = \varepsilon \partial_{t_1} + \varepsilon^2 \partial_{t_2} \quad (\text{A.7})$$

and the space derivative ∂_{r_α} becomes:

$$\partial_{r_\alpha} = \varepsilon \partial_{r_{1\alpha}}, \quad (\text{A.8})$$

where $\partial_{r_{1\alpha}}$ is the derivative with respect to the α -component of \mathbf{r}_1 .

The acceleration \mathbf{F} (external force per unit mass) implicitly involves double derivative with respect to the time variable, i.e.

$$\mathbf{F} = \partial_t \mathbf{v} = \partial_t (\partial_t \mathbf{r}) \quad (\text{A.9})$$

From the above equation, \mathbf{F} is clearly of order $O(\varepsilon^2)$ and higher, and can be expanded as:

$$\mathbf{F} = \varepsilon^2 \mathbf{F}^{(2)} + \varepsilon^3 \mathbf{F}^{(3)} + \dots \quad (\text{A.10})$$

A.2 Forcing term in the LB equation

The forcing term (F.T.) in the LB equation is:

$$\text{F.T.} = B_a \Delta t = \frac{\mathbf{F} \cdot (\mathbf{v}_a - \mathbf{u})}{RT} f_a^{eq} \Delta t \quad (\text{A.11})$$

Substituting f_a^{eq} yields:

$$\text{F.T.} = \frac{\mathbf{F} \cdot (\mathbf{v}_a - \mathbf{u})}{RT} w_a \left[1 + \frac{\mathbf{v}_a \cdot \mathbf{u}}{RT} + \frac{1}{2} \left(\frac{\mathbf{v}_a \cdot \mathbf{u}}{RT} \right)^2 - \frac{u^2}{2RT} \right] \Delta t \quad (\text{A.12})$$

Neglecting terms of order $O(u^2)$ or higher, we get:

$$\text{F.T.} = \frac{w_a}{RT} \mathbf{F} \cdot \left[(\mathbf{v}_a - \mathbf{u}) + \mathbf{v}_a \frac{\mathbf{v}_a \cdot \mathbf{u}}{RT} \right] \Delta t \quad (\text{A.13})$$

A.3 Order separation of LBE

The LB equation with the forcing term can now be written as:

$$\begin{aligned} f_a(\mathbf{r} + \mathbf{v}_a \Delta t, t + \Delta t) &= f_a(\mathbf{r}, t) - \frac{\Delta t}{\tau} \left[f_a(\mathbf{r}, t) - f_a^{eq}(\mathbf{r}, t) \right] \\ &\quad + \frac{w_a}{RT} \mathbf{F} \cdot \left[(\mathbf{v}_a - \mathbf{u}) + \mathbf{v}_a \frac{\mathbf{v}_a \cdot \mathbf{u}}{RT} \right] \Delta t \end{aligned} \quad (\text{A.14})$$

The left hand side of the above equation $f_a(\mathbf{r} + \mathbf{v}_a \Delta t, t + \Delta t)$ can be expanded in a Taylor series about \mathbf{r} and t up to terms of second order $O(\Delta t^2)$ to give:

$$\begin{aligned} f_a(\mathbf{r} + \mathbf{v}_a \Delta t, t + \Delta t) &= f_a(\mathbf{r}, t) + \Delta t v_{a\alpha} \partial_{r_\alpha} f_a + \Delta t \partial_t f_a \\ &\quad + \frac{(\Delta t)^2}{2} \left[v_{a\alpha} v_{a\beta} \partial_{r_\alpha} \partial_{r_\beta} f_a + 2v_{a\alpha} \partial_{r_\alpha} \partial_t f_a + \partial_t^2 f_a \right] \end{aligned} \quad (\text{A.15})$$

Substituting the above equation into equation (A.14) yields:

$$\begin{aligned} v_{a\alpha} \partial_{r_\alpha} f_a + \partial_t f_a + \frac{\Delta t}{2} \left[v_{a\alpha} v_{a\beta} \partial_{r_\alpha} \partial_{r_\beta} f_a + 2v_{a\alpha} \partial_{r_\alpha} \partial_t f_a + \partial_t^2 f_a \right] &+ \frac{1}{\tau} \left[f_a - f_a^{eq} \right] \\ &= \frac{w_a}{RT} \mathbf{F} \cdot \left[(\mathbf{v}_a - \mathbf{u}) + \mathbf{v}_a \frac{\mathbf{v}_a \cdot \mathbf{u}}{RT} \right] \end{aligned} \quad (\text{A.16})$$

Now, substituting new space and time-derivatives (from equations (A.7) and (A.8)) and the forcing term (from equation (A.10)) in the above equation gives:

$$\begin{aligned}
& \varepsilon v_{a\alpha} \partial_{r_{1\alpha}} f_a + (\varepsilon \partial_{t_1} f_a + \varepsilon^2 \partial_{t_2} f_a) + \frac{\Delta t}{2} \left[\begin{aligned} & \varepsilon^2 v_{a\alpha} v_{a\beta} \partial_{r_{1\alpha}} \partial_{r_{1\beta}} f_a \\ & + 2\varepsilon v_{a\alpha} \partial_{r_{1\alpha}} (\varepsilon \partial_{t_1} f_a + \varepsilon^2 \partial_{t_2} f_a) \\ & + (\varepsilon \partial_{t_1} + \varepsilon^2 \partial_{t_2}) (\varepsilon \partial_{t_1} f_a + \varepsilon^2 \partial_{t_2} f_a) \end{aligned} \right] + \frac{1}{\tau} [f_a - f_a^{eq}] \\
& = \frac{w_a}{RT} (\varepsilon^2 \mathbf{F}^{(2)} + \varepsilon^3 \mathbf{F}^{(3)} + \dots) \cdot \left[(\mathbf{v}_a - \mathbf{u}) + \mathbf{v}_a \frac{\mathbf{v}_a \cdot \mathbf{u}}{RT} \right]
\end{aligned} \tag{A.17}$$

In the above equation, neglecting higher order terms (i.e. terms of the order $O(\varepsilon^3)$ or higher) gives:

$$\begin{aligned}
& \varepsilon (v_{a\alpha} \partial_{r_{1\alpha}} + \partial_{t_1}) f_a + \varepsilon^2 \left(\partial_{t_2} + \frac{\Delta t}{2} [v_{a\alpha} v_{a\beta} \partial_{r_{1\alpha}} \partial_{r_{1\beta}} + 2v_{a\alpha} \partial_{r_{1\alpha}} \partial_{t_1} + \partial_{t_1}^2] \right) f_a + \frac{1}{\tau} [f_a - f_a^{eq}] \\
& = \frac{w_a}{RT} \varepsilon^2 \mathbf{F}^{(2)} \cdot \left[(\mathbf{v}_a - \mathbf{u}) + \mathbf{v}_a \frac{\mathbf{v}_a \cdot \mathbf{u}}{RT} \right]
\end{aligned} \tag{A.18}$$

Now, substituting expansion of f_a in the above equation and neglecting terms of the order $O(\varepsilon^3)$ or higher, we get:

$$\begin{aligned}
& \varepsilon (v_{a\alpha} \partial_{r_{1\alpha}} + \partial_{t_1}) f_a^{eq} + \varepsilon^2 (v_{a\alpha} \partial_{r_{1\alpha}} + \partial_{t_1}) f_a^{(1)} + \varepsilon^2 \left(\partial_{t_2} + \frac{\Delta t}{2} [v_{a\alpha} v_{a\beta} \partial_{r_{1\alpha}} \partial_{r_{1\beta}} + 2v_{a\alpha} \partial_{r_{1\alpha}} \partial_{t_1} + \partial_{t_1}^2] \right) f_a^{eq} \\
& + \frac{1}{\tau} [\varepsilon f_a^{(1)} + \varepsilon^2 f_a^{(2)}] = \frac{w_a}{RT} \varepsilon^2 \mathbf{F}^{(2)} \cdot \left[(\mathbf{v}_a - \mathbf{u}) + \mathbf{v}_a \frac{\mathbf{v}_a \cdot \mathbf{u}}{RT} \right]
\end{aligned} \tag{A.19}$$

Note that, the above equation, which is up to second order accurate with respect to ε , is sufficient to recover the Navier-Stokes equation in the incompressible limit. However, retaining higher order terms (order $O(\varepsilon^3)$ or higher) in the above equation leads to the recovery of *Burnett* and *Super-Burnett* equations.

After substituting the corresponding scale expansions, the LBE equation can be written in an order separated form as:

$$\varepsilon E_a^{(1)} + \varepsilon^2 E_a^{(2)} = 0 \quad (\text{A.20})$$

where

$$E_a^{(1)} = \left(v_{a\alpha} \partial_{r_{i\alpha}} + \partial_{t_1} \right) f_a^{eq} + \frac{1}{\tau} f_a^{(1)} = 0 \quad (\text{A.21})$$

and

$$\begin{aligned} E_a^{(2)} = & \left(\partial_{t_2} + \frac{\Delta t}{2} \left[v_{a\alpha} v_{a\beta} \partial_{r_{i\alpha}} \partial_{r_{i\beta}} + 2v_{a\alpha} \partial_{r_{i\alpha}} \partial_{t_1} + \partial_{t_1}^2 \right] \right) f_a^{eq} \\ & + \left(v_{a\alpha} \partial_{r_{i\alpha}} + \partial_{t_1} \right) f_a^{(1)} + \frac{1}{\tau} f_a^{(2)} - B_a^{(2)} = 0 \end{aligned} \quad (\text{A.22})$$

where

$$B_a^{(2)} = \frac{w_a}{RT} \mathbf{F}^{(2)} \cdot \left[(\mathbf{v}_a - \mathbf{u}) + \mathbf{v}_a \frac{\mathbf{v}_a \cdot \mathbf{u}}{RT} \right] \quad (\text{A.23})$$

A.4 First order macrodynamics: $E_a^{(1)}$

A.4.1 Mass conservation: $\sum_a E_a^{(1)} = 0$

Zeroth lattice-velocity moment of $E_a^{(1)}$ is:

$$\sum_a E_a^{(1)} = \sum_a v_{a\alpha} \partial_{r_{i\alpha}} f_a^{eq} + \sum_a \partial_{t_1} f_a^{eq} + \frac{1}{\tau} \sum_a f_a^{(1)} = 0 \quad (\text{A.24})$$

which is:

$$\partial_{t_1} \underbrace{\left(\sum_a f_a^{eq} \right)}_{=\rho} + \partial_{r_{i\alpha}} \underbrace{\left(\sum_a v_{a\alpha} f_a^{eq} \right)}_{=\rho u_\alpha} + \frac{1}{\tau} \underbrace{\left(\sum_a f_a^{(1)} \right)}_{=0} = 0 \quad (\text{A.25})$$

and, can be written in a more simplified form as:

$$\partial_{t_1} \rho + \partial_{r_{i\alpha}} (\rho u_\alpha) = 0 \quad (\text{A.26})$$

A.4.2 Momentum conservation: $\sum_a v_{a\alpha} E_a^{(1)} = 0$

First lattice-velocity moment of $E_a^{(1)}$ is:

$$\sum_a v_{a\alpha} E_a^{(1)} = \sum_a v_{a\alpha} v_{a\beta} \partial_{r_{i\beta}} f_a^{eq} + \sum_a v_{a\alpha} \partial_{t_1} f_a^{eq} + \frac{1}{\tau} \sum_a v_{a\alpha} f_a^{(1)} = 0 \quad (\text{A.27})$$

which is:

$$\partial_{t_1} \left(\underbrace{\sum_a v_{a\alpha} f_a^{eq}}_{=\rho u_\alpha} \right) + \partial_{r_{1\beta}} \left(\underbrace{\sum_a v_{a\alpha} v_{a\beta} f_a^{eq}}_{=\Pi_{\alpha\beta}^{(0)}} \right) + \frac{1}{\tau} \left(\underbrace{\sum_a v_{a\alpha} f_a^{(1)}}_{=0} \right) = 0 \quad (\text{A.28})$$

and, can be written in a more simplified form as:

$$\partial_{t_1} (\rho u_\alpha) + \partial_{r_{1\beta}} [\Pi_{\alpha\beta}^{(0)}] = 0 \quad (\text{A.29})$$

where

$$\Pi_{\alpha\beta}^{(0)} = \sum_a v_{a\alpha} v_{a\beta} f_a^{eq} \quad (\text{A.30})$$

is called the zeroth-order momentum flux tensor, which represents flux of the α -component of momentum transported along the β -axis.

A.4.3 Evaluation of $\Pi_{\alpha\beta}^{(0)}$

Second lattice-velocity moment of the discrete equilibrium distribution function f_a^{eq} can be evaluated as:

$$\begin{aligned} \Pi_{\alpha\beta}^{(0)} &= \sum_a v_{a\alpha} v_{a\beta} w_a \left(1 + \frac{v_{a\gamma} u_\gamma}{RT} + \frac{1}{2(RT)^2} v_{a\gamma} u_\gamma v_{a\xi} u_\xi - \frac{u_\gamma u_\xi}{2RT} \right) \\ &= \underbrace{\sum_a v_{a\alpha} v_{a\beta} w_a}_{=\rho RT \delta_{\alpha\beta}} + \frac{u_\gamma}{RT} \underbrace{\sum_a v_{a\alpha} v_{a\beta} v_{a\gamma} w_a}_{=0} + \frac{u_\gamma u_\xi}{2(RT)^2} \underbrace{\sum_a v_{a\alpha} v_{a\beta} v_{a\gamma} v_{a\xi} w_a}_{=\rho (RT)^2 (\delta_{\alpha\beta} \delta_{\gamma\xi} + \delta_{\alpha\gamma} \delta_{\beta\xi} + \delta_{\alpha\xi} \delta_{\beta\gamma})} \\ &\quad - \frac{u_\gamma u_\xi}{2RT} \underbrace{\sum_a v_{a\alpha} v_{a\beta} w_a}_{=\rho RT \delta_{\alpha\beta}} \\ &= p \delta_{\alpha\beta} + \rho u_\alpha u_\beta \end{aligned} \quad (\text{A.31})$$

where $p = \rho RT$ is the pressure of an ideal gas and hence, represents the inherent *ideal gas equation of state* of the isothermal LBE.

For a two-dimensional (xy) system:

$$\Pi_{\alpha\beta}^{(0)} = \begin{pmatrix} \Pi_{xx}^{(0)} & \Pi_{xy}^{(0)} \\ \Pi_{yx}^{(0)} & \Pi_{yy}^{(0)} \end{pmatrix} = p \delta_{\alpha\beta} + \rho \begin{pmatrix} u_x^2 & u_x u_y \\ u_x u_y & u_y^2 \end{pmatrix} \quad (\text{A.32})$$

At this point, since we have defined pressure in our system, we can calculate the sound speed c_s as:

$$c_s = \sqrt{\frac{dp}{d\rho}} = \sqrt{RT} \quad (\text{A.33})$$

A.5 Second order macrodynamics: $E_a^{(2)}$

A.5.1 Mass conservation: $\sum_a E_a^{(2)} = 0$

Zeroth lattice-velocity moment of $E_a^{(2)}$ is:

$$\sum_a E_a^{(2)} = \sum_a \left\{ \left(v_{a\alpha} \partial_{r_{1\alpha}} + \partial_{t_1} \right) f_a^{(1)} + \left(\partial_{t_2} + \frac{\Delta t}{2} \left[v_{a\alpha} v_{a\beta} \partial_{r_{1\alpha}} \partial_{r_{1\beta}} + 2v_{a\alpha} \partial_{r_{1\alpha}} \partial_{t_1} + \partial_{t_1}^2 \right] \right) f_a^{eq} + \frac{1}{\tau} f_a^{(2)} - B_a^{(2)} \right\} = 0 \quad (\text{A.34})$$

or,

$$\begin{aligned} & \partial_{t_2} \left(\sum_a f_a^{eq} \right) + \frac{\Delta t}{2} \partial_{r_{1\alpha}} \partial_{r_{1\beta}} \left(\sum_a v_{a\alpha} v_{a\beta} f_a^{eq} \right) + \Delta t \partial_{r_{1\alpha}} \partial_{t_1} \left(\sum_a v_{a\alpha} f_a^{eq} \right) \\ & + \frac{\Delta t}{2} \partial_{t_1}^2 \left(\sum_a f_a^{eq} \right) + \partial_{r_{1\alpha}} \left(\sum_a v_{a\alpha} f_a^{(1)} \right) + \partial_{t_1} \left(\sum_a f_a^{(1)} \right) + \frac{1}{\tau} \left(\sum_a f_a^{(2)} \right) - \sum_a B_a^{(2)} = 0 \end{aligned} \quad (\text{A.35})$$

The above equation reduces to:

$$\partial_{t_2} \rho + \frac{\Delta t}{2} \partial_{r_{1\alpha}} \partial_{r_{1\beta}} \Pi_{\alpha\beta}^{(0)} + \Delta t \partial_{r_{1\alpha}} \partial_{t_1} (\rho u_\alpha) + \frac{\Delta t}{2} \partial_{t_1}^2 \rho = 0 \quad (\text{A.36})$$

The third term on the right hand side of the above equation is equivalent to:

$$\Delta t \partial_{r_{1\alpha}} \partial_{t_1} (\rho u_\alpha) = -\Delta t \partial_{r_{1\alpha}} \partial_{r_{1\beta}} \left[\Pi_{\alpha\beta}^{(0)} \right] \quad (\text{A.37})$$

Furthermore, the last term on the right hand side of equation (A.36) is equivalent to:

$$\frac{\Delta t}{2} \partial_{t_1}^2 \rho = \frac{\Delta t}{2} \partial_{t_1} \left(\partial_{t_1} \rho \right) = -\frac{\Delta t}{2} \partial_{t_1} \left(\partial_{r_{1\alpha}} \left(\rho u_\alpha \right) \right) = \frac{\Delta t}{2} \partial_{r_{1\alpha}} \partial_{r_{1\beta}} \left[\Pi_{\alpha\beta}^{(0)} \right] \quad (\text{A.38})$$

Now, substituting these terms in equation (A.36), we get:

$$\partial_{t_2} \rho + \underbrace{\left(\frac{\Delta t}{2} \partial_{r_{1\alpha}} \partial_{r_{1\beta}} \Pi_{\alpha\beta}^{(0)} - \Delta t \partial_{r_{1\alpha}} \partial_{r_{1\beta}} \Pi_{\alpha\beta}^{(0)} + \frac{\Delta t}{2} \partial_{r_{1\alpha}} \partial_{r_{1\beta}} \Pi_{\alpha\beta}^{(0)} \right)}_{=0} = 0 \quad (\text{A.39})$$

which essentially is:

$$\partial_{t_2} \rho = 0 \quad (\text{A.40})$$

A.5.2 Momentum conservation: $\sum_a v_{a\alpha} E_a^{(2)} = 0$

First lattice-velocity moment of $E_a^{(2)}$ is:

$$\sum_a v_{a\alpha} E_a^{(2)} = \sum_a v_{a\alpha} \left\{ \left(v_{a\alpha} \partial_{r_{1\alpha}} + \partial_{t_1} \right) f_a^{(1)} + \left(\partial_{t_2} + \frac{\Delta t}{2} \left[v_{a\alpha} v_{a\beta} \partial_{r_{1\alpha}} \partial_{r_{1\beta}} + 2v_{a\alpha} \partial_{r_{1\alpha}} \partial_{t_1} + \partial_{t_1}^2 \right] \right) f_a^{eq} \right. \\ \left. + \frac{1}{\tau} f_a^{(2)} - B_a^{(2)} \right\} = 0 \quad (\text{A.41})$$

or,

$$\partial_{t_2} \left(\sum_a v_{a\alpha} f_a^{eq} \right) + \frac{\Delta t}{2} \partial_{r_{1\beta}} \partial_{r_{1\gamma}} \left(\sum_a v_{a\alpha} v_{a\beta} v_{a\gamma} f_a^{eq} \right) + \Delta t \partial_{t_1} \partial_{r_{1\beta}} \left(\sum_a v_{a\alpha} v_{a\beta} f_a^{eq} \right) + \frac{\Delta t}{2} \partial_{t_1}^2 \left(\sum_a v_{a\alpha} f_a^{eq} \right) \\ + \partial_{r_{1\beta}} \left(\sum_a v_{a\alpha} v_{a\beta} f_a^{(1)} \right) + \partial_{t_1} \left(\sum_a v_{a\alpha} f_a^{(1)} \right) + \frac{1}{\tau} \left(\sum_a v_{a\alpha} f_a^{(2)} \right) - \underbrace{\sum_a v_{a\alpha} B_a^{(2)}}_{=\rho F_\alpha^{(2)}} = 0 \quad (\text{A.42})$$

The above equation reduces to:

$$\partial_{t_2} \left(\rho u_\alpha \right) + \frac{\Delta t}{2} \partial_{r_{1\beta}} \partial_{r_{1\gamma}} \left(\sum_a v_{a\alpha} v_{a\beta} v_{a\gamma} f_a^{eq} \right) + \Delta t \partial_{t_1} \partial_{r_{1\beta}} \Pi_{\alpha\beta}^{(0)} + \frac{\Delta t}{2} \partial_{t_1} \left[\partial_{t_1} \left(\rho u_\alpha \right) \right] \\ + \partial_{r_{1\beta}} \left(\sum_a v_{a\alpha} v_{a\beta} \underbrace{f_a^{(1)}}_{=?} \right) - \rho F_\alpha^{(2)} = 0 \quad (\text{A.43})$$

We can write $f_a^{(1)}$ in terms of f_a^{eq} as:

$$f_a^{(1)} = -\tau \left(v_{a\gamma} \partial_{r_{1\gamma}} + \partial_{t_1} \right) f_a^{eq} \quad (\text{A.44})$$

Substituting $f_a^{(1)}$ in equation (A.43) gives:

$$\partial_{t_2} \left(\rho u_\alpha \right) + \left(\frac{\Delta t}{2} - \tau \right) \overbrace{\partial_{r_{1\beta}} \partial_{r_{1\gamma}} \left(\sum_a v_{a\alpha} v_{a\beta} v_{a\gamma} f_a^{eq} \right)}^{TERM-1} + \left(\frac{\Delta t}{2} - \tau \right) \overbrace{\partial_{t_1} \partial_{r_{1\beta}} \Pi_{\alpha\beta}^{(0)}}^{TERM-2} = 0 \quad (\text{A.45})$$

TERM-1 in the above equation can be evaluated as:

$$\begin{aligned}
& \partial_{r_{\beta}} \partial_{r_{\gamma}} \left(\sum_a v_{a\alpha} v_{a\beta} v_{a\gamma} f_a^{eq} \right) \\
&= \partial_{r_{\beta}} \partial_{r_{\gamma}} \left[\sum_a v_{a\alpha} v_{a\beta} v_{a\gamma} w_a \left(1 + \frac{v_{a\xi} u_{\xi}}{c_s^2} + \frac{v_{a\xi} u_{\xi} v_{a\psi} u_{\psi}}{2c_s^4} - \frac{u_{\xi} u_{\psi}}{2c_s^2} \right) \right] \\
&= \partial_{r_{\beta}} \partial_{r_{\gamma}} \left[\underbrace{\sum_a v_{a\alpha} v_{a\beta} v_{a\gamma} w_a}_{=0} + \frac{u_{\xi}}{c_s^2} \underbrace{\sum_a v_{a\alpha} v_{a\beta} v_{a\gamma} v_{a\xi} w_a}_{=\rho c_s^4 (\delta_{\alpha\beta} \delta_{\gamma\xi} + \delta_{\alpha\gamma} \delta_{\beta\xi} + \delta_{\alpha\xi} \delta_{\beta\gamma})} \right. \\
&\quad \left. + \frac{u_{\xi} u_{\psi}}{2c_s^4} \underbrace{\sum_a v_{a\alpha} v_{a\beta} v_{a\gamma} v_{a\xi} v_{a\psi} w_a}_{=0} - \frac{u_{\xi} u_{\psi}}{2c_s^2} \underbrace{\sum_a v_{a\alpha} v_{a\beta} v_{a\gamma} w_a}_{=0} \right] \\
&= c_s^2 \partial_{r_{\beta}} \partial_{r_{\gamma}} \rho u_{\xi} (\delta_{\alpha\beta} \delta_{\gamma\xi} + \delta_{\alpha\gamma} \delta_{\beta\xi} + \delta_{\alpha\xi} \delta_{\beta\gamma}) \\
&= c_s^2 (\delta_{\alpha\beta} \delta_{\gamma\xi} + \delta_{\alpha\gamma} \delta_{\beta\xi} + \delta_{\alpha\xi} \delta_{\beta\gamma}) \left[\partial_{r_{\beta}} \partial_{r_{\gamma}} (\rho u_{\xi}) \right]
\end{aligned} \tag{A.46}$$

TERM-2 in equation (A.45) can be evaluated as:

$$\begin{aligned}
\partial_{t_1} \partial_{r_{\beta}} \Pi_{\alpha\beta}^{(0)} &= \partial_{t_1} \partial_{r_{\beta}} (\rho c_s^2 \delta_{\alpha\beta}) \\
&= c_s^2 \partial_{r_{\beta}} (\partial_{t_1} \rho) \delta_{\alpha\beta} = -c_s^2 \delta_{\alpha\beta} \partial_{r_{\beta}} \partial_{r_{\gamma}} (\rho u_{\gamma})
\end{aligned} \tag{A.47}$$

Note that, in the above equation, terms of order $O(u^2)$ have been neglected.

Substituting TERM-1 and TERM-2 in the above equation, we get:

$$\partial_{t_2} (\rho u_{\alpha}) = \nu \left[\partial_{r_{\beta}} \partial_{r_{\beta}} (\rho u_{\alpha}) + \partial_{r_{\alpha}} \partial_{r_{\beta}} (\rho u_{\beta}) \right] + \rho F_{\alpha}^{(2)} \tag{A.48}$$

where ν is the kinematic viscosity, given by:

$$\nu = RT \left(\tau - \frac{\Delta t}{2} \right) \tag{A.49}$$

A.6 Order-combined macro-dynamics: $\varepsilon E_a^{(1)} + \varepsilon^2 E_a^{(2)}$

A.6.1 Mass conservation: $\sum_a (\varepsilon E_a^{(1)} + \varepsilon^2 E_a^{(2)}) = 0$

Combining corresponding first and second order macro-dynamic equations, we get:

$$\varepsilon \left[\partial_{t_1} \rho + \partial_{r_{\alpha}} (\rho u_{\alpha}) \right] + \varepsilon^2 \left[\partial_{t_2} \rho \right] = 0 \tag{A.50}$$

which essentially is:

$$\underbrace{(\varepsilon \partial_{t_1} + \varepsilon^2 \partial_{t_2})}_{\partial_t} \rho + \underbrace{\varepsilon \partial_{r_{\alpha}}}_{\partial_{r_{\alpha}}} (\rho u_{\alpha}) = 0 \tag{A.51}$$

and reduces to the continuity equation:

$$\partial_t \rho + \partial_{r_\alpha} (\rho u_\alpha) = 0 \quad (\text{A.52})$$

A.6.2 Momentum conservation: $\sum_a v_{a\alpha} (\varepsilon E_a^{(1)} + \varepsilon^2 E_a^{(2)}) = 0$

Combining corresponding first and second order macro-dynamic equations, we get:

$$\varepsilon \left[\partial_{t_1} (\rho u_\alpha) + \partial_{r_{1\beta}} \Pi_{\alpha\beta}^{(0)} \right] + \varepsilon^2 \left[\begin{array}{l} \partial_{t_2} (\rho u_\alpha) - \nu \left(\partial_{r_{1\beta}} \partial_{r_{1\beta}} (\rho u_\alpha) + \partial_{r_{1\alpha}} \partial_{r_{1\beta}} (\rho u_\beta) \right) \\ - \rho F_\alpha^{(2)} \end{array} \right] = 0 \quad (\text{A.53})$$

The above equation can be written as:

$$\partial_t (\rho u_\alpha) + \partial_{r_\beta} \Pi_{\alpha\beta}^{(0)} = \nu \left[\partial_{r_\beta} \partial_{r_\beta} (\rho u_\alpha) + \partial_{r_\alpha} \partial_{r_\beta} (\rho u_\beta) \right] + \rho F_\alpha \quad (\text{A.54})$$

A.6.3 Incompressible limit: $\rho = \text{constant}$

In the incompressible limit, $\rho = \text{constant}$, the continuity equation yields the *incompressible continuity equation*:

$$\partial_{r_\alpha} (u_\alpha) = 0 \quad (\text{A.55})$$

and the order-combined momentum conservation equation yields:

$$\partial_t (u_\alpha) + \frac{\partial_{r_\beta} \Pi_{\alpha\beta}^{(0)}}{\rho} = \nu \partial_{r_\beta} \partial_{r_\beta} (u_\alpha) + F_\alpha \quad (\text{A.56})$$

Substituting $\Pi_{\alpha\beta}^{(0)}$ in the above equation, we get the *incompressible Navier-Stokes equation*:

$$\partial_t (u_\alpha) + u_\beta \left(\partial_{r_\beta} u_\alpha \right) = -\frac{1}{\rho} \left(\partial_{r_\alpha} p \right) + \nu \left(\partial_{r_\beta} \partial_{r_\beta} u_\alpha \right) + F_\alpha \quad (\text{A.57})$$

A.7 Remarks on fluid viscosity in the LB equation

In the LBE, fluid viscosity is given by (see equation (A.49), which is in a non-dimensional form and is written without ‘bars’ over variables):

$$\bar{\nu} = \bar{c}_s^2 \left(\bar{\tau} - \frac{\Delta \bar{t}}{2} \right) \quad (\text{A.58})$$

which, for a D2Q9 lattice, is:

$$\bar{\nu} = \frac{\bar{c}^2 \Delta \bar{t}}{3} \left(\tau^* - \frac{1}{2} \right) \quad (\text{A.59})$$

where $\bar{c} = \frac{\Delta \bar{x}}{\Delta \bar{t}} = \frac{\Delta \bar{y}}{\Delta \bar{t}}$ and $\tau^* = \frac{\bar{\tau}}{\Delta \bar{t}}$.

In the first-order LBE simulations, τ^* has to be greater than 0.5 for a positive non-zero kinematic viscosity ν . Usually, for numerical stability considerations, τ^* is taken to be between 0.5 and 3.0. Here, we should note that, τ^* appears explicitly on the right hand side of the LB equation and is used as a pre-specified parameter in the LBM calculations.

For given non-dimensional kinematic viscosity ($\bar{\nu} = \text{Re}^{-1}$) and the spatial grid size $\Delta \bar{x} = \Delta \bar{y}$, we can calculate LBM time step as:

$$\Delta \bar{t} = \frac{\Delta \bar{x}^2}{3 \bar{\nu}} \left(\tau^* - \frac{1}{2} \right) = \frac{1}{3} \Delta \bar{x}^2 (\tau^* - 0.5) \text{Re} \quad (\text{A.60})$$

Appendix B

Code, Parallelization and Performance

For large applications to be solved on distributed memory machines (or clusters), the Message Passing Interface (MPI) is the most widely used approach and therefore, is used for parallelization of the LBM code.

B.1 Domain decomposition

Domain decomposition technique is a natural way of parallelization for a system in which the computation of a variable at any grid-point depends only on the variables at the neighboring grid-points. In this technique, the computational grid is partitioned into several smaller sub-domains (one for each processor) of desired size. Each processor performs computations on a certain sub-domain and exchanges information with the neighboring processors whenever necessary. For a 2D calculation, the computational domain may be divided by either a 1D or 2D partitioning scheme. A 1D partitioning scheme slices the domain only in one direction leading to horizontal or vertical slices. However, a 2D partitioning scheme slices the domain in both the directions (shown in Fig. B.1).

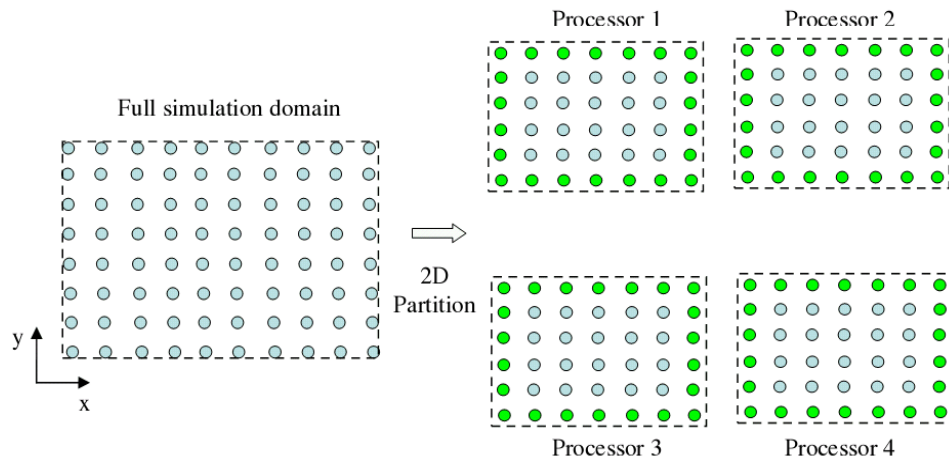


Fig. B.1: 2D block decomposition of the simulation domain. The calculation grid is divided into several sub-domains to be assigned to each of the participating processors. Every sub-domain (grey circles, \circ) is now padded with a ghost layer of grid-points (green circles, \bullet) on each side.

In a parallel LBM code, each of the sub-domains is subsequently padded with a ghost layer of grid-points at its boundaries. These ghost layers are essential to ensure accurate and simultaneous passing of boundary information to the neighboring processors.

B.2 Data partition and performance

Domain decomposition alone does not yield the expected speedup in a LBM code. It should be accompanied by a corresponding data-partitioning so that each processor only stores and computes the data of the assigned sub-domain. In a basic LBM code, most of the calculation involves the distribution function data which is usually stored in an array. Passing such an array (and many more for an advanced code) for large 3D problems to each and every processor will require large amount of memory and consequently, will slow down the calculation due to cache miss and page faults. Therefore, it is essential that each processor only sees the data for its sub-domain and communicates with other processors using ghost layers. The algorithm template dictates which discrete variables must be communicated to the neighboring processors.

An important feature of LBM scheme is the inherent spatial locality of the collision operator. From the evolution algorithm of the LBM, interactions between processors are only required before the execution of the propagation step. Processors interact by sending their boundary data to the neighboring processors and by receiving data in their ghost layers from the neighboring processors (see Figure B.2). By using ghost layer of grid points, the propagation step can be isolated from the data exchange step. Hence, the computation is independently carried out point-by-point in the LBM method.

B.3 Efficiency with fixed problem size per processor

Parallelization efficiency is best measured by increasing the size of the calculation with the increase in the number of processors. It is usually done by maintaining the constant calculation load for each processor by assigning the same size of sub-domain to each processor. A fixed number of LBM time steps are simulated for all the runs involving different number of processors and thus, different total problem sizes.

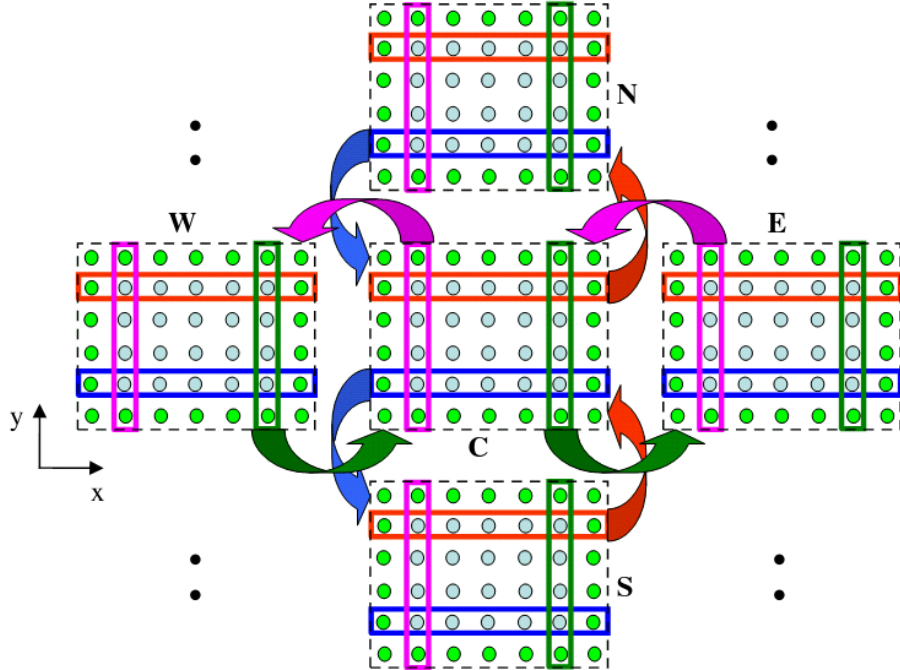


Fig. B.2: Data exchange among the participating processors. Processor in the center (C) communicates with its neighboring processors (N, S, W and E) in order to synchronize data at its boundaries and the surrounding ghost layers. Processor C sends data from its North, South, East and West boundary to the processors N, S, E and W, respectively. Simultaneously, it receives data in its North, South, East and West side ghost layer from the processors N, S, E and W's South, North, West and East boundaries, respectively. The respective exchange is shown by different colored arrows in the figure.

Since problem size per processor is fixed, therefore it is expected that the running time, in the absence of communication cost, should remain constant irrespective of the number of processors. Hence, speedup, S , for a fixed problem size is defined as,

$$S = \frac{pT_s}{T_p} \quad (\text{B.1})$$

and efficiency, E , is defined as

$$E = \frac{T_s}{T_p} \quad (\text{B.2})$$

where p is the number of processors, T_s is runtime when a single processor is used and T_p is runtime when p number of processors are used. Efficiency and speed-up of the LBM code,

written for single-phase flow and for simulating low-density spinodal decomposition of two-phases, are shown in Figure B.3 for varying number of processors.

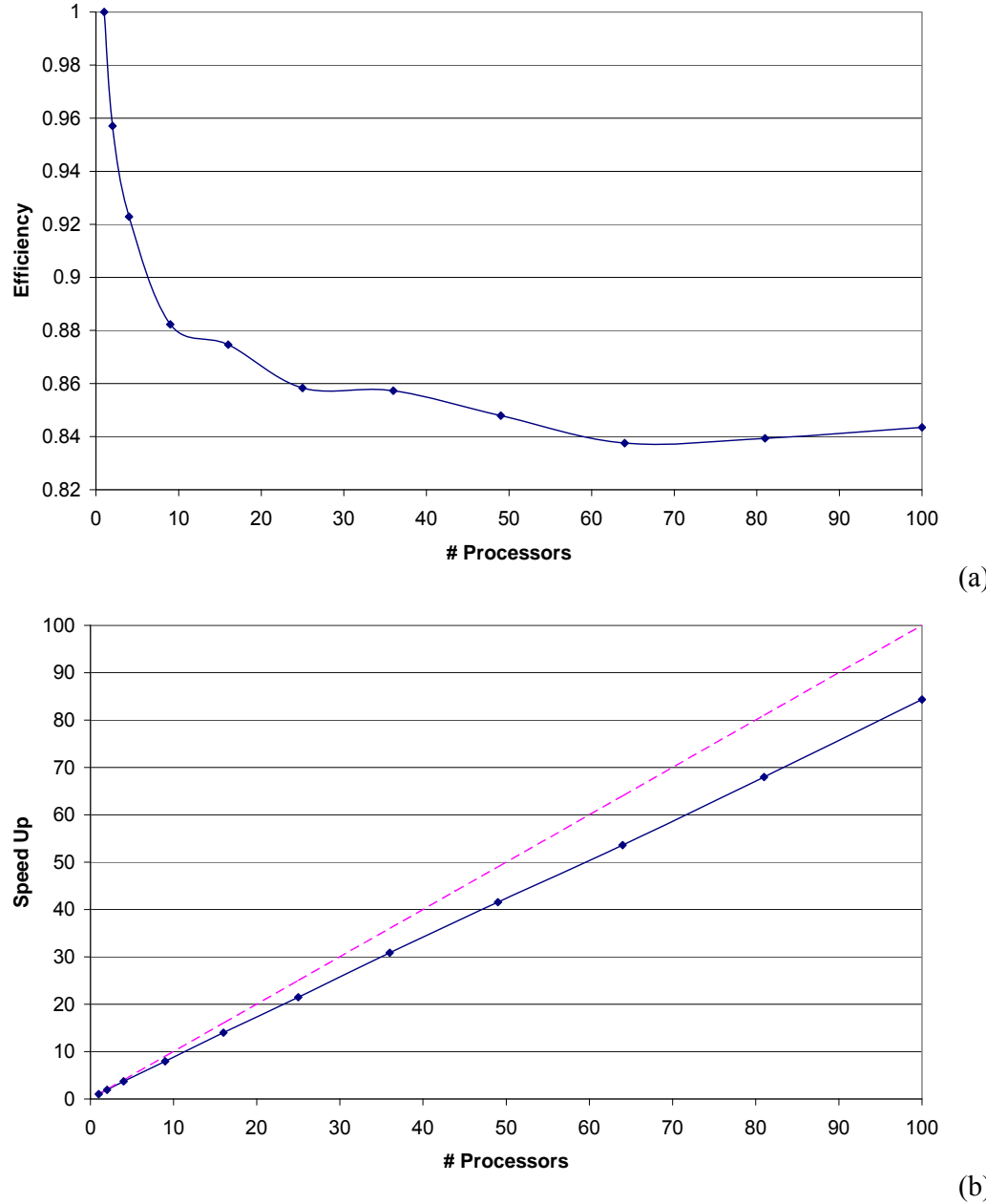


Fig. B.3: (a) Efficiency and (b) speed-up for a parallel LBM code running on a distributed memory machine (Turing cluster, University of Illinois at Urbana Champaign). Each processor runs the LBM calculation on a 2D sub-domain consisting of 66×66 grid points (including ghost layers). A fixed number of 10,000 time-steps are simulated in each run. Total size of the problem increases with increasing number of processors.

Appendix C

Velocity boundary conditions in 2D

In this appendix, velocity boundary conditions for the North, East and West boundaries in a 2D domain are presented. Since respective corners of the above boundaries are treated in a special way, results for them are also presented.

C.1 North boundary

Unknowns at the North boundary can be obtained following the process for the South boundary in Sec. 5.1.1. In this section, we only provide the resulting equations.

Below are the equations which should be solved in order to obtain the desired unknowns ρ_w , g_4 , g_7 and g_8 at the North boundary (see Fig. C.1).

$$\rho_w = \left\{ g_0 + g_1 + g_3 + 2(g_2 + g_5 + g_6) + \frac{\Delta t}{2} F_y^C \right\} / \left\{ 1 + U_{wy} \right\} \quad (C.1)$$

$$g_4 = g_2 + (g_4^{eq} - g_2^{eq}) \quad (C.2)$$

$$g_7 - g_8 = (g_1 + g_5) - (g_3 + g_6) - \rho_w U_{wx} + \frac{\Delta t}{2} F_x^C \quad (C.3)$$

$$g_7 + g_8 = g_2 + g_5 + g_6 - g_4 - \rho_w U_{wy} + \frac{\Delta t}{2} F_y^C \quad (C.4)$$

$$g_7 = \frac{(g_7 + g_8) + (g_7 - g_8)}{2} \quad (C.5)$$

$$g_8 = \frac{(g_7 + g_8) - (g_7 - g_8)}{2} \quad (C.6)$$

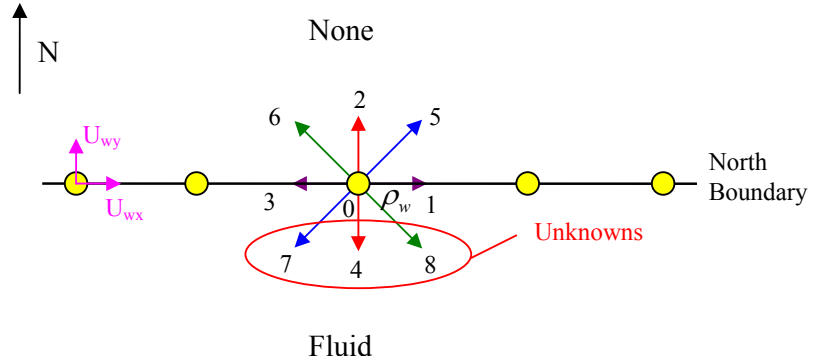


Fig. C.1: Velocity boundary condition at the North boundary. The x - and y -velocity of the fluid is specified to be U_{wx} and U_{wy} , respectively. Distribution functions g_4 , g_7 , g_8 and the density ρ_w are unknown.

C.2 West boundary

Unknowns at the West boundary can be obtained following the process for the South boundary in Sec. 5.1.1. In this section, we only provide the resulting equations.

Below are the equations which should be solved in order to obtain the desired unknowns ρ_w , g_1 , g_5 and g_8 at the West boundary (see Fig. C.2).

$$\rho_w = \left\{ g_0 + g_2 + g_4 + 2(g_3 + g_6 + g_7) - \frac{\Delta t}{2} F_x^C \right\} \left/ \left(1 - U_{wx} \right) \right. \quad (C.7)$$

$$g_1 = g_3 + (g_1^{eq} - g_3^{eq}) \quad (C.8)$$

$$g_5 - g_8 = (g_4 + g_7) - (g_2 + g_6) + \rho_w U_{wy} - \frac{\Delta t}{2} F_y^C \quad (C.9)$$

$$g_5 + g_8 = g_3 + g_6 + g_7 - g_1 + \rho_w U_{wx} - \frac{\Delta t}{2} F_x^C \quad (C.10)$$

$$g_5 = \frac{(g_5 + g_8) + (g_5 - g_8)}{2} \quad (C.11)$$

$$g_8 = \frac{(g_5 + g_8) - (g_5 - g_8)}{2} \quad (C.12)$$

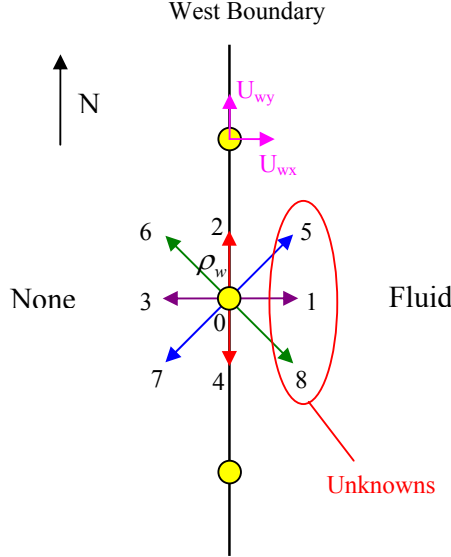


Fig. C.2: Velocity boundary condition at the West boundary. The x - and y -velocity of the fluid is specified to be U_{wx} and U_{wy} , respectively. Distribution functions g_1 , g_5 , g_8 and the density ρ_w are unknown.

C.3 East boundary

Unknowns at the East boundary can be obtained following the process for the South boundary in Sec. 5.1.1. In this section, we only provide the resulting equations.

Below are the equations which should be solved in order to obtain the desired unknowns ρ_w , g_3 , g_6 and g_7 at the East boundary (see Fig. C.3).

$$\rho_w = \left\{ g_0 + g_2 + g_4 + 2(g_1 + g_5 + g_8) + \frac{\Delta t}{2} F_x^C \right\} / \{1 + U_{wx}\} \quad (\text{C.13})$$

$$g_3 = g_1 + (g_3^{eq} - g_1^{eq}) \quad (\text{C.14})$$

$$g_7 - g_6 = (g_2 + g_5) - (g_4 + g_8) - \rho_w U_{wy} + \frac{\Delta t}{2} F_y^C \quad (\text{C.15})$$

$$g_7 + g_6 = g_1 + g_5 + g_8 - g_3 - \rho_w U_{wx} + \frac{\Delta t}{2} F_x^C \quad (\text{C.16})$$

$$g_7 = \frac{(g_7 + g_6) + (g_7 - g_6)}{2} \quad (\text{C.17})$$

$$g_6 = \frac{(g_7 + g_6) - (g_7 - g_6)}{2} \quad (C.18)$$

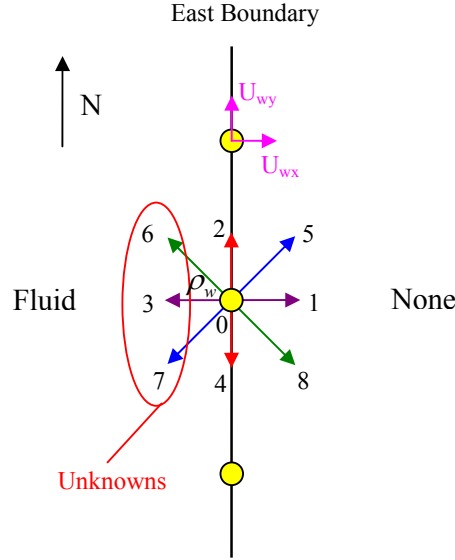


Fig. C.3: Velocity boundary condition at the East boundary. The x - and y -velocity of the fluid is specified to be U_{wx} and U_{wy} , respectively. Distribution functions g_3 , g_6 , g_7 and the density ρ_w are unknown.

C.4 South East (SE) corner

Unknowns at the SE corner can be obtained following the process for the SW corner in Sec. 5.1.2. In this section, we only provide the resulting equations.

Below are the equations which should be solved in order to obtain the desired unknowns at the SE corner (see Fig. C.4).

$$\rho_w = \rho_{NBR} \quad (C.19)$$

$$g_3 = g_1 + (g_3^{eq} - g_1^{eq}) \quad (C.20)$$

$$g_2 = g_4 + (g_2^{eq} - g_4^{eq}) \quad (C.21)$$

$$g_5 - g_6 - g_7 = g_3 - g_8 - g_1 + \rho_w U_{wx} - \frac{\Delta t}{2} F_x^C \quad (C.22)$$

$$g_5 + g_6 - g_7 = g_4 + g_8 - g_2 + \rho_w U_{wy} - \frac{\Delta t}{2} F_y^C \quad (C.23)$$

$$g_6 = \frac{(g_5 + g_6 - g_7) - (g_5 - g_6 - g_7)}{2} \quad (C.24)$$

$$g_5 - g_7 = (g_5 + g_6 - g_7) - g_6 \quad (C.25)$$

$$g_5 + g_7 = \rho_w - (g_0 + g_1 + g_2 + g_3 + g_4 + g_6 + g_8) \quad (C.26)$$

$$g_5 = \frac{(g_5 + g_7) + (g_5 - g_7)}{2} \quad (C.27)$$

$$g_7 = \frac{(g_5 + g_7) - (g_5 - g_7)}{2} \quad (C.28)$$

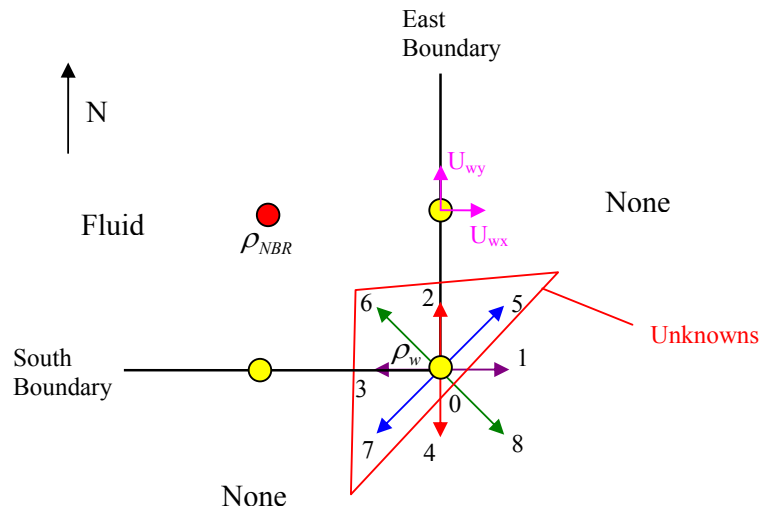


Fig. C.4: Velocity boundary condition at the South-East (SE) corner. The x - and y -velocity of the fluid is specified to be U_{wx} and U_{wy} , respectively. Distribution functions g_2 , g_3 , g_5 , g_6 , g_7 and the density ρ_w are unknown.

C.5 North East (NE) corner

Unknowns at the NE corner can be obtained following the process for the SW corner in Sec. 5.1.2. In this section, we only provide the resulting equations.

Below are the equations which should be solved in order to obtain the desired unknowns at the NE corner (see Fig. C.5).

$$\rho_w = \rho_{NBR} \quad (C.29)$$

$$g_3 = g_1 + (g_3^{eq} - g_1^{eq}) \quad (C.30)$$

$$g_4 = g_2 + (g_4^{eq} - g_2^{eq}) \quad (C.31)$$

$$-g_7 - g_6 + g_8 = g_3 - g_5 - g_1 + \rho_w U_{wx} - \frac{\Delta t}{2} F_x^C \quad (C.32)$$

$$-g_7 + g_6 - g_8 = g_4 - g_5 - g_2 + \rho_w U_{wy} - \frac{\Delta t}{2} F_y^C \quad (C.33)$$

$$g_7 = -\left\{ \frac{(-g_7 - g_6 + g_8) + (-g_7 + g_6 - g_8)}{2} \right\} \quad (C.34)$$

$$g_6 - g_8 = (-g_7 + g_6 - g_8) + g_7 \quad (C.35)$$

$$g_6 + g_8 = \rho_w - (g_0 + g_1 + g_2 + g_3 + g_4 + g_5 + g_7) \quad (C.36)$$

$$g_6 = \frac{(g_6 + g_8) + (g_6 - g_8)}{2} \quad (C.37)$$

$$g_8 = \frac{(g_6 + g_8) - (g_6 - g_8)}{2} \quad (C.38)$$

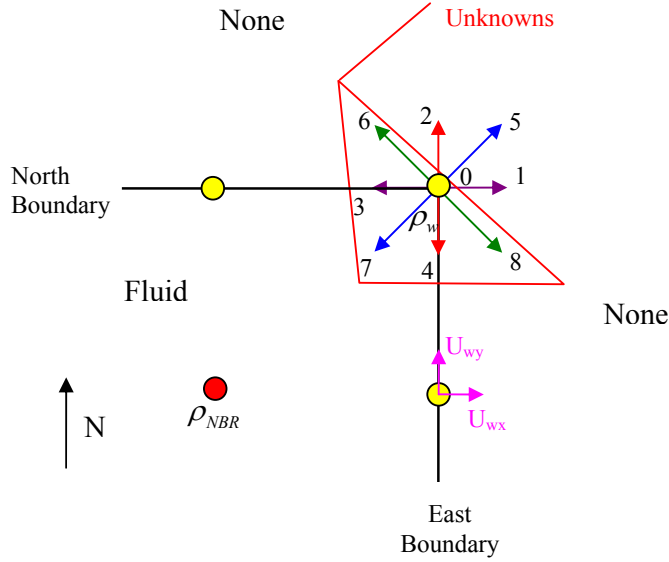


Fig. C.5: Velocity boundary condition at the North-East (NE) corner. The x - and y -velocity of the fluid is specified to be U_{wx} and U_{wy} , respectively. Distribution functions g_3, g_4, g_6, g_7, g_8 and the density ρ_w are unknown.

C.6 North West (NW) corner

Unknowns at the NW corner can be obtained following the process for the SW corner in Sec. 5.1.2. In this section, we only provide the resulting equations.

Below are the equations which should be solved in order to obtain the desired unknowns at the NW corner (see Fig. C.6).

$$\rho_w = \rho_{NBR} \quad (C.39)$$

$$g_1 = g_3 + (g_1^{eq} - g_3^{eq}) \quad (C.40)$$

$$g_4 = g_2 + (g_4^{eq} - g_2^{eq}) \quad (C.41)$$

$$g_5 - g_7 + g_8 = g_3 + g_6 - g_1 + \rho_w U_{wx} - \frac{\Delta t}{2} F_x^C \quad (C.42)$$

$$g_5 - g_7 - g_8 = g_4 - g_6 - g_2 + \rho_w U_{wy} - \frac{\Delta t}{2} F_y^C \quad (C.43)$$

$$g_8 = \frac{(g_5 - g_7 + g_8) - (g_5 - g_7 - g_8)}{2} \quad (C.44)$$

$$g_5 - g_7 = (g_5 - g_7 + g_8) - g_8 \quad (C.45)$$

$$g_5 + g_7 = \rho_w - (g_0 + g_1 + g_2 + g_3 + g_4 + g_6 + g_8) \quad (C.46)$$

$$g_5 = \frac{(g_5 + g_7) + (g_5 - g_7)}{2} \quad (C.47)$$

$$g_7 = \frac{(g_5 + g_7) - (g_5 - g_7)}{2} \quad (C.48)$$

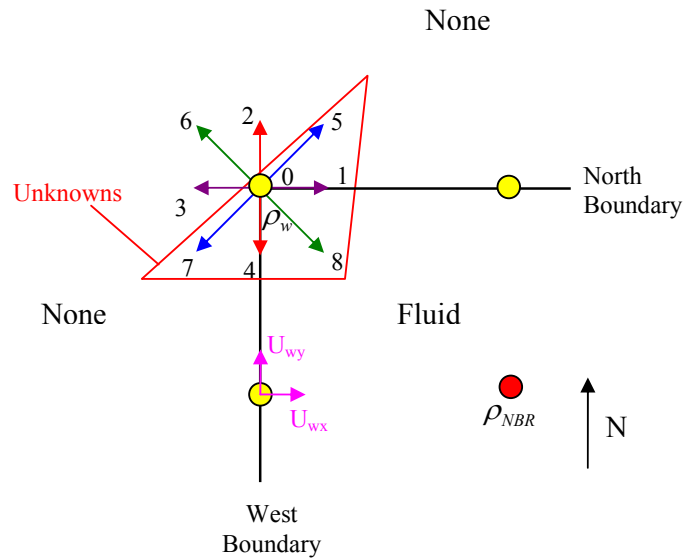


Fig. C.6: Velocity boundary condition at the North-West (NW) corner. The x - and y -velocity of the fluid is specified to be U_{wx} and U_{wy} , respectively. Distribution functions g_1, g_4, g_5, g_7, g_8 and the density ρ_w are unknown.

Appendix D

Density boundary conditions in 2D

In this appendix, density boundary conditions for the North, East and West boundaries in a 2D domain are presented. Since respective corners of the above boundaries are treated in a special way, results for them are also presented.

D.1 North, West and East boundaries

Unknowns at the North, West and East boundaries can be obtained following the process for the South boundary in Sec. 5.2.1. In this section, we only provide the resulting equations.

Below are the equations which should be solved in order to obtain the desired unknowns ρ_w , g_4 , g_7 and g_8 at the North boundary (see Fig. C.1).

$$U_{wy} = \left\{ g_0 + g_1 + g_3 + 2(g_2 + g_5 + g_6) + \frac{\Delta t}{2} F_y^C - \rho_w \right\} / \rho_w \quad (D.1)$$

$$g_4 = g_2 + (g_4^{eq} - g_2^{eq}) \quad (D.2)$$

$$g_7 - g_8 = (g_1 + g_5) - (g_3 + g_6) - \rho_w U_{wx} + \frac{\Delta t}{2} F_x^C \quad (D.3)$$

$$g_7 + g_8 = g_2 + g_5 + g_6 - g_4 - \rho_w U_{wy} + \frac{\Delta t}{2} F_y^C \quad (D.4)$$

$$g_7 = \frac{(g_7 + g_8) + (g_7 - g_8)}{2} \quad (D.5)$$

$$g_8 = \frac{(g_7 + g_8) - (g_7 - g_8)}{2} \quad (D.6)$$

Below are the equations which should be solved in order to obtain the desired unknowns ρ_w , g_1 , g_5 and g_8 at the West boundary (see Fig. C.2).

$$U_{wx} = \left\{ g_0 + g_2 + g_4 + 2(g_3 + g_6 + g_7) - \frac{\Delta t}{2} F_x^C - \rho_w \right\} / (-\rho_w) \quad (D.7)$$

$$g_1 = g_3 + (g_1^{eq} - g_3^{eq}) \quad (D.8)$$

$$g_5 - g_8 = (g_4 + g_7) - (g_2 + g_6) + \rho_w U_{wy} - \frac{\Delta t}{2} F_y^C \quad (D.9)$$

$$g_5 + g_8 = g_3 + g_6 + g_7 - g_1 + \rho_w U_{wx} - \frac{\Delta t}{2} F_x^C \quad (D.10)$$

$$g_5 = \frac{(g_5 + g_8) + (g_5 - g_8)}{2} \quad (D.11)$$

$$g_8 = \frac{(g_5 + g_8) - (g_5 - g_8)}{2} \quad (D.12)$$

Below are the equations which should be solved in order to obtain the desired unknowns ρ_w , g_3 , g_6 and g_7 at the East boundary (see Fig. C.3).

$$U_{wx} = \left\{ g_0 + g_2 + g_4 + 2(g_1 + g_5 + g_8) + \frac{\Delta t}{2} F_x^C - \rho_w \right\} / \rho_w \quad (D.13)$$

$$g_3 = g_1 + (g_3^{eq} - g_1^{eq}) \quad (D.14)$$

$$g_7 - g_6 = (g_2 + g_5) - (g_4 + g_8) - \rho_w U_{wy} + \frac{\Delta t}{2} F_y^C \quad (D.15)$$

$$g_7 + g_6 = g_1 + g_5 + g_8 - g_3 - \rho_w U_{wx} + \frac{\Delta t}{2} F_x^C \quad (D.16)$$

$$g_7 = \frac{(g_7 + g_6) + (g_7 - g_6)}{2} \quad (D.17)$$

$$g_6 = \frac{(g_7 + g_6) - (g_7 - g_6)}{2} \quad (D.18)$$

D.2 South East (SE), North East (NE) and North West (NW) corners

Unknowns at the SE, NE and NW corners can be obtained following the process for the SW corner in Sec. 5.2.2. In this section, we only provide the resulting equations.

Below are the equations which should be solved in order to obtain the desired unknowns at the SE corner (see Fig. C.4).

$$\rho_w = \rho_{NBR} \quad (D.19)$$

$$g_3 = g_1 + (g_3^{eq} - g_1^{eq}) \quad (D.20)$$

$$g_2 = g_4 + (g_2^{eq} - g_4^{eq}) \quad (D.21)$$

$$g_5 - g_6 - g_7 = g_3 - g_8 - g_1 + \rho_w U_{wx} - \frac{\Delta t}{2} F_x^C \quad (D.22)$$

$$g_5 + g_6 - g_7 = g_4 + g_8 - g_2 + \rho_w U_{wy} - \frac{\Delta t}{2} F_y^C \quad (D.23)$$

$$g_6 = \frac{(g_5 + g_6 - g_7) - (g_5 - g_6 - g_7)}{2} \quad (D.24)$$

$$g_5 - g_7 = (g_5 + g_6 - g_7) - g_6 \quad (D.25)$$

$$g_5 + g_7 = \rho_w - (g_0 + g_1 + g_2 + g_3 + g_4 + g_6 + g_8) \quad (D.26)$$

$$g_5 = \frac{(g_5 + g_7) + (g_5 - g_7)}{2} \quad (D.27)$$

$$g_7 = \frac{(g_5 + g_7) - (g_5 - g_7)}{2} \quad (D.28)$$

Below are the equations which should be solved in order to obtain the desired unknowns at the NE corner (see Fig. C.5).

$$\rho_w = \rho_{NBR} \quad (D.29)$$

$$g_3 = g_1 + (g_3^{eq} - g_1^{eq}) \quad (D.30)$$

$$g_4 = g_2 + (g_4^{eq} - g_2^{eq}) \quad (D.31)$$

$$-g_7 - g_6 + g_8 = g_3 - g_5 - g_1 + \rho_w U_{wx} - \frac{\Delta t}{2} F_x^C \quad (D.32)$$

$$-g_7 + g_6 - g_8 = g_4 - g_5 - g_2 + \rho_w U_{wy} - \frac{\Delta t}{2} F_y^C \quad (D.33)$$

$$g_7 = - \left\{ \frac{(-g_7 - g_6 + g_8) + (-g_7 + g_6 - g_8)}{2} \right\} \quad (D.34)$$

$$g_6 - g_8 = (-g_7 + g_6 - g_8) + g_7 \quad (D.35)$$

$$g_6 + g_8 = \rho_w - (g_0 + g_1 + g_2 + g_3 + g_4 + g_5 + g_7) \quad (D.36)$$

$$g_6 = \frac{(g_6 + g_8) + (g_6 - g_8)}{2} \quad (D.37)$$

$$g_8 = \frac{(g_6 + g_8) - (g_6 - g_8)}{2} \quad (D.38)$$

Below are the equations which should be solved in order to obtain the desired unknowns at the NW corner (see Fig. C.6).

$$\rho_w = \rho_{NBR} \quad (D.39)$$

$$g_1 = g_3 + (g_1^{eq} - g_3^{eq}) \quad (D.40)$$

$$g_4 = g_2 + (g_4^{eq} - g_2^{eq}) \quad (D.41)$$

$$g_5 - g_7 + g_8 = g_3 + g_6 - g_1 + \rho_w U_{wx} - \frac{\Delta t}{2} F_x^C \quad (D.42)$$

$$g_5 - g_7 - g_8 = g_4 - g_6 - g_2 + \rho_w U_{wy} - \frac{\Delta t}{2} F_y^C \quad (D.43)$$

$$g_8 = \frac{(g_5 - g_7 + g_8) - (g_5 - g_7 - g_8)}{2} \quad (D.44)$$

$$g_5 - g_7 = (g_5 - g_7 + g_8) - g_8 \quad (D.45)$$

$$g_5 + g_7 = \rho_w - (g_0 + g_1 + g_2 + g_3 + g_4 + g_6 + g_8) \quad (D.46)$$

$$g_5 = \frac{(g_5 + g_7) + (g_5 - g_7)}{2} \quad (D.47)$$

$$g_7 = \frac{(g_5 + g_7) - (g_5 - g_7)}{2} \quad (D.48)$$

Appendix E

Velocity boundary conditions in 3D

In this appendix, velocity boundary conditions for the Top, South, North, East and West boundaries in a 3D domain are presented.

E.1 Top boundary

Unknowns:

ρ_w , g_6 , g_{12} , g_{13} , g_{16} and g_{17}

Mass conservation:

$$\rho_w = \sum_{a=0}^{18} g_a \quad (E.1)$$

Momentum conservation:

$$\rho_w U_{wx} = (g_1 + g_7 + g_{10} + g_{11} + g_{12}) - (g_2 + g_8 + g_9 + g_{13} + g_{14}) + \frac{\Delta t}{2} F_x^C \quad (E.2)$$

$$\rho_w U_{wy} = (g_3 + g_7 + g_8 + g_{15} + g_{16}) - (g_4 + g_9 + g_{10} + g_{17} + g_{18}) + \frac{\Delta t}{2} F_y^C \quad (E.3)$$

$$\rho_w U_{wz} = (g_5 + g_{11} + g_{14} + g_{15} + g_{18}) - (g_6 + g_{12} + g_{13} + g_{16} + g_{17}) + \frac{\Delta t}{2} F_z^C \quad (E.4)$$

From equations (E.1) and (E.4):

$$\rho_w = \frac{1}{(1+U_{wz})} \left\{ g_0 + g_1 + g_2 + g_3 + g_4 + g_7 + g_8 + g_9 + g_{10} + 2(g_5 + g_{11} + g_{14} + g_{15} + g_{18}) + \frac{\Delta t}{2} F_z^C \right\} \quad (E.5)$$

Assuming the partial bounce back of the non equilibrium distribution functions,

$$g_a = g_{\bar{a}} + (g_a^{eq} - g_{\bar{a}}^{eq}) + (v_{a,x} \delta_x + v_{a,y} \delta_y + v_{a,z} \delta_z) \quad (E.6)$$

where $\{a, \bar{a}\} = \{6, 5\}, \{12, 14\}, \{13, 11\}, \{16, 18\}, \{17, 15\}$.

The above equation can be written in more explicit form as,

$$g_6 = g_5 + (g_6^{eq} - g_5^{eq}) - \delta_z \quad (E.7)$$

$$g_{13} = g_{11} + (g_{13}^{eq} - g_{11}^{eq}) - \delta_x - \delta_z \quad (E.8)$$

$$g_{12} = g_{14} + (g_{12}^{eq} - g_{14}^{eq}) + \delta_x - \delta_z \quad (E.9)$$

$$g_{17} = g_{15} + (g_{17}^{eq} - g_{15}^{eq}) - \delta_y - \delta_z \quad (E.10)$$

$$g_{16} = g_{18} + (g_{16}^{eq} - g_{18}^{eq}) + \delta_y - \delta_z \quad (E.11)$$

Algebraic manipulations give,

$$(g_{11} - g_{13}) - (g_{14} - g_{12}) = (g_{11}^{eq} - g_{13}^{eq}) - (g_{14}^{eq} - g_{12}^{eq}) + 2\delta_x \quad (E.12)$$

$$(g_{15} - g_{17}) - (g_{18} - g_{16}) = (g_{15}^{eq} - g_{17}^{eq}) - (g_{18}^{eq} - g_{16}^{eq}) + 2\delta_y \quad (E.13)$$

Now, using the momentum conservation relations,

$$\begin{aligned} \rho_w U_{wx} = & (g_1 + g_7 + g_{10}) - (g_2 + g_8 + g_9) + \frac{\Delta t}{2} F_x^C \\ & + (g_{11}^{eq} - g_{13}^{eq}) - (g_{14}^{eq} - g_{12}^{eq}) + 2\delta_x \end{aligned} \quad (E.14)$$

$$\begin{aligned} \rho_w U_{wy} = & (g_3 + g_7 + g_8) - (g_4 + g_9 + g_{10}) + \frac{\Delta t}{2} F_y^C \\ & + (g_{15}^{eq} - g_{17}^{eq}) - (g_{18}^{eq} - g_{16}^{eq}) + 2\delta_y \end{aligned} \quad (E.15)$$

$$\begin{aligned} \rho_w U_{wz} = & (g_5^{eq} + g_{11}^{eq} + g_{14}^{eq} + g_{15}^{eq} + g_{18}^{eq}) \\ & - (g_6^{eq} + g_{12}^{eq} + g_{13}^{eq} + g_{16}^{eq} + g_{17}^{eq}) + \frac{\Delta t}{2} F_z^C + 5\delta_z \end{aligned} \quad (E.16)$$

From the above equations, unknowns can be evaluated as:

$$\delta_x = \frac{1}{2} \left\{ \rho_w U_{wx} - (g_1 + g_7 + g_{10}) + (g_2 + g_8 + g_9) - \frac{\Delta t}{2} F_x^C \right. \\ \left. - (g_{11}^{eq} - g_{13}^{eq}) + (g_{14}^{eq} - g_{12}^{eq}) \right\} \quad (E.17)$$

$$\delta_y = \frac{1}{2} \left\{ \rho_w U_{wy} - (g_3 + g_7 + g_8) + (g_4 + g_9 + g_{10}) - \frac{\Delta t}{2} F_y^C \right. \\ \left. - (g_{15}^{eq} - g_{17}^{eq}) + (g_{18}^{eq} - g_{16}^{eq}) \right\} \quad (E.18)$$

$$\delta_z = \frac{1}{5} \left\{ \rho_w U_{wz} - (g_5^{eq} + g_{11}^{eq} + g_{14}^{eq} + g_{15}^{eq} + g_{18}^{eq}) \right. \\ \left. + (g_6^{eq} + g_{12}^{eq} + g_{13}^{eq} + g_{16}^{eq} + g_{17}^{eq}) - \frac{\Delta t}{2} F_z^C \right\} \quad (E.19)$$

E.2 South boundary

Unknowns:

ρ_w , g_3 , g_7 , g_8 , g_{15} and g_{16}

Mass conservation:

$$\rho_w = \sum_{a=0}^{18} g_a \quad (E.20)$$

Momentum conservation:

$$\rho_w U_{wx} = (g_1 + g_7 + g_{10} + g_{11} + g_{12}) - (g_2 + g_8 + g_9 + g_{13} + g_{14}) + \frac{\Delta t}{2} F_x^C \quad (E.21)$$

$$\rho_w U_{wy} = (g_3 + g_7 + g_8 + g_{15} + g_{16}) - (g_4 + g_9 + g_{10} + g_{17} + g_{18}) + \frac{\Delta t}{2} F_y^C \quad (E.22)$$

$$\rho_w U_{wz} = (g_5 + g_{11} + g_{14} + g_{15} + g_{18}) - (g_6 + g_{12} + g_{13} + g_{16} + g_{17}) + \frac{\Delta t}{2} F_z^C \quad (E.23)$$

From equations (E.20) and (E.22):

$$\rho_w = \frac{1}{(1 - U_{wy})} \left\{ g_0 + g_1 + g_2 + g_5 + g_6 + g_{11} + g_{12} + g_{13} + g_{14} + 2(g_4 + g_9 + g_{10} + g_{17} + g_{18}) - \frac{\Delta t}{2} F_y^C \right\} \quad (E.24)$$

Assuming the partial bounce back of the non equilibrium distribution functions,

$$g_a = g_{\bar{a}} + (g_a^{eq} - g_{\bar{a}}^{eq}) + (v_{a,x} \delta_x + v_{a,y} \delta_y + v_{a,z} \delta_z) \quad (E.25)$$

where $\{a, \bar{a}\} = \{3, 4\}, \{7, 9\}, \{8, 10\}, \{15, 17\}, \{16, 18\}$.

The above equation can be written in more explicit form as,

$$g_3 = g_4 + (g_3^{eq} - g_4^{eq}) + \delta_y \quad (E.26)$$

$$g_7 = g_9 + (g_7^{eq} - g_9^{eq}) + \delta_x + \delta_y \quad (E.27)$$

$$g_8 = g_{10} + (g_8^{eq} - g_{10}^{eq}) - \delta_x + \delta_y \quad (E.28)$$

$$g_{15} = g_{17} + (g_{15}^{eq} - g_{17}^{eq}) + \delta_y + \delta_z \quad (E.29)$$

$$g_{16} = g_{18} + (g_{16}^{eq} - g_{18}^{eq}) + \delta_y - \delta_z \quad (E.30)$$

Algebraic manipulations give,

$$(g_7 - g_9) - (g_8 - g_{10}) = (g_7^{eq} - g_9^{eq}) - (g_8^{eq} - g_{10}^{eq}) + 2\delta_x \quad (E.31)$$

$$(g_{15} - g_{17}) - (g_{16} - g_{18}) = (g_{15}^{eq} - g_{17}^{eq}) - (g_{16}^{eq} - g_{18}^{eq}) + 2\delta_z \quad (E.32)$$

Now, using the momentum conservation relations,

$$\begin{aligned} \rho_w U_{wx} &= (g_1 + g_{11} + g_{12}) - (g_2 + g_{13} + g_{14}) + \frac{\Delta t}{2} F_x^C \\ &\quad + (g_7^{eq} - g_9^{eq}) - (g_8^{eq} - g_{10}^{eq}) + 2\delta_x \end{aligned} \quad (E.33)$$

$$\begin{aligned}\rho_w U_{wy} = & \left(g_3^{eq} + g_7^{eq} + g_8^{eq} + g_{15}^{eq} + g_{16}^{eq} \right) \\ & - \left(g_4^{eq} + g_9^{eq} + g_{10}^{eq} + g_{17}^{eq} + g_{18}^{eq} \right) + \frac{\Delta t}{2} F_y^C + 5\delta_y\end{aligned}\quad (E.34)$$

$$\begin{aligned}\rho_w U_{wz} = & \left(g_5 + g_{11} + g_{14} \right) - \left(g_6 + g_{12} + g_{13} \right) + \frac{\Delta t}{2} F_z^C \\ & + \left(g_{15}^{eq} - g_{17}^{eq} \right) - \left(g_{16}^{eq} - g_{18}^{eq} \right) + 2\delta_z\end{aligned}\quad (E.35)$$

From the above equations, unknowns can be evaluated as:

$$\delta_x = \frac{1}{2} \left\{ \begin{aligned} & \rho_w U_{wx} - \left(g_1 + g_{11} + g_{12} \right) + \left(g_2 + g_{13} + g_{14} \right) \\ & - \frac{\Delta t}{2} F_x^C - \left(g_7^{eq} - g_9^{eq} \right) + \left(g_8^{eq} - g_{10}^{eq} \right) \end{aligned} \right\} \quad (E.36)$$

$$\delta_y = \frac{1}{5} \left\{ \begin{aligned} & \rho_w U_{wy} - \left(g_3^{eq} + g_7^{eq} + g_8^{eq} + g_{15}^{eq} + g_{16}^{eq} \right) \\ & + \left(g_4^{eq} + g_9^{eq} + g_{10}^{eq} + g_{17}^{eq} + g_{18}^{eq} \right) - \frac{\Delta t}{2} F_y^C \end{aligned} \right\} \quad (E.37)$$

$$\delta_z = \frac{1}{2} \left\{ \begin{aligned} & \rho_w U_{wz} - \left(g_5 + g_{11} + g_{14} \right) + \left(g_6 + g_{12} + g_{13} \right) \\ & - \frac{\Delta t}{2} F_z^C - \left(g_{15}^{eq} - g_{17}^{eq} \right) + \left(g_{16}^{eq} - g_{18}^{eq} \right) \end{aligned} \right\} \quad (E.38)$$

E.3 North boundary

Unknowns:

ρ_w , g_4 , g_9 , g_{10} , g_{17} and g_{18}

Mass conservation:

$$\rho_w = \sum_{a=0}^{18} g_a \quad (E.39)$$

Momentum conservation:

$$\rho_w U_{wx} = \left(g_1 + g_7 + g_{10} + g_{11} + g_{12} \right) - \left(g_2 + g_8 + g_9 + g_{13} + g_{14} \right) + \frac{\Delta t}{2} F_x^C \quad (E.40)$$

$$\rho_w U_{wy} = \left(g_3 + g_7 + g_8 + g_{15} + g_{16} \right) - \left(g_4 + g_9 + g_{10} + g_{17} + g_{18} \right) + \frac{\Delta t}{2} F_y^C \quad (E.41)$$

$$\rho_w U_{wz} = \left(g_5 + g_{11} + g_{14} + g_{15} + g_{18} \right) - \left(g_6 + g_{12} + g_{13} + g_{16} + g_{17} \right) + \frac{\Delta t}{2} F_z^C \quad (E.42)$$

From equations (E.39) and (E.41):

$$\rho_w = \frac{1}{(1+U_{wy})} \left\{ \begin{array}{l} g_0 + g_1 + g_2 + g_5 + g_6 + g_{11} + g_{12} + g_{13} + g_{14} \\ + 2(g_3 + g_7 + g_8 + g_{15} + g_{16}) + \frac{\Delta t}{2} F_y^C \end{array} \right\} \quad (E.43)$$

Assuming the partial bounce back of the non equilibrium distribution functions,

$$g_a = g_{\bar{a}} + (g_a^{eq} - g_{\bar{a}}^{eq}) + (v_{a,x} \delta_x + v_{a,y} \delta_y + v_{a,z} \delta_z) \quad (E.44)$$

where $\{a, \bar{a}\} = \{4, 3\}, \{9, 7\}, \{10, 8\}, \{17, 15\}, \{18, 16\}$.

The above equation can be written in more explicit form as,

$$g_4 = g_3 + (g_4^{eq} - g_3^{eq}) - \delta_y \quad (E.45)$$

$$g_9 = g_7 + (g_9^{eq} - g_7^{eq}) - \delta_x - \delta_y \quad (E.46)$$

$$g_{10} = g_8 + (g_{10}^{eq} - g_8^{eq}) + \delta_x - \delta_y \quad (E.47)$$

$$g_{17} = g_{15} + (g_{17}^{eq} - g_{15}^{eq}) - \delta_y - \delta_z \quad (E.48)$$

$$g_{18} = g_{16} + (g_{18}^{eq} - g_{16}^{eq}) - \delta_y + \delta_z \quad (E.49)$$

Algebraic manipulations give,

$$(g_7 - g_9) - (g_8 - g_{10}) = (g_7^{eq} - g_9^{eq}) - (g_8^{eq} - g_{10}^{eq}) + 2\delta_x \quad (E.50)$$

$$(g_{15} - g_{17}) - (g_{16} - g_{18}) = (g_{15}^{eq} - g_{17}^{eq}) - (g_{16}^{eq} - g_{18}^{eq}) + 2\delta_z \quad (E.51)$$

Now, using the momentum conservation relations,

$$\begin{aligned} \rho_w U_{wx} = & (g_1 + g_{11} + g_{12}) - (g_2 + g_{13} + g_{14}) + \frac{\Delta t}{2} F_x^C \\ & + (g_7^{eq} - g_9^{eq}) - (g_8^{eq} - g_{10}^{eq}) + 2\delta_x \end{aligned} \quad (E.52)$$

$$\begin{aligned} \rho_w U_{wy} = & (g_3^{eq} + g_7^{eq} + g_8^{eq} + g_{15}^{eq} + g_{16}^{eq}) \\ & - (g_4^{eq} + g_9^{eq} + g_{10}^{eq} + g_{17}^{eq} + g_{18}^{eq}) + \frac{\Delta t}{2} F_y^C + 5\delta_y \end{aligned} \quad (E.53)$$

$$\begin{aligned} \rho_w U_{wz} = & (g_5 + g_{11} + g_{14}) - (g_6 + g_{12} + g_{13}) + \frac{\Delta t}{2} F_z^C \\ & + (g_{15}^{eq} - g_{17}^{eq}) - (g_{16}^{eq} - g_{18}^{eq}) + 2\delta_z \end{aligned} \quad (E.54)$$

From the above equations, unknowns can be evaluated as:

$$\delta_x = \frac{1}{2} \left\{ \begin{array}{l} \rho_w U_{wx} - (g_1 + g_{11} + g_{12}) + (g_2 + g_{13} + g_{14}) \\ - \frac{\Delta t}{2} F_x^C - (g_7^{eq} - g_9^{eq}) + (g_8^{eq} - g_{10}^{eq}) \end{array} \right\} \quad (E.55)$$

$$\delta_y = \frac{1}{5} \left\{ \begin{array}{l} \rho_w U_{wy} - (g_3^{eq} + g_7^{eq} + g_8^{eq} + g_{15}^{eq} + g_{16}^{eq}) \\ + (g_4^{eq} + g_9^{eq} + g_{10}^{eq} + g_{17}^{eq} + g_{18}^{eq}) - \frac{\Delta t}{2} F_y^C \end{array} \right\} \quad (E.56)$$

$$\delta_z = \frac{1}{2} \left\{ \begin{array}{l} \rho_w U_{wz} - (g_5 + g_{11} + g_{14}) + (g_6 + g_{12} + g_{13}) \\ - \frac{\Delta t}{2} F_z^C - (g_{15}^{eq} - g_{17}^{eq}) + (g_{16}^{eq} - g_{18}^{eq}) \end{array} \right\} \quad (E.57)$$

E.4 West boundary

Unknowns:

$$\rho_w, g_1, g_7, g_{10}, g_{11} \text{ and } g_{12}$$

Mass conservation:

$$\rho_w = \sum_{a=0}^{18} g_a \quad (E.58)$$

Momentum conservation:

$$\rho_w U_{wx} = (g_1 + g_7 + g_{10} + g_{11} + g_{12}) - (g_2 + g_8 + g_9 + g_{13} + g_{14}) + \frac{\Delta t}{2} F_x^C \quad (E.59)$$

$$\rho_w U_{wy} = (g_3 + g_7 + g_8 + g_{15} + g_{16}) - (g_4 + g_9 + g_{10} + g_{17} + g_{18}) + \frac{\Delta t}{2} F_y^C \quad (E.60)$$

$$\rho_w U_{wz} = (g_5 + g_{11} + g_{14} + g_{15} + g_{18}) - (g_6 + g_{12} + g_{13} + g_{16} + g_{17}) + \frac{\Delta t}{2} F_z^C \quad (E.61)$$

From equations (E.58) and (E.59):

$$\rho_w = \frac{1}{(1 - U_{wx})} \left\{ \begin{array}{l} g_0 + g_3 + g_4 + g_5 + g_6 + g_{15} + g_{16} + g_{17} + g_{18} \\ + 2(g_2 + g_8 + g_9 + g_{13} + g_{14}) - \frac{\Delta t}{2} F_x^C \end{array} \right\} \quad (E.62)$$

Assuming the partial bounce back of the non equilibrium distribution functions,

$$g_a = g_{\bar{a}} + (g_a^{eq} - g_{\bar{a}}^{eq}) + (v_{a,x} \delta_x + v_{a,y} \delta_y + v_{a,z} \delta_z) \quad (E.63)$$

where $\{a, \bar{a}\} = \{1, 2\}, \{7, 9\}, \{10, 8\}, \{11, 13\}, \{12, 14\}$.

The equation above can be written in more explicit form as,

$$g_1 = g_2 + (g_1^{eq} - g_2^{eq}) + \delta_x \quad (E.64)$$

$$g_7 = g_9 + (g_7^{eq} - g_9^{eq}) + \delta_x + \delta_y \quad (E.65)$$

$$g_{10} = g_8 + (g_{10}^{eq} - g_8^{eq}) + \delta_x - \delta_y \quad (E.66)$$

$$g_{11} = g_{13} + (g_{11}^{eq} - g_{13}^{eq}) + \delta_x + \delta_z \quad (E.67)$$

$$g_{12} = g_{14} + (g_{12}^{eq} - g_{14}^{eq}) + \delta_x - \delta_z \quad (E.68)$$

Algebraic manipulations give,

$$(g_7 - g_9) - (g_{10} - g_8) = (g_7^{eq} - g_9^{eq}) - (g_{10}^{eq} - g_8^{eq}) + 2\delta_y \quad (E.69)$$

$$(g_{11} - g_{13}) - (g_{12} - g_{14}) = (g_{11}^{eq} - g_{13}^{eq}) - (g_{12}^{eq} - g_{14}^{eq}) + 2\delta_z \quad (E.70)$$

Now, using the momentum conservation relations,

$$\begin{aligned} \rho_w U_{wx} = & (g_1^{eq} + g_7^{eq} + g_{10}^{eq} + g_{11}^{eq} + g_{12}^{eq}) \\ & - (g_2^{eq} + g_8^{eq} + g_9^{eq} + g_{13}^{eq} + g_{14}^{eq}) + \frac{\Delta t}{2} F_x^C + 5\delta_x \end{aligned} \quad (E.71)$$

$$\begin{aligned} \rho_w U_{wy} = & (g_3 + g_{15} + g_{16}) - (g_4 + g_{17} + g_{18}) + \frac{\Delta t}{2} F_y^C \\ & + (g_7^{eq} - g_9^{eq}) - (g_{10}^{eq} - g_8^{eq}) + 2\delta_y \end{aligned} \quad (E.72)$$

$$\begin{aligned} \rho_w U_{wz} = & (g_5 + g_{15} + g_{18}) - (g_6 + g_{16} + g_{17}) + \frac{\Delta t}{2} F_z^C \\ & + (g_{11}^{eq} - g_{13}^{eq}) - (g_{12}^{eq} - g_{14}^{eq}) + 2\delta_z \end{aligned} \quad (E.73)$$

From the above equations, unknowns can be evaluated as:

$$\delta_x = \frac{1}{5} \left\{ \rho_w U_{wx} - (g_1^{eq} + g_7^{eq} + g_{10}^{eq} + g_{11}^{eq} + g_{12}^{eq}) \right. \\ \left. + (g_2^{eq} + g_8^{eq} + g_9^{eq} + g_{13}^{eq} + g_{14}^{eq}) - \frac{\Delta t}{2} F_x^C \right\} \quad (E.74)$$

$$\delta_y = \frac{1}{2} \left\{ \rho_w U_{wy} - (g_3 + g_{15} + g_{16}) + (g_4 + g_{17} + g_{18}) \right. \\ \left. - \frac{\Delta t}{2} F_y^C - (g_7^{eq} - g_9^{eq}) + (g_{10}^{eq} - g_8^{eq}) \right\} \quad (E.75)$$

$$\delta_z = \frac{1}{2} \left\{ \rho_w U_{wz} - (g_5 + g_{15} + g_{18}) + (g_6 + g_{16} + g_{17}) \right. \\ \left. - \frac{\Delta t}{2} F_z^C - (g_{11}^{eq} - g_{13}^{eq}) + (g_{12}^{eq} - g_{14}^{eq}) \right\} \quad (E.76)$$

E.5 East boundary

Unknowns:

ρ_w , g_2 , g_9 , g_8 , g_{13} and g_{14}

Mass conservation:

$$\rho_w = \sum_{a=0}^{18} g_a \quad (E.77)$$

Momentum conservation:

$$\rho_w U_{wx} = (g_1 + g_7 + g_{10} + g_{11} + g_{12}) - (g_2 + g_8 + g_9 + g_{13} + g_{14}) + \frac{\Delta t}{2} F_x^C \quad (E.78)$$

$$\rho_w U_{wy} = (g_3 + g_7 + g_8 + g_{15} + g_{16}) - (g_4 + g_9 + g_{10} + g_{17} + g_{18}) + \frac{\Delta t}{2} F_y^C \quad (E.79)$$

$$\rho_w U_{wz} = (g_5 + g_{11} + g_{14} + g_{15} + g_{18}) - (g_6 + g_{12} + g_{13} + g_{16} + g_{17}) + \frac{\Delta t}{2} F_z^C \quad (E.80)$$

From equations (E.77) and (E.78):

$$\rho_w = \frac{1}{(1+U_{wx})} \left\{ g_0 + g_3 + g_4 + g_5 + g_6 + g_{15} + g_{16} + g_{17} + g_{18} + 2(g_1 + g_7 + g_{10} + g_{11} + g_{12}) + \frac{\Delta t}{2} F_x^C \right\} \quad (E.81)$$

Assuming the partial bounce back of the non equilibrium distribution functions,

$$g_a = g_{\bar{a}} + (g_a^{eq} - g_{\bar{a}}^{eq}) + (v_{a,x} \delta_x + v_{a,y} \delta_y + v_{a,z} \delta_z) \quad (E.82)$$

where $\{a, \bar{a}\} = \{2, 1\}, \{9, 7\}, \{8, 10\}, \{13, 11\}, \{14, 12\}$.

The equation above can be written in more explicit form as,

$$g_2 = g_1 + (g_2^{eq} - g_1^{eq}) - \delta_x \quad (E.83)$$

$$g_9 = g_7 + (g_9^{eq} - g_7^{eq}) - \delta_x - \delta_y \quad (E.84)$$

$$g_8 = g_{10} + (g_8^{eq} - g_{10}^{eq}) - \delta_x + \delta_y \quad (E.85)$$

$$g_{13} = g_{11} + (g_{13}^{eq} - g_{11}^{eq}) - \delta_x - \delta_z \quad (E.86)$$

$$g_{14} = g_{12} + (g_{14}^{eq} - g_{12}^{eq}) - \delta_x + \delta_z \quad (E.87)$$

Algebraic manipulations give,

$$(g_7 - g_9) - (g_{10} - g_8) = (g_7^{eq} - g_9^{eq}) - (g_{10}^{eq} - g_8^{eq}) + 2\delta_y \quad (E.88)$$

$$(g_{11} - g_{13}) - (g_{12} - g_{14}) = (g_{11}^{eq} - g_{13}^{eq}) - (g_{12}^{eq} - g_{14}^{eq}) + 2\delta_z \quad (E.89)$$

Now, using the momentum conservation relations,

$$\begin{aligned} \rho_w U_{wx} = & (g_1^{eq} + g_7^{eq} + g_{10}^{eq} + g_{11}^{eq} + g_{12}^{eq}) \\ & - (g_2^{eq} + g_8^{eq} + g_9^{eq} + g_{13}^{eq} + g_{14}^{eq}) + \frac{\Delta t}{2} F_x^C + 5\delta_x \end{aligned} \quad (E.90)$$

$$\begin{aligned}\rho_w U_{wy} = & (g_3 + g_{15} + g_{16}) - (g_4 + g_{17} + g_{18}) + \frac{\Delta t}{2} F_y^C \\ & + (g_7^{eq} - g_9^{eq}) - (g_{10}^{eq} - g_8^{eq}) + 2\delta_y\end{aligned}\quad (E.91)$$

$$\begin{aligned}\rho_w U_{wz} = & (g_5 + g_{15} + g_{18}) - (g_6 + g_{16} + g_{17}) + \frac{\Delta t}{2} F_z^C \\ & + (g_{11}^{eq} - g_{13}^{eq}) - (g_{12}^{eq} - g_{14}^{eq}) + 2\delta_z\end{aligned}\quad (E.92)$$

From the above equations, unknowns can be evaluated as:

$$\delta_x = \frac{1}{5} \left\{ \begin{array}{l} \rho_w U_{wx} - (g_1^{eq} + g_7^{eq} + g_{10}^{eq} + g_{11}^{eq} + g_{12}^{eq}) \\ + (g_2^{eq} + g_8^{eq} + g_9^{eq} + g_{13}^{eq} + g_{14}^{eq}) - \frac{\Delta t}{2} F_x^C \end{array} \right\} \quad (E.93)$$

$$\delta_y = \frac{1}{2} \left\{ \begin{array}{l} \rho_w U_{wy} - (g_3 + g_{15} + g_{16}) + (g_4 + g_{17} + g_{18}) \\ - \frac{\Delta t}{2} F_y^C - (g_7^{eq} - g_9^{eq}) + (g_{10}^{eq} - g_8^{eq}) \end{array} \right\} \quad (E.94)$$

$$\delta_z = \frac{1}{2} \left\{ \begin{array}{l} \rho_w U_{wz} - (g_5 + g_{15} + g_{18}) + (g_6 + g_{16} + g_{17}) \\ - \frac{\Delta t}{2} F_z^C - (g_{11}^{eq} - g_{13}^{eq}) + (g_{12}^{eq} - g_{14}^{eq}) \end{array} \right\} \quad (E.95)$$

Appendix F

Mathematica routine for Maxwell construction

Below is the Mathematica algorithm to apply Maxwell equal-area construction and compute the equilibrium phase densities for the van der Waals equation of state:

! Define the van der Waals equation

! Rearrange for pressure

! Calculate critical constants (V_C and T_c)

! Calculate a and b in terms of critical constants (V_C and T_c)

! Calculate P_c

! List critical parameters (P_c , V_C and T_c)

! Calculate the critical compressibility factor $Z = \frac{P_c V_c}{R T_c}$

! Write the vdW equation of state in reduced variables

! Identify the limiting pressure values (pressures corresponding to points B and C) at a given reduced temperature (for example, at reduced temperature $T_R = 0.3$)

! Guess a suitable pressure value between the above two limiting values. One may choose the average of these two if it is non-zero.

! Calculate phase volumes corresponding to the intersection of the horizontal line described by above mid-pressure with the P-V curve.

! Define area under the horizontal line as ‘Area-1’

! Define area under the P-V curve as ‘Area-2’

! Find the equilibrium pressure value for which these two areas are equal

! List the equilibrium pressure and the volumes of two coexisting phases

(Actual code can be found in Prashant, 2010)

Appendix G

Conversion between physical and lattice units

One of the key steps in applying LBM to solve physical problems is the accurate conversion between physical and lattice units. There are two widely used methods: one is to directly convert between the physical and lattice units (which may be called direct conversion), and another is to perform the conversion via a non-dimensional formulation (which may be called dimensionless formulation). In the following sections, these two methods are discussed in detail:

G.1 Direct conversion

In the direct conversion approach, lattice units are related to the physical units via the time step Δt and spatial grid size h . A list of physical and lattice units, and their relationship are provided in the Table G.1 (taken from Feng et al., 2007).

Table G.1: Relationship between physical and lattice units in a LB calculation.

Variable	Physical	Lattice	Relationship
Density	ρ	$\bar{\rho}$	$\rho = \rho_{ref} \bar{\rho}$
Grid spacing	$\Delta x = \Delta y = h$	$\Delta \bar{x} = \Delta \bar{y} = \bar{h} = 1$	
Time step	Δt	$\Delta \bar{t} = 1$	
Lattice speed	$c = \frac{h}{\Delta t}$	$\bar{c} = \frac{\bar{h}}{\Delta \bar{t}} = 1$	
Coordinates/displacement	\mathbf{x}	$\bar{\mathbf{x}}$	$\mathbf{x} = h \bar{\mathbf{x}}$
Macroscopic velocity	$\mathbf{u} = \frac{\Delta \mathbf{x}}{\Delta t}$	$\bar{\mathbf{u}} = \frac{\Delta \bar{\mathbf{x}}}{\Delta \bar{t}}$	$\mathbf{u} = \frac{h}{\Delta t} \bar{\mathbf{u}}$
Speed of sound	$c_{s,phy} = \frac{1}{\sqrt{3}} \frac{h}{\Delta t}$	$\bar{c}_{s,lattice} = \frac{1}{\sqrt{3}} \frac{\bar{h}}{\Delta \bar{t}}$	$c_{s,phy} = \frac{h}{\Delta t} \bar{c}_{s,lattice}$
Acceleration	$\mathbf{a} = \frac{\Delta \mathbf{u}}{\Delta t}$	$\bar{\mathbf{a}} = \frac{\Delta \bar{\mathbf{u}}}{\Delta \bar{t}}$	$\mathbf{a} = \frac{h/\Delta t}{\Delta t} \bar{\mathbf{a}}$
Kinematic viscosity (for 1 st order discretization)	$\nu = \bar{c}_{s,lattice}^2 \left(\tau - \frac{1}{2} \right) \frac{h^2}{\Delta t}$	$\bar{\nu} = \bar{c}_{s,lattice}^2 \left(\tau - \frac{1}{2} \right) \frac{\bar{h}^2}{\Delta \bar{t}}$	$\nu = \bar{\nu} \frac{h^2}{\Delta t}$
(for 2 nd order discretization)	$\nu = \tau \bar{c}_{s,lattice}^2 \frac{h^2}{\Delta t}$	$\bar{\nu} = \tau \bar{c}_{s,lattice}^2 \frac{\bar{h}^2}{\Delta \bar{t}}$	

G.1.1 Acoustics based conversion

From Table G.1, we have:

$$v = \bar{c}_{s,lattice}^2 \tau^* \frac{h^2}{\Delta t} \quad (G.1)$$

where τ^* is either $(\tau - 0.5)$ or τ depending upon the discretization used in formulating the LBE.

$$c_{s,phy} = \frac{h}{\Delta t} \bar{c}_{s,lattice} \quad (G.2)$$

From the above equations, we can write:

$$v = c_{s,phy}^2 \tau^* \Delta t \quad (G.3)$$

or,

$$\Delta t = \frac{v}{c_{s,phy}^2 \tau^*} \quad (G.4)$$

and

$$h = \frac{c_{s,phy} \Delta t}{\bar{c}_{s,lattice}} = \frac{v}{\bar{c}_{s,lattice} c_{s,phy} \tau^*} \quad (G.5)$$

For example, if a system with the following known physical quantities for air at temperature = 300 K (Nourgaliev et al., 2003) is to be simulated:

Physical speed of sound $c_{s,phy} = 300$ m/s (in air)

Kinematic viscosity of air $\nu_{air,phy} = 10^{-5}$ m²/s

Then, from the above equations, one LB grid spacing and one LB time step correspond to (τ^* can be chosen to be 0.01 from numerical stability considerations):

$$\Delta t = \frac{10^{-5}}{(300)^2 (10^{-2})} = 1.1 \times 10^{-8} \text{ s} \quad (G.6)$$

$$h = \frac{10^{-5}}{\left(\frac{1}{\sqrt{3}}\right)(300)(10^{-2})} = 5.8 \times 10^{-6} \text{ m} \quad (G.7)$$

Similarly, for water, we have: $c_{s,phy} \approx 1500$ m/s and $\nu_{water} \approx 10^{-7}$ m²/s. Now, using these values and $\tau^* = 0.01$, we get:

$$\Delta t = \frac{10^{-7}}{(1500)^2 (10^{-2})} = 4.4 \times 10^{-12} s \quad (G.8)$$

$$h = \frac{10^{-7}}{\left(\frac{1}{\sqrt{3}}\right)(1500)(10^{-2})} = 1.1 \times 10^{-8} m \quad (G.9)$$

G.1.2 Gravity based conversion

For a simulation in which gravity is the driving force for the flow, one can find the time and space conversion factors by using the relations below.

$$\mathbf{g} = \frac{h/\Delta t}{\Delta t} \bar{\mathbf{g}} \quad (G.10)$$

$$\nu = \bar{c}_{s,lattice}^2 \tau^* \frac{h^2}{\Delta t} \quad (G.11)$$

The above equations yield:

$$\Delta t = \left[\frac{\nu}{\bar{c}_{s,lattice}^2 \tau^*} \left(\frac{\bar{\mathbf{g}}}{\mathbf{g}} \right)^2 \right]^{\frac{1}{3}} \quad (G.12)$$

and

$$h = \left[\frac{\nu}{\bar{c}_{s,lattice}^2 \tau^*} \sqrt{\frac{\bar{\mathbf{g}}}{\mathbf{g}}} \right]^{\frac{2}{3}} \quad (G.13)$$

For $\mathbf{g} = 10$ m/s² (physical), $\bar{\mathbf{g}} = 10^{-5}$ (LBM), $\nu_{air,phy} = 10^{-5}$ m²/s, $\tau^* = 0.01$ (chosen), $\bar{c}_{s,lattice}^2 = 1/3$ (for D₂Q₉ lattice), we get: $\Delta t = 3.1 \times 10^{-4}$ s and $h = 9.65 \times 10^{-4}$ m.

From equations (G.12) and (G.13), it is clear that an increase of lattice gravity means a simultaneous increase in spatial grid size and time steps (if other physical parameters remain the same), i.e. using a higher lattice gravity is equivalent to simulating a larger system (larger bubble).

Similarly, if one wants to keep the spatial grid resolution and time step of the simulation fixed (i.e. h and Δt fixed), then one needs to redefine the lattice gravity to simulate the same physics in different domain sizes.

G.1.3 How many “physical molecules” does a “LB particle” represent?

Let us suppose that each LB particle represents N molecules and at each lattice site, there are f LB particles (on an average) going in each of the lattice directions of a $D_d Q_b$ lattice. Then, total number of molecules at each lattice site is equal to Nfb (Succi, 2001).

In physical space, if the physical number density of molecules η (molecules per cubic meter) is known and spatial grid size is h then total number of molecules in one lattice cell of volume h^3 is equal to ηh^3 .

From the above arguments, we can calculate N from:

$$N = \frac{\eta h^3}{fb} \quad (\text{G.14})$$

For a $D_2 Q_9$ lattice, we have, $b = 9$, assuming $f = 0.1$ and $h = 1 \mu\text{m}$, we get:

$N = (1.11 \times 10^{-18})\eta$. For an ideal gas, number of molecules per cubic meter at standard temperature and pressure condition is equal to Loschmidt number $\eta = 2.687 \times 10^{25}$ per cubic meter, which gives $N = 3 \times 10^7$ molecules per lattice site (one reason why LBM is called a mesoscopic method).

G.2 Dimensionless formulation

This section is based on the dimensionless unit conversion approach discussed in the handout by Latt (2008). In this approach, the physical system (P) is first converted into a non-dimensional system (ND), and then the non-dimensional system is converted into a lattice Boltzmann system (LB). The three systems (P, ND and LB) are defined such that they have the same Reynolds (Re) number. The transition from P to ND is made by choosing a characteristic length l_0 and time t_0 , and the transition from ND to LB is made by choosing the discrete space step h and time step Δt .

G.2.1 Governing equations in physical units

Usually LB simulations are targeted towards solving an incompressible Navier-Stokes (N-S) equations, which are simply the laws of mass and momentum conservation. The mass conservation equation states that the macroscopic velocity field is divergence-free, i.e.

$$\nabla_p \cdot \mathbf{u}_p = 0 \quad (\text{G.15})$$

where \mathbf{u}_p is the macroscopic velocity and subscript ‘ p ’ indicates the physical units of evaluation.

The momentum conservation equation in physical units can be written as:

$$\partial_{t_p} u_p + (u_p \cdot \nabla_p) u_p = -\frac{1}{\rho_{0,p}} \nabla_p P_p + \nu_p \nabla_p^2 u_p \quad (\text{G.16})$$

where P_p is the pressure and ν_p is the kinematic viscosity in the physical units.

G.2.2 From physical (P) to non-dimensional (ND) system

In order to convert the physical system (P) governed by equations (G.15) and (G.16) into a non-dimensional system (ND), we have to first choose the characteristic length $l_{0,p}$ and time scale $t_{0,p}$ in physical units depending upon the problem being simulated. For example, $l_{0,p}$ can be the size of an obstacle immersed in the fluid or diameter of the bubble or droplet being simulated, and $t_{0,p}$ can be the time needed for a passive scalar to travel the characteristic length in the fluid. Using these characteristic scales, we can now non-dimensionalize the governing equations (G.15) and (G.16) to yield:

$$\nabla_{nd} \cdot \mathbf{u}_{nd} = 0 \quad (\text{G.17})$$

$$\partial_{t_{nd}} u_{nd} + (u_{nd} \cdot \nabla_{nd}) u_{nd} = -\nabla_{nd} P_{nd} + \frac{1}{\text{Re}} \nabla_{nd}^2 u_{nd} \quad (\text{G.18})$$

where $t_{nd} = \frac{t_p}{t_{0,p}}$, $r_{nd} = \frac{r_p}{l_{0,p}}$, $u_{nd} = \frac{u_p}{(l_{0,p}/t_{0,p})}$, $\partial_{t_{nd}} = \frac{1}{t_{0,p}} \partial_{t_p}$, $\nabla_{nd} = \frac{1}{l_{0,p}} \nabla_p$, $P_{nd} = \rho_{0,p} \left(\frac{l_{0,p}}{t_{0,p}} \right)^2 P_p$

and Re is the Reynolds number defined as:

$$\text{Re} = \frac{l_{0,p}^2}{t_{0,p} \nu_p} \quad (\text{G.19})$$

Now, expressing the reference physical variables $l_{0,p}$ and $t_{0,p}$ in non-dimensional units, we get:

$$l_{0,nd} = \frac{l_{0,p}}{l_{0,p}} = 1 \quad (\text{G.20})$$

$$t_{0,nd} = \frac{t_{0,p}}{t_{0,p}} = 1 \quad (\text{G.21})$$

Since Reynolds number remains the same in both the flow configurations (P and ND), we can write:

$$\text{Re} = \frac{l_{0,p}^2}{t_{0,p} \nu_p} = \frac{l_{0,nd}^2}{t_{0,nd} \nu_{nd}} = \frac{1}{\nu_{nd}} \quad (\text{G.22})$$

G.2.3 From non-dimensional (ND) to lattice Boltzmann (LB) system

The discrete space step h is defined as the reference non-dimensional length $l_{0,nd}$ divided by the number of cells N_{cells} used to discretize the length. Similarly, discrete time step Δt is calculated by dividing the reference non-dimensional time $t_{0,nd}$ by the number of time steps $N_{timesteps}$ needed to reach a desired time. Since $l_{0,nd} = 1$ and $t_{0,nd} = 1$, we get:

$$h = \frac{1}{N_{cells}} \quad (\text{G.23})$$

$$\Delta t = \frac{1}{N_{timesteps}} \quad (\text{G.24})$$

Other variables can be converted between (ND) and (LB) systems using:

$$u_{lb} = \frac{u_{nd}}{(h/\Delta t)} \quad (\text{G.25})$$

$$\nu_{lb} = \frac{\Delta t}{h^2} \nu_{nd} = \frac{\Delta t}{h^2} \frac{1}{\text{Re}} \quad (\text{G.26})$$

G.2.4 Illustrative example

In an attempt to explain the unit conversion from (P) to (LB), an example (again, taken from Latt (2008)) is presented below.

Suppose we want to simulate flow in a 2D lid-driven cavity, in which the fluid is confined within a box of size 3 cm x 3 cm. The lid at the top moves with a speed of 2 cm/min. The viscosity of the fluid is 5 cm²/min (Raspberry Jam). The following steps outline the unit conversion process (Latt, 2008):

- Define the physical characteristic length and time scale. Let us select $l_{0,p} = 3$ cm

and $t_{0,p} = \frac{l_{0,p}}{U_{lid}} = 1.5$ min (time taken by the lid to traverse the characteristic length).

- Compute the flow Reynolds number, i.e. $Re = \frac{l_{0,p}^2}{t_{0,p} \nu_p} = 1.2$
- Choose the discretization parameters (grid space and time step). Suppose we want to pick 101 x 101 lattice points to discretize our 2D simulation domain (lattice points lie on the domain boundaries), then $N_{cells} = 100$ which gives the discrete

grid spacing to be $h = \frac{1}{N_{cells}} = 0.01$. Furthermore, let us select Δt to be 2×10^{-4}

(how to appropriately pick Δt will be discussed in the next section).

- Having selected h and Δt , we can now establish u_{lb} (equivalent lattice velocity to simulate the lid velocity) and ν_{lb} (lattice viscosity) from equations (G.25) and (G.26) as:

$$u_{lb} = \frac{u_{nd}}{(h/\Delta t)} = \frac{U_{lid}}{(l_{0,p}/t_{0,p})(h/\Delta t)} = 0.02 \quad (G.27)$$

$$\nu_{lb} = \frac{\Delta t}{h^2} \nu_{nd} = \frac{\Delta t}{h^2} \frac{1}{Re} = 1.67 \quad (G.28)$$

Once lattice viscosity is determined, one can calculate the single-relaxation time τ from its relationship with the lattice viscosity.

G.2.5 How to appropriately pick Δt ?

As discussed in Latt (2008), there is no straightforward intuitive way to choose Δt in a LB simulation. In several other numerical methods, time-step Δt is often linked with space step h from the relation $\Delta t \square h^2$ due to numerical stability considerations. However, in LBM, the relationship between Δt and h results from other constraints.

From equation (G.27), we know that velocities measured in the lattice units are of the order $\Delta t / h$ (i.e. $u_{lb} \square \frac{\Delta t}{h}$), and since the LB velocity should be less than the lattice speed of sound, c_s (i.e. $u_{lb} < c_s$, for subsonic flows), there is a constraint in the form of $\Delta t < \frac{h}{\sqrt{3}}$ where $c_s = \frac{1}{\sqrt{3}}$ for a D₂Q₉ lattice (Latt, 2008).

Another constraint on Δt can be obtained for the simulation of incompressible flows. Since LBM is a quasi-compressible method, i.e. the system in LB simulations enters a slightly compressible regime to solve the pressure equation of the fluid. The compressible effects, however, do affect the numerical accuracy of the system. Since the compressibility error of the LB simulations ε_{comp} scales with the square of Mach-number, Ma^2 (i.e. $\varepsilon \square Ma^2$), we can keep the system close to incompressible by choosing a low Mach number (i.e. low $Ma \equiv \frac{u_{lb}}{c_s}$). From the above discussion, we can write:

$$\varepsilon_{comp} \square Ma^2 \square u_{lb}^2 \square \left(\frac{\Delta t}{h} \right)^2 \quad (G.29)$$

For a second order accurate LBM, the lattice resolution error scales with h as $\varepsilon_{lattice} \square h^2$. In order to keep the order of both error terms the same (i.e. $\varepsilon_{comp} \square \varepsilon_{lattice}$), one can scale the Δt as $\Delta t \square h^2$, which apparently is the same constraint that one encounters in explicit fluid solvers (Latt, 2008).

G.3 References

Feng, Y.T., Han, K., Owen, D.R.J., 2007. Coupled lattice Boltzmann method and discrete element modelling of particle transport in turbulent fluid flows: Computational issues. *Int. J. Numer. Meth. Engng* 72, 1111-1134.

Latt, J, 2008. Choice of units in lattice Boltzmann simulations. Available online from: http://lbmethod.org/_media/howtos:lbunits.pdf. Accessed: November 19, 2009.

Nourgaliev, R.R., Dinh, T.N., Theofanous, T.G., Joseph, D., 2003. The lattice Boltzmann equation method: theoretical interpretation, numerics and implications. *Int. J. Multiphase Flows* 29, 117-169.

Succi, S., 2001. The Lattice Boltzmann Equation—for Fluid Dynamics and Beyond. Appendix D. Oxford Science Publications, UK.